

Advanced Data Assimilation and Predictability Studies on High-Impact Weather and Climate

GUEST EDITORS: ZHAOXIA PU, SONG-YOU HONG, YAOHUI LI,
AND HANN-MING HENRY JUANG





Advanced Data Assimilation and Predictability Studies on High-Impact Weather and Climate

Advances in Meteorology

Advanced Data Assimilation and Predictability Studies on High-Impact Weather and Climate

Guest Editors: Zhaoxia Pu, Song-You Hong, Yaohui Li,
and Hann-Ming Henry Juang



Copyright © 2010 Hindawi Publishing Corporation. All rights reserved.

This is a special issue published in volume 2010 of “Advances in Meteorology.” All articles are open access articles distributed under the Creative Commons Attribution License, which permits unrestricted use, distribution, and reproduction in any medium, provided the original work is properly cited.

Editorial Board

Paulo Artaxo, Brazil
Rebecca Barthelmie, USA
Guy Brasseur, USA
Mladjen Ćurić, Serbia
Raymond Desjardins, Canada
Klaus Dethloff, Germany
Panuganti Devara, India
Ellsworth Dutton, USA
Shouting Gao, China
Luis Gimeno, Spain
C. S. B. Grimmond, UK

Branko Grisogono, Croatia
Sven-Erik Gryning, Denmark
Ismail Gultepe, Canada
Hiroyuki Hashiguchi, Japan
Didier Hauglustaine, France
Qi Hu, USA
I. S. A. Isaksen, Norway
Yasunobu Iwasaka, Japan
Hann-Ming Henry Juang, USA
George Kallos, Greece
Harry D. Kambezidis, Greece

Markku Kulmala, Finland
Richard Leaitch, Canada
Monique Leclerc, USA
Barry Lefer, USA
Zhanqing Li, USA
Edward Llewellyn, Canada
Kyaw Tha Paw U, USA
Sara C. Pryor, USA
Eugene Rozanov, Switzerland

Contents

Advanced Data Assimilation and Predictability Studies on High-Impact Weather and Climate,
Zhaoxia Pu, Song-You Hong, Yaohui Li, and Hann-Ming Henry Juang
Volume 2010, Article ID 121763, 2 pages

Forward Sensitivity Approach to Dynamic Data Assimilation, S. Lakshmivarahan and J. M. Lewis
Volume 2010, Article ID 375615, 12 pages

A 3.5-Dimensional Variational Method for Doppler Radar Data Assimilation and Its Application to Phased-Array Radar Observations, Qin Xu, Li Wei, Wei Gu, Jiandong Gong, and Qingyun Zhao
Volume 2010, Article ID 797265, 14 pages

Reconstruct the Mesoscale Information of Typhoon with BDA Method Combined with AMSU-A Data Assimilation Method, Yunfeng Wang, Haiyang Zhang, Bin Wang, Yueqi Han, and Xiaoping Cheng
Volume 2010, Article ID 346516, 11 pages

An Intercomparison of GPS RO Retrievals with Colocated Analysis and In Situ Observations within Tropical Cyclones, Henry R. Winterbottom and Qingnong Xiao
Volume 2010, Article ID 715749, 10 pages

An Observing System Simulation Experiment (OSSE) to Assess the Impact of Doppler Wind Lidar (DWL) Measurements on the Numerical Simulation of a Tropical Cyclone, Lei Zhang and Zhaoxia Pu
Volume 2010, Article ID 743863, 14 pages

Impacts of Oceanic Preexisting Conditions on Predictions of Typhoon Hai-Tang in 2005,
Akiyoshi Wada and Norihisa Usui
Volume 2010, Article ID 756071, 15 pages

Towards Direct Simulation of Future Tropical Cyclone Statistics in a High-Resolution Global Atmospheric Model, Michael F. Wehner, G. Bala, Phillip Duffy, Arthur A. Mirin, and Raquel Romano
Volume 2010, Article ID 915303, 13 pages

Numerical Modeling of the Severe Cold Weather Event over Central Europe (January 2006),
D. Hari Prasad, Joanna Wibig, and Marcin Rzepa
Volume 2010, Article ID 619478, 15 pages

Orography-Induced Gravity Wave Drag Parameterization in the Global WRF: Implementation and Sensitivity to Shortwave Radiation Schemes, Hyeyum Hailey Shin, Song-You Hong, Jimmy Dudhia, and Young-Joon Kim
Volume 2010, Article ID 959014, 8 pages

Evaluation of the WRF Double-Moment 6-Class Microphysics Scheme for Precipitating Convection,
Song-You Hong, Kyo-Sun Sunny Lim, Yong-Hee Lee, Jong-Chul Ha, Hyung-Woo Kim, Sook-Jeong Ham, and Jimmy Dudhia
Volume 2010, Article ID 707253, 10 pages

Sensitivity Study of Four Land Surface Schemes in the WRF Model, Jiming Jin, Norman L. Miller, and Nicole Schlegel
Volume 2010, Article ID 167436, 11 pages



Impact of Land Use Change on the Local Climate over the Tibetan Plateau, Jiming Jin, Shihua Lu,
Suosuo Li, and Norman L. Miller
Volume 2010, Article ID 837480, 6 pages

Beating the Uncertainties: Ensemble Forecasting and Ensemble-Based Data Assimilation in Modern Numerical Weather Prediction, Hailing Zhang and Zhaoxia Pu
Volume 2010, Article ID 432160, 10 pages

Editorial

Advanced Data Assimilation and Predictability Studies on High-Impact Weather and Climate

Zhaoxia Pu,¹ Song-You Hong,² Yaohui Li,³ and Hann-Ming Henry Juang⁴

¹Department of Atmospheric Sciences, University of Utah, Salt Lake City, UT 84112, USA

²Department of Atmospheric Sciences, Global Environment Laboratory, Yonsei University, Seoul 120-749, Republic of Korea

³Institute of Arid Meteorology, Chinese Academy of Meteorological Sciences, Lanzhou 730020, China

⁴Environmental Modeling Center, National Centers for Environmental Prediction, NOAA, Camp Springs, MD 20746, USA

Correspondence should be addressed to Zhaoxia Pu, zhaoxia.pu@utah.edu

Received 31 December 2010; Accepted 31 December 2010

Copyright © 2010 Zhaoxia Pu et al. This is an open access article distributed under the Creative Commons Attribution License, which permits unrestricted use, distribution, and reproduction in any medium, provided the original work is properly cited.

High-impact weather and climate systems refer to those events that have significant social, ecological, and economic impacts (such as tropical cyclones, winter storms, floods, droughts, etc.). Accurate forecasts of these systems more rely on our understanding of the systems and better representation of them in numerical models. Over the last decade, significant progress has been made in data assimilation, model development, and model diagnostics to enhance the predictability of these high-impact weather and climate systems. This special issue was motivated by rapid development in these areas. Total 13 papers in this volume address various issues in related topics.

Accurate initial conditions are one of key factors that influence the predictability of high-impact weather and climate systems. Modern data assimilation techniques combine observations and model information to form dynamically and physically consistent initial conditions for numerical models. A number of contributions addressed the new development in data assimilation. So S. Lakshmivarahan and J. M. Lewis presented a forward sensitivity approach to dynamic data assimilation. Duality between the method and the standard 4D-Var assimilation using adjoint equations has been proved. Q. Xu et al. developed a 3.5-dimensional variational method for Doppler radar data assimilation, which could be potentially beneficial to the predictability of severe weather systems.

Tropical cyclones are among the most destructive weather-related natural phenomena. They are responsible for some of the costliest and deadliest natural disasters in the world. A number of contributors addressed the tropical cyclone

predictability problem from various angles. Y. Wang et al. presented a mesoscale data assimilation method for tropical cyclone initialization, which particularly improves the representation of tropical cyclone vortex and environment conditions in model initial conditions. H. R. Winterbottom and Q. Xiao's paper emphasized on an intercomparison of observations from four Global Position System (GPS) Radio Occultation (RO) and in situ observations within tropical cyclones, making a suggestion for better utilize these data in data assimilation. The paper by L. Zhang and Z. Pu assessed the impact of wind profile measurements from the future satellite based Doppler wind lidar mission with observing system simulation experiments. A. Wada and N. Usui's study examined the impact of ocean pre-existing conditions on the predictability of a typhoon case using a couple-atmosphere-ocean model at high resolution. They found that ocean preexisting conditions remarkably affect typhoon rainbands.

While many efforts have been made in improving mesoscale regional model's ability in tropical cyclone predictability, an effort has also been made in the use of global model for tropical cyclone forecasts. M. F. Wehner et al. presented a set of high-resolution global atmospheric simulations with a general circulation model, focusing on the model's ability to represent tropical storms and their statistics. They found that the model produces storms of hurricane strength with realistic dynamic features and reasonable statistics. Some issues arose from global model simulations were also addressed.

Cold waves commonly occur in higher latitudes during winter season. They could cause serious economical loss

and cold-related death. The contribution by D. H. Prasad et al. presented numerical simulation results to a severe cold wave event occurred during January 2006 over Europe. They found that the model is able to simulate the occurrence of the cold wave in 1 to 3 days range though the intensity is weaker than observations.

The ultimate predictability of high-impact weather systems relies on the improvement in computer models themselves, since model errors are the key factors that cause inaccurate forecasts. A number of contributions addressed the improvement or evaluation of the physical parameterization in a numerical model, specifically, a popular mesoscale community Weather Research and Forecasting (WRF) model. H. H. Shin et al. described the implementation of the orographic gravity wave drag process induced by subgrid-scale orography in the global version of the WRF model. The sensitivity of this new implementation to shortwave radiation was evaluated. S. Y. Hong et al. evaluated the WRF double-moment 6-class microphysics scheme for precipitating convection, making a step forward to improve the quantitative precipitation forecasting. In paper by J. Jin et al., four land surface schemes in the WRF model were evaluated for their sensitivities to accurately simulate temperature over the western United States. As a follow-up study of the WRF land surface schemes, J. Jin et al. also presented results to examine the impact of land change on the local climate over the Tibetan Plateau.

Although there have been many efforts made in improving initial conditions and computer models, due to inadequate observations, our limited understanding of the physical processes of the atmosphere, and the chaotic nature of atmospheric flow, uncertainties always exist in modern numerical weather and climate prediction. Recent developments in ensemble forecasting and ensemble-based data assimilation have proved that there are promising ways to beat the forecast uncertainties. A contribution by H. Zhang and Z. Pu gave a comprehensive overview of fundamental problems and recent progress associated with ensemble forecasting and ensemble-based data assimilation. The usefulness of these methods in improving high-impact weather forecasting was also discussed.

Acknowledgments

We, the guest editors of this special issue of *Advances in Meteorology* (AMET), are grateful to all the authors, reviewers, and AMET staff. We hope that the papers in this issue will stimulate further development and confidence building for improving predictability of high impact weather and climate systems.

Zhaoxia Pu
Song-You Hong
Yaohui Li
Hann-Ming Henry Juang

Research Article

Forward Sensitivity Approach to Dynamic Data Assimilation

S. Lakshmivarahan¹ and J. M. Lewis^{2,3}

¹ School of Computer Sciences, University of Oklahoma, Norman, OK 73072, USA

² Forecast R&D, National Severe Storms Laboratory, Norman, OK 73072, USA

³ Division of Atmospheric Sciences, Desert Research Institute, Reno, NV 89512, USA

Correspondence should be addressed to S. Lakshmivarahan, varahan@ou.edu

Received 3 December 2009; Accepted 15 February 2010

Academic Editor: Zhaoxia Pu

Copyright © 2010 S. Lakshmivarahan and J. M. Lewis. This is an open access article distributed under the Creative Commons Attribution License, which permits unrestricted use, distribution, and reproduction in any medium, provided the original work is properly cited.

The least squares fit of observations with known error covariance to a strong-constraint dynamical model has been developed through use of the time evolution of sensitivity functions—the derivatives of model output with respect to the elements of control (initial conditions, boundary conditions, and physical/empirical parameters). Model error is assumed to stem from incorrect specification of the control elements. The optimal corrections to control are found through solution to an inverse problem. Duality between this method and the standard 4D-Var assimilation using adjoint equations has been proved. The paper ends with an illustrative example based on a simplified version of turbulent heat transfer at the sea/air interface.

1. Introduction

Sensitivity function analysis has proved valuable as a mean to both build models and to interpret their output in chemical kinetics (Rabitz et al. [1], Seefeld and Stockwell [2]) and air quality modeling (Russell et al. [3]). Yet, the ubiquitous systematic errors that haunt dynamical prediction cannot be fully understood with sensitivity functions alone. We now include an optimization component that leads to an improved fit of model to observations. The methodology is termed forward sensitivity method (FSM)—a method based on least squares fit of model to data, but where algorithmic structure and correction procedure are linked to the sensitivity functions. In essence, corrections to control (the initial conditions, the boundary conditions, and the physical and empirical parameters) are found through solution to an inverse problem.

In this paper we derive the governing equations for corrections to control and show their equivalence to equations governing the so-called 4D-Var assimilation method (four-dimensional variational method)—least squares fit of model to observations under constraint (LeDimet and Talagrand [4]). Beyond this equivalence, we demonstrate the value of the FSM as a diagnostic tool that can be used to understand the relationship between sensitivity and correction to control.

We begin our investigation by laying down the dynamical framework for the FSM: general form of the governing dynamical model, the type and representation of model error that can be identified through the FSM, and the evolution of the sensitivity functions that are central to execution of the FSM. The dual relationship between 4D-Var/adjoint equations is proved. The step-by-step process of assimilating data by FSM is outlined, and we demonstrate its usefulness by application to a simplified air-sea interaction model.

2. Foundation Dynamics for the FSM

We have included a list of mathematical symbols used in this paper. These symbols and associated nomenclature are found in Table 1.

2.1. Prediction Equations. Let $x(t) \in R^n$ denote the state and let $\alpha \in R^p$ denote the parameters of a deterministic dynamical system, where $x(t) = (x_1(t), x_2(t), \dots, x_n(t))^T$ and $\alpha = (\alpha_1, \alpha_2, \dots, \alpha_p)^T$ are column vectors, n and p are positive integers, $t \geq 0$ denotes the time, and superscript T denotes the transpose of the vector or matrix. Let $f : R^n \times R^p \times R \rightarrow R^n$ be a mapping, where $f(x, \alpha, t) = (f_1, f_2, \dots, f_n)^T$ with $f_i = f_i(x, \alpha, t)$ for $1 \leq i \leq n$. The vector spaces R^n and R^p are called the model space and parameter space, respectively.

TABLE 1: Symbolism and nomenclature.

Symbol	Nomenclature
n	Dimension of state vector
m	Dimension of observation vector
p	Dimension of parameter vector
$q = n + p$	Dimension of control vector
N	Number of observation vectors
t	Time
$\hat{x}(t) \in R^n$	True model state vector
$x(t) = (x_1, x_2, \dots, x_n)^T \in R^n$	Model state vector
$f : R^n \times R^p$	Vector field of the model
$x(0) \in R^n$	Initial condition for model state vector
$\alpha \in R^p$	Parameter vector
$c = (x(0), \alpha) \in R^n \times R^p$	Control vector
$z(t) \in R^m$	Observation vector
$h(x(t)) : R^n \rightarrow R^m$	Forward operator relating model state and observations
$h(x(t)) \in R^m$	Model counterpart of the observation
$v(t) \in R^m$	Observation error vector
$\mathbf{R}(t) \in R^{m \times n}$	Covariance of observation error vector $v(t)$
e_F	Forecast error
$b(t)$	Systematic component of forecast error
$D_x(f) = [\partial f_i / \partial x_j] \in R^{n \times n}$	Model Jacobian w. R. T. x
$D_\alpha(f) = [\partial f_i / \partial \alpha_j] \in R^{n \times p}$	Model Jacobian w. R. T. α
$D_\alpha(x) = [\partial x_i / \partial \alpha_j] \in R^{n \times p}$	Sensitivity matrix w. R. T. Parameters
$D_{x(0)}(x) = [\partial x_i / \partial x_j(0)] \in R^{n \times n}$	Sensitivity matrix w. R. T. Initial condition
$D_x(h) \in R^{m \times n}$	Jacobian of the forward operator w. R. T. x
$H_1(t) = D_x(h)D_{x(0)}(x) \in R^{m \times n}$	Sensitivity matrix accounting for $h(x(t))$
$H_2(t) = D_x(h)D_\alpha(x) \in R^{m \times p}$	Sensitivity matrix accounting for $h(x(t))$
$\langle a, b \rangle$	Inner product
$J(c), J_1(c)$	Objective or cost functions
$\delta J, \delta J_1, \delta x(t), \delta \alpha$	First variations
$\nabla J, \nabla J_1$	Gradients of cost functions
$M(t, s)$	Model state transition matrix (Appendix A)
$L(t, s)$	Matrix that determines particular solution (Appendix A)

Consider a dynamical system described by a system of ordinary nonlinear differential equations of the form

$$\frac{dx}{dt} = f(x, \alpha, t), \quad (1a)$$

or in component form

$$\frac{dx_i}{dt} = f_i(x, \alpha, t), \quad (1b)$$

where dx/dt denotes the time derivative of the state $x(t)$, with $x(0) \in R^n$ the given initial condition. The control vector for the model is given by $c = (x(0), \alpha) \in R^n \times R^p$, the combination of initial condition and parameters referred to as the control space. It is tacitly assumed that the map of f in (1a) and (1b) is such that the solution $x(t) = x(t, x(0), \alpha) = x(t, c)$ exists and is unique. It is further assumed that $x(t)$ has a smooth dependence on the control vector c such that the first k (≥ 1) partial derivatives of $x(t)$ with respect to the components of c also exist. The solution $x(t)$ of (1a) and (1b) is known as the deterministic forecast of the state of the system at time $t > 0$. If the map $f(\cdot)$ in (1a) and (1b) depends explicitly on t , then this system is called a time varying or nonautonomous system; if $f(\cdot)$ does not depend on t , then the system is known as a time invariant or autonomous system.

Let $z(t) \in R^m$ be the observation vector obtained from the field measurements at time $t \geq 0$. Let $h : R^n \rightarrow R^m$ be the mapping from the model space R^n to the observation space R^m .

If $\hat{x}(t)$ denotes the (unknown) true state, then we assume that $z(t)$ is given by

$$z(t) = h(\hat{x}(t)) + v(t), \quad (2)$$

where $v(t) \in R^m$ is the additive (unobservable and unavoidable) noise. The mapping $h(\cdot)$ is known as the forward operator or the observation operator. It is further assumed that $v(t)$ is a white Gaussian noise with mean zero possessing a known covariance matrix $\mathbf{R}(t) \in R^{m \times m}$. That is, $v(t) \sim N(0, \mathbf{R}(t))$.

2.2. A Classification of Forecast Errors. The forecast error $e_F(t) \in R^m$ is defined as follows:

$$e_F(t) \equiv z(t) - h(x(t)) = b(t) + v(t), \quad (3)$$

the sum of a deterministic part

$$b(t) = h(\hat{x}(t)) - h(x(t)), \quad (4)$$

and the random part $v(t)$ induced by the observation noise. Our immediate goal is to analyze and isolate sources and types of forecast errors.

First, if the model map $f(\cdot)$ and the forward operator $h(\cdot)$ are without error, that is, exact, and if the control vector c is also error free, then the deterministic forecast $x(t)$ must be correct in the sense that $x(t) = \hat{x}(t)$, the true state. Then from (3), the forecast error is purely random or white Gaussian noise. That is,

$$e_F(t) = v(t). \quad (5)$$

Second, if $f(\cdot)$ and $h(\cdot)$ are known perfectly but c has an error, then the forecast $x(t)$ will have a deterministic error

induced by the incorrect control vector. In such a case, we can, in principle, decompose the forecast error as a sum

$$e_F(t) = b(c, t) + v(t), \quad (6)$$

where the deterministic part, $b(c, t) = h(\hat{x}(t)) - h(x(t))$, is purely a function of the control vector error.

Third, if $f(\cdot)$, $h(\cdot)$, and c are in error, then the forecast error can be represented as

$$e_F(t) = b(c, f, h, t) + v(t), \quad (7)$$

where the deterministic part $b(c, f, h, t)$ may have a complex (additive and/or multiplicative) dependence on errors in c , $f(\cdot)$, and $h(\cdot)$.

The following assumption is key to our analysis that follows. The model of choice is faithful to the phenomenon under study. The system is predicted with fidelity—the forecasted state is creditable and useful in understanding the dynamical processes that underpin the phenomenon. Certainly, the forecast will generally exhibit some error, but the primary physical processes are included; that is, the vector field f includes the pertinent physical processes. In this situation the forecast error stems from erroneously specified elements of control. Thus, in our study the forecast error assumes the form shown in (6). Dee's work [5] contains a very good discussion of the estimation of the bias b in (7) arising from errors in the model and/or observations.

2.3. Dynamics of First-Order Sensitivity Function Evolution. Since our approach is centered on sensitivity functions, we develop the dynamics of evolution of the forward sensitivities in this section.

Differentiating both sides of (1b) with respect to α_j , interchanging the order of differentiation on the left-hand side, we obtain

$$\frac{\partial(dx_i/dt)}{\partial\alpha_j} = \frac{d}{dt} \left(\frac{\partial x_i}{\partial\alpha_j} \right) = \sum_{k=1}^n \left[\left(\frac{\partial f_i}{\partial x_k} \right) \left(\frac{\partial x_k}{\partial\alpha_j} \right) + \frac{\partial f_i}{\partial\alpha_j} \right] \quad (8)$$

for $1 \leq i \leq n$ and $1 \leq j \leq p$ with $\partial x_i(0)/\partial\alpha_j = 0$ as the initial condition.

These np equations can be succinctly written in matrix form as

$$\frac{d}{dt} [D_\alpha(x)] = D_x(f) D_\alpha(x) + D_\alpha(f) \quad (9)$$

with $D_\alpha(x(0)) = 0$ as initial condition. This system of linear time-varying ordinary nonhomogeneous differential equations describe the evolution of the elements of $D_\alpha(x) = [\partial x_i/\partial\alpha_j] \in R^{n \times p}$, where the Jacobian matrices $D_x(f) \in R^{n \times n}$ and $D_\alpha(f) \in R^{n \times p}$ are given by

$$D_x(f) = \left[\frac{\partial f_i}{\partial x_j} \right], \quad (10)$$

$$D_\alpha(f) = \left[\frac{\partial f_i}{\partial\alpha_j} \right]. \quad (11)$$

Similarly, by differentiating both sides of (1b) with respect to $x_j(0)$, we obtain

$$\frac{\partial(dx_i/dt)}{\partial x_j(0)} = \frac{d}{dt} \left(\frac{\partial x_i}{\partial x_j(0)} \right) = \sum_{k=1}^n \left(\frac{\partial f_i}{\partial x_k} \right) \left(\frac{\partial x_k}{\partial x_j(0)} \right) \quad (12)$$

for $1 \leq i, j \leq n$, with $\partial x_i(0)/\partial x_j(0) = \delta_{ij}$, where δ_{ij} is the standard Kronecker delta. These n^2 equations can be succinctly represented as

$$\frac{d}{dt} [D_{x(0)}(x)] = D_x(f) D_{x(0)}(x) \quad (13)$$

with $D_{x(0)}(x(0)) = I$, the identity matrix. This system of linear, time-varying homogeneous equations governs the evolution of the elements of the matrix $D_{x(0)}(x) = [\partial x_i/\partial x_j(0)] \in R^{n \times p}$. Notice that (9) and (13) are independent of the observations and have the same system matrix $D_x(f)$ on the right-hand sides; thus, the homogeneous solutions to (9) and (13) have the same structure.

The evolution of the sensitivities (solution to (9) and (13)) is dependent on the solution to the governing dynamical equations ((1a) and (1b)). Generally, these equations are solved numerically using the standard fourth-order Runge-Kutta method. Rabitz et al. work [1] contains more details relating to solutions of (9) and (13). In special cases such as in air quality modeling, the sensitivity equations (9) and (13) exhibit extreme stiffness. Special methods are needed to handle the inherent stiffness of these equations. Seefeld and Stockwell work [2] includes a discussion of these issues. Gear's work [6] is a good reference for a general discussion of stiff equations.

3. Duality between the FSM and 4D-Var Based on Adjoint Method

Let $z(t_1), z(t_2), \dots, z(t_N)$ be a sequence of N observation vectors at times $t_0 = 0 < t_1 < t_2 < \dots < t_N$. The goal is to use these observations to improve the estimate of the control vector c . This estimation problem is recast as a constrained minimization of an objective function $J : R^n \times R^p \rightarrow R$ given by

$$J(c) = \frac{1}{2} \sum_{i=1}^N [z(t_i) - h(x(t_i))]^T \mathbf{R}^{-1}(t_i) [z(t_i) - h(x(t_i))], \quad (14)$$

where the model state $x(t)$ evolves according to (1a), (1b), and $\mathbf{R}(t_i) \in R^{m \times m}$ is the known covariance of the observational errors $v(t_i)$ at time t_i , $1 \leq i \leq N$.

Fundamental to minimizing (14) is the computation of the gradient of $J(c)$, denoted by $\nabla_c J(c)$. In the following we describe two ways of characterizing

$$\nabla_c J(c) = \begin{bmatrix} \nabla_{x(0)} J \\ - \\ \nabla_\alpha J \end{bmatrix}, \quad (15)$$

where $\nabla_{x(0)} J \in R^n$ and $\nabla_\alpha J \in R^p$.

3.1. The Adjoint Method. This method is based on the basic principle that if δJ is the first variation of $J(c)$ induced by the perturbation δc in c , then

$$\delta J = \langle \nabla_c J, \delta c \rangle, \quad (16)$$

where $\langle a, b \rangle$ denotes the standard inner product of two vectors a and b of the same dimension. Once the first variation δJ is determined, the gradient can be found. In the following we exploit two basic properties of inner product:

(i) linearity

$$\langle a + b, x \rangle = \langle a, x \rangle + \langle b, x \rangle, \quad (17)$$

(ii) adjoint property

$$\langle a, Gb \rangle = \langle G^T a, b \rangle, \quad (18)$$

where G^T is the transpose or the adjoint of the matrix G .

From first principles (Chapter 24 in Lewis et al. [7]), it can be verified that the first variation δJ of J in (14) is given by

$$\delta J = - \sum_{k=1}^N \langle \mathbf{R}^{-1}(t_k) e_F(t_k), D_x(h) \delta x(t_k) \rangle, \quad (19)$$

where the forecast error given by

$$\begin{aligned} e_F(t_k) &= z(t_k) - h(x(t_k)), \\ D_x(h) &= \left[\frac{\partial h_i}{\partial x_j} \right] \in R^{m \times n} \end{aligned} \quad (20)$$

is the Jacobian of forward operator $h(x)$ with respect to x .

By invoking the adjoint property in (17), (19) becomes

$$\delta J = - \sum_{k=1}^N \langle \eta(t_k), \delta x(t_k) \rangle, \quad (21)$$

where

$$\eta(t_k) = D_x^T(h) \mathbf{R}^{-1}(t_k) e_F(t_k). \quad (22)$$

The first variation $\delta x(t_k)$ in $x(t)$ at $t = t_k$ resulting from the perturbation δc in c is given by (A.4) in Appendix A. Using (A.4) and the linearity of the inner product it follows that

$$\begin{aligned} \delta J &= - \sum_{k=1}^N \langle \eta(t_k), M(t_k, 0) \delta x(0) \rangle \\ &\quad - \sum_{k=1}^N \langle \eta(t_k), M(t_k, 0) L(t_k, 0) \delta \alpha \rangle, \end{aligned} \quad (23)$$

where we will refer to the first term on the right-hand side of (23) as ‘‘Term I’’ and the second as ‘‘Term II.’’ Using the adjoint and linearity property in (17), we get

$$\text{Term I} = - \left\langle \sum_{k=1}^N M^T(t_k, 0) \eta(t_k), \delta x(0) \right\rangle \quad (24)$$

from which we obtain

$$\nabla_{x(0)} J = - \sum_{k=1}^N M^T(t_k, 0) \eta(t_k). \quad (25)$$

Similarly, rewriting Term II as

$$\text{Term II} = - \left\langle \sum_{k=1}^N L^T(t_k, 0) M^T(t_k, 0) \eta(t_k), \delta \alpha \right\rangle, \quad (26)$$

we get

$$\nabla_{\alpha} J = - \sum_{k=1}^N L^T(t_k, 0) M^T(t_k, 0) \eta(t_k). \quad (27)$$

Hence, we obtain the components of $\nabla_c J$ which are used in conjunction with the minimization algorithm to find the optimal c^* that minimizes $J(c)$ in (14).

We conclude this discussion with an efficient recursive method for evaluating the expressions in (25) and (27). Define

$$\lambda_N = \eta(t_N), \quad (28)$$

and for $k = N - 1, N - 2, \dots, 2, 1, 0$,

$$\lambda_k = M^T(t_{k+1}, t_k) \lambda_{k+1} + \eta(t_k). \quad (29)$$

It can be verified that $\nabla_{x(0)} J = M^T(t_1, 0) \lambda_1$ in (25).

Details on the recursive computation of (27) are given in Appendix C.

3.2. Sensitivity-Based Approach. Let us first consider the special case when $N = 1$. Then (14) becomes

$$J_1(c^-) = \frac{1}{2} [z - h(x)]^T \mathbf{R}^{-1}(t) [z - h(x)], \quad (30)$$

where we recall that $c \in R^n \times R^p$ and $x = x(t, c)$ is the solution of the model equations (1a) and (1b) at time t .

Setting $q = (n + p)$ and $A = \mathbf{R}^{-1}(t)$, the expression $J_1(c)$ in (30) becomes identical to $Q(c)$ in (B.16) (Appendix B). Hence, by using (B.20) it follows that

$$\nabla_c J_1(c) = -D_c^T(x) \eta(t), \quad (31)$$

where $\eta(t)$ is given by (22) and

$$D_c^T(x) = \begin{bmatrix} D_{x(0)}^T(x) \\ - - - - \\ D_{\alpha}^T(x) \end{bmatrix} \in R^{(n+p) \times n}. \quad (32)$$

Now comparing (32) with (25)–(27), we obtain the duality relation:

$$\begin{aligned} D_{x(0)}(x) &\longleftrightarrow M(t, 0), \\ D_{\alpha}(x) &\longleftrightarrow M(t, 0) L(t, 0). \end{aligned} \quad (33)$$

The sensitivity matrices on the left-hand side of (33) are obtained by solving the forward sensitivity equations, whereas the matrix products $M(t, 0)$ and $L(t, 0)$ are obtained by integrating along the path as given by (A.3) and (A.5) (Appendix A).

The primary advantage of the sensitivity-based approach is that it provides a natural interpretation of the expression for the gradient in (31). Recall from (22) that $\eta(t) \in R^n$ is the weighted version of the forecast error $R^{-1}(t)e_F(t) \in R^m$ mapped onto the model space by the linear operator $D_x^T(h)$. Also the i th column of $D_c^T(x)$ is the sensitivity of the i th component $x_i(t)$ of the state vector $x(t) \in R^n$ with respect to the control vector $c \in R^q$ given by $(\partial x_i / \partial c_1, \partial x_i / \partial c_2, \dots, \partial x_i / \partial c_q)$. Thus, it follows from (31) that $\nabla_c J_1$ is a linear combination of the columns of $D_c^T(x)$ which are the sensitivity vectors, where the coefficients of the linear terms are the components of $\eta(t)$. Thus, columns of $D_c^T(x)$ with large norms that are associated with large forecast errors will be dominant in determination of the components of $\nabla J_1(c)$. In other words, we gain some insight into the interplay between corrections to control and forecast errors—something that can be seen through a careful examination of the sensitivity vector at various times from initial state to forecast horizon. (The illustrative example in Section 5 further explores this diagnostic function.) Expression (31) also enables us to isolate the effect of different components x_i of $x(t)$ on the performance index $J_1(c)$.

For the general case of observations at multiple times, (31) assumes the following form:

$$\nabla_c J = - \sum_{i=1}^N D_c^T(x(t_i)) \eta(t_i). \quad (34)$$

This gradient is the sum of linear combinations of the columns of $D_c^T(x(t_i))$ at various time instances. With so many directions (the directions associated with the columns of $D_c^T(x(t_i))$) contributing to the components of $\nabla_c J$, the connection between sensitivity, and forecast error is obscured.

4. Data Assimilation Using Sensitivity

We seek to find the solution to the following problem using the FSM. Given $f(\cdot)$ and $h(\cdot)$, the control vector c , the observation $z(t)$, and the error covariance of observations $R(t)$, find a correction δc to the control vector such that the new model forecast starting from $(c + \delta c)$ will render the forecast error $e_F(t)$ purely random; that is, the systematic forecast error is removed and accordingly $E(e_F(t)) = 0$.

We start by quantifying the change Δx in the solution $x(t) = x(t, c)$ resulting from a change δc in c . Invoking the standard Taylor series expansion, we obtain

$$\Delta x = x(t, c + \delta c) - x(t, c) = \sum_j \delta^j x, \quad (35)$$

where $\delta^k x$ is the k th variation of $x(t)$, the fraction of the total change that can be accounted by the k th partial derivatives of $x(t)$ with respect to c and the perturbation δc . Since practical considerations dictate that the total number of correction

terms on the right-hand side of (35) be finite, we often settle for an approximation of only k terms (k generally ≤ 2). This is a tradeoff between improved accuracy resulting from a large value of k and the complexity of the resulting inverse problem. Although we have developed the methodology for second-order analysis ($k = 2$, where Δx is approximated by the sum $\delta x + \delta^2 x$) (Lakshmivarahan and Lewis [8]), our development will follow the first-order analysis ($k = 1$, where Δx is given by the first variation δx). Second-order analysis is justified when $\delta^2 x$ is a significant fraction of δx —this occurs when $f(x)$ and/or $h(x)$ exhibit strong nonlinearity. It is further shown in Section 5 that iterative application of the first-order method often leads to improved results.

4.1. First-Order Analysis. From first principles and (35) we obtain

$$\Delta x \approx \delta x = D_{x(0)}(x) \delta x(0) + D_\alpha(x) \delta \alpha, \quad (36)$$

where $D_{x(0)}(x) \in R^{n \times n}$ is the Jacobian of $x(t)$ with respect to $x(0)$, and $D_\alpha(x) \in R^{n \times p}$ is the Jacobian of $x(t)$ with respect to α . The matrices $D_{x(0)}(x)$ and $D_\alpha(x)$, found as solutions of (13) and (9), respectively, are known as the first-order sensitivity of the solution $x(t)$ with respect to $x(0)$ and α , respectively, and the elements of these matrices are called sensitivity functions.

4.1.1. Observations at One Time Only. We first consider the case where observation $z(t) \in R^m$ is available at one time t . The first variation δx in $x(t)$ induces a variation Δh in the forward operator $h(x(t))$. Again, by approximating Δh by the first variation, we get

$$\Delta h \approx \delta h = D_x(h) \delta x, \quad (37)$$

where $D_x(h) \in R^{m \times n}$ is the Jacobian of $h(\cdot)$ with respect to x and is given by

$$D_x(h) = \left[\frac{\partial h_i}{\partial x_j} \right], \quad 1 \leq i \leq m, \quad 1 \leq j \leq n. \quad (38)$$

substituting (36) into (37), we obtain

$$\delta h = H_1 \delta x(0) + H_2 \delta \alpha, \quad (39)$$

where $H_1(t) = D_x(h) D_{x(0)}(x) \in R^{m \times n}$ and $H_2(t) = D_x(h) D_\alpha(x) \in R^{m \times p}$. Setting $H(t) = [H_1(t), H_2(t)] \in R^{m \times (n+p)}$ and $\zeta = (\zeta_1, \zeta_2) \in R^{n+p}$, where $\zeta_1 = \delta x(0)$ and $\zeta_2 = \delta \alpha$, (39) becomes

$$\delta h = H(t) \zeta. \quad (40)$$

Given the operating point c , our goal is to find the perturbation δc such that the observation is equal to the model counterpart, that is,

$$z(t) = h(x(t, c + \delta c)) \approx h(x(t)) + \delta h, \quad (41)$$

or

$$e_F(t) \equiv z(t) - h(x(t)) = \delta h. \quad (42)$$

From (43), it follows that the required perturbation $\varsigma \in R^{n+p}$ is obtained by solving the linear inverse problem

$$H(t)\varsigma = e_F(t), \quad (43)$$

where $H(t) \in R^{m \times (n+p)}$ and $e_F(t) \in R^m$.

4.1.2. Observations at Multiple Times. The above analysis can be readily extended to the case where observations are available at N times. We denote these sets of observation vectors by $z(t_1), z(t_2), \dots, z(t_N)$, where $0 < t_1 < t_2 < \dots < t_N$. The forecast error $e_F(t_i)$ is given by

$$e_F(t_i) = z(t_i) - h(x(t_i)), \quad 1 \leq i \leq N. \quad (44)$$

Define

$$\begin{aligned} H_1(t_i) &= D_{x(t_i)}(h)D_{x(0)}(x(t_i)) \in R^{m \times n}, \\ H_2(t_i) &= D_{x(t_i)}(h)D_a(x(t_i)) \in R^{m \times p}. \end{aligned} \quad (45)$$

Then at time t_i we have

$$H(t_i)\varsigma = e_F(t_i), \quad 1 \leq i \leq N, \quad (46)$$

where

$$H(t_i) = [H_1(t_i), H_2(t_i)] \in R^{m \times (n+p)}. \quad (47)$$

Now define a matrix $H \in R^{Nm \times (n+p)}$ and a vector $e_F \in R^{Nm}$ as

$$H = \begin{bmatrix} H(t_1) \\ H(t_2) \\ \vdots \\ H(t_N) \end{bmatrix}, \quad e_F = \begin{bmatrix} e_F(t_1) \\ e_F(t_2) \\ \vdots \\ e_F(t_N) \end{bmatrix}. \quad (48)$$

Then, the N relations in (46) can be succinctly denoted by

$$H\varsigma = e_F. \quad (49)$$

A number of special cases arise depending on (a) the value of Nm relative to $(n+p)$, namely, over (under) determined cases when $Nm > (<)(n+p)$ and (b) the rank of the matrix $H(t)$, namely, $H(t)$ is of full rank or rank deficient. In all these cases, the linear inverse problem (43) is recast as a minimization problem using the standard least squares framework (Lawson and Hanson [9]). The resulting minimization problem can then be solved using one of many standard methods, for example, the conjugate gradient method (Lewis et al. [7]; Nash and Sofer [10]).

As an illustration, consider the case when $Nm > (n+p)$ and that the rank of H is $(n+p)$, that is, full rank. The solution ς is then obtained by minimizing the weighted least squares criterion

$$\begin{aligned} J_N(\varsigma) &= \frac{1}{2} \sum_{i=1}^N (e_F(t_i) - H(t_i)\varsigma)^T \mathbf{R}^{-1}(t_i) (e_F(t_i) - H(t_i)\varsigma) \\ &= \frac{1}{2} (e_F - H\varsigma)^T \mathbf{R}^{-1} (e_F - H\varsigma), \end{aligned} \quad (50)$$

where

$$\mathbf{R} = \text{Diag}[\mathbf{R}(t_1), \mathbf{R}(t_2), \dots, \mathbf{R}(t_N)] \quad (51)$$

is an $Nm \times Nm$ diagonal matrix with $\mathbf{R}(t_i)$ as its i th diagonal block.

Although it is computationally efficient to minimize (50) by using a method like conjugate gradient, there is an advantage to analyze the properties of the optimal solution via the classical approach, that is, by setting the gradient of $J_N(\varsigma)$ to zero. It can be verified that the minimizing J_N is found by solving the symmetric linear system

$$\left[\sum_{i=1}^N H^T(t_i) \mathbf{R}^{-1}(t_i) H(t_i) \right] \varsigma = \sum_{i=1}^N \left(H^T(t_i) \mathbf{R}^{-1}(t_i) e_F(t_i) \right) \quad (52)$$

or succinctly as

$$\varsigma_{\text{LS}} = \left(H^T \mathbf{R}^{-1} H \right)^{-1} H^T \mathbf{R}^{-1} e_F, \quad (53)$$

where H , e_F , and \mathbf{R} are defined in (48) and (51), and subscript “LS” refers to the least squares solution.

From the discussion relating to the classification of forecast errors, recall that the forecast error inherits its randomness from the (unobservable) observation noise. The vector e_F on the right hand side of (53) is random and hence the solution ς of (53) is also random.

Since we are interested in forecast errors in response to incorrect control, we have

$$e_F(t_i) = b(c, t_i) + v(t_i) \quad \text{for } 1 \leq i \leq N. \quad (54)$$

Now define

$$b = \begin{bmatrix} b(c, t_1) \\ b(c, t_2) \\ \vdots \\ b(c, t_N) \end{bmatrix}, \quad v = \begin{bmatrix} v(t_1) \\ v(t_2) \\ \vdots \\ v(t_N) \end{bmatrix}. \quad (55)$$

Hence, the vector e_F in (48) can be expressed as

$$e_F = b + v \quad (56)$$

with $E(e_F) = b$ since $E(v) = 0$. Substituting (56) into (53) and taking the expectation give

$$E(\varsigma_{\text{LS}}) = \left[\left(H^T \mathbf{R}^{-1} H \right)^{-1} H^T \mathbf{R}^{-1} \right] b. \quad (57)$$

Thus, the expected value of the correction to control is indeed a linear function of the forecast error b itself. It can be verified (Lewis et al. [7]) that the covariance of the least squares estimate [(53)] is given by

$$\text{cov}(\varsigma_{\text{LS}}) = \left(H^T \mathbf{R}^{-1} H \right)^{-1} = [\nabla^2 J_N(\varsigma)]^{-1}, \quad (58)$$

where $\nabla^2 J_N(\varsigma)$ is the Hessian of $J_N(\varsigma)$ in (50).

5. A Practical Example: Air/Sea Interaction

We choose a simple but nontrivial differential equation to demonstrate the applicability of the forward-sensitivity method to identification of error in a dynamical model. We break this discussion into three parts as follows: (1) the model, (2) discussion of the diagnostic value of FSM, and (3) numerical experiments with data assimilation using FSM.

5.1. The Model. Consider the case where cold continental air moves out over an ocean of constant surface temperature. We follow a column of air in a Lagrangian frame; that is, the column of air moves with the prevailing low-level wind speed. Turbulent transfer of heat from the ocean to air warms the column. The governing equation is taken to be

$$\frac{d\theta}{d\tau} = \frac{C_T V}{H}(\theta_s - \theta), \quad (59)$$

where

θ : temperature of the air column ($^{\circ}\text{C}$),

θ_s : temperature of the sea surface ($^{\circ}\text{C}$),

C_T : turbulent heat exchange coefficient (nondimensional),

V : speed of air column (ms^{-1}),

H : height of the column (mixed layer)(m),

τ : time (h). Equation (59) is nondimensionalized by the following scaling:

$$\begin{aligned} \theta &= \pi \cdot x \quad (\pi = 1.0^{\circ}\text{C}), \\ \theta_s &= \pi \cdot x_s, \\ \tau &= T \cdot t \quad (T = 1.0 \text{ h}). \end{aligned} \quad (60)$$

The governing equation then takes the form

$$\frac{dx(t)}{dt} = \frac{C_T V T}{H}(x_s - x(t)). \quad (61)$$

Assuming $H \sim 150 \text{ m}$, $V \sim 10 \text{ ms}^{-1}$, $C_T \sim 10^{-3}$, then

$$k = \frac{C_T V T}{H} \approx \frac{1}{4}. \quad (62)$$

Thus, we take our governing equation to be

$$\frac{dx(t)}{dt} = f(x, \alpha) = k(x_s - x(t)), \quad (63)$$

where $k = 0.25$. The solution to (63) is

$$x(t, x(0), \alpha) = [x(0) - x_s]e^{-kt} + x_s \quad (64)$$

with $c = (x(0), \alpha) \in R \times R^2$, and $\alpha = (x_s, k)^T \in R^2$, that is, $n = 1$ and $p = 2$. The solution depends linearly on $x(0)$ and x_s but nonlinearly on k .

There are three elements of control: initial condition, $x(0)$, boundary condition, x_s , and parameter, k .

5.2. Diagnostic Aspects of FSM. The Jacobians of f with respect to x and α are given by

$$\begin{aligned} D_x(f) &= -k \in R, \\ D_\alpha(f) &= [k, x_s - x(t)] \in R^{1 \times 2}, \end{aligned} \quad (65)$$

and the Jacobians of the solution $x(t)$ with respect to α and $x(0)$ are given by

$$D_\alpha(x(t)) = \left[\frac{\partial x(t)}{\partial x_s}, \frac{\partial x(t)}{\partial k} \right] \in R^{1 \times 2}, \quad (66)$$

$$D_{x(0)}(x(t)) = \left[\frac{\partial x(t)}{\partial x(0)} \right] \in R.$$

From (9) and (13) the evolution of the forward sensitivities is given by

$$\frac{d}{dt} \left(\frac{\partial x(t)}{\partial x_s} \right) = -k \left(\frac{\partial x(t)}{\partial x_s} \right) + k, \quad (67)$$

$$\frac{d}{dt} \left(\frac{\partial x(t)}{\partial k} \right) = -k \left(\frac{\partial x(t)}{\partial k} \right) + (x_s - x(t)), \quad (68)$$

$$\frac{d}{dt} \left(\frac{\partial x(t)}{\partial x(0)} \right) = -k \left(\frac{\partial x(t)}{\partial x(0)} \right), \quad (69)$$

where

$$\left[\frac{\partial x(t)}{\partial x_s} \right]_{t=0} = 0 = \left[\frac{\partial x(t)}{\partial k} \right]_{t=0}, \quad \left[\frac{\partial x(t)}{\partial x(0)} \right]_{t=0} = 1. \quad (70)$$

Either by solving (67)–(70) or by computing directly from (64), it can be verified that the required sensitivities evolve according to

$$\begin{aligned} \frac{\partial x(t)}{\partial x(0)} &= e^{-kt}, & \frac{\partial x(t)}{\partial x_s} &= 1 - e^{-kt}, \\ \frac{\partial x(t)}{\partial k} &= [x_s - x(0)]te^{-kt}. \end{aligned} \quad (71)$$

The plots of the solution and the three sensitivities are given in Figure 1.

Let $z(t)$ be the direct observation of the state $x(t)$, namely,

$$z(t) = x(t) + v(t). \quad (72)$$

In this case, $h(t)$ is the forecast variable and therefore $D_x(h) = 1$. Then

$$e_F(t) = z(t) - x(t) \quad (73)$$

is the forecast error.

Following the developments in Section 4 for the case of a single observation described by (39)–(46), we obtain the analog of (46) as

$$H\zeta = e_F(t), \quad (74)$$

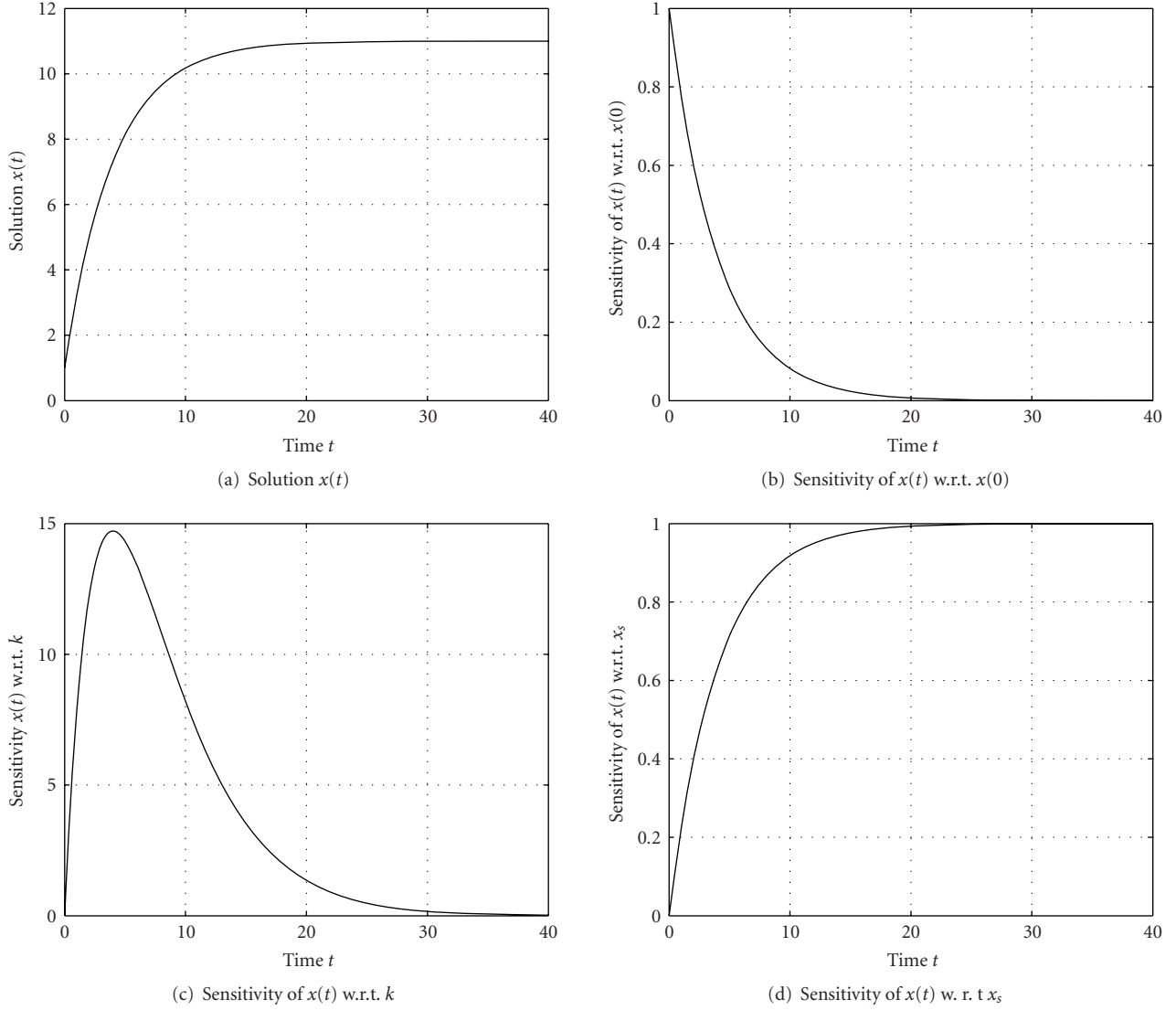


FIGURE 1: Evolution of the solution of $x(t)$ and its sensitivities to $c = (x(0), x_s, k) = (1.0, 11.0, 0.25)$.

where $H = H(t) = [\partial x(t)/\partial x(0), \partial x(t)/\partial x_s, \partial x(t)/\partial k]$ is the forward sensitivity vector and $\varsigma = [\delta x(0), \delta x_s, \delta k]^T$. Clearly, (74) corresponds to an under-determined linear least squares problem, whose optimal solution is given by [7, chapter 5]

$$\varsigma_{\text{LS}} = H^T (H H^T)^{-1} e_F(t) = \frac{H^T}{\|H\|} \frac{e_F(t)}{\|H\|}, \quad (75)$$

where $H^T/\|H\|$ is the unit forward sensitivity vector at time t and $e_F(t)/\|H\|$ is a scalar that is the forecast error normalized by the norm of the forward sensitivity vector H . In other words, the direction of the optimal corrections to the control that annihilate the forecast error is a constant multiple of the unit forward sensitivity vector.

If we assume the following control vector: $c = (1.0, 11.0, 0.25)$, that is, $[x(0) = 1^\circ\text{C}, x_s = 11^\circ\text{C}, \text{ and } k = 0.25 \text{ (nondimensional)}]$, we get

$$H^T = \begin{bmatrix} e^{-0.25t} \\ 1 - e^{-0.25t} \\ 10te^{-0.25t} \end{bmatrix} = \begin{bmatrix} \frac{\partial x(t)}{\partial x(0)} \\ \frac{\partial x(t)}{\partial x_s} \\ \frac{\partial x(t)}{\partial k} \end{bmatrix}. \quad (76)$$

The time variations of elements of H are given in Table 2 (also refer to Figure 1). From this table, it is clear that the direction of corrections to control varies as t increases. At $t = 0$, the corrections lie in the direction $(1, 0, 0)^T$, where $x(t)$ is only sensitive to the initial condition $x(0)$. For large

TABLE 2: Sensitivities of model state to initial conditions and parameters for the sea/air turbulent transfer model.

Time (hours)	$t = 0$	$t = 1$	$t = 5$	$t = 10$	$t = 15$	$t = 20$
$\partial x(t)/\partial x(0)$	1.0	0.7788	0.2865	0.0821	0.0235	0.0007
$\partial x(t)/\partial x_s$	0.0	0.2212	0.7135	0.9179	0.9765	0.9993
$\partial x(t)/\partial k$	0.0	7.788	14.325	8.2100	3.525	0.1400

t , the corrections lie in the direction $(0, 1, 0)^T$, where $x(t)$ is only sensitive to the boundary condition x_s (the sea-surface temperature). For intermediate times, all the components of control have nonzero sensitivities. $\partial x(t)/\partial k$ reaches its maximum at $t = 4.0$.

5.3. Numerical Experiments. We assume that the incorrect control vector is $c' = (x'(0), x'_s, k') = (2.0, 10.0, 0.30)$; in dimensional form, $x'(0) = 2^\circ\text{C}$, $x'_s = 10^\circ\text{C}$, and $k' = 0.30$ (non-dimensional). Thus, for an ideal correction to control,

$$\delta c = (-1.0, +1.0, -0.05). \quad (77)$$

To mimic reality, the correction process uses sensitivity functions that stem from the erroneous solution, that is, where the incorrect control is used.

We have explored both the goodness and failure of recovery of control under two different scenarios, where either 3 or 6 observations are used to recover the control vector. Since there are 3 unknowns, the case for 6 observations is an over-determined system.

We execute numerical experiments where the observations are spread over different segments of the temporal range—generally divided into an “early stage” and a “saturated stage.” By saturated stage we refer to that segment where the solution becomes close to the asymptotic state, that is, $x \rightarrow x_s$. The dividing time between these segments is arbitrary; but generally, based on experimental results to follow, we divide the segments at $t = 24$ where $\hat{x}(24) = 10.975$, 0.025 less than $\hat{x}_s = 11.0$ (see Figure 1).

The following general statement can be made. If more than one of the observations falls in the saturated zone, the matrix becomes illconditioned. As can be seen from (39) and the plots of sensitivity functions in Figure 1, $\partial x/\partial x_s \rightarrow 1$ and $\partial x/\partial x(0)$ and $\partial x/\partial k \rightarrow 0$ as $t \rightarrow \infty$. Accordingly, if two of the observations are made in the saturated zone, this induces linear dependency between the associated rows of the H matrix and in turn leads to ill-conditioning. This illconditioning is exhibited by a large value of the condition number, the ratio of the largest to the smallest eigenvalue of the matrix $H^T H$. The inversion of this matrix is central to the optimal adjustments of control (see (55)).

Illconditioning can also occur as a function of the observation spacing in certain temporal segments. This is linked to lack of variability or lack of change of sensitivity from one observation time to another. And, as can be seen in Figure 1, the absolute value of the slope in sensitivity function curves is generally large at the early stages of evolution and small at later stages. As an example, we find satisfactory recovery, $\delta c = (-0.882, -0.067, +0.922)$, when the observations are located at 5.0, 5.1, and 5.2 (a uniform

spacing of $\Delta t = 0.1$). Yet, near the saturated state, at $t = 20.0$, 20.1, and 20.2, again a spacing of 0.1, the recovery is poor with the result $\delta c = (+5.317, -0.142, +0.998)$. The associated condition numbers for these two experiments are 1.0×10^3 and 1.0×10^6 , respectively. Similar results follow from the case where 6 observations are taken. In all of these cases, the key factor is the condition number of $H^T H$. For our dynamical constraint, a condition number less than $\sim 10^4$ portends a good result.

For the case where we have 6 observations at $t = 2, 7, 12, 17, 22$, and 27, with a random error of 0.01 (standard deviation), we have executed an ensemble experiment with 100 members to recover control. In this case, the condition number is 2.4×10^3 . Results are plotted three dimensionally and in two-dimensional planes in the space of control, that is, plots of correction in the $x_s/x(0)$, x_s/k , and $x(0)/k$ planes. Results are shown in Figure 2.

Finally, we explore the iterative process of finding corrections to control. Here, the results from the 1st iteration are used to find the new control vector. This vector is then used to make another forecast and find a new set of sensitivity functions. The error of the forecast is obtained, and along with the new sensitivity functions, a second correction to control is found, and so forth. For the experiment with 6 observations that has been discussed in the previous paragraph, we apply this iterative methodology. As can be seen in Figure 3, the correct value of control is found in 3 iterations.

6. Concluding Remarks

The basic contributions of this paper may be stated as follows.

(1) While the 4D-Var has been the primary methodology for operational data assimilation in meteorology/oceanography (Lewis and Lakshmivarahan [11]), and while forward sensitivity has been a primary tool for reaction kinetics and chemistry (Rabitz et al. [1]) and air quality modeling (Russell et al. [3]), to our knowledge these two methodologies have not been linked. We have now shown that the method of computing the gradient of $J(c)$ by these two approaches exhibits a duality hitherto unknown.

(2) By treating the forward sensitivity problem as an inverse problem in data assimilation, we are able to understand the fine structure of the forecast error. This is not possible with the standard 4D-Var formulation using adjoint equations.

(3) While it is true that computation of the evolution of the forward sensitivity involves computational demands beyond those required for solving the adjoint equations in

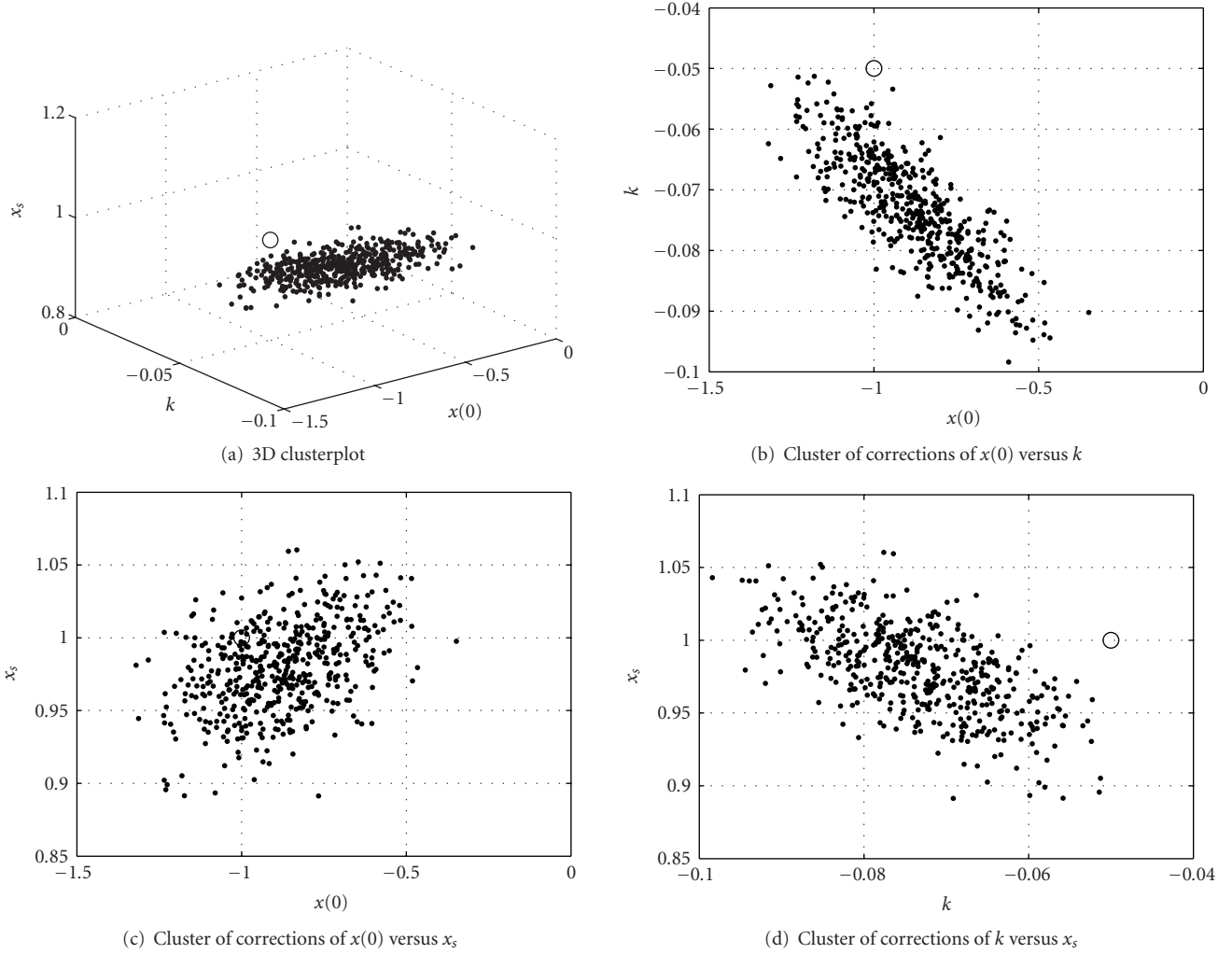


FIGURE 2: 3D cluster and its projections where corrections are computed using observations at the following times: $t = 2, 7, 12, 17, 22$, and 27 . An ensemble of 100 members is used where the standard deviation of the observation noise is 0.01.

the standard 4D-Var methodology, there is a richness or augmentation to the information that comes with this added computational demand. In essence, it allows us to make judicious decisions on placement of observations through understanding of the time dependence of correction to control.

Appendices

A. Dynamics of Evolution of Perturbations

Let $\delta c = (\delta x^T(0), \delta \alpha^T)^T \in R^n \times R^p$ be the perturbation in the control vector c and $\delta x(t)$ the resulting perturbation in the state $x(t)$ induced by the dynamics (1a) and (1b). Our goal is to derive the dynamics of evolution of $\delta x(t)$.

From first principles, the evolutionary dynamics of $\delta x(t)$ are given by the variational equation (Hirsch et al. [12]) or the tangent linear model (Lewis et al. [7])

$$\frac{d}{dt}\delta x(t) = A(t)\delta x(t) + B(t)\delta \alpha, \quad (A.1)$$

where the Jacobians $A(t)$ and $B(t)$ are given by

$$\begin{aligned} A(t) &= D_x(f) = \left[\frac{\partial f_i}{\partial x_j} \right] \in R^{n \times m}, \\ B(t) &= D_\alpha(f) = \left[\frac{\partial f_i}{\partial \alpha_j} \right] \in R^{n \times p}. \end{aligned} \quad (A.2)$$

Define the integrating factor

$$M(t, s) = \exp \left[\int_s^t A(u) du \right] \in R^{n \times n}. \quad (A.3)$$

premultiplying both sides of (A.1) by $M^{-1}(t, 0)$ and integrating, we get the solution of the linear nonhomogeneous and nonautonomous equation (A.1) as

$$\delta x(t) = M(t, 0)\delta x(0) + M(t, 0)L(t, 0)\delta \alpha, \quad (A.4)$$

where

$$L(t, s) = \int_s^t M^{-1}(u, 0)B(u)du \in R^{n \times p}. \quad (A.5)$$

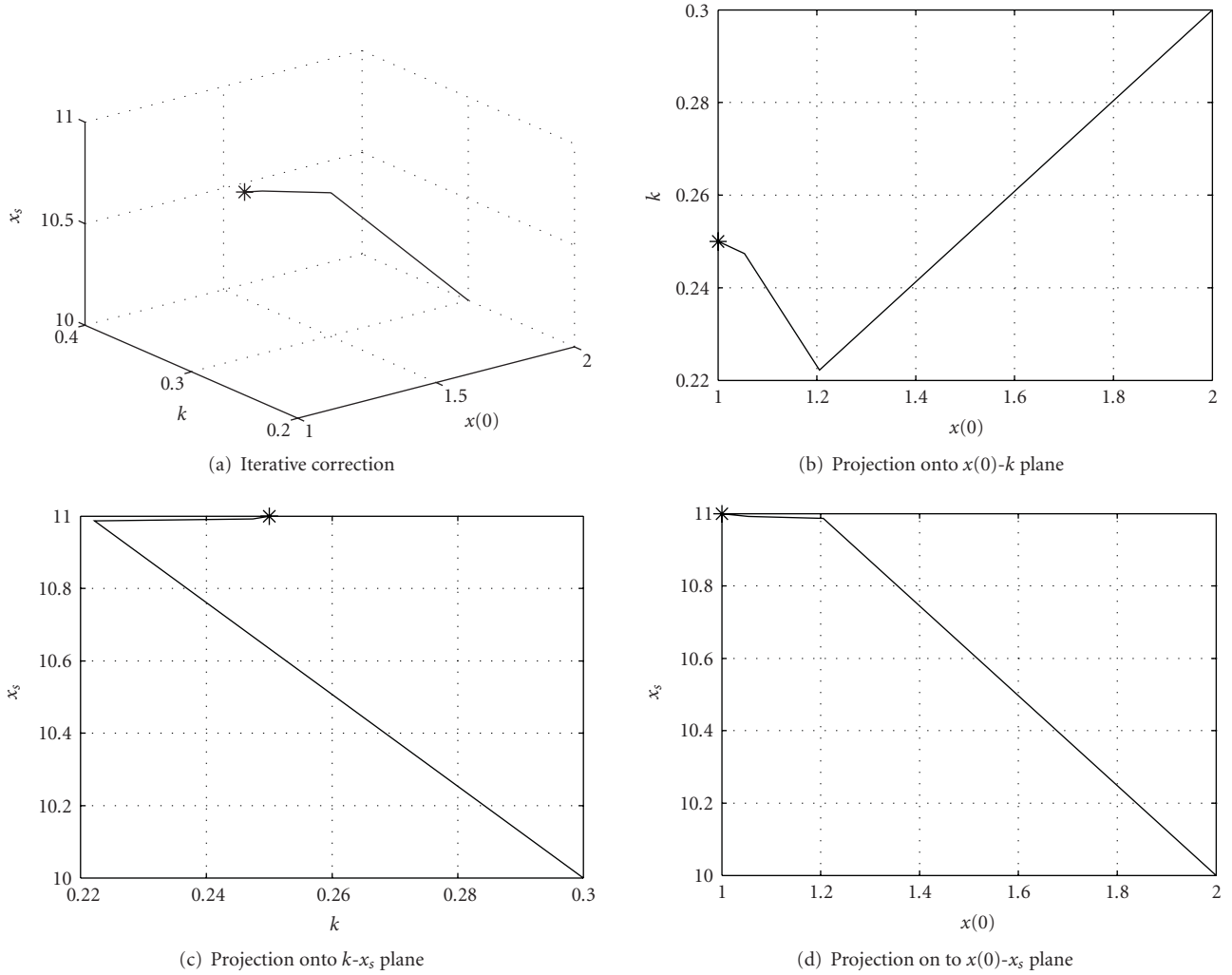


FIGURE 3: An illustration of the progression of first-order iterative corrections using six observations at $t = 2, 7, 12, 17, 22$, and 27 .

From definitions (A.3)–(A.5), it can be verified that, for $u < s < t$,

$$\begin{aligned} M(t, u) &= M(t, s)M(s, u), \\ L(t, u) &= L(t, s) + L(s, u). \end{aligned} \quad (\text{A.6})$$

We now consider two special cases.

Case A. Let $\delta\alpha = 0$, that is, the initial perturbations are confined only to the initial condition, $x(0)$. Then setting $B(t) \equiv 0$, from (A.5) we see that $L(t, 0) \equiv 0$. From (A.4) we get

$$\delta x(t) = M(t, 0)\delta x(0). \quad (\text{A.7})$$

Case B. Let $\delta x(0) = 0$, that is, the initial perturbations are confined only to the parameter, α . Then setting $A(t) \equiv 0$, from (A.3), we see that $M(t, s) \equiv I$, the identity matrix. Now from (A.4) it follows that

$$\delta x(t) = L(t, 0)\delta\alpha. \quad (\text{A.8})$$

B. Computation of Sensitivity Functions

Let $c = (c_1, c_2, \dots, c_q)^T \in R^q$, where $x = x(t, c) = (x_1(t, c), x_2(t, c), \dots, x_n(t, c))^T \in R^n$ and $h(x) = (h_1(x), h_2(x), \dots, h_m(x))^T \in R^m$. Let $a = (a_1, a_2, \dots, a_m)^T \in R^m$ and consider

$$\phi_1(c) = a^T h(x) = \sum_{i=1}^m a_i h_i(x). \quad (\text{B.9})$$

By applying the standard chain rule it can be verified that the gradient $\nabla_c \phi_1(c)$ with respect to c is given by

$$\nabla_c \phi_1(c) = D_c^T(x) D_x^T(h) a, \quad (\text{B.10})$$

where

$$D_x(h) = \left[\frac{\partial h_i}{\partial x_j} \right] \in R^{m \times n} \quad (\text{B.11})$$

is the Jacobian of h and

$$D_c(x) = \left[\frac{\partial x_i}{\partial c_j} \right] \in R^{n \times q} \quad (\text{B.12})$$


```

DO j = N to 1
  DO i = N to j
     $\eta(t_i) = M^T(t_j, t_{j-1})\eta(t_i)$ 
  END
END
 $\mu(1) = L(t_1, 0)$ 
DO i = 2 to N
   $\mu(i) = \mu(i-1) + L(t_i, t_{i-1})$ 
END
Grad = 0
DO i = 1 to N
  Grad = Grad +  $\mu(i)\eta(t_i)$ 
END

```

ALGORITHM 1

is the (Jacobian) sensitivity of the vector x with respect to c at time t .

Now consider a quadratic form

$$\phi_2(c) = h^T(x)Ah(x), \quad (\text{B.13})$$

where $A \in R^{m \times m}$ is a symmetric and positive definite matrix.

Then by the product rule

$$\nabla_c \phi_2(c) = \nabla_c [h^T b] + \nabla_c [a^T h], \quad (\text{B.14})$$

where $b = Ah = a$. By applying (B.10) to each of the two terms on the right side of (B.14), it follows that

$$\nabla_c \phi_2(c) = 2D_c^T(x)D_x^T(h)Ah. \quad (\text{B.15})$$

Finally, if

$$Q(c) = [z - h(x)]^T A [z - h(x)], \quad (\text{B.16})$$

then expand

$$Q(c) = z^T A z - 2z^T A h(x) + h^T(x) A h(x) \quad (\text{B.17})$$

since z does not depend on c , by using (B.10) and (B.15), we get

$$Q(c) = -2D_c^T(x)D_x^T(h)A[z - h(x)]. \quad (\text{B.18})$$

Define

$$\xi = D_x^T(h)A[z - h(x)] \in R^n, \quad (\text{B.19})$$

then

$$\nabla_c Q(c) = -2D_c^T(x)\xi. \quad (\text{B.20})$$

That is, the gradient of Q with respect to c is the linear combination of the sensitivity vectors, that is, the columns of $D_c^T(x)$, where the coefficients in this linear combination are the elements of the vector ξ .

C. Computation of $\nabla_\alpha J$ in (27)

Given $\eta(t_i)$, $M^T(t_i, t_{i-1})$, $L^T(t_i, t_{i-1})$ for $1 \leq i \leq N$, the expression on the right-hand side of (27) can be efficiently computed as shown in Algorithm 1.

Then $\nabla_\alpha J = -\text{Grad}$. It is to be noticed that there is only matrix-vector multiplication involved in these operations and not matrix-matrix multiplication.

Acknowledgments

At an early stage of formulating our ideas on this method of data assimilation, Fedor Mesinger and Qin Xu offered advice and encouragement. Qin Xu and Jim Purser carefully checked the mathematical development, and suggestions from the following reviewers went far to improve the presentation: Yoshi Sasaki, Bill Stockwell, and anonymous formal reviewers of the manuscript. S. Lakshmivarahan's work is supported in part by NSF EPSCoR RII Track 2 Grant 105-155900 and by NSF Grant 105-15400, and J. Lewis acknowledges the Office of Naval Research (ONR), Grant No. N00014-08-1-0451, for research support on this project.

References

- [1] H. Rabitz, M. Kramer, and D. Dacol, "Sensitivity analysis in chemical kinetics," *Annual Review of Physical Chemistry*, vol. 334, pp. 419–461, 1983.
- [2] S. Seefeld and W. R. Stockwell, "First-order sensitivity analysis of models with time-dependent parameters: an application to PAN and ozone," *Atmospheric Environment*, vol. 33, no. 18, pp. 2941–2953, 1999.
- [3] A. Russell, J. Milford, M. S. Bergin, et al., "Urban ozone control and atmospheric reactivity of organic gases," *Science*, vol. 269, no. 5223, pp. 491–495, 1995.
- [4] F.-X. Le Dimet and O. Talagrand, "Variational algorithms for analysis and assimilation of meteorological observations: theoretical aspects," *Tellus A*, vol. 38, no. 2, pp. 97–110, 1986.
- [5] D. P. Dee, "Bias and data assimilation," *Quarterly Journal of the Royal Meteorological Society*, vol. 131, no. 613, pp. 3323–3343, 2006.
- [6] C. W. Gear, *Numerical Initial Value Problems in Ordinary Differential Equations*, Prentice-Hall, Englewood Cliffs, NJ, USA, 1971.
- [7] J. M. Lewis, S. Lakshmivarahan, and S. Dhall, *Dynamic Data Assimilation: A Least Squares Approach*, Cambridge University Press, Cambridge, UK, 2006.
- [8] S. Lakshmivarahan and J. M. Lewis, "Forecast error correction using forward sensitivity analysis: framework," Tech. Rep., School of Computer Sciences, University of Oklahoma, Norman, Okla, USA, 2009.
- [9] C. L. Lawson and R. J. Hanson, "Solving least squares problems," in *Classics in Applied Mathematics*, vol. 15, p. 337, SIAM, Philadelphia, Pa, USA, 1995.
- [10] S. G. Nash and A. Sofer, *Linear and Nonlinear Programming*, McGraw-Hill, New York, NY, USA, 1996.
- [11] J. M. Lewis and S. Lakshmivarahan, "Sasaki's pivotal contribution: calculus of variations applied to weather map analysis," *Monthly Weather Review*, vol. 136, no. 9, pp. 3553–3567, 2008.
- [12] M. W. Hirsch, S. Smale, and R. L. Devaney, *Differential Equations, Dynamical Systems and Linear Algebra*, Academic Press, New York, NY, USA, 2nd edition, 2004.

Research Article

A 3.5-Dimensional Variational Method for Doppler Radar Data Assimilation and Its Application to Phased-Array Radar Observations

Qin Xu,¹ Li Wei,² Wei Gu,³ Jiandong Gong,⁴ and Qingyun Zhao⁵

¹ National Severe Storms Laboratory, Norman, OK 73072, USA

² Cooperative Institute for Mesoscale Meteorological Studies, University of Oklahoma, Norman, OK 73072, USA

³ Global Modeling and Assimilation Office, NASA Goddard Space Flight Center,
Science Application International Corporation, Greenbelt, MD 20771, USA

⁴ National Meteorological Center, China Meteorological Administration, Beijing 100081, China

⁵ Marine Meteorology Division, Naval Research Laboratory, Monterey, CA 93943-5502, USA

Correspondence should be addressed to Qin Xu, qin.xu@noaa.gov

Received 1 January 2010; Accepted 3 April 2010

Academic Editor: Zhaoxia Pu

Copyright © 2010 Qin Xu et al. This is an open access article distributed under the Creative Commons Attribution License, which permits unrestricted use, distribution, and reproduction in any medium, provided the original work is properly cited.

A 3.5-dimensional variational method is developed for Doppler radar data assimilation. In this method, incremental analyses are performed in three steps to update the model state upon the background state provided by the model prediction. First, radar radial-velocity observations from three consecutive volume scans are analyzed on the model grid. The analyzed radial-velocity fields are then used in step 2 to produce incremental analyses for the vector velocity fields at two time levels between the three volume scans. The analyzed vector velocity fields are used in step 3 to produce incremental analyses for the thermodynamic fields at the central time level accompanied by the adjustments in water vapor and hydrometeor mixing ratios based on radar reflectivity observations. The finite element B-spline representations and recursive filter are used to reduce the dimension of the analysis space and enhance the computational efficiency. The method is applied to a squall line case observed by the phased-array radar with rapid volume scans at the National Weather Radar Testbed and is shown to be effective in assimilating the phased-array radar observations and improve the prediction of the subsequent evolution of the squall line.

1. Introduction

Because the radar network provides only single-Doppler scanning over most areas in the U.S., research efforts have been undertaken to develop various methods for meteorological parameter retrievals from single-Doppler observations (Sun et al. [1]; Kapitza [2]; Qiu and Xu [3]; Sun and Crook [4]; Xu et al. [5, 6]; Laroche and Zawadzki [7]; Shapiro et al. [8]; Zhang and Gal-Chen [9]; Liou [10]; Gao et al. [11]; Weygandt et al. [12]). These previous efforts, however, were focused mainly on retrievals with zero background information. By utilizing the background information provided by model predictions, some of the previous retrieval methods can be upgraded for radar data assimilation (Sun and Crook [13]; Xu et al. [14]; Gu et al. [15]

Gao et al. [16]; Hu et al. [17]). This paper presents a 3.5-dimensional variational method for radar data assimilation developed by upgrading and combining the previous retrieval methods (Qiu and Xu [18]; Xu et al. [19]; Gal-Chen [20]; Hane and Scott [21]). This method uses simplified dynamical and thermodynamical equations of a numerical weather prediction (NWP) model (in this study we use the Coupled Ocean/Atmosphere Mesoscale Prediction System or COAMPS (COAMPS is a registered trademark of the Naval Research Laboratory.), Hodur [22]) as constraints while the background information is provided by the model forecasts. The concept and basic design of the method are described in the next section in connection with the general variational formulation derived from the estimation theory. The detailed formulations are presented for the three steps of the method

in Sections 3–5. The method is applied to phased-array radar observations for a squall line case in Section 6. Conclusions follow in Section 7.

2. Estimate Theory and Variational Methods

Equations in an NWP model can be expressed symbolically in the following vector form:

$$\mathbf{x}_k - \mathbf{f}(\mathbf{x}_{k-1}) = \mathbf{q}_k, \quad (1)$$

where \mathbf{x}_k is the state vector representing the discrete fields of the prognostic variables, \mathbf{f} the forward model operator, \mathbf{q}_k the model error, and the subscript k denotes the k th time level of the model integration. A prior estimate of the state vector \mathbf{x}_0 at the initial time ($k = 0$) is given by the model prediction from the previous data assimilation cycle. The state vector \mathbf{x}_0 at the initial time ($k = 0$) can be expressed by

$$\mathbf{x}_0 = \langle \mathbf{x}_0 \rangle + \mathbf{b}, \quad (2)$$

where $\langle (\cdot) \rangle$ denotes the probabilistic mean (expectation) of (\cdot) , and \mathbf{b} the random part of \mathbf{x}_0 . A prior estimate of $\langle \mathbf{x}_0 \rangle$ is given by the model prediction from the previous data assimilation cycle. This background estimate is assumed to be unbiased. The observations can be expressed by

$$\mathbf{y}_m - \mathbf{h}(\mathbf{x}_m) = \mathbf{r}_m, \quad (3)$$

where \mathbf{y}_m is the vector of observations, \mathbf{h} the observation operator, and \mathbf{r}_m the observation error, and the subscript m denotes the m th time level of the observations. In general, we assume that the data assimilation period covers M observation time levels (from $m = 1$ to M) and K model time levels (from $k = 1$ to K), and the M observation time levels are a subset of the K model time levels.

Assume that \mathbf{q}_k is a white Gaussian sequence and \mathbf{x}_k generated by (1) is Markov, which would be the case with linear dynamics. Assume also that \mathbf{b} and \mathbf{r}_m are Gaussian random, unbiased (with zero mean), not cross-correlated and not correlated with \mathbf{q}_k . Then, according to Sherman and Bayes theorems (see Jazwinski [23, Chapter 5]), given observations \mathbf{y}_m ($m = 1, 2, \dots, M$), the conditional maximum likelihood estimate of \mathbf{x}_k is also the conditional mean of \mathbf{x}_k ($k = 0, 1, \dots, K$), and is given by the minimizer of the following cost function:

$$\begin{aligned} J = & (\mathbf{x}_0 - \langle \mathbf{x}_0 \rangle)^T \mathbf{B}^{-1} (\mathbf{x}_0 - \langle \mathbf{x}_0 \rangle) \\ & + \sum_m [\mathbf{y}_m - \mathbf{h}(\mathbf{x}_m)]^T \mathbf{R}_m^{-1} [\mathbf{y}_m - \mathbf{h}(\mathbf{x}_m)] \\ & + \sum_k \mathbf{q}_k^T \mathbf{Q}_k^{-1} \mathbf{q}_k \\ & + \sum_k \boldsymbol{\lambda}_k^T [\mathbf{x}_k - \mathbf{f}(\mathbf{x}_{k-1}) - \mathbf{q}_k], \end{aligned} \quad (4)$$

where $\mathbf{B} = \langle \mathbf{b}\mathbf{b}^T \rangle$, $\mathbf{R}_m = \langle \mathbf{r}_m \mathbf{r}_m^T \rangle$ and $\mathbf{Q}_k = \langle \mathbf{q}_k \mathbf{q}_k^T \rangle$ are the error covariance matrices for the background, observations, and model equations, respectively, \sum_m denotes the summation

over m (from 1 to M), \sum_k denotes the summation over k (from 1 to K), $(\cdot)^T$ denotes the transpose of (\cdot) , and $\boldsymbol{\lambda}_k$ is the vector Lagrangian multiplier for the vector constraint given by (1).

The cost function in (4) presents a general formulation for four-dimensional variational (4dVar) data assimilation. The related methods of solution (Jazwinski [23]; Bennett [24]), however, are computationally too expensive for radar data assimilation. By setting $\mathbf{q}_k = 0$ in (4), the above 4dVar reduces to the perfect-model 4dVar (P4dVar), so the cost function minimum can be searched effectively by the adjoint method especially if \mathbf{B}^{-1} and \mathbf{R}_m^{-1} are simply prescribed (Lewis and Derber [25]; Le Dimet and Talagrand [26]). Note that a volume scan from a single Doppler radar can contain up to 10^6 observations. To assimilate high-resolution radar observations over a mesoscale area, the model state vector \mathbf{x}_k often needs to contain at least as many as 10^6 gridded variables. In this case, the P4dVar is still too expensive and unpractical for real-time radar data assimilation.

A further simplification can be made by setting not only $\mathbf{q}_k = 0$ but also $M = 1$, $K = 0$ ($\sum_k = 0$) and $\boldsymbol{\lambda} = 0$ in (4). In this case, the observations are assimilated at a single time level without using any model equation constraint, so the 4dVar reduces to a three-dimensional variational (3dVar) formulation (Parrish and Derber [27]; Gao et al. [16]). Such a 3dVar is computationally efficient for real-time operational radar data assimilation, but it assimilates radar observed reflectivity and radial velocity (along the radar beam) at only a single time level. The tangential-velocity component (perpendicular to the radar beam) is not observed by the radar but often critical for model initialization and prediction. The same is true for the thermodynamic variables such as pressure and temperature which are not observed by the radar. These unobserved variables can be partially retrieved from four-dimensional radar observations (at two or more consecutive time levels) by using a P4dVar (Sun and Crook [4]) or a simple-model 4dVar (Xu et al. [14]). The required computations, however, are not practical for real-time applications unless the model size is sufficiently small (such as the one used in Xu et al. [14] with a $20 \times 20 \times 14$ grid for a $8 \times 8 \times 2.8 \text{ km}^3$ domain). To solve the above problems, the simple-model 4dVar (Xu et al. [14]) needs to be further simplified to achieve the required computational efficiency but not overly reduced to a 3dVar, so that four-dimensional radar observations can still be used to extract information for the unobserved variables. Such simplifications are made in three steps based on the previous retrieval methods (Qiu and Xu [18]; Gal-Chen [20]; Hane and Scott [21]), which leads to the method presented in this paper.

As shown by the flowchart in Figure 1, the method assimilates four-dimensional radar observations (from three consecutive time levels of radar volume scans) in three steps. In step 1, raw level II radial velocity data (from a single or multiple radars) are quality-controlled and analyzed on the model grids by using a 3dVar. The cost function of this 3dVar is a simplification of (4) by setting $M = 1$ and $K = 0$ (with $\sum_k = 0$ and $\boldsymbol{\lambda} = 0$) to retain only the background and observation terms (see (6)–(10)). The above analysis is performed for each of three consecutive volume scans at

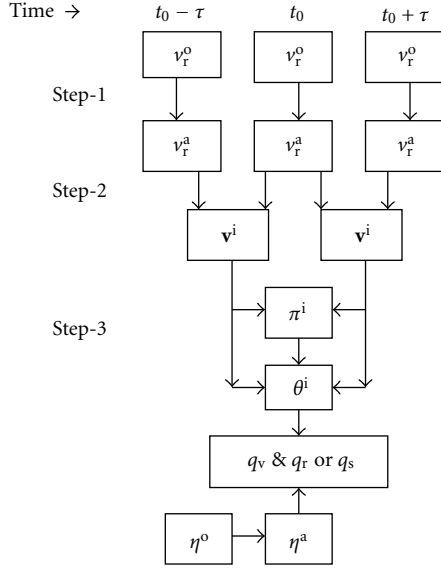


FIGURE 1: Flowchart for the three steps of the method. Step 1 controls the quality of radial velocity observations v_r^o and produces radial velocity analyses v_r^a (on model grid) by minimizing J_1 in (6) at $t_0 - \tau$, t_0 and $t_0 + \tau$, respectively, for three consecutive radar volume scans. Step 2 produces the vector velocity increments \mathbf{v}^i by minimizing J_2 in (11) at $t_0 - \tau/2$ and $t_0 + \tau/2$, respectively. Step 3 produces the perturbation pressure increment π^i by minimizing J_π in (16) first, and then produces the perturbation potential temperature increment θ^i by minimizing J_θ in (18) at t_0 , and finally adjusts the water vapor mixing ratio q_v and the rain (or snow) mixing ratio q_r (or snow mixing ratio q_s) below (or above) the freezing level.

their respective central time levels: $t_0 - \tau$, t_0 and $t_0 + \tau$ (see Figure 1), where τ is the duration of one volume scan (about 1.5 minutes for the phased-array radar data used in this paper). The analyzed radial velocity fields are then used as gridded observations in step 2. The cost function used in step 2 is a simplification of (4) by setting $M = K = 1$ and $\lambda = 0$. This cost function retains the mass continuity equation and radial momentum equation (i.e., the radial component of the vector momentum equation) in \mathbf{q}_k in addition to the background and observation terms, but the two retained equations are simplified into incremental forms (see (13) and (15)). By fitting the radial momentum equation to the analyzed radial velocity observations (from step 1) at the time levels $t_0 - \tau$ and t_0 (or t_0 and $t_0 + \tau$) in four-dimensional space, the vector velocity increment can be estimated at $t_0 - \tau/2$ (or $t_0 + \tau/2$). Once the vector velocity fields are updated at $t_0 - \tau/2$ and $t_0 + \tau/2$ in step 2, they are used as input data in step 3 to produce incremental analyses for the perturbation pressure and potential temperature at t_0 . The cost function in step 3 is a simplification of (4) by setting $M = 0$ (with $\sum_m = 0$), $K = 1$ and $\lambda = 0$, but only the two horizontal momentum equations are retained and simplified into incremental forms for the perturbation pressure analysis (see (16)) and only the vertical momentum equation is retained and simplified into an incremental form for the perturbation potential temperature analysis (see (17)). At the end of step 3, the

water vapor and hydrometeor mixing ratios are also adjusted based on the radar observed reflectivity. In the above step 2 and step 3, the input data are fitted at two time levels in four-dimensional space, but the output incremental analyses are three-dimensional. In this sense, the method is called a three-and-half-dimensional variational (3.5dVar) method. The detailed formulations and computation procedures are presented for each step in the following three sections.

3. Data Quality Control and Radial Velocity Analysis

3.1. Data Quality Control. The quality control procedure checks for and corrects two types of errors in raw level II radial velocity data. First, it corrects the possible velocity alias error (if any) caused by the finite range of radar velocity measurements limited by the Nyquist velocity v_N . Since the model predicted velocity $\mathbf{v}^f = (u^f, v^f, w^f)$ is used as the reference field, the dealiasing technique used in this paper is a simplified version of the three-step dealiasing of Gong et al. [28]. The dealiasing procedure is described as follows:

- (i) Interpolate \mathbf{v}^f from model grid to each observation point with the radar beam height computed by using the equivalent Earth model (see Doviak and Zrnić [29, Section 2.2.3.1]). Project the interpolated \mathbf{v}^f onto the radial direction (along the radar beam) to obtain the background radial velocity $v_r^f = \mathbf{r}_o \cdot \mathbf{v}^f$, where \mathbf{r}_o is the unit vector tangential to the radar beam at the observation point and is computed by considering the effects of the standard atmospheric refraction and Earth curvature (see Doviak and Zrnić [29, (2.28) and (9.9)]). Calculate the innovation $v_r^d = v_r^o - v_r^f$ at each observation point, where v_r^o denotes the observation.
- (ii) Take the integer n nearest to $v_r^d/(2v_N)$ (where v_N is the Nyquist velocity) and adjust the observational radial velocity to $v_r^o - 2nv_N$ so that the adjusted innovation (i.e., the adjusted observation minus the background value) is between $\pm v_N$.
- (iii) If the absolute value of the adjusted innovation is less than $0.5v_N$, then the adjusted observation is accepted as a “good” one and used to replace the original v_r^o . Otherwise, perform the continuity check (buddy check) which is similar to the third step described in Gong et al. [28, Section 2d] but the threshold value is set to $0.25v_N$ for the acceptable absolute difference between the adjusted observation and the averaged value of “good” neighborhood observations.

For the second type of correction, the data quality control removes the error caused by the precipitation terminal velocity. The terminal velocity, w_T , is estimated empirically (Kessler [30]) by

$$w_T = -3.088 \times 10^{0.00957Z}, \quad (5)$$

where Z is the observed reflectivity in dBZ. The projection of the terminal velocity on the radial direction is $w_T \sin \alpha$

where α is the local tilt angle of the radar beam. Thus, with the above two types of correction, the originally observed v_r^o is replaced by $v_r^o - 2nv_N - w_T \sin \alpha$ at each observation point where $n \neq 0$ or $w_T \neq 0$. For simplicity, the corrected radial velocity observation will still be denoted by v_r^o in the remaining part of this paper.

3.2. Radial Velocity Analysis. The radial velocity analysis is performed by minimizing the following cost function:

$$J_1 = J_{bk} + J_{ob}, \quad (6)$$

where J_{bk} is the background term and J_{ob} the observation term. This cost function is a 3dVar formulation derived from (4) by setting $M = 1$ and $K = 0$, as explained in Section 2. The control variable for J_1 is the analysis increment defined by $\mathbf{v}^i = (u^i, v^i, w^i) = \mathbf{v}^a - \mathbf{v}^b$ where \mathbf{v}^a and \mathbf{v}^b denote the analysis and background velocities, respectively. Since the analyzed radial velocity fields obtained in step 1 will be used as observed “tracer” fields to retrieve the vector wind field in step 2 (see Figure 1), the analysis in step 1 should “interpolate” as accurate as possible the observed radial velocity fields onto the model grid. Because of this, the analysis is performed with zero background ($\mathbf{v}^b = 0$) but the background error covariance is nonzero in the background term J_{bk} , and the ratio between the background and observation error variance is set to $\sigma_{vr}^2/\sigma_{ob}^2 = 10$, where σ_{vr}^2 and σ_{ob}^2 denote the radial velocity background and observation error variances, respectively.

To facilitate the formulation and computation of the background term, \mathbf{v}^a or, equivalently, \mathbf{v}^i (since $\mathbf{v}^b = 0$ in step 1) is treated as an intermediate control variable with its two horizontal components (u^i, v^i) expressed in terms of stream function and velocity potential by

$$u^i = -\partial \frac{\psi^i}{\partial y} + \partial \frac{\chi^i}{\partial x}, \quad v^i = \partial \frac{\psi^i}{\partial x} + \partial \frac{\chi^i}{\partial y}. \quad (7)$$

The grid field of (u^i, v^i) can be computed from the grid field of (ψ^i, χ^i) by using the standard central finite difference scheme (in the horizontal). Denote by $(\psi^i, \chi^i, \mathbf{w}^i)$ the state vectors of the grid fields of (ψ^i, χ^i, w^i) . These three state vectors can be related to three new intermediate vectors (ψ, χ, \mathbf{w}) by

$$(\psi^i, \chi^i, \mathbf{w}^i) = (\mathbf{B}_1^{1/2} \psi, \mathbf{B}_2^{1/2} \chi, \mathbf{B}_3^{1/2} \mathbf{w}), \quad (8)$$

where \mathbf{B}_1 , \mathbf{B}_2 , and \mathbf{B}_3 are the univariate error covariance matrices for the background fields ψ^f , χ^f , and w^f , respectively. The background term is then given by

$$J_{bk} = |\psi|^2 + |\chi|^2 + |\mathbf{w}|^2. \quad (9)$$

Here, it is assumed that the background errors are not cross-correlated between ψ^f , χ^f , and w^f . With this assumption, ψ^i , χ^i , and \mathbf{w}^i are decoupled in the background term as shown by (9), so the computation is simplified.

The background error covariances for $(\psi^b, \chi^b, \mathbf{w}^b)$ are modeled by horizontally isotropic Gaussian functions. The

decorrelation length and depth are the parameters that need to be predefined empirically. Since the analyzed radial velocity fields obtained in this step will be used as observed “tracer” fields to retrieve the vector wind field in step 2, a relatively small horizontal decorrelation length should be used in step 1 to prevent the analyzed “tracer” field from becoming overly smoothed. On the other hand, the decorrelation length should not be too small to filter spurious $2\Delta x$ waves. Based on these considerations, we set the horizontal decorrelation length to $L_\psi = L_\chi = 3\sqrt{2}\Delta x$ (which is 1/2 of that used in step 2 as shown Section 4) and the vertical decorrelation depth to $D_\psi = D_\chi = \Delta z/\sqrt{3}$ for (ψ^b, χ^b) in step 1. This gives $L_w = L_\chi/\sqrt{3} = \sqrt{6}\Delta x$ and $D_w = \Delta z$ for w^b according to (A.8) and (A.9), where Δx (=6 km in this study) is the horizontal grid spacing and Δz is the vertical grid spacing (from 0.02 to 0.25 km in the boundary layer, and about 1 km in the middle troposphere). The error variance for (ψ^b, χ^b) and w^b is then related to σ_{vr}^2 by $\sigma_\psi^2 = \sigma_\chi^2 = 0.5\sigma_{vr}^2 L_\chi^2$ and $\sigma_w^2 = 4\sigma_{vr}^2 D_w^2/L_\chi^2$, respectively, (see (A.19) and (A.20)). The covariance matrices in (8) are too large to compute explicitly, but their represented linear transformations in (8) can be simulated efficiently by either recursive filters (Purser et al. [31]) or differential operators (Xu [32]). Each horizontal field of (ψ, χ, \mathbf{w}) is further expressed by an expansion of quadratic B-spline basis functions on coarse finite element meshes (Xu et al. [19]), so the final control variables are the B-spline coefficients of (ψ, χ, \mathbf{w}) .

The observation term has the following general form (for step 1 and step 2)

$$J_{ob} = \frac{\{ \{ (v_r^i - v_r^d)^2 \} \}}{\sigma_{ob}^2}, \quad (10)$$

where $\{ \{ \} \}$ denotes the summation over all observation points, $v_r^d = v_r^o - v_r^b$ is the innovation, $v_r^i = \mathbf{r}_o \cdot \mathbf{v}^i$ is the incremental radial velocity at each observational point, and \mathbf{r}_o is the unit vector tangential to the radar beam at the observation point (computed by considering the effects of the standard atmospheric refraction and Earth curvature as in Doviak and Zrnić [29, (2.28) and (9.9)]). As explained earlier, since $\mathbf{v}^b = 0$, we have $v_r^b = \mathbf{r}_o \cdot \mathbf{v}^b = 0$ and thus $v_r^d = v_r^o$ and $v_r^i = v_r^a = \mathbf{r}_o \cdot \mathbf{v}^a$ in step 1. In (10), the observation errors are assumed to be not correlated between different observation points, so \mathbf{R}_m (with $m = M = 1$) reduces to $\mathbf{I}\sigma_{ob}^2$ in (4). This assumption should be a valid approximation because radial velocity observation errors are correlated only between neighboring observation points (Xu et al. [33]). By setting $\sigma_{vr}^2/\sigma_{ob}^2 = 10$ as explained earlier, there is no need to estimate σ_{ob}^2 and σ_{vr}^2 separately for the analysis in step 1.

As in (9), \mathbf{v}^i and v_r^i in (10) are also converted to (ψ, χ, \mathbf{w}) by using (7) and (8). Each horizontal field of (ψ, χ, \mathbf{w}) is then further expressed by an expansion of quadratic B-spline basis functions on coarse finite element meshes (Xu et al. [19]), so the final control variables are the B-spline coefficients of (ψ, χ, \mathbf{w}) . The B-spline representation enhances the filtering and reduces the dimension of the analysis space. By using the standard conjugate gradient algorithm, the cost function in (6) is minimized efficiently in the reduced space spanned by the final control variables—the B-spline coefficients. As

\mathbf{v}^i is linearly related to the B-spline coefficients, \mathbf{v}^i is readily estimated once the cost function is minimized. Since only one time level of radial velocity observations is used, the estimated \mathbf{v}^i is not accurate, but its radial component $v_r^i = \mathbf{r}_o \cdot \mathbf{v}^i$ ($=v_r^a$ in step 1) should be accurate and can be used as gridded observations for the vector velocity analysis in step 2 in the next section.

4. Vector Velocity Analysis

The vector velocity analysis is performed by minimizing the following cost function:

$$J_2 = J_{bk} + J_{ob} + J_{rm} + J_{ms}. \quad (11)$$

This cost function is derived from (4) by setting $M = K = 1$ and $\lambda = 0$ to retain only the mass continuity equation and the radial momentum equation in \mathbf{q}_k , so the equation term in (4) reduces to the sum of the mass continuity equation term J_{ms} and radial momentum equation term J_{rm} in (11).

The background term in (11) has the same form as in (9) except that the background velocity is no longer set to zero (as in step 1) and is given by $\mathbf{v}^b = \mathbf{v}^f$, where \mathbf{v}^f is the model forecast. The error covariance functions for the model background winds were estimated from a time series of the radar innovations for the same case considered in the paper. As shown in Xu et al. [34, Figure 3], the main part of the error correlation function for the horizontal background winds can be modeled approximately by a Gaussian function over the range of 40 km, but the tail part oscillates around zero and reaches a secondary peak (≈ 0.1) at the separation distance of 125 km. The decorrelation length estimated from this error correlation function was $L = 43$ km, but this estimated value was affected by the second peak in the tail part. For the main Gaussian part, the estimated decorrelation length should be reduced at least to 36 km ($= 6\Delta x$). Thus, the decorrelation lengths for (ψ^f, χ^f) and w^f can be estimated by $L_\psi = L_\chi = 6\sqrt{2}\Delta x$ and $L_w = L_\chi/\sqrt{3}$ (see (A.15)–(A.17)). The vertical decorrelation depth is set empirically to $D_w = \Delta z$ for w^f , so $D_\psi = D_\chi = \Delta z/\sqrt{3}$ for (ψ^f, χ^f) (see (A.8) and (A.10)). The analysis time level for J_{bk} in (11) is at $t_0 - \tau/2$ (or $t_0 + \tau/2$)—the middle time level between $t_0 - \tau$ and t_0 (or t_0 and $t_0 + \tau$), so the incremental field \mathbf{v}^i ($= \mathbf{v}^a - \mathbf{v}^f$) and background velocity field \mathbf{v}^f are also all at $t_0 - \tau/2$ (or $t_0 + \tau/2$).

The observation term J_{ob} for J_2 in (11) has the same form as that in (10) for J_1 , but the background velocity is given by $\mathbf{v}^b = \mathbf{v}^f$ (instead of $\mathbf{v}^b = 0$ as in step 1) and the observations are binned from the two time levels at $t_0 - \tau$ and t_0 (or t_0 and $t_0 + \tau$) to the middle-time level at $t_0 - \tau/2$ (or $t_0 + \tau/2$). Since the background and observation errors are uncorrelated (Xu and Wei [35]), the sum of their error variances is given by the innovation variance $\sigma_{vr}^2 + \sigma_{ob}^2 = \sigma_d^2$, where σ_d^2 denotes the radial velocity innovation variance, σ_{vr}^2 and σ_{ob}^2 denote the radial velocity background and observation error variances, respectively. Since zero background is used in step 1, the spatial variance of the innovation (v_r^o minus v_r^f in the observation space) is used to estimate σ_d^2 in each assimilation cycle. The background error variance is estimated by $\sigma_{vr}^2 =$

$\sigma_d^2 - \sigma_{ob}^2$ with σ_{ob} given by a pre-estimated value. For the phased-array radar data used in this paper, $\sigma_{ob} = 2 \text{ ms}^{-1}$ is pre-estimated according to the statistical analysis of the phased-array radar innovation data (Xu et al. [34]).

The third term in (11) is the mass continuity equation term given by

$$J_{ms} = \frac{[[E_{ms}^2]]}{\sigma_{ms}^2}, \quad (12)$$

where $[[\]]$ denotes summation over all grid points, E_{ms} is the mass continuity equation constraint for \mathbf{v}^i , and σ_{ms}^2 is the equation error variance or, specifically, the variance of the residual error of E_{ms} . The equation errors are assumed to be not correlated between different grid points and different equations. In COAMPS, the mass continuity equation is embedded in the pressure tendency equation (see Hodur [22, (5) and (20)]). From the COAMPS pressure tendency equation, the extracted mass continuity equation has the following incremental form:

$$E_{ms} = (\partial_x + G_x \partial_\sigma)(\rho \Theta_v u^i) + (\partial_y + G_y \partial_\sigma)(\rho \Theta_v v^i) + G_z \partial_\sigma(\rho \Theta_v w^i), \quad (13)$$

where $G_x = a\partial_x z_s$, $G_y = a\partial_y z_s$, $G_z = \partial_z \sigma$, $a = (s - H)/(H - z_s)$, $\sigma = H(z - z_s)/(H - z_s)$, H and z_s are the heights of the model top and bottom terrain boundaries, respectively, Θ_v the basic state virtual potential temperature, and ρ the basic state density. Here, the equation errors are assumed to be not spatially correlated, so \mathbf{Q}_k (with $k = K = 1$) reduces to $\mathbf{I}\sigma_{ms}^2$ and the equation term in (4) reduces to J_{ms} . The first two terms on the right-hand side of (13) are the horizontal divergence and the associated RMS error can be estimated by $\sigma_{div}/L_{div} = \sqrt{2}\sigma_{vr}/L_\chi$ (see (A.16) and (A.18)). The last term in (13) is smaller than the first two terms, and its RMS error should be relatively small. Based on this consideration, $\sigma_{ms} = 2\sigma_{vr}/L_\chi$ is estimated.

The last term in (11) is given by

$$J_{rm} = \frac{[[E_{rm}^2]]}{\sigma_{rm}^2}, \quad (14)$$

where E_{rm} is the radial momentum equation in an incremental form, and σ_{rm}^2 is the variance of the residual error of E_{rm} . The radial momentum equation is obtained by projecting the model vector momentum equation (Hodur [22, (2)–(4)]) onto the radial direction along the radar beam, and then converted into the following incremental form:

$$E_{rm} = \partial_t v_r^i + \mathbf{v}^a \cdot \nabla v_r^i + \mathbf{v}^i \cdot \nabla v_r^f - \frac{[\mathbf{v}^i \cdot (\mathbf{v}^i + 2\mathbf{v}^f) - (v_r^a)^2 + (v_r^f)^2]}{r} + \mathbf{r}_o \cdot (f\mathbf{k} \times \mathbf{v}^i) - Dv_r^i, \quad (15)$$

where $\mathbf{v}^a = \mathbf{v}^f + \mathbf{v}^i$, f is the Coriolis parameter, r is the radial distance from the radar, $\nabla = (\partial_x, \partial_y, \partial_\sigma)$ is the gradient operator in the σ -coordinates, D is the diffusion operator

for subgrid-scale turbulent mixing as in COAMPS, and \mathbf{k} is the unit vector in the vertical direction. Note that the thermodynamic variables are not updated yet, so they have zero increment at this step, as assumed in (15).

The time derivative term $\partial_t v_r^i$ in (15) is discretized by the standard central finite difference scheme with v_r^a given by the gridded observations (obtained from step 1) at $t_0 - \tau$ and t_0 (or t_0 and $t_0 + \tau$). All the remaining terms in (11) are at the middle time level $t_0 - \tau/2$ (or $t_0 + \tau/2$), so v_r^a is interpolated to the middle time level in these terms. A further simplified version of (15) was used by Qiu and Xu [18] as a weak constraint with zero background velocity to retrieve low-altitude winds from single-Doppler radar scans. The radial momentum equation in (15) and cost function in (11) are extensions and improvements relative to their counterparts used in (1) and (2) of Qiu and Xu [18].

The radial momentum equation in (15) is formulated at the middle time level and the equation errors are assumed to be spatially uncorrelated, so the associated equation term in (4) reduces to J_{rm} and \mathbf{Q}_k reduces to $\mathbf{I}\sigma_{rm}^2$, as shown in (14). The second and third terms on the right-hand side of (14) are the horizontal advection increment, and the associated RMS error can be roughly estimated by $\sigma_{vr}\sigma_{rot}/L_{rot} + \sigma_{vr}\sigma_{div}/L_{div} = 2\sqrt{2}\sigma_{vr}^2/L_\chi$ (see (A.15)–(A.16) and (A.18)). The remaining terms in (4) are relatively small and so are their RMS errors. Based on this consideration, $\sigma_{rm} = 3\sqrt{2}\sigma_{vr}^2/L_\chi$ is estimated.

As in step 1, by using (7)–(8) and the B-spline representation, \mathbf{v}^i and \mathbf{v}_r^i in (15) are all expressed as linear functions of the B-spline coefficients. With the use of the standard conjugate gradient algorithm, the cost function J_2 in (11) is minimized efficiently in the reduced space spanned by the B-spline coefficients—the final control variables. The estimated B-spline coefficients are then transformed back to (ψ, χ, \mathbf{w}) and finally to \mathbf{v}^i . The total vector velocity analysis is given by $\mathbf{v}^a = \mathbf{v}^f + \mathbf{v}^i$ on the model grid.

5. Thermodynamic Analysis

5.1. Perturbation Pressure Analysis. The estimated fields of \mathbf{v}^i at $t_0 - \tau/2$ and $t_0 + \tau/2$ from step 2 are used as input data to estimate the thermodynamic fields at t_0 in step 3. Note that the Exner function $\pi = (p'/p_{00})^{R/C_p}$ is used in place of the perturbation pressure p' in COAMPS, where p_{00} is a constant reference pressure, R is the gas constant for dry air, and C_p is the specific heat at constant pressure for the atmosphere. In this paper, we simply call π “perturbation pressure”. The perturbation pressure increment π^i is estimated by minimizing the following cost function:

$$J_\pi = \frac{|\boldsymbol{\pi}|^2}{\sigma_\pi^2} + \frac{[[E_u^2 + E_v^2]]}{\sigma_{uv}^2}. \quad (16)$$

Here, $|\boldsymbol{\pi}|^2/\sigma_\pi^2 = \boldsymbol{\pi}^T \mathbf{C}_\pi^{-1} \boldsymbol{\pi}/\sigma_\pi^2$ is the background term and $\boldsymbol{\pi}(= \mathbf{C}_\pi^{-1/2} \boldsymbol{\pi}^i)$ is the control variable. In this term, $\boldsymbol{\pi}^i$ is the state vector of the grid field of π^i , \mathbf{C}_π is the error correlation matrix for the background perturbation pressure π^f , σ_π^2 is the error variance for π^f , and thus $\sigma_\pi^2 \mathbf{C}_\pi$ is the error covariance matrix for π^f . The second term on the right-hand side of (16) is the equation term. In this term, E_u and E_v are the two

horizontal momentum equations retained from COAMPS (see Hodur [22, (2)–(3)]) in the following incremental forms:

$$\begin{aligned} E_u &= \partial_t u^i + \mathbf{v}^a \cdot \nabla u^i + \mathbf{v}^i \cdot \nabla u^f \\ &\quad - f v^i - D u^i + C_p \Theta_v (\partial_x \pi^i + G_x \partial_\sigma \pi^i), \\ E_v &= \partial_t v^i + \mathbf{v}^a \cdot \nabla v^i + \mathbf{v}^i \cdot \nabla v^f \\ &\quad + f u^i - D v^i + C_p \Theta_v (\partial_y \pi^i + G_y \partial_\sigma \pi^i), \end{aligned} \quad (17)$$

and σ_{uv}^2 is the equation error variance for E_u and E_v . Here, $\partial_t u^i$ and $\partial_t v^i$ are computed by the standard central finite difference scheme from the grid fields of (u^i, v^i) at $t_0 - \tau/2$ and $t_0 + \tau/2$ produced in step 2. All the remaining terms in (17) are at the middle time level t_0 .

As explained in Section 2, the cost function in (16) is derived from (4) by setting $M = 0$ ($\sum_m = 0$) and $K = 1$ with $\boldsymbol{\lambda} = 0$, retaining only E_u and E_v in \mathbf{q}_k , and reducing \mathbf{Q}_k to $\mathbf{I}\sigma_{uv}^2$. The two error variances σ_π^2 and σ_{uv}^2 in (16) are difficult to estimate. Their ratio, however, can be tuned adaptively to make the cost function J_π approximately equally partitioned by the two terms on the right-hand side of (16) when J_π reaches the minimum. This approach is used in this paper. In (16), the grid field of $\boldsymbol{\pi}(= \mathbf{C}_\pi^{-1/2} \boldsymbol{\pi}^i)$ is further expressed by a B-spline expansion on coarse finite element meshes (Xu et al. [19]), so the final control variables are the B-spline coefficients of $\boldsymbol{\pi}$ and J_π is minimized efficiently in the reduced B-spline space. The estimated B-spline coefficients are then transformed back to $\boldsymbol{\pi}$ and finally to $\boldsymbol{\pi}^i(= \mathbf{C}_\pi^{1/2} \boldsymbol{\pi})$. The transformation represented by $\mathbf{C}_\pi^{1/2}$ is simulated by a recursive filter (Purser et al. [31]), in which the error covariance for π^f is modeled by a horizontally isotropic Gaussian function. In this filter, the horizontal decorrelation length is set to L_ψ as for (ψ^f, χ^f) in (A.3) and (A.10), while the vertical decorrelation depth is set to D_w as for w^f in (A.4).

5.2. Perturbation Temperature Analysis. After π^i is computed, the perturbation potential temperature increment θ^i is estimated by minimizing the following cost function:

$$J_\theta = \frac{|\boldsymbol{\theta}|^2}{\sigma_\theta^2} + \frac{[[E_w^2]]}{\sigma_{Ew}^2}. \quad (18)$$

Here, $|\boldsymbol{\theta}|^2/\sigma_\theta^2 = \boldsymbol{\theta}^T \mathbf{C}_\theta^{-1} \boldsymbol{\theta}/\sigma_\theta^2$ is the background term and $\boldsymbol{\theta}(= \mathbf{C}_\theta^{-1/2} \boldsymbol{\theta}^i)$ is the control variable. In this term, $\boldsymbol{\theta}^i$ is the state vector of the grid field of θ^i , \mathbf{C}_θ is the error correlation matrix for the background perturbation potential temperature θ^f , σ_θ^2 is the error variance for θ^f , and thus $\sigma_\theta^2 \mathbf{C}_\theta$ is the error covariance matrix for θ^f . The second term on the right-hand side of (18) is the equation term. In this term, E_w is the vertical momentum equation retained from COAMPS in the following incremental form:

$$\begin{aligned} E_w &= \partial_t w^i + C_p \Theta_v G_z \partial_\sigma \pi^i - \frac{g \theta^i}{\Theta} \\ &\quad + (\mathbf{v}^i + \mathbf{v}^f) \cdot \nabla w^i + \mathbf{v}^i \cdot \nabla w^f - D w^i, \end{aligned} \quad (19)$$

and $\sigma_{E_w}^2$ is the equation error variance for E_w . In (19), Θ is the basic state potential temperature and $g\theta/\Theta$ is the buoyancy increment caused by the perturbation potential temperature increment. Note that the mixing ratios of water vapor and hydrometeors are not updated yet, so they have zero increment at this step and thus no contribution to the buoyancy increment, as assumed in (16) (see Hodur [22, (4)]). Here, $\partial_t w^i$ are computed by the standard central finite difference scheme from the grid fields of w^i at $t_0 - \tau/2$ and $t_0 + \tau/2$ produced in step 2. All the remaining terms in (19) are at the middle time level t_0 .

The cost function in (18) is derived from (4) by setting $M = 0$ ($\sum_m = 0$) and $K = 1$ with $\lambda = 0$, retaining only E_w in \mathbf{q}_k , and reducing \mathbf{Q}_k to $\mathbf{I}\sigma_{E_w}^2$. Again, as those in (16), the two error variances σ_θ^2 and $\sigma_{E_w}^2$ in (18) are hard to estimate, but their ratio can be tuned adaptively to make the cost function J_θ approximately equally partitioned by the two terms on the right-hand side of (18) when J_θ reaches the minimum. In (18), the grid field of θ is further expressed by a B-spline expansion on coarse finite element meshes similarly to that for π in (16). The final control variables are the B-spline coefficients of θ , so J_θ can be minimized efficiently in the reduced B-spline space. The estimated B-spline coefficients are then transformed back to θ and finally to $\theta^i (= \mathbf{C}_\theta^{1/2}\theta)$. The transformation represented by $\mathbf{C}_\theta^{1/2}$ is simulated by a recursive filter with the decorrelation length and depth set to be the same as those for (ψ^f, χ^f) .

The analyzed total perturbation pressure and potential temperature are given by $\pi^f + \pi^i$ and $\theta^f + \theta^i$, respectively, on model grid. The basic idea for the above thermodynamic analysis is the same as Gal-Chen [20] and Hane and Scott [21], but the formulation is derived by considering not only the equation constraints but also the background constraint in connection with the general variational formulation in (4).

5.3. Moisture and Hydrometeor Adjustments. After the perturbation pressure and potential temperature fields are updated by the above incremental analyses, the relative humidity is altered and thus needs to be recovered by adjusting the water vapor mixing ratio q_v . After this, q_v is further adjusted based on the radar observed reflectivity through the following three substeps:

- (i) Interpolate the radar observed reflectivity η^o onto the model grid by minimizing the following cost function:

$$J_\eta = |\boldsymbol{\eta}|^2 + \frac{\left\{ \left\{ (\eta^a - \eta^o)^2 \right\} \right\}}{\sigma_{\eta^o}^2}, \quad (20)$$

where $\boldsymbol{\eta} = \mathbf{B}_\eta^{-1/2}\boldsymbol{\eta}^a$, \mathbf{B}_η is the error covariance matrix for zero reflectivity background, $\boldsymbol{\eta}^a$ is the state vector of the analyzed reflectivity η^a , and σ_{η^o} (≈ 1 dBZ) is the reflectivity observation error standard deviation. Again, the grid field of $\boldsymbol{\eta}$ is further expressed by a B-spline expansion on coarse finite element meshes. As the final control variables are the B-spline coefficients of $\boldsymbol{\eta}$, J_π can be minimized efficiently in the reduced B-spline space. The estimated B-spline coefficients

are then transformed back to $\boldsymbol{\eta}$ and finally to $\boldsymbol{\eta}^a (= \mathbf{B}_\eta^{1/2}\boldsymbol{\eta})$. The transformation represented by $\mathbf{B}_\eta^{1/2}$ is simulated by a recursive filter, in which the decorrelation length and depth are set to be as small as Δx and Δz , respectively, and the error variance for zero reflectivity background is estimated by the spatial variance of the model predicted reflectivity η^f . With the above parameter settings, the analyzed reflectivity $\boldsymbol{\eta}^a$ obtained by minimization J_η in (20) is an optimal interpolation of the observed reflectivity η^o onto the model grid. After this interpolation, $\boldsymbol{\eta}^a$ is further extrapolated downward from the lower radar beam height to the surface level (to fill the reflectivity data void area below the lowest beam in the boundary layer).

- (ii) Check each grid point for the conditions of $\eta^a > 10$ dBZ and $\eta^f < 10$ dBZ. If these two conditions are both satisfied, then adjust q_v to the saturated value if the analyzed vertical velocity is nonnegative ($w \geq 0$) or to 80% of the saturated value if the analyzed vertical velocity is negative ($w < 0$) and the relative humidity is below 80% at this grid point.
- (iii) Check each grid point for the conditions of $\eta^a < 10$ dBZ and $\eta^f > 10$ dBZ. If these two conditions are both satisfied, then adjust q_v to the value interpolated in x - and y -directions from the nearest grid points where the two conditions are not both satisfied. This adjustment is designed to reduce q_v and thus correct the model's tendency of overpredicting precipitation locally in areas detected by the above two conditions.

In companion with the q_v adjustment, the rain mixing ratio q_r (or snow mixing ratio q_s) is adjusted below (or above) the freezing level to make the computed reflectivity match η^a at each grid point. The above moisture and hydrometeor adjustments have not been extensively tested and currently are used only as an option for case studies (including the example presented in the next section). For operational applications, the radar reflectivity observations are used together with the GOES satellite observations to adjust the moisture field together with the cloud field in a sophisticated cloud analysis package (Wei et al. [36], Zhao et al. [37, 38]).

6. Application to Phased Array Radar Data

The 3.5dVar is applied to the phased array radar radial velocity and reflectivity observations collected during the period of 2100–2200 UTC 2 June 2004 when a four-quadrant electronic scan strategy was tested. During this period, a squall line moved southeastward through the central Oklahoma area in the radial range (140 km) of the phased array radar scans (Figure 2). The radar scanned roughly every two minutes per volume. Total 26 volume scans were collected. Among these 26 volume scans, there is one volume scan that covers only a single quadrant and this volume is not used. The remaining 25 volume scans cover all the four quadrants and are used in this study. Each volume scan has

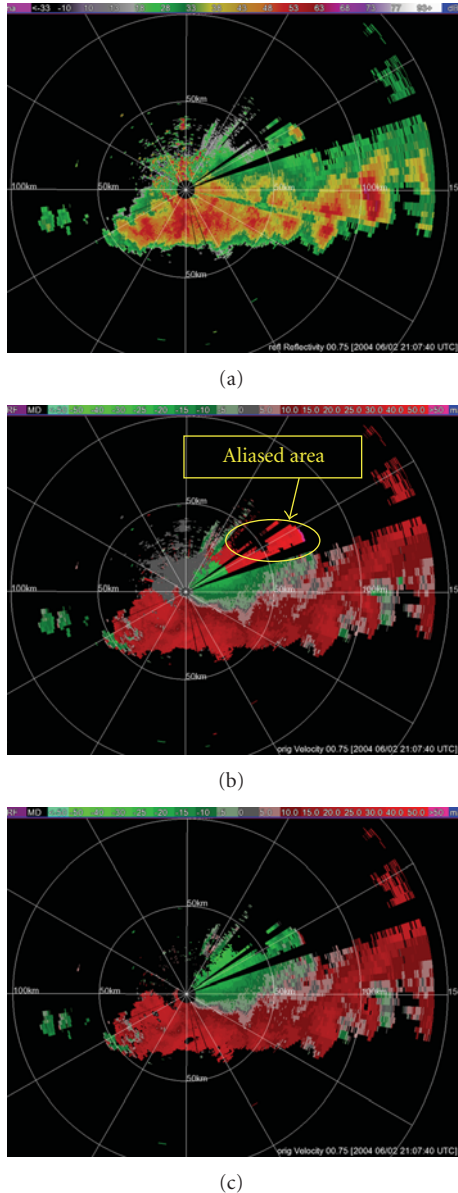


FIGURE 2: Phased-array radar observed reflectivity (a), radial velocity (b) at 0.75° , and dealiased radial velocity (c) at 2107 UTC on 2 June 2004. Aliased velocity areas are highlighted in (b).

7 tilts with elevation angles of 0.75° , 2.27° , 3.78° , 5.28° , 6.78° , 8.28° , and 9.28° . On each tilt, the spatial resolutions are 240 m in the radial direction and approximately 1.5° in the azimuthal direction.

The COAMPS is used to produce the background fields. The model is configured with three nested domains centered over the state of Oklahoma with resolutions of 54, 18, and 6 km for the coarse, medium, and fine grids, respectively, and 30 levels in the vertical. The three nested domains are shown in Figure 3. All other parameters are set to be the same as in Zhao et al. [38]. For the control run, the model is initialized (cold start) at 0000 UTC 2 June 2004. After the first 12-hr model run, the conventional observations are assimilated,

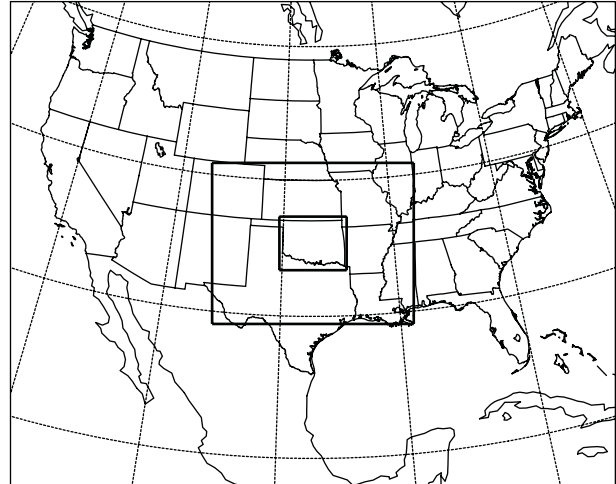


FIGURE 3: COAMPS domains nested with 54, 18, and 6 km grids.

and then another 12-hr run is launched (warm start). The predicted wind fields on the 6 km grid are used as the reference by the dealiasing technique described in Section 3.1 to detect and correct alias errors in the radar radial velocity observations. The technique is found to be effective (as shown Figure 2) and better than the operationally used technique. The radial velocity innovations produced from the 25 volume scans of dealiased radial velocities and COAMPS predicted background fields were used in Xu et al. [34] to estimate the background and observation error variances. The estimated observation error variance is used in this paper to estimate the background error variance adaptively in each assimilation cycle, as explained in Section 3.2.

By using the 3.5dVar, three consecutive volume scans of the dealiased radial velocity and reflectivity data are assimilated through a single cycle around 2108 UTC, and then a test run, called Test 1, is launched for 58-minute forecast to 2200 UTC. Another test run, called Test 3, is also performed by assimilating the first nine volume scans of the dealiased radial velocity and reflectivity data in three cycles from 2108 to 2118 UTC. The velocity and reflectivity fields at $z = 3.1$ km produced by the prediction valid at 2108 UTC in the control run and by the analysis at 2108 UTC in Test 1 are plotted against the observed reflectivity (analyzed onto the grid) at 2108 UTC in Figures 4(a) and 4(b), respectively. The predicted velocity and reflectivity fields in Figure 4(a) are the background fields for the analysis at 2108 UTC in Test 1. As shown in Figure 4(a), the background wind field from the control run is dynamically self-consistent and is consistent with the reflectivity field of its predicted squall line, but the predicted reflectivity reveals a significant location error for the predicted squall line in comparison with the observed reflectivity field. In particular, the leading edge of the predicted squall line is lagged by about 30 km behind the observed. This location error is largely corrected by the analysis in Test 1 as shown in Figure 4(b).

The 5-minute forecasts of velocity and reflectivity fields valid at 2118 UTC from the second cycle (at 2113 UTC) in Test 3 are given Figure 5(a) while the analyses from the

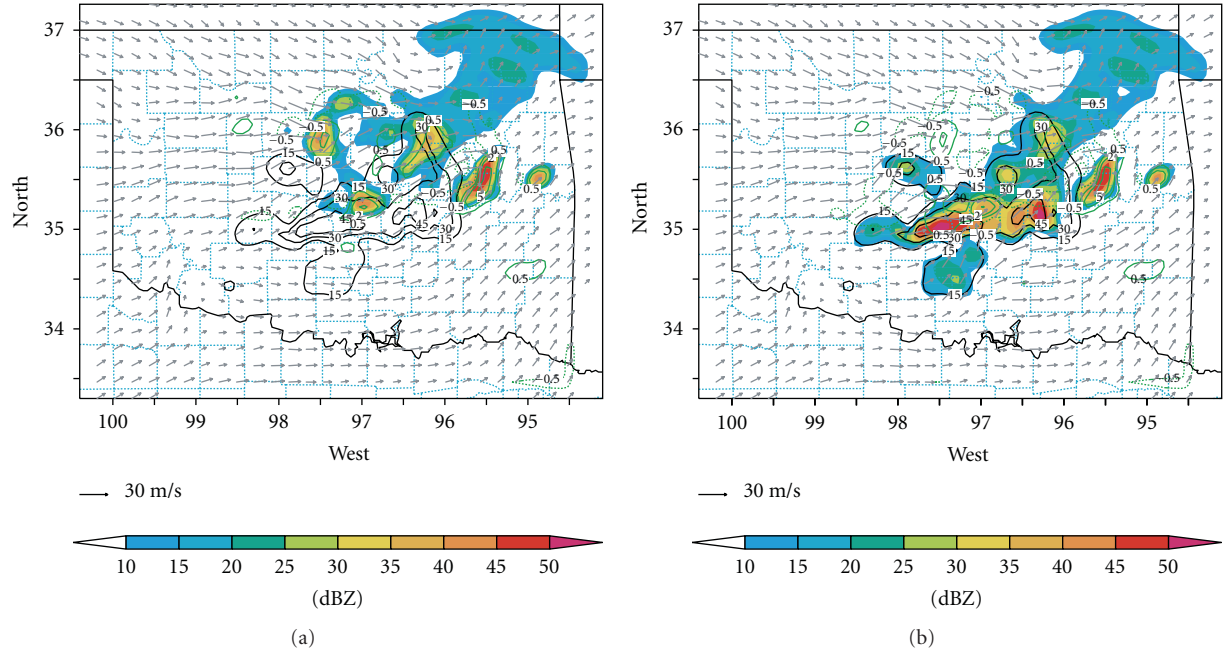


FIGURE 4: Velocity (arrows for the horizontal wind and green contours for the vertical velocity) and reflectivity (color field) at $z = 3.1$ km produced by (a) the prediction in the control run and (b) the analysis in Test 1 at 2108 UTC. The black contours are plotted every 10 dBZ for the observed reflectivity (analyzed onto the grid). The vertical velocity contours are plotted in green for ± 0.5 , ± 2 , and $\pm 5 \text{ m s}^{-1}$. The arrow ($= 30 \text{ m s}^{-1}$) at the lower-left corner is the vector scale for the horizontal velocity.

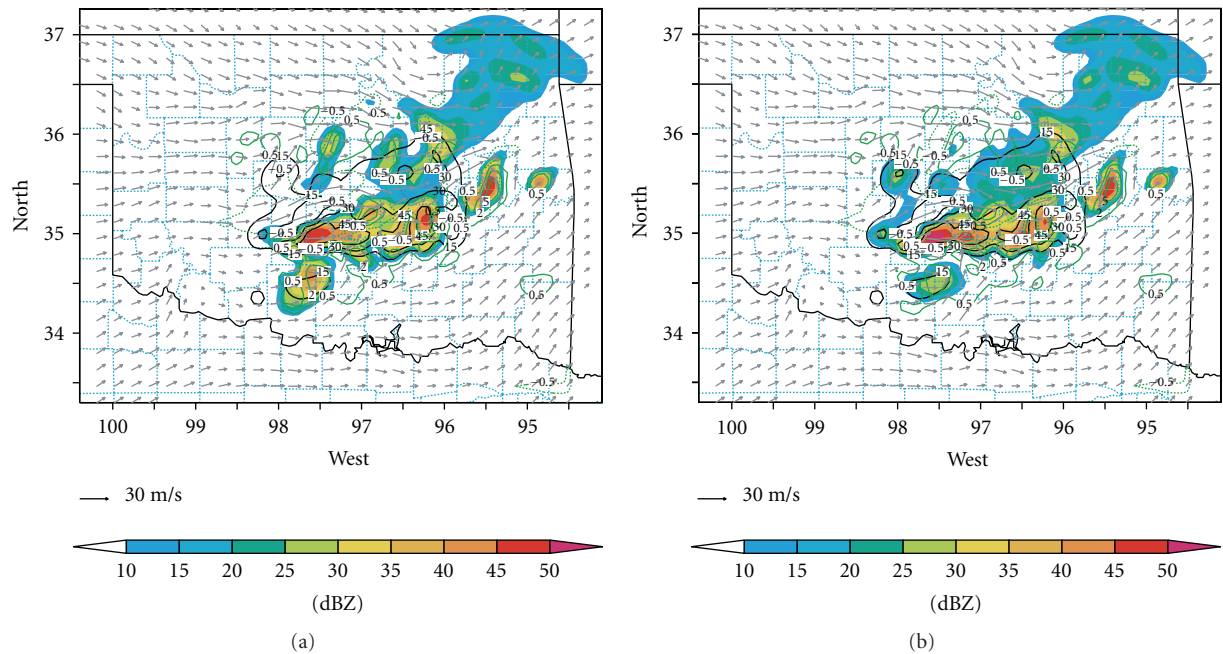


FIGURE 5: As in Figure 4 but for velocity and reflectivity produced by (a) the 5-minute prediction (from the second cycle at 2113 UTC) and (b) analysis of the third cycle at 2118 UTC in Test 3.

third cycle at 2118 UTC are plotted in Figure 5(b). For comparison, radar observations of reflectivity at 2118 UTC are also shown (by solid contours) in Figures 5(a) and 5(b). It should be mentioned again that the analyzed fields in Figure 5(b) use the predicted velocity and reflectivity

fields in Figure 5(a) as background fields. It is apparent that the predicted background reflectivity in Figure 5(a) already becomes quite close to the observations, and the minor miss-matches are further corrected by the analysis as shown by the analyzed reflectivity in Figure 5(b).

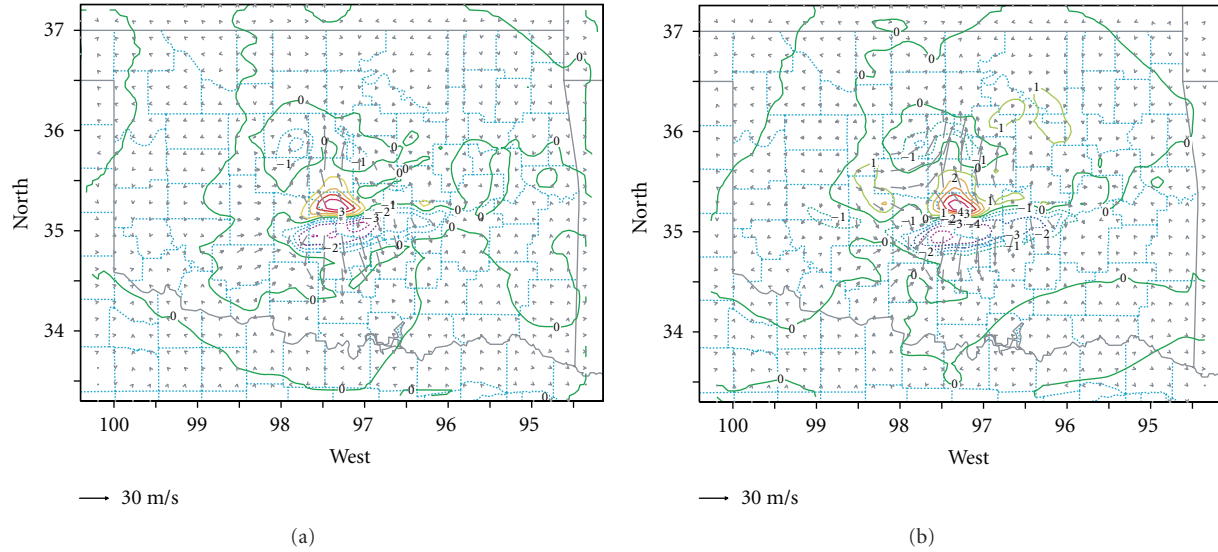


FIGURE 6: As in Figure 4 but for the incremental horizontal velocity (arrows) and incremental potential temperature (contours every 1 degree, dashed for negative values) in the boundary layer (at $z = 0.5$ km) from (a) the 10-minute prediction (integrated from the analysis at 2108 UTC) in Test 1 and (b) the third analysis in Test 3 with respect to those produced by the control run valid at 2118 UTC.

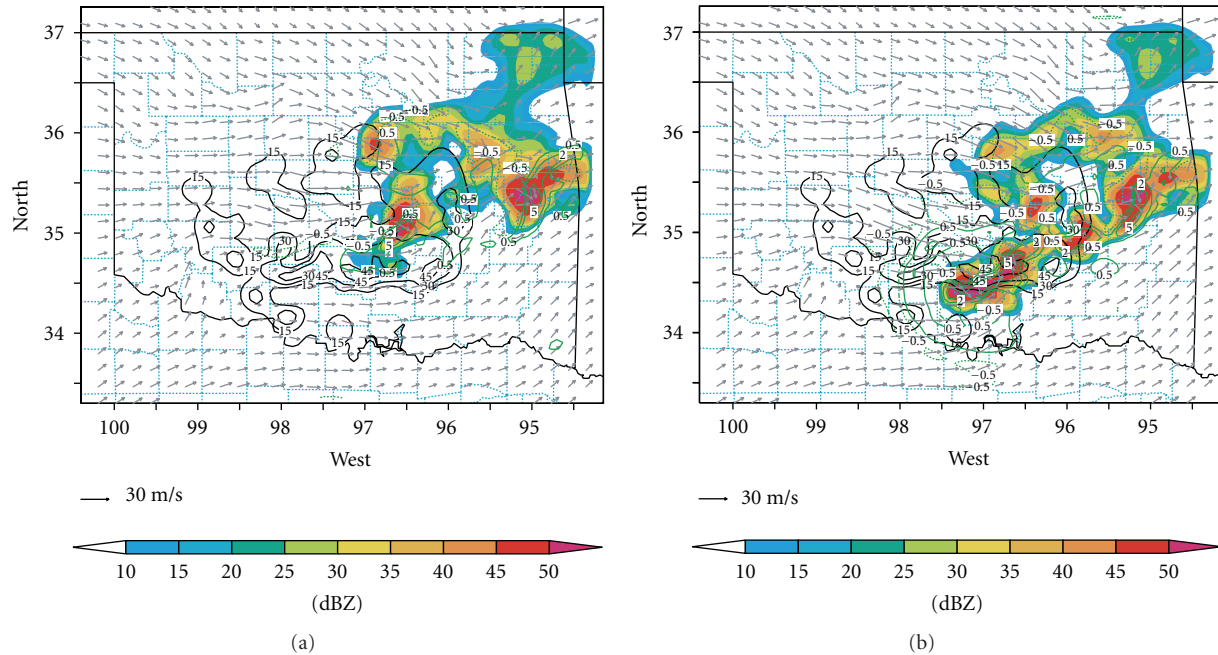


FIGURE 7: As in Figure 4 but for velocity and reflectivity produced by the predictions valid at 2200 UTC in (a) the control run and (b) Test 1.

Figure 6(a) plots the incremental horizontal velocity and potential temperature (at $z = 0.5$ km) produced by the 10-minute prediction from the analysis in Test 1 with respect to those produced by the control run valid at 2118 UTC. As shown, the potential temperature increment is negative and the horizontal wind increment is divergent over an elongated region along the leading edge of the squall line produced in Test 1. Note that this elongated region is to the south immediately ahead of the background squall line

(produced by the control run valid at 2118 UTC), which implies that the under-predicted southward movement of the squall line in the control run is largely corrected at 2118 UTC in Test 1. The above features become slightly more distinct in the incremental fields produced at 2118 UTC by the three assimilation cycles in Test 3 as shown in Figure 6(b), which implies that the under-predicted southward movement of the squall line in the control run is further corrected at 2118 UTC after the second cycle and the third analysis in Test 3.

It is necessary to mention that the incremental potential temperature produced by the thermodynamic analysis is relatively small (within $\pm 0.5^\circ\text{K}$ in the boundary layer) and nearly hydrostatically balanced with the perturbation pressure increment, while the latter is related to the horizontal wind increment through the horizontal momentum equations (see (17)). Thus, the potential temperature increment in either Figure 6(a) or Figure 6(b) is caused mainly by the moisture adjustment and subsequent model integration. Due to the very limited coverage of radial velocities from only one Doppler radar, the thermodynamic analysis is not well constrained and thus does not have the desired accuracy and significance to directly and adequately correct the background thermodynamic field. Instead, the main benefit of the thermodynamic analysis performed in this paper is to improve the overall dynamic and thermodynamic balance of the analyzed total field, and this explains why the thermodynamic analysis improves the subsequent forecast slightly in comparison with the forecast without thermodynamic analysis (not shown in this paper).

The velocity and reflectivity forecasts from the control run and Test 1 valid at 2200 UTC are plotted against the observed reflectivity at $z = 3.1\text{ km}$ in Figures 7(a) and 7(b), respectively. As shown, the reflectivity field predicted by Test 1 is much closer to the observations than that from the control run, but slightly less close to the observations than that predicted by Test 3 (not shown). The spatial correlation coefficients between the predicted and observed reflectivity fields are plotted as functions of time for the control run and the two test runs in Figure 8(a). As shown by the plotted correlation coefficients, the predicted reflectivity and precipitation are significantly improved in Test 1 and further improved in Test 3.

To verify the three-dimensional winds, the model-produced (analyzed and predicted) radial velocity fields are interpolated (using the observational operator) back to the phased-array radar observation points and compared with their respective observed values. The RMS differences between the predicted and observed radial velocities are plotted as functions of time for the control run and the two test runs in Figure 8(b). As one can see, the RMS difference is reduced by the analysis in each assimilation cycle, although the reductions by the analyses in the second and third assimilation cycles are relatively small and last only for about 0.5 hour. Clearly, the predicted reflectivity (associated with predicted precipitation) and velocity are both improved in Test 1 and both further improved in Test 3.

7. Conclusions

This paper presents a variational approach for Doppler radar data assimilation. This method analyzes four-dimensional radar observations (three consecutive volume scans) but updates the model state only in three-dimensional space at the central time level in each assimilation cycle, and therefore we call it three-and-half-dimensional variational (3.5dVar) method. The method can be considered as an upgraded combination of the previous retrieval methods (Qiu and Xu [18];

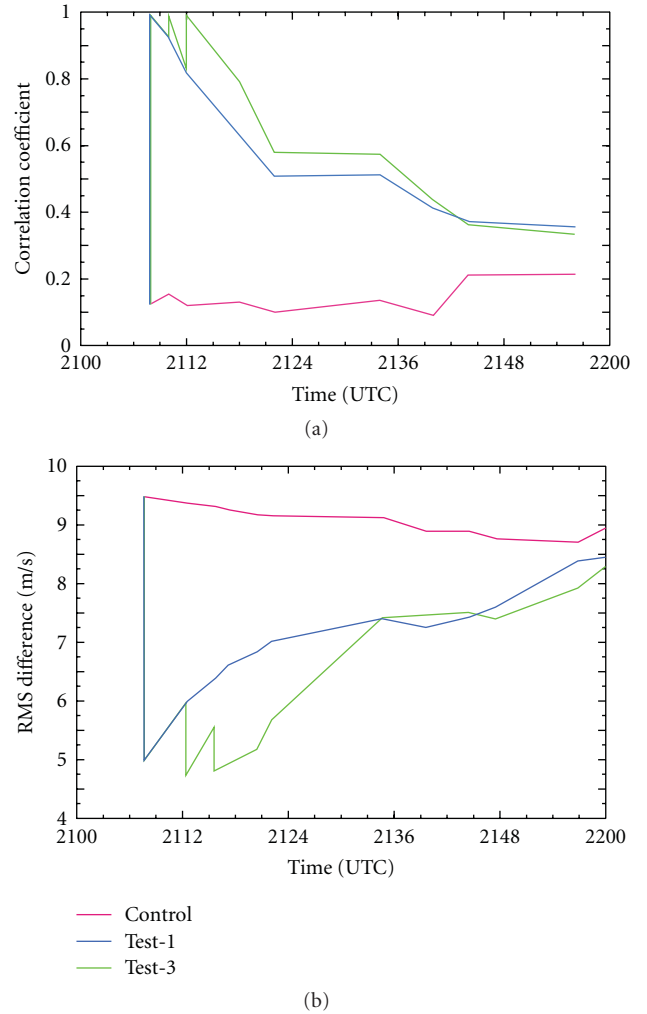


FIGURE 8: (a) Correlation coefficient between the predicted and observed reflectivity fields. (b) RMS differences between the predicted and observed radial velocities. The red, blue, and green curves are for the results obtained from the control run, Test 1 and Test 3, respectively.

Gal-Chen [20]; Hane and Scott [21]) with the background information from NWP model forecasts. The finite element B-spline representations (Xu et al. [19]) and recursive filter (Purser et al. [31]) are used to reduce the dimension of the analysis space and enhance the computational efficiency. The method is tested with real radar data collected by the phased-array radar at Norman, Oklahoma for the squall line event on June 2, 2004. The effectiveness of the 3.5dVar is demonstrated by the improved short-term predictions of the squall line (see Section 6).

The 3.5dVar method has also been tested and applied to many other cases, either as a stand-alone package (Gu et al. [15]; Xu et al. [34, 39]; Zhao et al. [40]) or in combination with a cloud analysis package (Zhao et al. [37, 38]). The 3.5dVar method is currently being further refined in combination with a cloud analysis package for

the Navy's nowcasting applications. According to recent real-time tests, the current 3.5dVar algorithm code can be easily setup and run on a PC workstation. It takes only about 5 minutes to assimilate 9 volume scans from three radars (each radar provides three consecutive volume scans) on a high-resolution ($100 \times 100 \times 30$) COAMPS grid that covers a mesoscale area ($600 \times 600 \text{ km}^2$). The 3.5dVar is thus sufficiently efficient for real-time applications.

Because simplifications are made to the general variational formulation in each of the three steps in the method to achieve the desired computational efficiency for real-time applications, the resulting analyses are suboptimal (relative to the desired maximum likelihood estimates). This implies that the method can be improved by reducing the involved simplifications and refining the error covariance estimation and representation. Such an improvement is made in the current 3.5dVar over the early version (Gu et al. [15]) by recovering the matrix forms of background error covariances. Room still exists for further improvements. For example, including the vorticity equation as an additional constraint could substantially improve the thermodynamic analysis (at least in areas covered by two or more Doppler radars, as shown by Protat and Zawadzki [41]). The analysis may also be improved by considering nonisotropic flow-dependent forms of background error covariances, which is under our current investigation in connection with the ensemble Kalman filter.

Appendix

Background Error Variances and Decorrelation Lengths for Derived Variables

The mass continuity equation in (13) can be applied approximately to the background velocity \mathbf{v}^f . By neglecting the effect of terrain slope, this equation can be written into the following form:

$$\Delta_h \chi^f = -\partial_\sigma w^f, \quad (\text{A.1})$$

where $\Delta_h = \partial_x^2 + \partial_y^2$ is the Laplacian. Assume that the random error fields of χ^f and w^f are also constrained by (A.1), so their covariance functions (see Xu and Wei [35, (2.3) and (A.1)]) satisfy the following relationship:

$$\Delta_h^2 C_{\chi\chi}(r, \eta) = -\partial_\eta^2 C_{ww}(r, \eta), \quad (\text{A.2})$$

where r and η are the horizontal and vertical distances, respectively, between the two correlated points, and the two covariance functions are assumed to be horizontally isotropic and separable between the horizontal and vertical directions.

Assume that $C_{\chi\chi}(r, \eta)$ can be modeled by a Gaussian function in the horizontal direction, so

$$C_{\chi\chi}(r, \eta) = \sigma_\chi^2 G\left(\frac{r}{L_\chi}\right) R_{\chi\chi}(\eta), \quad (\text{A.3})$$

where σ_χ^2 and $R_{\chi\chi}(\eta)$ denote, respectively, the error variance and vertical error correlation for χ^f , $G(\cdot) \equiv$

$\exp[-(\cdot)^2/2]$ denotes the Gaussian function form, and L_χ is the horizontal decorrelation length defined by $L_\chi = [2C_{\chi\chi}(0)]^{1/2} [-\Delta_h C_{\chi\chi}(r)|_{r=0}]^{-1/2}$ as in Daley [42, (4.3.12)]. By assuming that $C_{ww}(r, \eta)$ can be modeled by a Gaussian function in the vertical, we get

$$C_{ww}(r, \eta) = \sigma_w^2 R_{ww}(r) G\left(\frac{\eta}{D_w}\right), \quad (\text{A.4})$$

where σ_w^2 and $R_{ww}(r)$ denote, respectively, the error variance and vertical error correlation for w^f , and D_w is the vertical decorrelation depth defined by $D_w = [C_{ww}(0)]^{1/2} [-\partial_\eta^2 C_{ww}(\eta)|_{\eta=0}]^{-1/2}$. Substituting (A.3) and (A.4) into (A.2) and setting $r = 0$ with $R_{ww}(0) = 1$, we have

$$8\sigma_\chi^2 L_\chi^{-4} R_{\chi\chi}(\eta) = \sigma_w^2 (D_w^{-2} - \eta^2 D_w^{-4}) G\left(\frac{\eta}{D_w}\right). \quad (\text{A.5})$$

Substituting (A.3) and (A.4) into (A.2) again and setting $\eta = 0$ with $R_{\chi\chi}(0) = 1$, we have another equation

$$\sigma_\chi^2 (8L_\chi^{-4} - 8r^2 L_\chi^{-6} - r^4 L_\chi^{-8}) G\left(\frac{r}{L_\chi}\right) = \sigma_w^2 D_w^{-2} R_{ww}(r). \quad (\text{A.6})$$

Setting $\eta = 0$ in (A.5) or $r = 0$ in (A.6) gives the ratio of the two variances

$$\frac{\sigma_w^2}{\sigma_\chi^2} = \frac{8D_w^2}{L_\chi^4}. \quad (\text{A.7})$$

Note that $R_{\chi\chi}(\eta)$ and $R_{ww}(r)$ are obtained explicitly in (A.5) and (A.6), respectively. Substituting (A.5) into (A.3) gives the explicit form of $C_{\chi\chi}(r, \eta)$, and substituting (A.6) into (A.4) results in another explicit form for $C_{ww}(r, \eta)$. Using these explicit forms, we can verify that the vertical decorrelation depth for the random error field of χ^f is given by

$$D_\chi = [R_{\chi\chi}(\eta)|_{\eta=0}]^{1/2} [-\partial_\eta^2 R_{\chi\chi}(\eta)|_{\eta=0}]^{-1/2} = \frac{D_w}{\sqrt{3}}, \quad (\text{A.8})$$

while the horizontal decorrelation length for the random error field of w^f is given by

$$L_w = [2R_{ww}(r)|_{r=0}]^{1/2} [-\Delta_h R_{ww}(r)|_{r=0}]^{-1/2} = \frac{L_\chi}{\sqrt{3}}. \quad (\text{A.9})$$

Denote by \mathbf{v}_h the horizontal component of \mathbf{v}^f and represent by \mathbf{v}_{rot} and \mathbf{v}_{div} the rotational and divergent parts of \mathbf{v}_h , respectively. Then we have $\mathbf{v}_{\text{rot}} = \mathbf{k} \times \nabla_h \psi^f$, $\mathbf{v}_{\text{div}} = \nabla_h \chi^f$, and $\mathbf{v}_h = \mathbf{v}_{\text{rot}} + \mathbf{v}_{\text{div}}$. Also assume that the error covariance function for ψ^f can be modeled by a Gaussian function in the horizontal, so

$$C_{\psi\psi}(r, \eta) = \sigma_\psi^2 G\left(\frac{r}{L_\psi}\right) R_{\psi\psi}(\eta), \quad (\text{A.10})$$

where σ_ψ^2 and $R_{\psi\psi}(\eta)$ denote, respectively, the error variance and vertical error correlation for ψ^f , and L_ψ is the horizontal decorrelation length. $C_{\text{rot}}(r, \eta)$ and $C_{\text{div}}(r, \eta)$ represent the

traces of the error covariance tensors for \mathbf{v}_{rot} and \mathbf{v}_{div} , respectively. By using (2.14) of Xu and Wei [35] with (A.4) and (A.10), one can get

$$\begin{aligned} C_{\text{rot}}(r, \eta) &= -\nabla_h^2 C_{\psi\psi}(r, \eta) \\ &= \sigma_\psi^2 (2L_\psi^{-2} - r^2 L_\psi^{-4}) G\left(\frac{r}{L_\psi}\right) R_{\psi\psi}(\eta), \end{aligned} \quad (\text{A.11})$$

$$\begin{aligned} C_{\text{div}}(r, \eta) &= -\nabla_h^2 C_{\chi\chi}(r, \eta) \\ &= \sigma_\chi^2 (2L_\chi^{-2} - r^2 L_\chi^{-4}) G\left(\frac{r}{L_\chi}\right) R_{\chi\chi}(\eta). \end{aligned} \quad (\text{A.12})$$

The error variances for \mathbf{v}_{rot} and \mathbf{v}_{div} can be then obtained by setting $r = 0$ and $\eta = 0$ in (A.11) and (A.12), that is,

$$\sigma_{\text{rot}}^2 = 2\sigma_\psi^2 L_\psi^{-2}, \quad (\text{A.13})$$

$$\sigma_{\text{div}}^2 = 2\sigma_\chi^2 L_\chi^{-2}. \quad (\text{A.14})$$

Using (A.11) and (A.12), one can verify that the horizontal decorrelation lengths for the random error fields of \mathbf{v}_{rot} and \mathbf{v}_{div} are given, respectively, by

$$L_{\text{rot}} = [2C_{\text{rot}}(r, 0)|_{r=0}]^{1/2} [-\nabla^2 C_{\text{rot}}(r, 0)|_{r=0}]^{-1/2} = \frac{L_\psi}{\sqrt{2}}, \quad (\text{A.15})$$

$$L_{\text{div}} = [2C_{\text{div}}(r, 0)|_{r=0}]^{1/2} [-\nabla^2 C_{\text{div}}(r, 0)|_{r=0}]^{-1/2} = \frac{L_\chi}{\sqrt{2}}. \quad (\text{A.16})$$

For mesoscale flows, we may assume that \mathbf{v}_{rot} and \mathbf{v}_{div} have roughly the same error variances and decorrelation lengths. In this case, we have

$$L_\psi = L_\chi = \sqrt{3}L_w, \quad (\text{A.17})$$

$$\sigma_{\text{rot}}^2 = \sigma_{\text{div}}^2 = 0.5\sigma_h^2 = \sigma_{\text{vr}}^2, \quad (\text{A.18})$$

where σ_h^2 is the error variance for \mathbf{v}_h (the horizontal component of \mathbf{v}^f), and σ_{vr}^2 is the error variance for v_r^f . Note that $\mathbf{v}_h = \mathbf{v}_{\text{rot}} + \mathbf{v}_{\text{div}}$, and therefore $\sigma_h^2 = \sigma_{\text{rot}}^2 + \sigma_{\text{div}}^2$. Also note that v_r^f is the radial component of \mathbf{v}^f and approximately the radial component of \mathbf{v}_h , so $\sigma_{\text{vr}}^2 = 0.5\sigma_h^2$ is a reasonable approximation (Xu and Gong [43]). These relationships are used in the derivation of (A.18). Substituting (A.18) into (A.13) and (A.7) gives

$$\sigma_\psi^2 = \sigma_\chi^2 = 0.5\sigma_{\text{vr}}^2 L_\chi^2, \quad (\text{A.19})$$

$$\sigma_w^2 = \frac{4\sigma_{\text{vr}}^2 D_w^2}{L_\chi^2}. \quad (\text{A.20})$$

Acknowledgments

The authors are thankful to Carl Hane, Jidong Gao, and the anonymous reviewer for their comments and suggestions that improved the presentation of the paper and to Douglas Forsyth, Kurt Hondl, Richard Adams, Pengfei

Zhang and Kang Nai for their help in obtaining and processing the phased-array radar data. The research work was supported by the NOAA HPCC program, the FAA contract IA# DTFA03-01-X-9007 to NSSL, the ONR Grants N000140410312 to the University of Oklahoma, and the NOAA-University of Oklahoma Cooperative Agreement no. NA17RJ1227.

References

- [1] J. Sun, D. W. Flicker, and D. K. Lilly, "Recovery of three-dimensional wind and temperature fields from simulated single-Doppler radar data," *Journal of the Atmospheric Sciences*, vol. 48, no. 6, pp. 876–890, 1991.
- [2] H. Kapitza, "Numerical experiments with the adjoint of a nonhydrostatic mesoscale model," *Monthly Weather Review*, vol. 119, no. 12, pp. 2993–3011, 1991.
- [3] C. Qiu and Q. Xu, "A simple adjoint method of wind analysis for single-Doppler data," *Journal of Atmospheric & Oceanic Technology*, vol. 9, no. 5, pp. 588–598, 1992.
- [4] J. Sun and A. Crook, "Wind and thermodynamic retrieval from single-Doppler measurements of a gust front observed during Phoenix II," *Monthly Weather Review*, vol. 122, no. 6, pp. 1075–1091, 1994.
- [5] Q. Xu, C. Qiu, and J. Yu, "Adjoint-method retrievals of low-altitude wind fields from single-Doppler reflectivity measured during Phoenix II," *Journal of Atmospheric & Oceanic Technology*, vol. 11, no. 2, pp. 275–288, 1994.
- [6] Q. Xu, C. Qiu, and J. Yu, "Adjoint-method retrievals of low-altitude wind fields from single-Doppler wind data," *Journal of Atmospheric & Oceanic Technology*, vol. 11, no. 2, pp. 579–585, 1994.
- [7] S. Laroche and I. Zawadzki, "A variational analysis method for the retrieval of three-dimensional wind field from single-Doppler radar data," *Journal of the Atmospheric Sciences*, vol. 51, pp. 2664–2682, 1994.
- [8] A. Shapiro, S. Ellis, and J. Shaw, "Single-Doppler velocity retrievals with Phoenix II data: clear air and microburst wind retrievals in the planetary boundary layer," *Journal of the Atmospheric Sciences*, vol. 52, no. 9, pp. 1265–1287, 1995.
- [9] J. Zhang and T. Gal-Chen, "Single-Doppler wind retrieval in the moving frame of reference," *Journal of the Atmospheric Sciences*, vol. 53, no. 18, pp. 2609–2623, 1996.
- [10] Y.-C. Liou, "Single radar recovery of cross-beam wind components using a modified moving frame of reference technique," *Journal of Atmospheric and Oceanic Technology*, vol. 16, no. 8, pp. 1003–1016, 1999.
- [11] J. Gao, M. Xue, A. Shapiro, Q. Xu, and K. K. Droegemeier, "Three-dimensional simple adjoint velocity retrievals from single-Doppler radar," *Journal of Atmospheric and Oceanic Technology*, vol. 18, no. 1, pp. 26–38, 2001.
- [12] S. S. Weygandt, A. Shapiro, and K. K. Droegemeier, "Retrieval of model initial fields from single-Doppler observations of a supercell thunderstorm. Part I: single-Doppler velocity retrieval," *Monthly Weather Review*, vol. 130, no. 3, pp. 433–453, 2002.
- [13] J. Sun and N. A. Crook, "Real-time low-level wind and temperature analysis using single WSR-88D data," *Weather and Forecasting*, vol. 16, no. 1, pp. 117–132, 2001.
- [14] Q. Xu, H. Gu, and W. Gu, "A variational method for Doppler radar data assimilation," in *Proceedings of the 5th Symposium on Integrated Observing Systems*, pp. 118–121, The American Meteor Society, Albuquerque, New Mexico, 2001.

- [15] W. Gu, H. Gu, and Q. Xu, "Impact of single-Doppler radar observations on numerical prediction of 7 May 1995 Oklahoma squall line," in *Proceedings of the 5th Symposium on Integrated Observing Systems*, pp. 139–142, The American Meteor Society, Albuquerque, New Mexico, 2001.
- [16] J. Gao, M. Xue, K. Brewster, and K. K. Droegemeier, "A three-dimensional variational data analysis method with recursive filter for Doppler radars," *Journal of Atmospheric and Oceanic Technology*, vol. 21, no. 3, pp. 457–469, 2004.
- [17] M. Hu, M. Xue, J. Gao, and K. Brewster, "3DVAR and cloud analysis with WSR-88D level-II data for the prediction of the Fort Worth, Texas, tornadic thunderstorms. Part II: impact of radial velocity analysis via 3DVAR," *Monthly Weather Review*, vol. 134, no. 2, pp. 699–721, 2006.
- [18] C.-J. Qiu and Q. Xu, "Least squares retrieval of microburst winds from single-Doppler radar data," *Monthly Weather Review*, vol. 124, no. 6, pp. 1132–1144, 1996.
- [19] Q. Xu, H. Gu, and S. Yang, "Simple adjoint method for three-dimensional wind retrievals from single-Doppler radar," *Quarterly Journal of the Royal Meteorological Society*, vol. 127, no. 573, pp. 1053–1067, 2001.
- [20] T. Gal-Chen, "A method for the initialization of the anelastic equations: implications for matching models with observations," *Monthly Weather Review*, vol. 106, pp. 587–606, 1978.
- [21] E. C. Hane and B. C. Scott, "Temperature and pressure perturbations within convective clouds derived from detailed air motion information: preliminary testing," *Monthly Weather Review*, vol. 106, pp. 654–661, 1978.
- [22] R. M. Hodur, "The naval research laboratory's coupled ocean/atmosphere mesoscale prediction system (COAMPS)," *Monthly Weather Review*, vol. 125, no. 7, pp. 1414–1430, 1997.
- [23] A. H. Jazwinski, *Stochastic Processes and Filtering Theory*, Academic Press, New York, NY, USA, 1970.
- [24] A. F. Bennett, *Inverse Method in Physical Oceanography*, Cambridge University Press, Cambridge, UK, 1992.
- [25] J.-M. Lewis and J. C. Derber, "The use of adjoint Equations to solve a variational adjustment problem with advective constraints," *Tellus*, vol. 37A, pp. 309–322, 1985.
- [26] F.-X. Le Dimet and O. Talagrand, "Variational algorithms for analysis and assimilation of meteorological observations: theoretical aspects," *Tellus*, vol. 38, no. 2, pp. 97–110, 1986.
- [27] D. F. Parrish and J. C. Derber, "The National Meteorological Center's spectral statistical- interpolation analysis system," *Monthly Weather Review*, vol. 120, no. 8, pp. 1747–1763, 1992.
- [28] J. Gong, L. Wang, and Q. Xu, "A three-step dealiasing method for Doppler velocity data quality control," *Journal of Atmospheric and Oceanic Technology*, vol. 20, no. 12, pp. 1738–1748, 2003.
- [29] R. J. Doviak and D. S. Zrnić, *Doppler Radar and Weather Observations*, Dover Publications, New York, NY, USA, 2nd edition, 2006.
- [30] E. Kessler, "On the distribution and continuity of water substance in atmospheric circulation. Meteor. Monogr," *The American Meteor Society*, vol. 10, no. 32, p. 84, 1969.
- [31] R. J. Purser, W.-S. Wu, D. F. Parrish, and N. M. Roberts, "Numerical aspects of the application of recursive filters to variational statistical analysis. Part I: spatially homogeneous and isotropic Gaussian covariances," *Monthly Weather Review*, vol. 131, no. 8, pp. 1524–1535, 2003.
- [32] Q. Xu, "Representations of inverse covariances by differential operators," *Advances in Atmospheric Sciences*, vol. 22, no. 2, pp. 181–198, 2005.
- [33] Q. Xu, K. Nai, and L. Wei, "An innovation method for estimating radar radial-velocity observation error and background wind error covariances," *Quarterly Journal of the Royal Meteorological Society*, vol. 133, no. 623, pp. 407–415, 2007.
- [34] Q. Xu, K. Nai, L. Wei, et al., "Progress in Doppler radar data assimilation," in *Proceedings of the 32nd Conference on Radar Meteorology*, pp. 24–29, The American Meteor Society, Albuquerque, New Mexico, 2005, CD-ROM, JP1J7.
- [35] Q. Xu and L. Wei, "Estimation of three-dimensional error covariances. Part II: analysis of wind innovation vectors," *Monthly Weather Review*, vol. 129, no. 12, pp. 2939–2954, 2001.
- [36] L. Wei, Q. Xu, and Q. Zhao, "Using GOES data to improve COAMPS cloud analysis and forecast," in *Proceedings of the 5th Symposium on Integrated Observing Systems*, pp. 126–129, The American Meteor Society, Albuquerque, New Mexico, 2001.
- [37] Q. Zhao, J. Cook, and L. Phegley, "Assimilation of radar observations into a high-resolution numerical weather analysis and prediction system at NRL," in *Proceedings of the 31th Conference on Radar Meteorology*, pp. 169–172, The American Meteor Society, Seattle, Wash, USA, 2001.
- [38] Q. Zhao, J. Cook, Q. Xu, and P. R. Harasti, "Improving short-term storm predictions by assimilating both radar radial-wind and reflectivity observations," *Weather and Forecasting*, vol. 23, pp. 373–391, 2008.
- [39] Q. Xu, L. Wang, P. Zhang, et al., "Progress in radar data quality control and assimilation," in *Proceedings of the 6th International Symposium of Hydrological Applications of Weather Radar*, Bureau of Meteorology & Australian Meteor, Melbourne, Australia, 2001, The Oceanography Society, Conference CD.
- [40] Q. Zhao, J. Cook, Q. Xu, and P. R. Harasti, "Using radar wind observations to improve mesoscale numerical weather prediction," *Weather and Forecasting*, vol. 21, no. 4, pp. 502–522, 2006.
- [41] A. Protat and I. Zawadzki, "Optimization of dynamic retrievals from a multiple-Doppler radar network," *Journal of Atmospheric and Oceanic Technology*, vol. 17, no. 6, pp. 753–760, 2000.
- [42] R. Daley, *Atmospheric Data Analysis*, Cambridge University Press, Cambridge, UK, 1991.
- [43] Q. Xu and J. Gong, "Background error covariance functions for Doppler radial-wind analysis," *Quarterly Journal of the Royal Meteorological Society*, vol. 129, no. 590, pp. 1703–1720, 2003.

Research Article

Reconstruct the Mesoscale Information of Typhoon with BDA Method Combined with AMSU-A Data Assimilation Method

Yunfeng Wang,^{1,2} Haiyang Zhang,¹ Bin Wang,² Yueqi Han,¹ and Xiaoping Cheng¹

¹ Laboratory of Military Meteorology, Institute of Meteorology, PLA University of Science and Technology, Nanjing, 211101, China

² LASG, Institute of Atmospheric Physics, Chinese Academy of Sciences, Beijing 100029, China

Correspondence should be addressed to Yunfeng Wang, wangyf@mail.iap.ac.cn

Received 28 December 2009; Revised 24 March 2010; Accepted 20 April 2010

Academic Editor: Zhaoxia Pu

Copyright © 2010 Yunfeng Wang et al. This is an open access article distributed under the Creative Commons Attribution License, which permits unrestricted use, distribution, and reproduction in any medium, provided the original work is properly cited.

This paper conducts the assimilating experiments and simulating experiments on typhoon “Aere” (No. 0418), by use of bogus data assimilation (BDA) method combined with advanced microwave sounding unit-A (AMSU-A) data assimilation method in the fifth-generation National Center for Atmospheric Research (NCAR)/Penn State Mesoscale Model Version-3 (MM5V3), the Radiative Transfer for TIROS-N Operational Vertical Sounder Version-7 (RTTOV) model, and their adjoint models. The Bogus data constructed with BDA technique are mainly located at sea level, while the peak energy contribution levels of the sounder channels selected in AMSU-A data assimilation technique are mainly located at upper troposphere. The two types of data can reconstruct the meso-scale information and improve the typhoon initial fields under the model dynamic forcing effect, respectively from the low level and the upper level of atmosphere during the assimilating process. Numerical results show that with four-dimensional variational data assimilation (4DVAR) technique the circulation of initial fields is improved, the “warm core” of typhoon is enhanced, the “cloud water” phenomenon that occurs in the optimal initial fields and the numerical model is changed into “warm start” from “cold start”.

1. Introduction

Typhoon is one of the most frequent disasters affecting human beings. With the development of numerical forecasting techniques, numerical forecasting of typhoon has entered an operational stage. However, the prediction accuracy is far from meeting the requirements of disaster prevention and reduction. If the track and intensity of typhoon can be accurately forecasted, necessary preparedness can be performed beforehand and serious economic loss can be much reduced. Due to severe deficiency of conventional observation data over sea, the results of objective analysis can not precisely describe the thermal structure and circulation characteristics of initial typhoon, especially its mesoscale structure, which is one of the main reasons for serious errors in typhoon numerical forecasting. Therefore, how to provide more rational initial values is an urgent task.

Since 1990s, an initializing method of artificial typhoon mode is introduced into typhoon forecasting research [1–3]. With this method, an ideal bogus typhoon mode with

3-dimensional circulation structure and thermal structure is constructed according to the observation data, and then it is implanted into the initial typhoon analysis fields to construct new initial typhoon optimal fields. This method is now widely applied in Typhoon Numerical Prediction Operational System in many countries, which improves the typhoon numerical forecast skill greatly. However, there are still a lot of shortcomings in this method.

The concept of 4DVAR was initially put forward and then developed by Lewis and Derber [4], Le Dimet and Talagrand [5], and Courtier and Talagrand [6]. Later, with 4DVAR technique, a new method to optimize the rough initial fields of tropical cyclone was proposed [7, 8], which is named bogus data assimilation (BDA) method, that is, with 4DVAR technique, through assimilating the sea level pressure of ideal vortex and gradually adjusting the model background field, more actual vortex with dynamical and physical balance is obtained. Numerical experiments on hurricane “Felix” show that this method effectively improves the characteristics of hurricane eye and forecasting of hurricane intensity.

Through numerical simulation of hurricane Georges and Bonnie, Pu and Braun [9] thought that assimilating the wind data of bogus vortex was also important to the adjustment of initial field. A hybrid variational scheme (HVAR) is developed by Weng et al. [10] and it was applied in two hurricane cases, resulting in improved analyses of three-dimensional structures of temperature and wind fields as compared to operational model analysis fields. It is found that HVAR reproduces detailed structures for the hurricane warm core at the upper troposphere. Both lower-level wind speed and upper-level divergence are enhanced, with reasonable asymmetric structure. With the weather research and forecasting three-dimensional variational data assimilation system (WRF 3D-VAR), it is indicated that hurricane initialization with the BDA technique can improve the forecast skills of track and intensity in the Advanced Research WRF (ARW) [11]. Besides, many other researchers also have done much work on studying the BDA method [12, 13].

With the rapid development of satellite observing system, the satellite remote sensing data gradually becomes one of the major observation data sources due to its wide coverage and high-spatial and -temporal resolution; the assimilation of satellite data also turns to be an important instrument to reconstruct the mesoscale structure of typhoon. The fast radiative transfer modeling and its components, critical for satellite data assimilation, are summarized and discussed for their potential applications in operational global data assimilation systems [14]. Since the microwave radiation can pass through deep cloud layer and its brightness temperature data can well indicate the vertical structure of atmosphere under cloud, it is very useful to improve typhoon circulation structure and determinate typhoon initial location.

Zou et al. [15] successfully assimilated Geostationary Operational Environmental Satellite (GOES) brightness temperature data into the initial field of typhoon by use of the 4DVAR technique in their study of the hurricane on the east coast of America. The results indicated that the forecasting of typhoon intensity, track and precipitation could be greatly improved. Le Marshall et al. [16] assimilated all the available high-density data and satellite data into the initial field of typhoon to reconstruct the inner structure of typhoon, and the 48 hours track forecasting error was reduced from 400 km in the control experiment to 150 km in the assimilating experiment. Wang et al. [17] effectively improved the intensity forecasting and track forecasting of typhoon, by simultaneously assimilating the large-scale background fields data, bogus data, cloud-derived wind data, satellite inverse data, high-resolution infrared radiation sounder data (HIRS), and so forth. into the numerical forecasting model.

Zhang et al. [18] adopted 3-dimensional variational assimilation (3DVAR) technique to assimilate AMSU brightness temperature data into numerical model in the study of the typhoon structure and its evolution in different stages on Northwest Pacific. The numerical results showed that the direct assimilation of AMSU brightness temperature data could accurately describe the 3-dimensional structure and evolution of typhoon on Northwest Pacific, which is difficult

to achieve with conventional observation data. The study shows that the AMSU data provide improvement to track forecasts of tropical cyclone [19].

Though BDA method and AMSU-A data assimilation method have been used many times in numerical simulating of hurricane, there is few research work combining the two methods by 4DVAR technique in typhoon simulating. Selecting typhoon "Aere" (No. 0418) as the case, this paper combines BDA method with AMSU-A data assimilation method to conduct assimilating experiments and numerical simulating experiments to reconstruct mesoscale information of typhoon, and also studies the intensity forecasting and track forecasting. The numerical models, the observation data, and the objective function are briefly introduced in Section 2. Experiment design of numerical scheme and the corresponding numerical results are shown in Section 3. Section 4 provides conclusions and discussion.

2. Numerical Models, Observation Data, and Objective Function

2.1. Numerical Models. The MM5V3 model, the RTTOV-7 model, and their adjoint models are adopted in this paper. The MM5 model is a mesoscale numerical forecasting model which is developed jointly by National Center for Atmospheric Research (NCAR) and Pennsylvania University (PSU). In this paper, the central point of the numerical simulating domain is (124.5°E, 22.5°N). The assimilating experiments are conducted on single-nest domain with 54 km horizontal resolution and the horizontal grid number is 75×91 . The simulating experiments are conducted on double-nest domain. The horizontal resolutions are, respectively, 54 km, 18 km, and horizontal grids are, respectively, 75×91 , 121×130 . The σ -coordinate is used in the numerical model and there are totally 23 levels in the vertical direction. Parameterization schemes used in simulation are as the followings: Grell cumulus parameterization scheme [20], MRF PBL scheme [21], relaxation inflow/outflow boundary condition, and so forth.

The RTTOV radiative transfer model is to compute very rapid calculations of top of atmosphere radiances for a range of space-borne infrared and microwave radiometers viewing the Earth's atmosphere and surface. The original basis for the RTTOV fast computation of transmittances is described by Eyre and Woolf [22]. The development of RTTOV-7 has been carried out as part of collaboration between the Met Office (UK), Météo France, and ECMWF in the framework of the EUMETSAT-funded NWP Satellite Application Facility and also other EUMETSAT sponsored activities. The RTTOV-7 model describes the complicated nonlinear relationship between the satellite radiation brightness temperature and the model variables. Various physical fields such as temperature profile and water vapor profile required by the RTTOV-7 model are provided by the MM5V3 model. In the RTTOV-7 model, the atmosphere is divided into 43 layers from 0.1 hPa to 1013 hPa and the channel transmissivity is calculated layer by layer according to the actual vertical structure of atmosphere so that the radiant brightness temperature of every channel can be finally synthesized. Different from

the traditional radiant model, the optics thickness d in the RTTOVS-7 model can be expressed as

$$d_{i,j} = d_{i,j-1} + Y_j \sum_{k=1}^K a_{i,j,k} X_{k,j}, \quad (1)$$

where Y_j and $X_{k,j}$ are factors related with the actual atmospheric condition, $a_{i,j,k}$ is the forecast factor obtained by the accurate transmissivity model, i is the serial number of channels, j is the serial number of different levels, and k is the serial number of forecast factors.

2.2. Observation Data. The National Centers for Environmental Prediction (NCEP) Global Forecast System (GFS) final (FNL) girded analysis datasets, with horizontal resolution of $1^\circ \times 1^\circ$, are used to produce the background fields of model.

In BDA method, the bogus data, including the sea level pressure and wind fields, are calculated based on observational typhoon information by the following formulas:

$$P_0(r) = P_c + \Delta P \left\{ 1 - \left[1 + \frac{1}{2} \left(\frac{r}{R} \right)^2 \right]^{-1/2} \right\}, \quad (2)$$

$$V_0(r) = \left(\frac{r}{\rho} \frac{\partial P_0}{\partial r} + \frac{f^2 r^2}{4} \right)^{1/2} - \frac{r|f|}{2},$$

where P_c is the sea level pressure of typhoon center; ΔP is a parameter related with the sea level pressure gradient and is determined by the maximum wind speed of typhoon; R is the radius of the maximum pressure gradient, usually that of the maximum wind speed; r is the radius of vortex; ρ is the air density. The bogus typhoon is regarded as quasi-stationary in the first 32 minutes. The time window of assimilating bogus data is set to 32 minutes, and the same “observed data” is read every 4 minutes [8].

The NOAA-16 AMSU-A data provided by National Aeronautics and Space Administration (NASA) are used in this paper. There are totally 15 detective channels of AMSU-A data, which has been interpolated to match the horizontal resolution of HIRS data. Finally, the resolution of subsatellite point is 17.4 km. In every scanning line there are 56 detective pixels which are axisymmetric along the satellite orbit. In this paper, the presence of precipitation cloud has already been checked before the performance of 4DVAR process. Despite that AMSU has the ability to penetrate the cloud layer to detect atmospheric temperature and humidity, while the water droplets and ice crystals in precipitation cloud are larger than the radiance wavelength, so the resulting scatter can weaken the signal below the cloud layer. Since it influences the detection, the presence of precipitation cloud must be checked. The test formula of the precipitation probability P (unit: %) of the ATOVS is expressed as follows [18]:

$$P = \frac{1}{1 + e^{-f}}, \quad (3)$$

$$f = 10.5 + 0.184TB_1 - 0.221TB_{15},$$

where TB_1 and TB_{15} are the observation brightness temperature in channel 1 and channel 15, respectively. When $P \geq 70$, the radiance brightness temperature must be rejected. During the assimilation procedure of AMSU-A data, quality control method and channel choosing method are both taken into consideration. Two quality control techniques are employed: extreme value check and a check for departures between the simulated observation value and the actual observation value. The channel is selected according to the peak energy contribution level of the sounder channel and the influence of the sounding objective on the retrieval results of temperature and water vapor. In fact, the 4 channels from 6 to 9 are adopted in this paper.

2.3. Objective Function. When the bogus data and AMSU-A data are assimilated into model at the same time, the total objective function J can be defined as

$$J = J_1 + J_2 + J_3, \quad (4)$$

where J_1 is the deviation between the model control variable X and the background variable X_B , J_2 is that between the model control variable and the bogus data, and J_3 is that between the simulated AMSU-A brightness temperature and the actual satellite observation data. Their general form can be expressed as follows:

$$J = \frac{1}{2} \sum_i (X - X_B)^T B^{-1} (X - X_B),$$

$$J_2 = \frac{1}{2} \sum_t \sum_i \left\{ [P(r) - P_0(r)]^T W_P [P(r) - P_0(r)] \right. \\ \left. + [V(r) - V_0(r)]^T W_V [V(r) - V_0(r)] \right\},$$

$$J_3 = \frac{1}{2} \sum_t \sum_i [H_{BTA}(X) - BTA]^T W_{BTA} [H_{BTA}(X) - BTA], \quad (5)$$

where the superscript “ T ” denotes transpose, B is the error covariance matrix of background fields, $P(r)$ and $V(r)$ are, respectively, sea level pressure and sea level wind of model atmosphere, W_P and W_V are the corresponding weighting coefficients, “ \sum ” denotes the sum, the subscript sign “ t ” denotes different observing times, the subscript sign “ i ” denotes different spatial observing positions at the same time, H_{BTA} denotes the observed operator of calculating the simulated brightness temperature with model atmospheric variables, BTA denotes the actual AMSU-A observation data, and W_{BTA} denotes the weighting coefficient of detective channels. We take $W_p = 1.61/\text{hPa}^2$ and $W_v = 0.185 \text{ S}^2/\text{m}^2$ in all experiments, just like Xiao et al. [8]. W_{BTA} is taken according to the following principle: the weighting coefficients of different channels should have the same contribution to the total cost function. In this paper, they are, respectively, 10.41, 9.24, 12.54, and 11.90.

3. Numerical Experiments

3.1. Scheme Designs. Typhoon “Aere” (no. 0418) was generated over the sea at about 1400 km away from the east

TABLE 1: The schemes of numerical simulation and assimilating experiment.

Scheme	Initial fields of model
Control experiment (Scheme 1)	Provided by NCEP data
Bogus data assimilation experiment (Scheme 2)	Provided by BDA method
Total data assimilation experiment (Scheme 3)	Provided by BDA method combined with AMSU-A data assimilation method

of Luzon, Philippines on August 20, 2004, and then it moved west-northward under the lead of the subtropical high, with maximum wind speed of up to 43 m/s. “Aere” swept the adjacent waters to northern Taiwan on dawn of August 25 and in the same afternoon it landed on Fujian province of China with wind speed of 35 m/s. After landing it gradually downgraded to a tropical depression. This paper focuses on typhoon intensity forecasting, typhoon track changing, landing and vapor variation. Numerical simulation is performed for 72 hours with the initial time set at 12:00 on August 23. The satellite profiles at 17:45 on August 23 are assimilated within 345 minutes, with the assimilating window set to 360 minutes.

The schemes of numerical simulation and assimilating experiments are shown in Table 1, including a control experiment (Scheme 1) and two assimilating experiments (Schemes 2 and 3).

3.2. Numerical Results

3.2.1. The Initial Fields. The initial fields of three schemes are shown in Figure 1, in which the left panels are sea level pressure fields (units: hPa) and the right are temperature fields at 500 hPa (units: °C).

Figure 1(a) shows that the isobars on sea level at initial time provided by NCEP data are very sparse. The minimum central sea level pressure is 988 hPa while the actual observed value is 975 hPa. Figure 1(c) indicates that the intensity of initial typhoon is effectively enhanced, with central sea level pressure of 975 hPa after the bogus data is assimilated, which is in accordance with the observed value. Figure 1(e) indicates that the intensity of initial typhoon in Scheme 3 is also 975 hPa when BDA method and AMSU-A data assimilation method are combined. In fact, when only the AMSU-A data is assimilated, the intensity of initial typhoon would not obviously be improved. This implies that BDA method is more effective than AMSU-A data assimilation method in improving the intensity of initial typhoon.

Figure 1(b) shows that the “warm core” structure of initial temperature fields in NCEP data is not obvious and the central temperature of initial typhoon is about 0°C. Therefore, the weak “warm core” will greatly influence the forecasting intensity and forecasting track. Figures 1(d) and 1(f) show that there are obvious “warm core” structures both in Schemes 2 and 3, in which the maximum central temperature is 3.5° and 3.3°, respectively. It denotes that data assimilation is effective in improving temperature fields of initial typhoon, especially in Scheme 3, when AMSU-A data are assimilated, more mesoscale information are added into initial temperature fields. In the two assimilating

schemes, although temperature data is not directly assimilated, temperature fields can still be adjusted correspondingly under the constraints of model dynamics whenever the other observation data are assimilated; it is a significant advantage of 4DVAR technique.

The vorticity fields of typhoon at initial time in the three schemes are shown in Figure 2. The left panels denote the horizontal vorticity patterns on 300 hPa at initial time and the right ones denote the vertical vorticity patterns at initial time (vertical sections are given cross the center of typhoon along the zonal direction, where arrows denote the synthetic effect of horizontal velocity v and vertical velocity $w \times 200$). Comparing Figure 2(a) with Figure 2(c), it can be found that the effect of the BDA method is not remarkable in improving vorticity fields at upper troposphere. Figure 2(e) indicates that when AMSU-A data is assimilated the vorticity fields of typhoon at initial time change obviously and many mesoscale structures are reconstructed. Comparison between Figures 2(b) and 2(d) shows that although the BDA method can enhance the inner vertical circulation of the initial typhoon, it has little influence on the typhoon circulation at upper troposphere. Figure 2(f) shows that when BDA method is combined with AMSU-A data assimilation method, a lot of meso- and microscale information are introduced into the vertical vorticity fields, which proves the positive effect of assimilating AMSU-A brightness temperature data on typhoon numerical forecasting. Though the BDA method is not very effective in improving the initial typhoon circulation fields at high level, it is more effective in decreasing sea level pressure of initial typhoon. And the direct assimilation of AMSU-A data is not effective in improving the intensity of initial typhoon, but it does well in improving the circulation structure of initial typhoon at upper troposphere. Therefore, in order to improve typhoon numerical forecasting, combining BDA method and AMSU-A data assimilation method would be beneficial to optimize the initial fields separately from low level and high level. In this way, not only the intensity of initial typhoon can be improved, but also the mesoscale structure of initial typhoon can be reconstructed.

It is well known that there is no cloud water in the initial fields of numerical model, just like in Scheme 1. But the cloud water of the optimal initial fields will increase during the 4DVAR iterative process by assimilating observation data. That is to say, the cloud water is formed by MM5 adjoint model under the constraints of model dynamics. Figure 3 shows the cloud water content (units: kg/kg) of the optimal initial fields on 400 hPa in Schemes 2 and 3. In Scheme 2, the circular cloud water is formed in the optimal initial fields due to assimilating the bogus data. While in Scheme 3, a

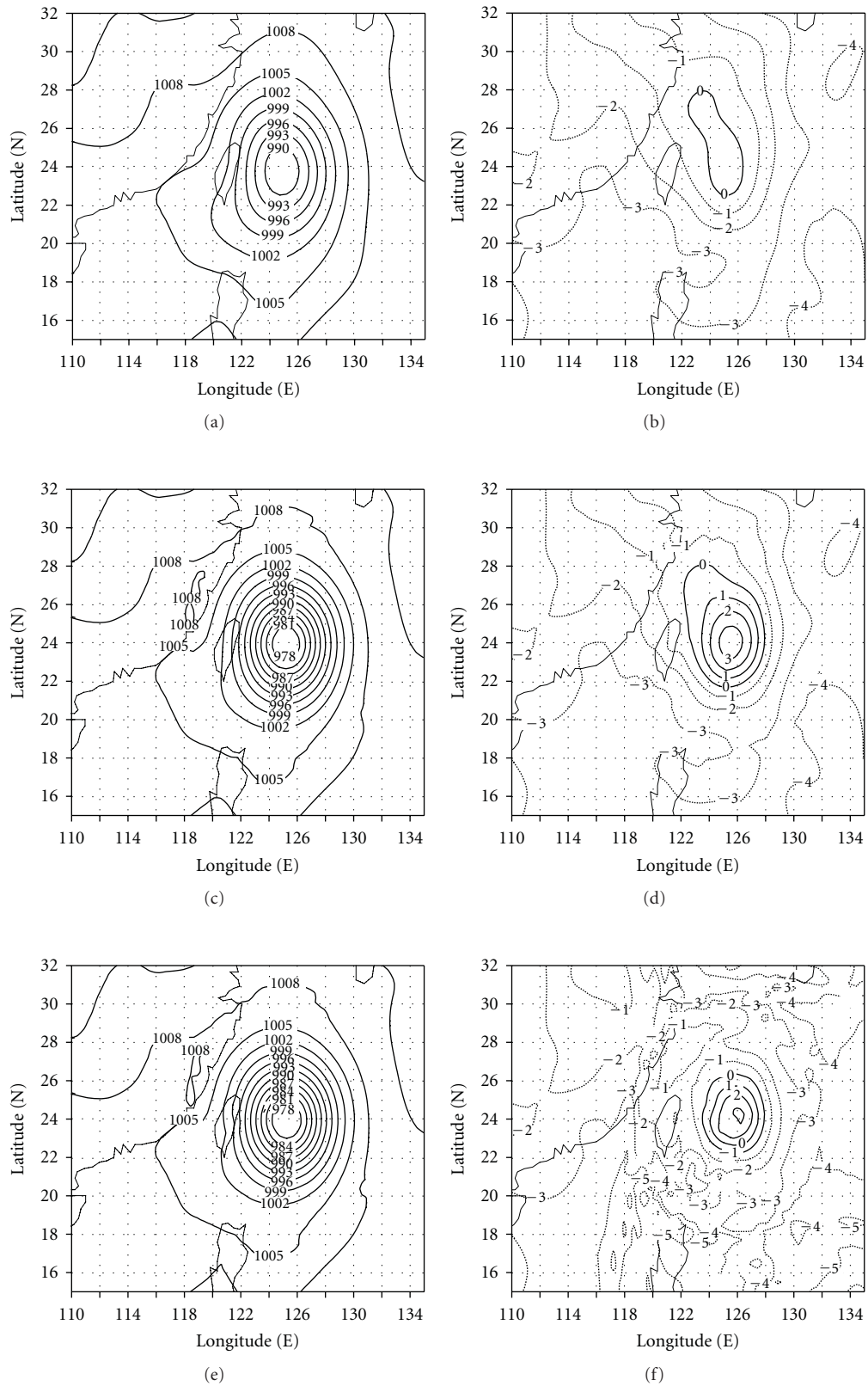


FIGURE 1: The initial fields of sea level pressure ((a) Scheme 1, (c) Scheme 2, (e) Scheme 3; hPa) and temperature ((b) Scheme 1, (d) Scheme 2, (f) Scheme 3; °C) simulated by various experiments at 500 hPa.

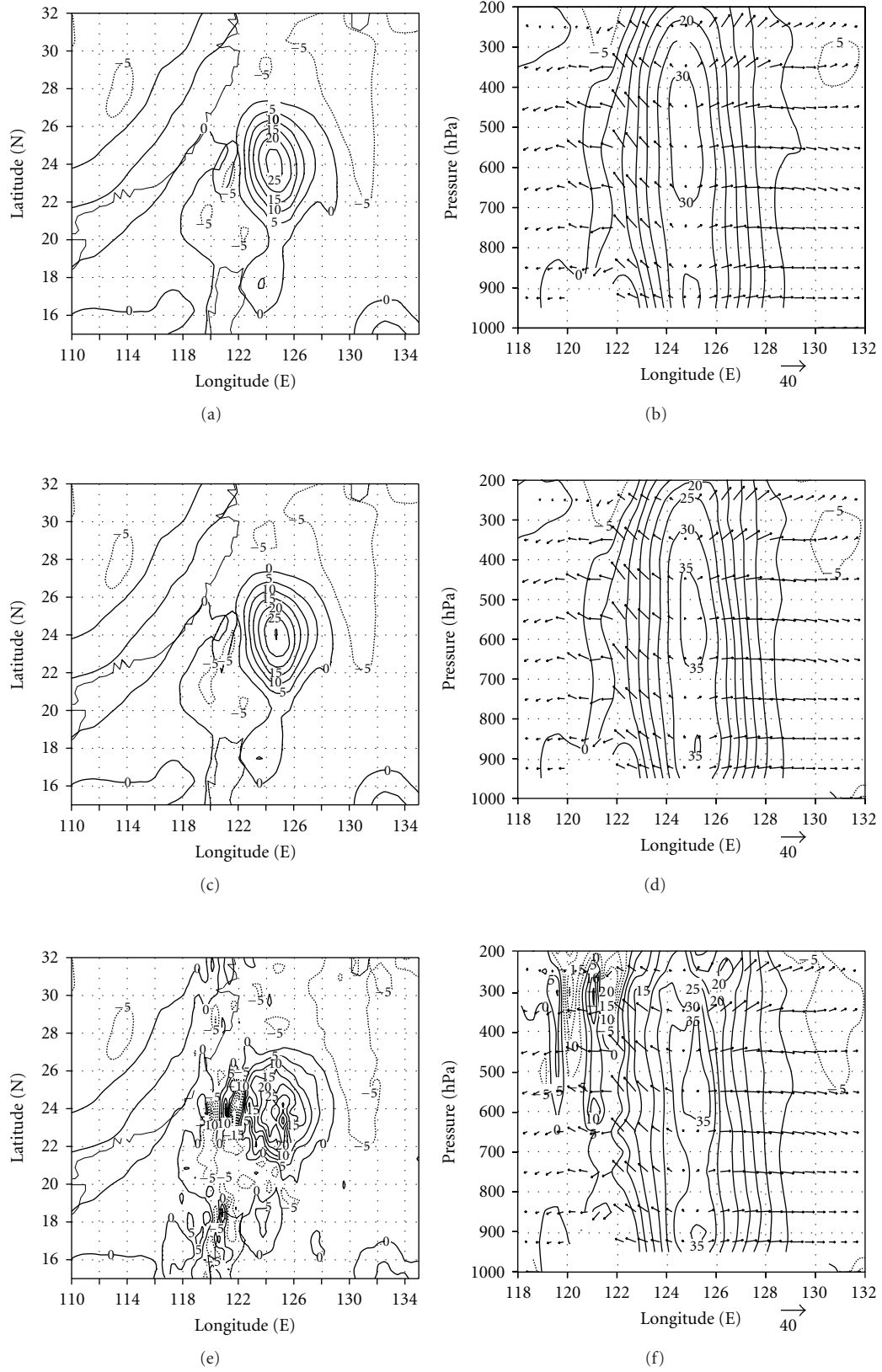


FIGURE 2: The initial horizontal vorticity fields ($\times 1.e + 5$) on 300 hPa ((a) Scheme 1, (c) Scheme 2, (e) Scheme 3; s^{-1}) and vertical vorticity fields and wind fields ($w \times 200$) cross the center of typhoon along the zonal direction ((b) Scheme 1, (d) Scheme 2, (f) Scheme 3; s^{-1}) simulated by various experiments.

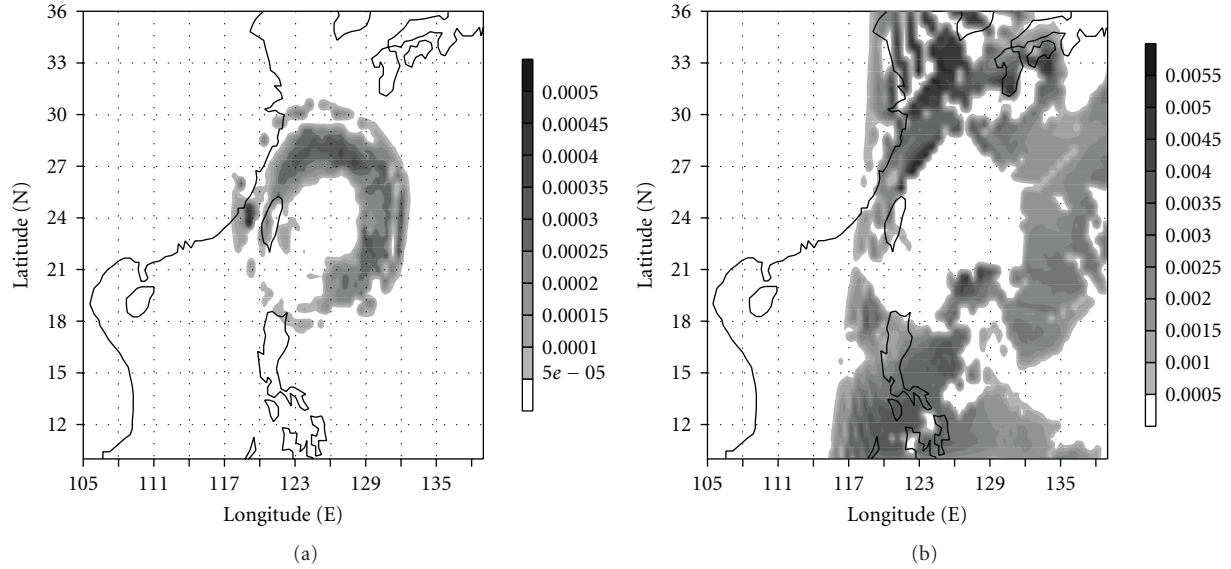


FIGURE 3: Cloud water of optimal initial fields in different Schemes on 400 hPa ((a) Scheme 2, (b) Scheme 3; kg/kg).

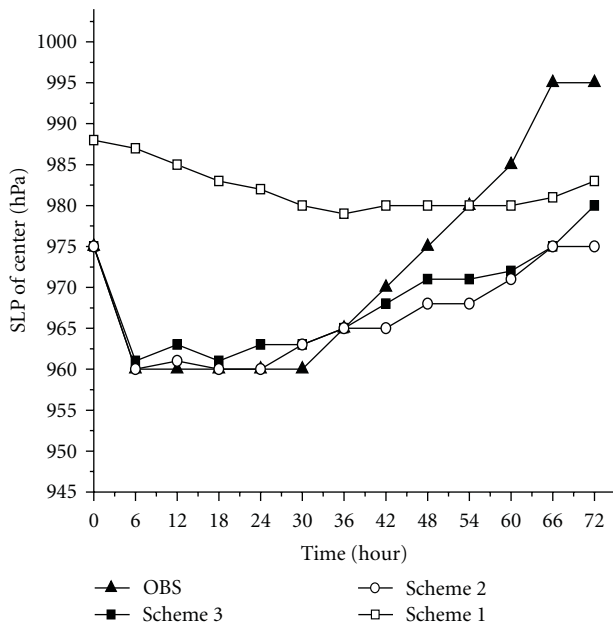


FIGURE 4: Simulated SLP of the center of typhoon during 72 hours in the three schemes Triangle point line: Observed data (OBS); Hollow square point line: Scheme 1; Hollow dot point line: Scheme 2; Solid square point line: Scheme 3.

reasonable cloud water pattern is formed due to assimilating the AMSU-A data. The coverage of satellite scanning can also be clearly shown in Figure 3(b), especially the location of actual typhoon, which is denoted by blank section in the center of figure.

3.2.2. Intensity of Simulated Typhoon during 72 Hours in the Three Schemes. The varying curves of SLP (sea level pressure) of simulated typhoon during 72 hours in the

three schemes are shown in Figure 4. Figure 4 shows that the typhoon intensity in Scheme 1 varies gently during the whole period, which is quite different from the trend of observed data, with the bias of 13 hPa at the initial time, the maximum bias of 27 hPa and the mean bias of 15 hPa. In Schemes 2 and 3, the advantage of BDA method is brought into fullest play. In both schemes, the central intensity of initial typhoon is improved greatly, and the central intensity of initial typhoon is in complete accordance with observation data (975 hPa). Furthermore, the simulated SLP during 72 hours is also improved greatly and its general varying trend is in accordance with OBS, with the mean bias of 6.3 hPa in Scheme 2 and 5.6 hPa in Scheme 3. The best one is the former 48 hours, during which the maintaining stage of typhoon is well simulated, with the mean biases of less than 3 hPa. The intensity changes are closely related with landfall. If the landfall time is not well predicted, it is difficult to have a good intensity prediction of landfall typhoons. The typhoons in Schemes 1 and 2 do not land at all, while it is delayed for about 12 hours in Scheme 3. So for the last 24 hours, the observed typhoon is weakened rapidly after landfall, while the simulated typhoon intensities in three schemes are varying slowly. However, Scheme 3 is better than Scheme 2 in the last 24 hours, and both Schemes 2 and 3 are far better than Scheme 1 when the whole period is concerned. Besides, because the assimilating of AMSU-A data is added into Scheme 3, the mesoscale information of initial fields is further increased and the surrounding fields of initial typhoon can be well simulated. Since the initial fields are further adjusted with AMSU-A data assimilation method, the simulating results of Scheme 3 are better than those of Scheme 2.

3.2.3. Track of Simulated Typhoon during 72 Hours in the Three Schemes. Comparison of typhoon track in the three schemes with observed typhoon track during the simulated

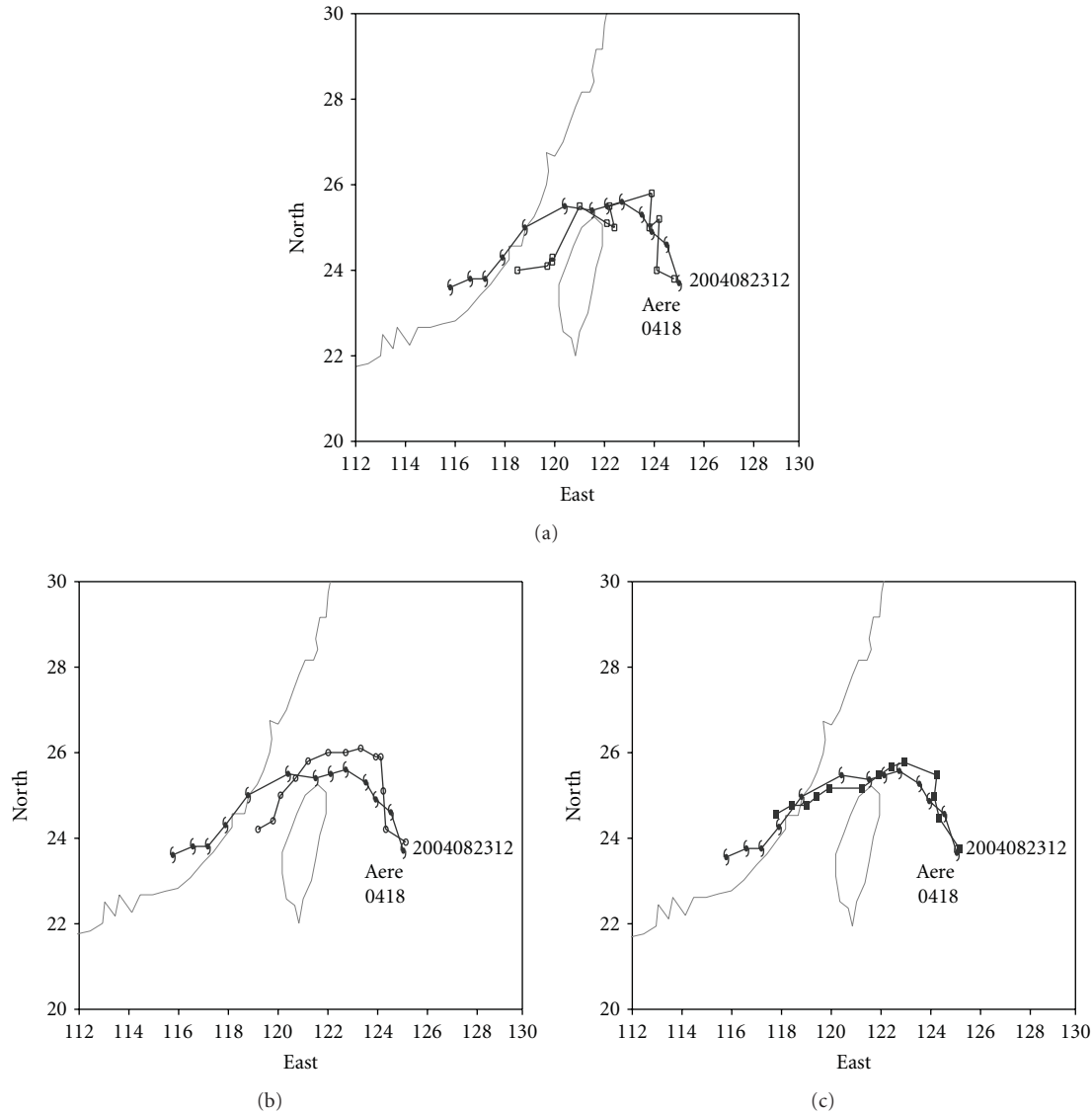


FIGURE 5: The varying curves of simulated typhoon track during 72 hours in the three schemes ((a) Scheme 1, (b) Scheme 2, (c) Scheme 3) Typhoon marker point line: Observed data; Hollow square point line: Scheme 1; Hollow dot point line: Scheme 2; Solid square point line: Scheme 3.

72 hours is shown in Figure 5. The figure shows that the observed typhoon firstly moves to the west-north and then sweeps over the adjacent waters to northern Taiwan, and finally lands on Fujian province of China. Figure 5(a) shows that the simulated track of typhoon in Scheme 1 is greatly different from the observed track; the simulated typhoon moves with irregular speed. Figure 5(b) shows that the simulated track of typhoon in Scheme 2 is close to the observed data, but the typhoon moves slowly and does not land on Fujian province of China at last. Figure 5(c) shows that the simulated track of typhoon in Scheme 3 is the best one, in which the whole moving trend of typhoon is closest to the observed data and the simulated typhoon finally lands on Fujian province of China, with landing location in accordance with the observed data, although its moving speed is still smaller than that of the observed data.

The bias curves of simulated typhoon track in three schemes from the observed track during 72 hours are shown in Figure 6. From Figure 6 it can be found that the location of typhoon at initial time in Scheme 3 is the closest to the observed typhoon location, with 15 km distance away from each other. In the following period, the biases of Scheme 3 are also smaller than those of other schemes, with 112 km in Scheme 3 while 228 km in Scheme 1 and 256 km in Scheme 2 in 48 hours; 231 km in Scheme 3 while 278 km in Scheme 1 and 351 km in Scheme 2 in 72 hours. Therefore, it can be concluded that although the BDA method is effective in improving typhoon intensity in the simulation, it could not much effectively improve typhoon track. The AMSU-A data assimilation method has no significant effect on improving typhoon intensity but it can greatly reconstruct mesoscale information of initial fields and greatly improve

TABLE 2: The mean forecast biases of 72 hours for different typhoons.

Typhoon	Intensity biases (hPa)			Track biases (km)		
	Scheme 1	Scheme 2	Scheme 3	Scheme 1	Scheme 2	Scheme 3
Aere (0418)	15	6.3	5.6	146	179	97
Meari (0422)	39	5	4	220	195	136
Dianmu (0406)	54	8.7	8.6	191	121	115

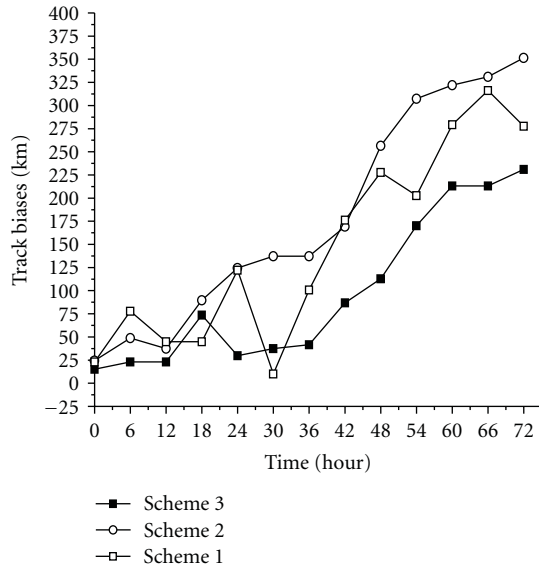


FIGURE 6: Biases of simulated typhoon track during 72 hours in the three schemes (Hollow square point line, Scheme 1; Hollow dot point line, Scheme 2; Solid square point line, Scheme 3).

typhoon track simulation. Besides, the intensity changes are closely related with landfall. If the landfall time is not well predicted, it is difficult to have a good intensity prediction of landfall typhoons. So for the last 24 hours, the simulated typhoon intensity in Scheme 3 is closer to the observed one than in Scheme 2. It further proves that typhoon intensity simulation and typhoon track simulation can be improved simultaneously by combining BDA method and AMSU-A data assimilation method. The typhoons in Schemes 1 and 2 do not land at all, while in Scheme 3 it is delayed for about 12 hours.

By comparing Figure 1(d) (Scheme 2) with Figure 1(f) (Scheme 3), and by comparing Figure 2(d) (Scheme 2) with Figure 2(f) (Scheme 3), we can find that many mesoscale/microscale systems are introduced into initial vorticity fields at high level of atmosphere when AMSU-A data is assimilated, and the AMSU-A data helps to improve the circulation of typhoon at high level. In our cases, the AMSU-A data assimilation is helpful to improve typhoon track forecast. In order to reveal the reasons, we also study the vertical structure of temperature fields and geopotential height fields. It is shown that temperature difference and geopotential height difference of optimal fields (Scheme 3 minus Scheme 2) are both located at high level, especially

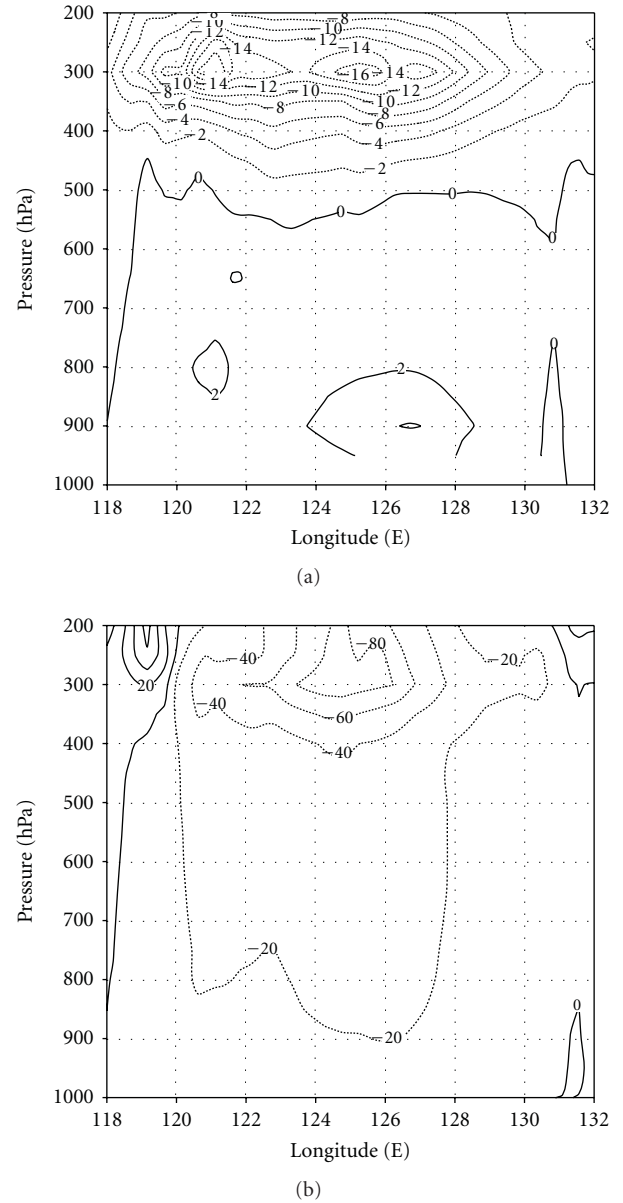


FIGURE 7: The vertical sections of temperature difference ((a); °C) and geopotential height difference cross the center of typhoon along the zonal direction ((b); m) between Schemes 3 and 2 (Scheme 3 minus Scheme 2) in optimal initial fields.

at 300 hPa (shown as Figure 7). The results illustrate that AMSU-A data assimilation can be helpful to improve the high-level fields. In this paper, channels 6–9 of AMSU-A

data are selected in assimilation experiments. Because their peak energy contribution levels are mainly located at upper troposphere, the observed information of AMSU-A data mainly concentrates at upper troposphere and AMSU-A data assimilation can have a positive effect on reconstructing the mesoscale information at upper troposphere. This is the reason that though the direct assimilation of AMSU-A data is not effective in improving the intensity of initial typhoon, it does well in improving the circulation structure of initial typhoon at upper troposphere.

Some assimilating experiments and simulating experiments on other typhoons are also performed by use of BDA method combined with AMSU-A data assimilation method, and the same numerical conclusions can also be achieved. The results are shown in Table 2.

4. Conclusions

With BDA method combined with AMSU-A data assimilation method, the assimilating experiments and simulating experiments about some typhoons are carried out in this paper by using the MM5V3 model, the RTTOV-7 model and their adjoint models. The numerical results show the following.

- (1) If the initial fields are directly provided by NCEP data, the isobars on sea level at initial time are very sparse and the “warm core” structure of initial temperature fields is not obvious. Compared with the real observations, there are big biases both in intensity simulation and track simulation.
- (2) After being adjusted with the BDA method, the initial fields can effectively describe the initial circulation structure of typhoon. The BDA method can enhance initial typhoon intensity and improve initial typhoon thermal structure such as “warm core” structure. Though this method is effective in improving typhoon intensity simulating, it has no significant effect on improving typhoon track.
- (3) Combining BDA method and AMSU-A data assimilation method can improve not only typhoon intensity simulation but also typhoon track simulation. By use of 4DVAR technique, the circulation structure of analytical typhoon is greatly improved and the “warm core” structure is also enhanced. “Cloud water” arises in optimal initial fields of typhoon after observed data are assimilated. The running status of numerical model is changed into “warm start” from “cold start”, which is more reasonable. So combining BDA method and AMSU-A data assimilation method effectively may be an important way to increase the accuracy of typhoon numerical forecasting.

Though some interesting results have been obtained in this paper, further more experiments on other typhoons should be performed to confirm them. And AMSU-B data and HIRS data will be assimilated in further research work to improve the initial fields of typhoon.

Acknowledgments

This paper is jointly supported by the National Natural Science Foundation of China (no. 40405019, no. 40805046, and no. 10871099), the Commonwealth Trade (Meteorology) Program (no. GYHY(QX)2007-6-15 and no. GYHY200906009), and the National Basic Research Program of China (973 Program) (no. 2009CB421500).

References

- [1] T. Iwasaki, H. Nakano, and H. Sugi, “The performance of a typhoon track prediction model,” *Journal of the Meteorological Society of Japan*, vol. 65, pp. 555–570, 1987.
- [2] M. B. Mathur, “The National Meteorological Center’s quasi-lagrangian model for hurricane prediction,” *Monthly Weather Review*, vol. 119, no. 6, pp. 1419–1447, 1991.
- [3] Y. Kurihara, M. A. Bender, and R. J. Ross, “An initialization scheme of hurricane models by vortex specification,” *Monthly Weather Review*, vol. 121, no. 7, pp. 2030–2045, 1993.
- [4] J. M. Lewis and J. C. Derber, “The use of adjoint equation to solve a variational adjustment problem with advective constraints,” *Tellus*, vol. 37A, pp. 309–322, 1985.
- [5] F.-X. Le Dimet and O. Talagrand, “Variational algorithms for analysis and assimilation of meteorological observations: theoretical aspects,” *Tellus*, vol. 38A, no. 2, pp. 97–110, 1986.
- [6] P. Courtier and O. Talagrand, “Variational assimilation of meteorological observations with the adjoint vorticity equation. Part I: theory,” *Quarterly Journal of the Royal Meteorological Society*, vol. 113, no. 478, pp. 1311–1328, 1987.
- [7] X. Zou and Q. Xiao, “Studies on the initialization and simulation of a mature hurricane using a variational bogus data assimilation scheme,” *Journal of the Atmospheric Sciences*, vol. 57, no. 6, pp. 836–860, 2000.
- [8] Q. Xiao, X. Zou, and B. Wang, “Initialization and simulation of a landfalling hurricane using a variational bogus data assimilation scheme,” *Monthly Weather Review*, vol. 128, no. 7, pp. 2252–2269, 2000.
- [9] Z.-X. Pu and S. A. Braun, “Evaluation of bogus vortex techniques with four-dimensional variational data assimilation,” *Monthly Weather Review*, vol. 129, no. 8, pp. 2023–2039, 2001.
- [10] F. Weng, T. Zhu, and B. Yan, “Satellite data assimilation in numerical weather prediction models. Part II: uses of rain-affected radiances from microwave observations for hurricane vortex analysis,” *Journal of the Atmospheric Sciences*, vol. 64, no. 11, pp. 3910–3925, 2007.
- [11] Q. Xiao, L. Chen, and X. Zhang, “Evaluations of BDA scheme using the advanced research WRF (ARW) model,” *Journal of Applied Meteorology and Climatology*, vol. 48, no. 3, pp. 680–689, 2009.
- [12] Y. Zhao, B. Wang, and Y. Wang, “Initialization and simulation of a landfalling typhoon using a variational bogus mapped data assimilation (BMDA),” *Meteorology and Atmospheric Physics*, vol. 98, no. 3–4, pp. 269–282, 2007.
- [13] K.-H. Chou and C.-C. Wu, “Typhoon initialization in a mesoscale combination of the bogus vortex and the dropwindsonde data in DOTSTAR,” *Monthly Weather Review*, vol. 136, no. 3, pp. 865–879, 2008.
- [14] F. Weng, “Advances in radiative transfer modeling in support of satellite data assimilation,” *Journal of the Atmospheric Sciences*, vol. 64, no. 11, pp. 3799–3807, 2007.
- [15] X. Zou, Q. Xiao, A. E. Lipton, and G. D. Modica, “A numerical study of the effect of GOES sounder cloud-cleared brightness

- temperatures on the prediction of Hurricane Felix,” *Journal of Applied Meteorology*, vol. 40, no. 1, pp. 34–55, 2001.
- [16] J. F. Le Marshall, L. M. Leslie, R. F. Abbey Jr., and L. Qi, “Tropical cyclone track and intensity prediction: the generation and assimilation of high-density, satellite-derived data,” *Meteorology and Atmospheric Physics*, vol. 80, no. 1–4, pp. 43–57, 2002.
 - [17] Y.-F. Wang, B. Wang, G. Ma, and Y.-S. Wang, “Effects of 4DVAR with multifold observed data on the typhoon track forecast,” *Chinese Science Bulletin*, vol. 48, pp. 93–98, 2003.
 - [18] H. Zhang, J. Xue, G. Zhu, S. Zhuang, X. Wu, and F. Zhang, “Application of direct assimilation of ATOVS microwave radiances to typhoon track prediction,” *Advances in Atmospheric Sciences*, vol. 21, no. 2, pp. 283–290, 2004.
 - [19] T. H. Zapotocny, J. A. Jung, J. F. Le Marshall, and R. E. Treadon, “A two-season impact study of four satellite data types and rawinsonde data in the NCEP global data assimilation system,” *Weather and Forecasting*, vol. 23, no. 1, pp. 80–100, 2008.
 - [20] G. A. Grell, J. Dudhia, and D. R. Stauffer, “A description of the fifth-generation penn state/NCAR Mesoscale Model (MM5),” NCAR Technical Note NCAR/TN-398 + STR, National Center for Atmospheric Research, Boulder, Colo, USA, 1994.
 - [21] I. B. Troen and L. Mahrt, “A simple model of the atmospheric boundary layer; sensitivity to surface evaporation,” *Boundary-Layer Meteorology*, vol. 37, no. 1-2, pp. 129–148, 1986.
 - [22] J. R. Eyre and H. M. Woolf, “Transmittance of atmospheric gases in the microwave region: a fast model,” *Applied Optics*, vol. 27, pp. 3244–3249, 1988.

Research Article

An Intercomparison of GPS RO Retrievals with Colocated Analysis and In Situ Observations within Tropical Cyclones

Henry R. Winterbottom¹ and Qingnong Xiao²

¹ Department of Meteorology, The Florida State University, Tallahassee, FL 32306, USA

² College of Marine Science, University of South Florida, Saint Petersburg, FL 33701, USA

Correspondence should be addressed to Qingnong Xiao, qxiao@marine.usf.edu

Received 13 January 2010; Accepted 8 April 2010

Academic Editor: Zhaoxia Pu

Copyright © 2010 H. R. Winterbottom and Q. Xiao. This is an open access article distributed under the Creative Commons Attribution License, which permits unrestricted use, distribution, and reproduction in any medium, provided the original work is properly cited.

Observations from four Global Position System (GPS) Radio Occultation (RO) missions: Global Positioning System/Meteorology, CHAallenging Minisatellite Payload, Satellite de Aplicaciones Cientificas-C, and Constellation Observing System for Meteorology, Ionosphere and Climate and Taiwan's FORMOSA SATellite Mission #3 (COSMIC/FORMOSAT-3) are collected within a 600 km radius and ± 180 minute temporal window of all observed tropical cyclones (TCs) from 1995 to 2006 that were recorded in the global hurricane best-track reanalysis data set (Jarvinen et al. (1984); Davis et al. (1984)). A composite analysis of tropical cyclone radial mean temperature and water vapor profiles is carried out using the GPS RO retrievals which are colocated with global analysis profiles and available in situ radiosonde observations. The differences between the respective observations and analysis profiles are quantified and the preliminary results show that the observations collected within TCs correspond favorably with both the analysis and radiosonde profiles which are colocated. It is concluded that GPS RO observations will contribute significantly to the understanding and modeling of TC structures, especially those related to vertical variability of the atmospheric state within TCs.

1. Introduction

A tropical cyclone (TC) spends most of its lifetime over the global oceans and often in regions where regularly collected in situ observations are scarce. As a result, the kinematic and thermodynamic structures of TCs were largely unobserved using the conventional observation network. During the mid-1960s through the late 1970s, the advent of aircraft reconnaissance missions provided scientists the ability to create composite analyses of the energy budgets within these events. Many case studies have been executed using the collected data which include Riehl and Malkus [1], Miller [2], LaSeur and Hawkins [3], Gray and Shea [4], Shea and Gray [5], and Jorgensen [6].

More recent advancements, especially for those which apply remote sensing technologies, have provided even more detailed insight into the kinematic and thermodynamic structure for TCs. Example applications include the use of airborne Doppler radar [7–10], stereoscopic and infrared satellite observations [11, 12], and field programs [13]. As a

result of these observations, further studies investigating the inner-core structures, dynamics, and wind fields of TCs have been performed, which have led to further understandings of the characteristics for TCs.

In 1995, a proof-of-concept mission, GPS/MET (Global Positioning System/METeorology.) [14, 15] for the Global Positioning System (GPS) Radio Occultation (RO) technique was launched. The GPS RO technique was developed and has been continuously refined by the Jet Propulsion Laboratory (JPL) and Stanford University. Nearly five years after the success of GPS/MET, a collaborative effort between Germany, Argentina, and the United States resulted in the launch of 2 additional experiments—CHAMP (CHALLENGING Minisatellite Payload.) [16] and SAC-C (Satellite de Aplicaciones Cientificas-C.) [17]. Finally, a collaborative effort between Taiwan and the United States (COSMIC/FORMOSAT-3 (Constellation Observing System for Meteorology, Ionosphere and Climate/FORMOSA SATellite Mission #3.)—henceforth COSMIC) resulted in the successful launch of 6 satellites, in addition to still functioning CHAMP.

For meteorological studies, some of the most appealing characteristics of the GPS RO observations is the large number of observations within the middle latitudes, the high vertical resolution (nearly 100-meter), and the ability of the radio signals to penetrate cloud cover while remaining (largely) unaffected by precipitation. The focus and purpose of this study is to evaluate GPS RO observations collected within TCs and compare to available and colocated in situ observations (radiosondes) and global model analysis profiles. Composite analysis techniques, which are required due to the low horizontal resolution of vertical profiles, are utilized with the intent of providing a basis for which TC GPS RO observations can be used in the initialization Numerical Weather Prediction (NWP) using a variant of data assimilation techniques. The error statistics calculated in this study, between the observations and colocated analysis profiles, provide useful information regarding how the GPS retrieval can be weighted for use in advanced data assimilation procedures.

The remainder of this manuscript is organized as follows: the following section briefly describes the GPS RO technique which is followed by a description of the data collection and sampling methodology used to construct the composite analysis profiles. Section 4 provides a intercomparison of the resulting composite analyses while this manuscript concludes with a discussion and summary of the current results.

2. The GPS RO Technique as Applied to Meteorology

The GPS system was first implemented by the military for the purpose of communicating position and time information to different global battle fields. Presently, there are 24 satellites in orbit, each inclined at 55° to the ecliptic plane. An RO occurs as a GPS satellite—transmitting a radio signal either rising or setting behind the Earth, comes within view of a Low-Earth Orbiting (LEO) satellite with an on-board GPS receiver. As an RO occurs, the transmitted radio signal is Doppler shifted as a result of the atmospheres vertical density gradients. This Doppler shift can be related to the bending angle of the ray path which reflects the integrated effect of refraction along the ray path [14, 16, 18].

The LEO maintains the position and velocity measurements for each of the GPS satellites. Given the precision of these measurements, the *expected* Doppler shift of the radio signal can be calculated. Applying a double-difference technique [19], the clock error shift (or excess Doppler shift) is determined from the refracted radio signal. This excess Doppler shift is the measurement obtained by subtracting the observed shift from the clock error shift. The quantities of bending angle (α), impact parameter (a), and tangent point describe this excess Doppler shift [18]. The refraction index (n) is related to the above quantities via

$$\ln(n(a)) = \frac{1}{\pi} \int_a^\infty \frac{\alpha(x)}{x^2 - a^2} dx. \quad (1)$$

If the refraction index is assumed constant within each atmospheric layer while the assumption is made that no

TABLE 1: GPS RO missions providing RO measurements through tropical cyclone regions defined via the respective years HBTRA.

Mission	Mission ID	Operation	1DVAR
GPS METeorology	GPS/MET	1995–1997	ECMWF
Satellite de Aplicaciones Cientificas-C	SAC-C	2001–2002	ECMWF
CHALLENGING Minisatellite Payload	CHAMP	2001	ECMWF
Constellation Observing System for Meteorology, Ionosphere, and Climate	COSMIC	2006	GFS/AVN

significant asymmetric horizontal variations in temperature and moisture are present [20], the relation in (1) can be solved via an Abel transform [21, 22]. The atmospheric refractivity is then related to various tropospheric, stratospheric, and ionospheric quantities using the following relation:

$$N = 77.6 \frac{P}{T} + 3.73 \times 10^5 \frac{e}{T^2} - 40.3 \times 10^6 \frac{n_e}{f^2}. \quad (2)$$

Pressure (P) and temperature (T) compose the *dry* refractivity term while water vapor pressure (e) and virtual temperature constitute the *wet* refractivity term. Finally, the electron density (n_e) and the carrier frequency (f) contribute the ionospheric refractivity component. For the purposes of tropospheric studies, $n_e \approx 0$ and only the variables P , T , and e contribute information along the refractivity profile which reduces (2) to

$$N \approx 77.6 \frac{P}{T} + 3.73 \times 10^5 \frac{e}{T^2}. \quad (3)$$

The calculation to find each of the atmospheric quantities in (3) is inherently an underspecified problem. For the dry atmosphere, the refractivity profile and the hydrostatic equation define T and P . However, when water vapor (e) is present, specifically below 10 km, a situation occurs involving 2 equations with 3 unknowns. Independent knowledge of either T , P , or e is required to solve for the remaining two variables [23]. Using a 1-dimensional variational (1DVAR) assimilation technique, global analysis fields which have been interpolated to GPS RO positions, allow moisture observation to be obtained from the dry-refractivity profiles [24]. For the GPS/MET, SAC-C, and CHAMP missions, the analyses obtained from the European Center for Medium-Range Weather Forecasting (ECMWF) global model provide the analysis profiles for the estimation of e while the National Center for Environmental Prediction (NCEP) Global Forecasting System (formally the Aviation model—GFS/AVN) provide the profiles for the COSMIC retrievals.

3. Observation Sampling

This study utilizes both GPS RO observations obtained via the GPS missions listed in Table 1 and the hurricane best-track reanalysis (see, [25, 26], Joint Typhoon Warning Center) (HBTRA) data sets during the respective missions.

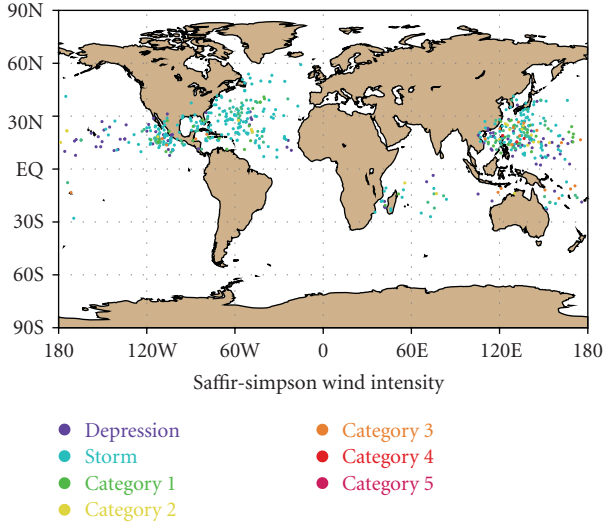


FIGURE 1: GPS RO profiles located within a 600 km radius and ± 180 temporal windows of the HBTRA TC positions for each Saffir-Simpson intensity classification. 741 observations are collected during the 1995–2006 era within the North-Atlantic, Eastern Pacific, Western Pacific, Southern Indian, and Southern Pacific ocean basins while the respective GPS RO missions are active.

The GPS RO observations are retrieved from the COSMIC online database which also provides colocated global analysis and in situ observational profiles for the respective dry- and moist-refractivity profiles. For this study, the moist-refractivity profiles are investigated and compared to the available colocated global analysis and available in situ observation (radio- and dropsonde) profiles. The derivation of the moist-refractivity profile follows the approach of Kursinski et al. [24] discussed above.

The HBTRA contains latitude and longitude positions (at 0.1° horizontal resolution), minimum central sea-level pressure (hPa) and maximum one-minute surface wind speed (kts). If a GPS RO observation is temporally colocated within ± 180 minutes and spatial located within a radial distance of 600-km (relative to the TC position in the HBTRA) it is included in the composite analysis. Since TCs are rarely homogenous in size and in order to account for varying translational speeds, the radial distance value of 600-km is chosen so as not to exclude profiles which may have also occurred within the immediate environment surrounding the respective TC. The 600-km radial distance also corresponds to the standard proxy value which defines a TC's radial region of influence (NOAA/NHC/NWS, 1999). This methodology is applied for each of the previously stated missions (see Table 1) in the North Atlantic, Eastern Pacific, Western Pacific, South Indian, and Southern Pacific ocean basins. Figure 1 illustrates the positions of 741 observations which were collected within TCs of the color-coded Saffir-Simpson wind-speed intensity classification.

The distribution of observations, as functions of both radial distance and elevation, are nonhomogenous as suggested by Figures 2 and 3. As the relative distance from the observation to the TC center decreases (increases),

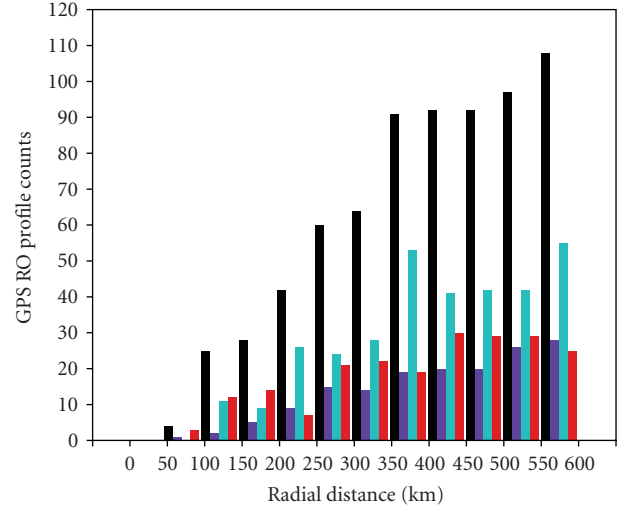


FIGURE 2: Histogram of GPS RO observations collected within depression (purple), tropical storm (cyan), hurricane (red), and all TC (black) environments as a function of radial distance. Radial distance interval is 50 km.

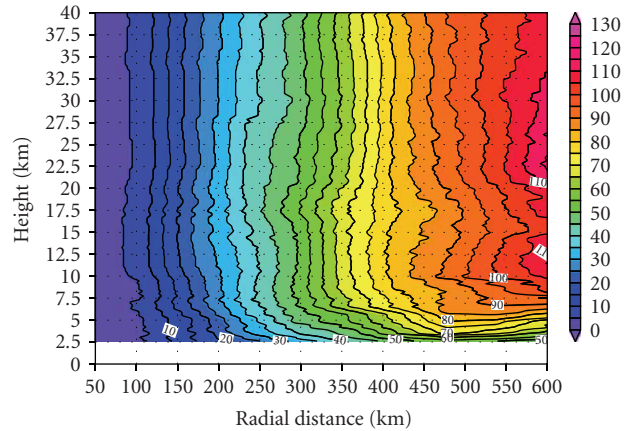


FIGURE 3: Radial cross-section of GPS RO counts for all TCs in different 50 km radial distance bands. Contour interval is 5 observations.

the number of observations also decreases (increases). The number of observations also increases (decreases) as the elevation increases (decreases). There exists a number of plausible explanations for this phenomenon. Among the possibilities is the impact of water vapor (and the associated gradients) as profiles extend deeper through the troposphere. As shown in Figure 1, a large number of observations are collected between 20°S and 20°N . The tropospheric component with the largest variation in the tropics is water vapor [27]. Water vapor gradients can impact the profiles by inducing instances of super-refractivity [Leroy, S.—personal communication] and multipath propagation [Lohmann, M.—personal communication]. Another reason for profile truncation may be the GPS-LEO geometry for the RO occurrences. A dry-refractivity profile may be terminated abruptly if the GPS sets behind the Earth's limb before

reaching a certain depth (distance) into the troposphere. However, determining the precise causes for the vertical depth variances for the collected profiles is not addressed in this study.

The primary assumption made when creating the composite mean structures from the collected observations is of a warm-cored thermodynamic structure. For the extratropical transitioning events (cases typically 40 degrees north and south of the equator), this assumption may not be valid [28–30]. However, as illustrated in Figure 1, a majority of the TCs within which observations are collected occur within the tropics and only some weaker and/or decaying systems persist into the mid-latitudes. It has been shown that weaker TCs and those having undergone extratropical transition may also contain vast asymmetries in their respective thermodynamic fields. These asymmetries, when used to calculate composite means, may result in the creation of features which may appear nonrepresentative of TC thermodynamics. Noting that there remains a large number of observations collected from weaker systems at lower latitudes, we believe the current sample size is large enough to mitigate the profound effects for weak and largely asymmetric systems. Based on Figures 2 and 3, the composite means are calculated from observations collected at radial distances between 200 and 600 km. Although there exists a small sample of observations at radii less than 200 km (as illustrated in Figures 2 and 3), the inner-core composite appear dramatically different from the results of previous studies [1–6] which may be caused by the aforementioned impact of water vapor gradients which are known to occur within the eye-wall and convective rain-bands of TCs. The composite analyses constructed using the observations collected within the 200- to 600-km range correspond more readily with the results from previous studies.

4. Intercomparisons for Observation-Derived Profiles and Colocated Ancillary Profiles

In order to provide a fair inter-comparison, only GPS RO profiles having either a corresponding colocated global analysis or (in situ) radiosonde profile, are considered for the composite mean calculations. This results in 634 and 209 profiles for the global analysis and radiosonde-derived profiles, respectively. The GPS RO observations are defined along a fixed vertical grid, while the global analysis and in situ (henceforth, ancillary) profiles are defined along irregular vertical grids. Therefore the colocated ancillary profiles are interpolated to the same fixed vertical levels of the GPS RO observations. No extrapolation is performed above or below the maximum and minimum elevations for the respective ancillary profiles. The composite radial mean values are calculated for the observations and ancillary profiles assuming a 50-km radial interval. This interval is chosen in order to minimize the number of missing datum values which occur when using a more narrow distance interval while also attempting to mitigate the impact of smoothing which occurs when using more broad intervals. Only those radial mean values calculated from more than 5 observations within the respective interval are maintained in order to mitigate

the effects of erroneous values. These intercomparisons are conducted between the available observations and the derived profiles from the respective colocated ancillary data.

Figure 4 illustrates radial mean comparisons for the composite temperature profiles derived from the GPS RO observations and the corresponding colocated profiles. When comparing the GPS RO retrieved temperature (and moisture) with the global analysis profiles, one expects minimal variance between the respective data sets since the GPS RO moisture profiles are derived using the GPS RO dry-refractivity observations and a 1DVAR assimilation technique to estimate the impact of the characteristics within the atmospheric column nearest to where the respective observation was collected [24]. Inspecting Figures 4(a) and 4(b), we see that this is generally true for the composite temperatures. Figure 4(c) presents the differences between the composite temperatures and colocated global analysis radial mean profiles. The largest values are on the order of 1.5°C and generally concentrated within the lower elevations where the GPS RO retrievals are known to be (negatively) impacted by the lower-troposphere moisture gradients. Figures 4(d) and 4(e) are similar to Figures 4(a) and 4(b), but for GPS RO-derived temperature profiles which have corresponding colocated (in situ) radiosonde temperature profiles. Similar features as those seen in the previous comparison are noted. The large differences near the surface (on the order of 3.5°C), as seen in Figure 4(e), are due to erroneous measurements from a colocated radiosonde.

Figure 5 is similar to Figure 4, except that it illustrates radial mean composite computed from the vapor pressure profiles. We consider only the lowest 10-km of the troposphere due to the lack of appreciable water vapor content at higher elevations. Again, small variances between the GPS RO observations and the colocated global analysis profiles are shown. We note the large number of missing values near the surface in Figure 5(a), due to the aforementioned caveats of the GPS RO retrieval algorithm and subsequent data processing. Figure 5(c) demonstrates that there is general agreement between the observations and analysis, with the greatest difference between the composite observations and analyses is of about 1.6 hPa. This is a result of the contrasting resolutions in the observations and the colocated global analysis profiles used to derive the moisture within the respective atmospheric column. It is noted, however, that the majority of the (larger) differences exist near the surface and within the regions impacted by the water vapor gradient induced multipath propagation and/or super-refractivity.

The relationship between observations and colocated comparison profiles is illustrated in Figure 6. All observation values collected from GPS RO moisture retrievals reside along the x -axis while the respective comparison profiles are along the y -axis. Figure 6(a) compares GPS RO retrieved temperatures (°C) versus colocated global analysis profile temperatures (°C) while Figure 6(b) does the same but for colocated radiosonde temperature profiles. Figures 6(c) and 6(d) are similar, except that they provide an inter-comparison between water vapor pressure (hPa) observations and colocated profiles. There exists a correlation coefficient of 0.997 between the collected GPS RO

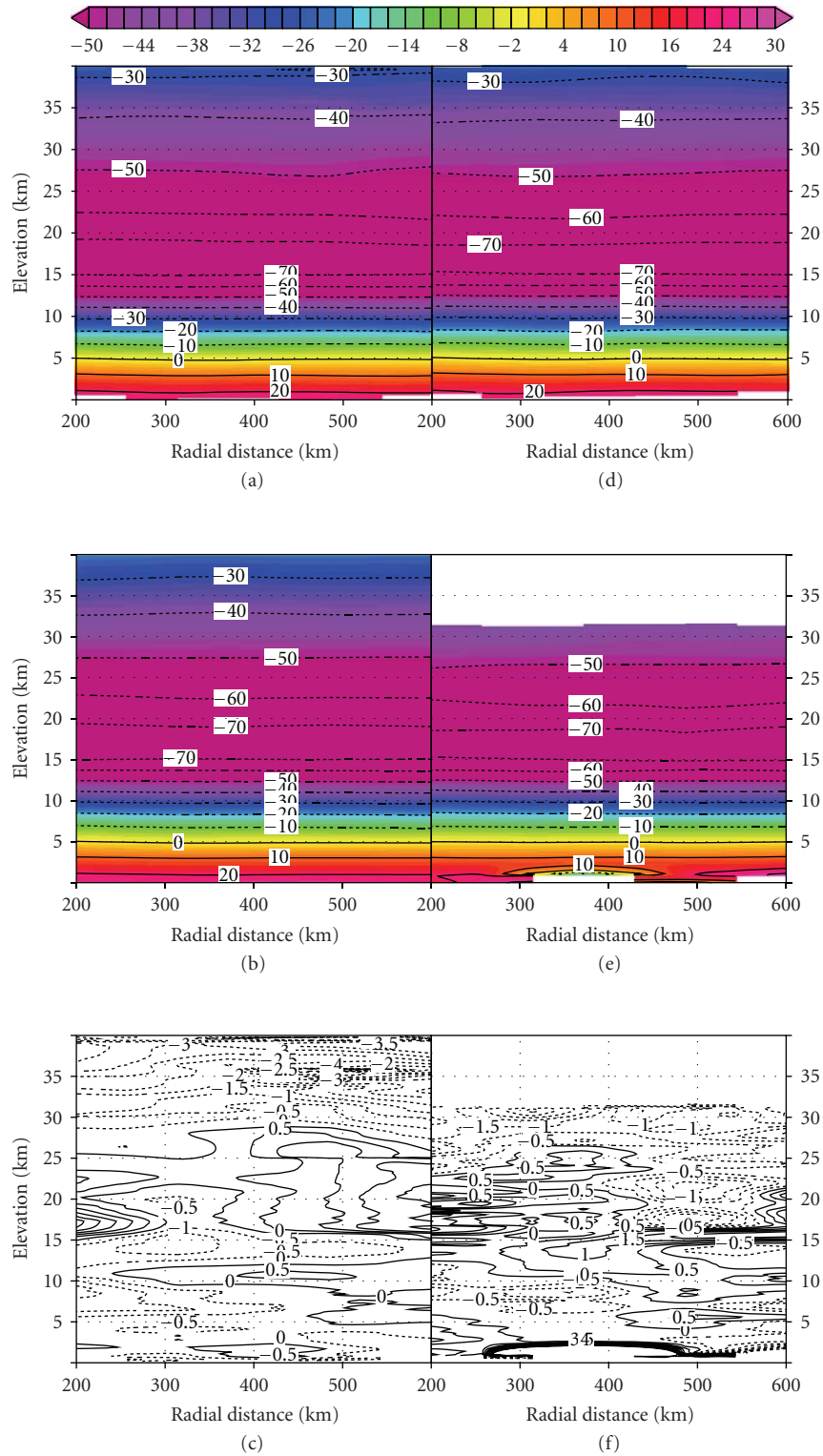


FIGURE 4: Radial mean temperature ($^{\circ}\text{C}$) intercomparisons for observations colocated with both global analysis profiles and radiosondes. The x -axis is radial distance (km) while the y -axis is vertical elevation (km). (a) Radial mean temperatures from GPS RO observations with available colocated global analysis profiles. (b) Radial mean temperatures from colocated global analysis profiles. (c) Radial mean differences between colocated observations and global analysis profiles. (d) Radial mean temperatures from GPS RO observations with available colocated radiosonde observations. (e) Radial mean temperatures from colocated radiosonde observations. (f) Radial mean differences between colocated observations and radiosonde observations. White regions in (a), (b), (d), and (e) represent where either the observations or colocated profiles are missing data.

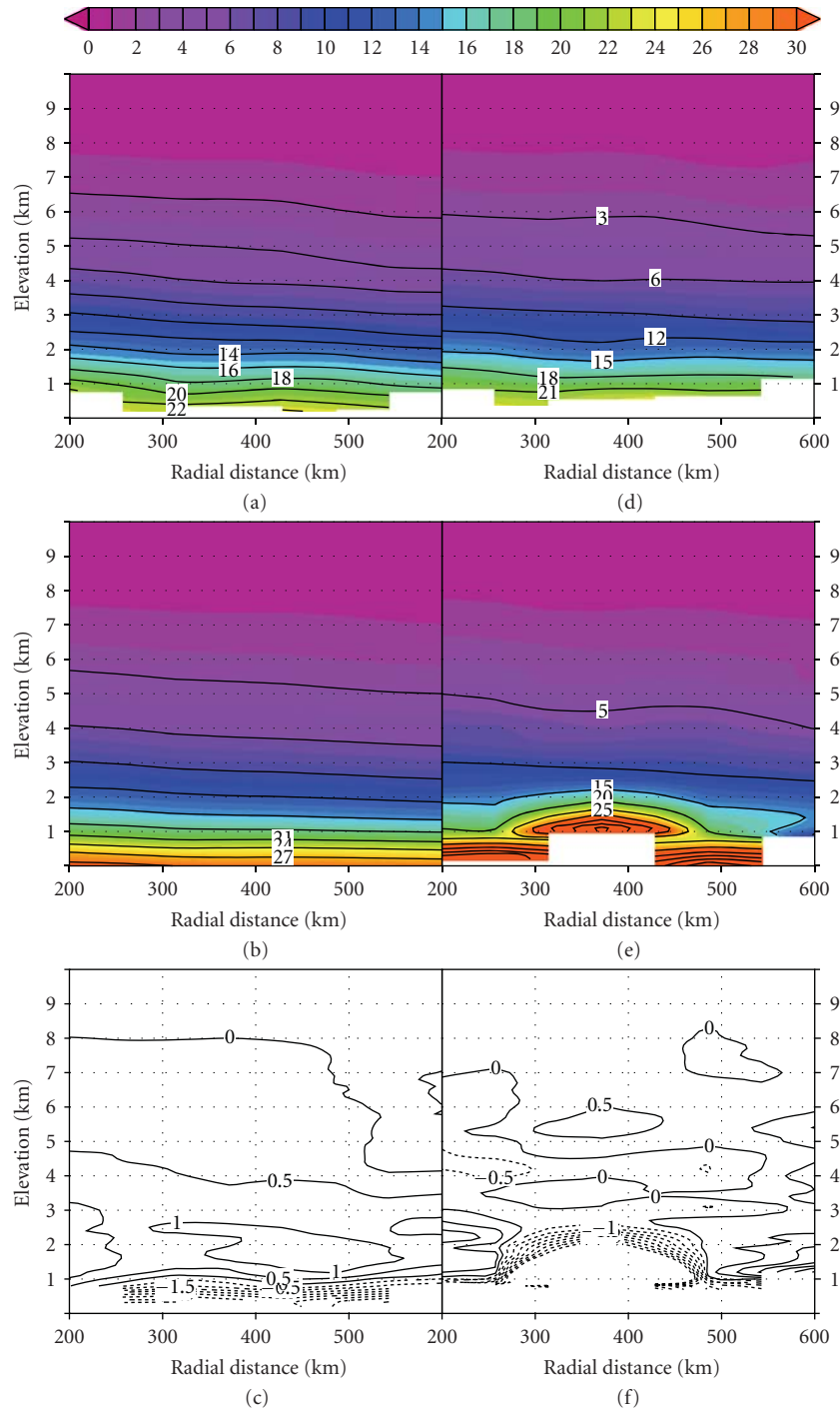


FIGURE 5: Same as Figure 4 except for water vapor pressure (hPa). Elevations from the surface to 10-meters are only considered due the lack of appreciable water vapor in the middle- to upper-troposphere.

observations and the colocated global analysis temperature profiles (Figure 6(a)) while and the inter-comparison of the observations and the radiosondes yields a correlation coefficient of 0.994. The outliers are attributed to errors in the radiosonde observations. Figures 6(c) and 6(d) demonstrate more variability within the water vapor pressure (hPa) fields than within the temperature fields. However,

high correlations still exist. The inter-comparison for the collected observations and the colocated global analysis profiles (Figure 6(c)) correlate to about 0.994 while the inter-comparison between the observations and radiosondes (Figure 6(d)) are correlated at approximately 0.892.

Finally, Figures 7(a) and 7(b), respectively, illustrate the differences for the mean temperature profiles—for each

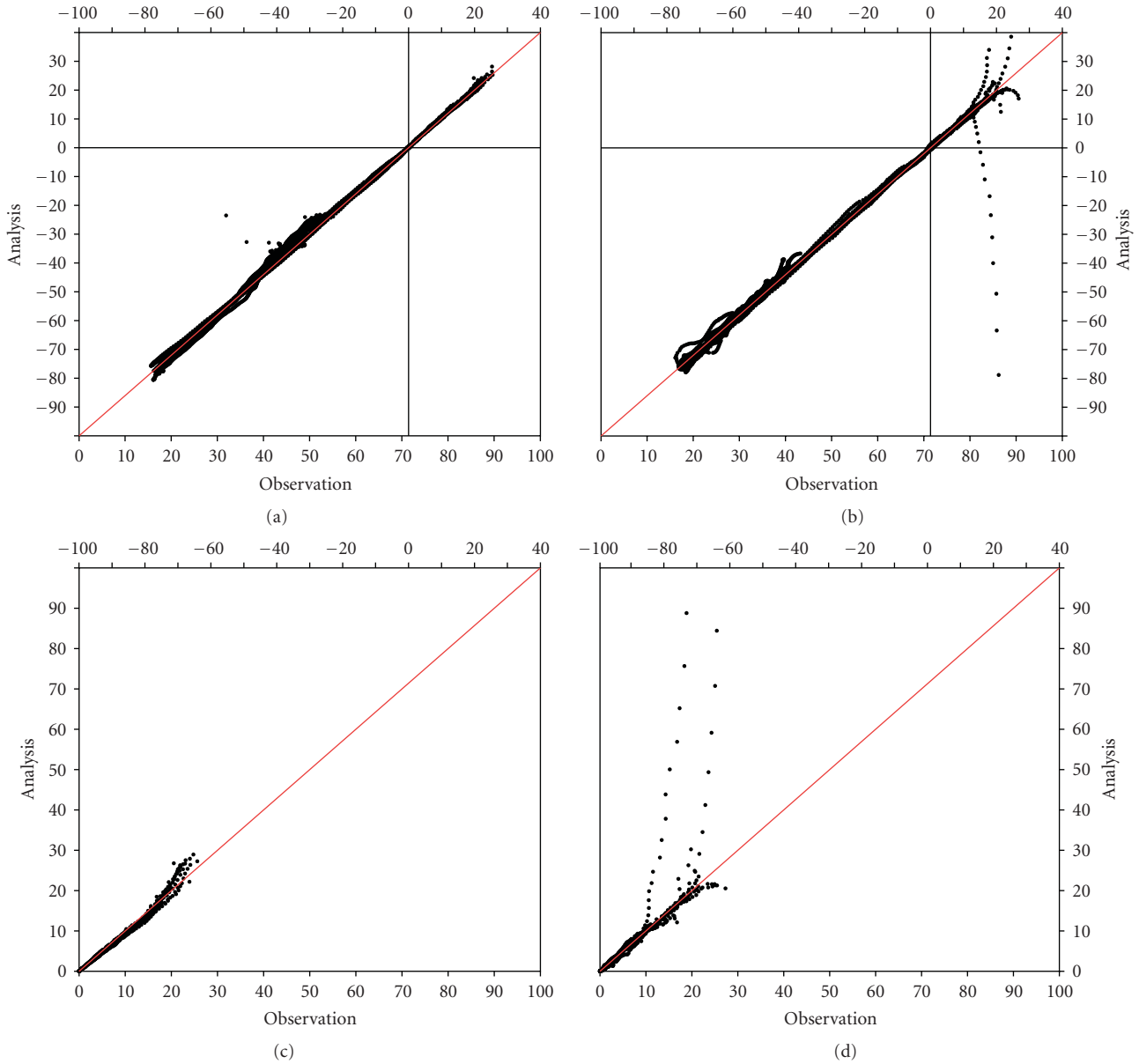


FIGURE 6: Scatter-plot of observations (x -axis) versus colocated global analysis profiles and/or radiosonde observations (y -axis). Red line represents *best-fit* line. (a) Radial mean temperature ($^{\circ}\text{C}$) observations versus radial mean colocated global analysis temperature ($^{\circ}\text{C}$) profiles. (b) Radial mean temperature ($^{\circ}\text{C}$) observations versus radial mean colocated radiosonde observation temperature ($^{\circ}\text{C}$) profiles. (c) Radial mean water vapor pressure (hPa) observations versus radial mean colocated global analysis water vapor pressure profiles, from the surface to 10-km. (d) Radial mean water vapor pressure (hPa) observations versus radial mean colocated radiosonde observation water vapor pressure profiles (hPa).

50-km radial interval, which compare observations to the colocated global analysis profiles and radiosondes. The blue shading indicates that the GPS RO retrieved radial mean temperature along the profile is colder than the colocated analysis (or radiosonde) profile, while the red shading indicates that the observation is warmer. Within the lower 15-km of the troposphere, for each radial interval in Figure 7(a), the GPS RO observation temperature is warmer with exception of the 400-km interval which fluctuates slightly by being

either warmer or cooler at irregular intervals along the profile. The inversion in the respective profiles represents the mean tropopause height within each interval. Above the inversion (near the tropopause), we see that the observation temperatures are generally cooler than the colocated profiles. Above this layer and into the troposphere, the observations suggest a warmer temperature in the stratosphere than do the colocated profiles. The spread of the blue and red shadings increases as a function of increasing elevation. This

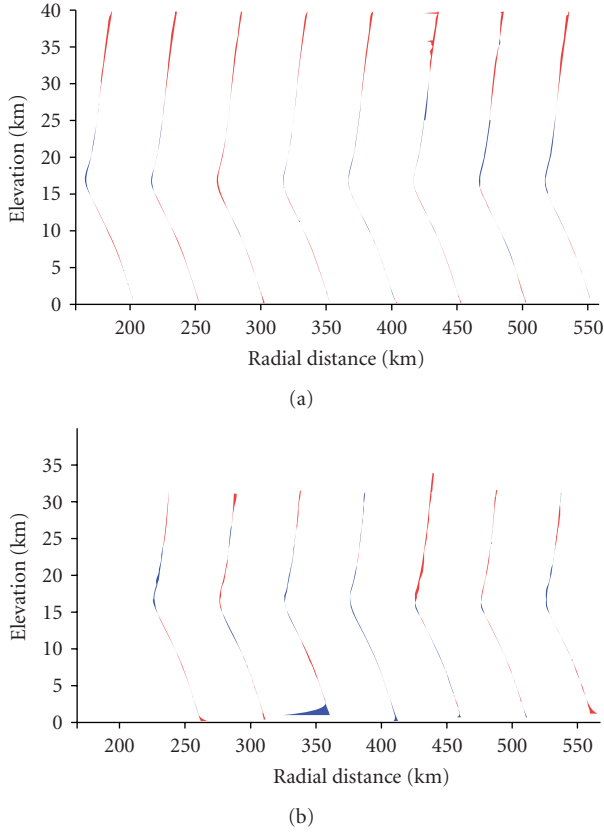


FIGURE 7: Radial-interval mean intercomparisons for GPS RO observations and (a) colocated global analysis, and (b) colocated radiosonde observation temperature ($^{\circ}\text{C}$) profiles. Red shading indicates where radial-interval mean temperature is less than the colocated profiles while the blue shading indicates where the observation temperature is greater than the colocated profiles. The x -axis represents the radial distance (km) the mean profile while the y -axis is vertical elevation (km).

is due to the lack of resolution for the colocated analysis profile resolutions in the upper-troposphere and lower-stratosphere.

Figure 7(b) is similar to Figure 7(a), but for GPS RO observations and colocated radiosonde mean temperature profiles. There are evident spikes which indicate warmer temperatures via the observations (250-km and 550-km) and colder temperatures via the observations (350-km, 400-km, and 450-km). In previous discussions we have noted some mean values from the radiosonde analysis profiles which seemed unrealistic (and possibly in error) which may in-part explain the largely colder observational profile at 350-km. It is also noted that the radiosonde and observations are not colocated exactly in space and time with the observation, but act as verification for selected GPS RO observations. This offset in time and space, can lead to differences which do not necessarily indicate deficiencies for the temperature derived from the GPS RO. This artifact of the collocation offset may become even more pronounced within TCs. Above 5-km, the differences toward a cold or warm bias are small (on the

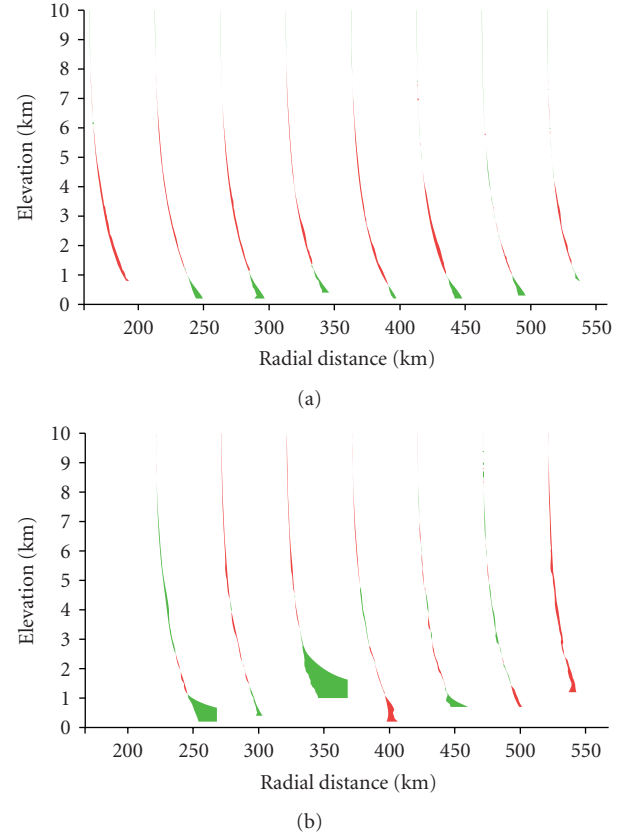


FIGURE 8: Same as Figure 7, but for Radial-interval mean intercomparisons for GPS RO observations and (a) colocated global analysis, and (b) colocated radiosonde water vapor pressure (hPa). Elevations from the surface to 10-km are only considered due the lack of appreciable water vapor in the middle- to upper-troposphere. Red shading indicates where radial-interval mean vapor pressure is less than the colocated profiles while the green shading indicates where the observation vapor pressure is greater than the colocated profiles.

order of 1°C) such that we conclude that observations and the colocated radiosonde derived mean temperature profiles are in satisfactory agreement.

Figures 8(a) and 8(b) provide analyses similar to those in Figures 7(a) and 7(b), except for mean water vapor pressure profiles. The red shading indicates where the GPS RO observations are less than the colocated analysis profiles while the green shading indicates that there exists a larger mean vapor pressure than the colocated profiles. For the colocated GPS RO and analysis profiles (Figure 8(a)), the general trend is that the surface observations indicate a greater water vapor pressure than do the colocated analysis profiles. However, it is noted, once again that as the water vapor gradients increase toward the surface, the information obtained from the respective refractivity profile subject to the impacts of multipath propagation and/or super-refractivity. Thus, the accuracy of these profiles should be scrutinized. The mean profiles within the inner 200- to 450-km indicate that the column contains less water vapor than does the colocated analysis profile by approximately 1- to 2-hPa.

Beyond a radial distance of 450-km, the observations begin to report slightly more water vapor in the column.

Figure 8(b) compares the water vapor pressure mean-profiles from colocated GPS RO observations and radiosondes. We note the large disagreements (larger water vapor pressure content) at 250- and 350-km. The remaining profiles show a general agreement between the observations and analysis with no more than a 2-hPa bias relative to the colocated analysis profile. The increased spread at 550-km is likely attributed to the previously discussed spatial and temporal offsets.

5. Summary and Conclusions

A methodology applied for the collection of 741 GPS RO observations spatially and temporally colocated with TC positions within the HBTRA—from 1995–2006, is employed to assess the quality of GPS RO retrievals collected within TCs. These events often occur in regions known to have large lower-troposphere water vapor gradients and are regions where the GPS RO retrieval algorithm is known to become degraded via multipath propagation and super-refractivity (amongst other effects). In order to understand the impact that these caveats may have on the collected retrievals, available colocated global analysis and in situ radiosonde observation profiles are also collected. Both the global analysis and radiosonde observations provide an inter-comparison, used as a metric to validate the collected observations. It is shown, via the respective intercomparisons, that there exist high correlations between the observations (GPS RO) and analyses (global and radiosonde observations).

Based on the high correlations, it is plausible to suggest that the GPS RO observations—collected within regions, which are often devoid of regular observations—provide a realistic observation of the atmospheric temperature and moisture within the rain-band regions (i.e., 200- to 600-km) of TCs. The composite methodology cannot represent the small scale variability which may be represented by individual profiles collected within specific TC events. Due to the nonuniform distribution (both temporally and spatially) of the observations, collecting a sufficient number of profiles for the purpose of a similar study using a single event is difficult. However, the opportunity exists, pending the continuation of the GPS missions, to collect more observations (in addition to those presented here), to create an even larger composite data set. These unique profiles provide an opportunity to further both the understanding related to the observational and modeling aspects of TC events. These high-resolution thermodynamic observations within the middle- and upper-troposphere of the TC may help to provide additional insights for the current NWP TC initialization methodologies and as a result contribute to the overall understanding related to the existing NWP deficiencies plaguing TC track and intensity forecasts.

References

- [1] H. Riehl and J. S. Malkus, "Some aspects of Hurricane Daisy, 1958," *Tellus*, vol. 13, pp. 181–231, 1961.
- [2] B. I. Miller, "On the momentum and energy balance of Hurricane Helene (1958)," NHRP Rep. 53, NOAA Weather Bureau, Miami Office, Miami, Fla, USA, 1962.
- [3] N. E. LaSeur and H. F. Hawkins, "An analysis of hurricane Cleo (1958) based on data from research reconnaissance aircraft," *Monthly Weather Review*, vol. 91, pp. 694–709, 1963.
- [4] W. M. Gray and D. J. Shea, "The Hurricane's inner core region. II. Thermal stability and dynamic characteristics," *Journal of the Atmospheric Sciences*, vol. 30, pp. 1565–1576, 1973.
- [5] D. J. Shea and W. M. Gray, "The Hurricane's inner core region. I. Symmetric and asymmetric structure," *Journal of the Atmospheric Sciences*, vol. 30, pp. 1544–1564, 1973.
- [6] D. P. Jorgensen, "Mesoscale and convective-scale characteristics of mature hurricanes. Part I: general observations by research aircraft," *Journal of the Atmospheric Sciences*, vol. 41, no. 8, pp. 1268–1285, 1984.
- [7] F. D. Marks and R. A. Houze, "Inner core structure of Hurricane Alicia from airborne Doppler radar observations," *Journal of the Atmospheric Sciences*, vol. 44, pp. 1296–1317, 1987.
- [8] J. L. Franklin, S. J. Lord, and F. D. Marks Jr., "Dropwindsonde and radar observations of the eye of Hurricane Gloria (1985)," *Monthly Weather Review*, vol. 116, no. 5, pp. 1237–1244, 1988.
- [9] J. L. Franklin, S. J. Lord, S. E. Feuer, and F. D. Marks Jr., "The kinematic structure of Hurricane Gloria (1985) determined from nested analyses of dropwindsonde and Doppler radar data," *Monthly Weather Review*, vol. 121, no. 9, pp. 2433–2451, 1993.
- [10] P. D. Reasor, M. T. Montgomery, F. D. Marks Jr., and J. F. Gamache, "Low-wavenumber structure and evolution of the hurricane inner core observed by airborne dual-Doppler radar," *Monthly Weather Review*, vol. 128, no. 6, pp. 1653–1680, 2000.
- [11] A. F. Hasler and K. R. Morris, "Hurricane structure and wind field from stereoscopic and infrared satellite observations and radar data," *Journal of Climate and Applied Meteorology*, vol. 25, no. 6, pp. 709–727, 1986.
- [12] J. Simpson, R. F. Adler, and G. R. North, "A proposed tropical rainfall measuring mission (TRMM) satellite," *Bulletin of the American Meteorological Society*, vol. 69, pp. 278–295, 1988.
- [13] J. B. Halverson, J. Simpson, G. Heymsfield, H. Pierce, T. Hock, and L. Ritchie, "Warm core structure of Hurricane Erin diagnosed from high altitude dropsondes during CAMEX-4," *Journal of the Atmospheric Sciences*, vol. 63, no. 1, pp. 309–324, 2006.
- [14] R. Ware, M. Exner, D. Feng, et al., "GPS sounding of the atmosphere from low earth orbit: preliminary results," *Bulletin of the American Meteorological Society*, vol. 77, no. 1, pp. 19–40, 1996.
- [15] E. R. Kursinski, G. A. Hajj, W. I. Bertiger, et al., "Initial results of radio occultation observations of Earth's atmosphere using the global positioning system," *Science*, vol. 271, no. 5252, pp. 1107–1110, 1996.
- [16] J. Wickert, C. Reigber, G. Beyerle, et al., "Atmosphere sounding by GPS radio occultation: first results from CHAMP," *Geophysical Research Letters*, vol. 28, no. 17, pp. 3263–3266, 2001.
- [17] R. Colomb, C. Alonso, and I. Nollmann, "SAC-C mission and the International AM Constellation for Earth Observation," in *Proceedings of the 3rd IAA Symposium on Small Satellites for Earth Observation*, Berlin, Germany, April 2001.

- [18] W. S. Schreiner, D. C. Hunt, C. Rocken, and S. Sokolovskiy, "Precise GPS data processing for the GPS/MET radio occultation mission at UCAR," in *Proceedings of the National Technical Meeting of the Institute of Navigation*, pp. 103–112, Long Beach, Calif, USA, January 1998.
- [19] C. Alber, R. Ware, C. Rocken, and J. Braun, "Obtaining single path phase delays from GPS double differences," *Geophysical Research Letters*, vol. 27, no. 17, pp. 2661–2664, 2000.
- [20] Y. H. Kuo and S. Businger, "COSMIC—Space based GPS," presented at Kona 20-22, March 2007.
- [21] G. Fjeldbo and V. R. Eshleman, "The atmosphere of mars analyzed by integral inversion of the Mariner IV occultation data," *Planetary and Space Science*, vol. 16, no. 8, pp. 1035–1059, 1968.
- [22] G. Fjeldbo, A. J. Kliore, and V. R. Eshelman, "The neutral atmosphere of Venus studies with the Mariner V radio occultation experiments," *The Astronomical Journal*, vol. 76, no. 2, pp. 123–140, 1971.
- [23] X. Zou, F. Vandenberghe, B. Wang, et al., "A ray-tracing operator and its adjoint for the use of GPS/MET refraction angle measurements," *Journal of Geophysical Research D*, vol. 104, no. 18, pp. 22301–22318, 1999.
- [24] E. R. Kursinski, S. B. Healy, and L. J. Romans, "Initial results of combining GPS occultations with ECMWF global analyses within a 1DVar framework," *Earth, Planets and Space*, vol. 52, no. 11, pp. 885–892, 2000.
- [25] B. R. Jarvinen, C. J. Neumann, and M. A. S. Davis, "A tropical cyclone data tape for the North Atlantic basin, 1886–1983: Contents, limitations, and uses," Tech. Memo. NHC 22, NOAA/National Hurricane Center, Miami, Fla, USA, 1984.
- [26] M. A. S. Davis, G. M. Brown, and P. Leftwich, "A tropical cyclone data tape for the eastern and central North Pacific basins, 1949–1983," Tech. Memo. NHC-25, National Technical Information Service, Springfield, Va, USA, 1984.
- [27] D.-Z. Sun and R. S. Lindzen, "Distribution of tropical tropospheric water vapor," *Journal of the Atmospheric Sciences*, vol. 50, no. 12, pp. 1643–1660, 1993.
- [28] R. E. Hart, "A cyclone phase space derived from thermal wind and thermal asymmetry," *Monthly Weather Review*, vol. 131, no. 4, pp. 585–616, 2003.
- [29] J. L. Evans and R. E. Hart, "Objective indicators of the life cycle evolution of extratropical transition for Atlantic tropical cyclones," *Monthly Weather Review*, vol. 131, no. 5, pp. 909–925, 2003.
- [30] S. C. Jones, P. A. Harr, J. Abraham, et al., "The extratropical transition of tropical cyclones: forecast challenges, current understanding, and future directions," *Weather and Forecasting*, vol. 18, no. 6, pp. 1052–1092, 2003.

Research Article

An Observing System Simulation Experiment (OSSE) to Assess the Impact of Doppler Wind Lidar (DWL) Measurements on the Numerical Simulation of a Tropical Cyclone

Lei Zhang and Zhaoxia Pu

Department of Atmospheric Sciences, University of Utah, 135 S 1460 E, Rm. 819, Salt Lake City, UT 84112, USA

Correspondence should be addressed to Lei Zhang, lsea.zhang@utah.edu

Received 31 December 2009; Revised 1 April 2010; Accepted 10 April 2010

Academic Editor: Song Y. Hong

Copyright © 2010 L. Zhang and Z. Pu. This is an open access article distributed under the Creative Commons Attribution License, which permits unrestricted use, distribution, and reproduction in any medium, provided the original work is properly cited.

The importance of wind observations has been recognized for many years. However, wind observations—especially three-dimensional global wind measurements—are very limited. A satellite-based Doppler Wind Lidar (DWL) is proposed to measure three-dimensional wind profiles using remote sensing techniques. Assimilating these observations into a mesoscale model is expected to improve the performance of the numerical weather prediction (NWP) models. In order to examine the potential impact of the DWL three-dimensional wind profile observations on the numerical simulation and prediction of tropical cyclones, a set of observing simulation system experiments (OSSEs) is performed using the advanced research version of the Weather Research and Forecasting (WRF) model and its three-dimensional variational (3DVAR) data assimilation system. Results indicate that assimilating the DWL wind observations into the mesoscale numerical model has significant potential for improving tropical cyclone track and intensity forecasts.

1. Introduction

Although numerical weather prediction (NWP) models have been improved significantly over the past two decades, the forecast accuracy of high-impact weather events, such as tropical cyclones, is still a challenging problem in practical applications. Since most tropical cyclones occur over tropical oceans, where conventional observations are sparse, large uncertainties are presented in the numerical simulations and predictions due to inaccurate initial conditions. Remote sensing techniques provide an opportunity to observe the atmosphere, especially the atmospheric temperature, moisture, and ozone over the oceans either directly or indirectly. However, among all the variables used to represent the state of the atmosphere, wind measurements are the most limited, although the importance of wind observations for meteorological analysis has been recognized for many years [1–3]. Previous studies indicate that wind information plays an important role in improving the tropical and extratropical cyclone forecasts [4–14]. However, the current global observing system does not provide a uniform distribution of

tropospheric wind measurements, especially in the tropics, southern hemisphere, and northern hemispheric oceans, where conventional observations are very sparse. During the past two decades there have been several satellites measuring wind over the oceans, such as the Geosat altimeter, the National Aeronautics and Space Administration (NASA) Scatterometer (NSCAT), Quick Scatterometer (QuikSCAT), the Special Sensor Microwave Imager (SSM/I), and European Space Agency Remote Sensing Satellites (ERS-1/2). QuikSCAT, which was launched in 1999, can provide ocean surface wind observations. Some previous studies [15, 16] showed that assimilating QuikSCAT ocean surface wind observations had a positive impact on improving the numerical simulation and prediction of tropical cyclones. Other studies also indicated that including SSM/I wind information had the potential to improve low-level wind simulation [15]. Since SSM/I only provides ocean surface wind speed measurements, not wind directions, this makes the viewing of SSM/I winds confusing. NSCAT wind also showed a positive impact on tropical cyclone simulation [10], but NSCAT only provides near-surface wind vectors

over the oceans. Therefore, although wind measurements have been improved to some extent during the past years, the direct three-dimensional global wind profile measurement is still limited. None of the aforementioned satellite instruments directly provides wind profile information in the troposphere.

In recent years, it has been proposed to use Doppler wind lidar (DWL) to measure the three-dimensional wind profiles either globally, with a polar-orbiting satellite [17], or regionally, if mounted on aircraft [18]. The DWL uses a technique similar to that of Doppler radars except that a lidar emits pulses of laser light instead of radio waves [18, 19]. It is able to measure the wind profile from surface to high altitudes (e.g., 18 km) with very high vertical resolution. The objective of this paper is to examine the potential impact of DWL measurements from the polar-orbiting satellite on the numerical simulation and prediction of tropical cyclones.

Generally, the best way to examine the impact of the proposed observations on NWP is to conduct Observing System Simulation Experiments (OSSEs) [20–22]. There are several advantages of OSSEs: such as easy control of the experiments, precise knowledge of the data properties and errors, and knowledge of the truth, and so forth [21]. In this study, the potential impact of the simulated space-based DWL three-dimensional (3-D) wind profile measurements on the numerical simulation and prediction of tropical cyclone formation and intensification is examined by conducting a set of OSSEs using the advanced research version of the weather research and forecasting (WRF) model and its three-dimensional variational (3DVAR) data assimilation system.

The advanced research version of the mesoscale community WRF model and its 3DVAR system are briefly described in Section 2. Details of OSSEs setup are presented in Section 3. The potential impact of assimilating space-based three-dimensional wind profiles on tropical cyclone simulation and prediction based on OSSE results is examined in Section 4. Conclusions and discussions about some practical issues are addressed in Section 5.

2. Numerical Model and Data Assimilation System

2.1. The WRF Model. The advanced research version WRF model (ARW) was developed by the Mesoscale and Microscale Meteorology (MMM) Division of the National Center for Atmospheric Research (NCAR). The ARW is designed to be a flexible, state-of-art atmospheric simulation system. This system is suitable for use in a wide range of applications across scales ranging from meters to thousands of kilometers. It is useful for studies of physical parameterizations, data assimilation, real-time NWP, and so forth. The ARW model is a fully compressible and non-hydrostatic model with a terrain-following vertical coordinate. The horizontal grid system is the Arakawa C-grid. The ARW solver uses the Runge-Kutta 2nd and 3rd order time integration schemes and 2nd and 6th order advection schemes in both horizontal and vertical directions.

A small step time-split scheme is used for acoustic and gravity wave modes. A complete description of the WRF model can be found in the WRF users guide posted on the website: <http://www.mmm.ucar.edu/wrf/users/docs/>. For this study, the version 3.0.1 was used in all experiments.

2.2. The WRF 3DVAR System. The WRF 3DVAR assimilation system is designed to provide optimal initial and boundary conditions to the WRF model by using various observational information sources both from conventional and nonconventional measurements, such as satellite radiance data, radar observations, GPS measurements, and so forth. The WRF 3DVAR is a multivariable data assimilation system. The control variables are the stream function, the unbalanced part of potential velocity, the unbalanced part of temperature, the unbalanced surface pressure, and pseudo relative humidity. The background error correlation is generated using a so-called NMC method [23], which is a popular method for estimating climatological background error covariances. In the NMC method, the background errors are approximated by averaging the statistics of the differences between two sets of the model forecasts (such as 24 hr and 12 hr forecasts) valid at the same time. The observation errors are assumed to be uncorrelated, so the observation error covariance matrix is a diagonal matrix. A detailed description of the 3DVAR system can be found in Barker et al. [24, 25].

3. Experimental Designs

3.1. Case Description. In reality, we do not know the true state of the atmosphere. In order to quantitatively assess the potential impact of the proposed observing systems on the NWP models in OSSEs, we need to simulate an atmosphere status that has the same statistical behavior as that of the real atmosphere. The simulated “true” atmosphere status is the so-called nature run (NR). The accuracy of NR is important to an OSSE because the OSSE results cannot show the realistic observational impact on numerical weather simulation and predictions unless the simulated “true” atmosphere represents most of the characteristics of the real atmosphere.

In order to support community needs in OSSEs, the European Center for Medium-Range Weather Forecasts (ECMWF) produced global nature runs using a spectral prediction model in July 2006 [26]. There are two nature runs with different resolutions: one is at T511 (about 40 km horizontal resolution) spectral truncation with 91 vertical levels and 3-hour frequency output from 1200 UTC May 1 2005 to 0000 UTC June 1 2006. The other one is the higher resolution simulation at T799 (about 25 km horizontal resolution) spectral truncation with 91 vertical levels and hourly output from September 27 2005 to November 1 2005. For simplification, we refer these two global nature runs as T511 NR and T799 NR, respectively. According to the early evaluation by Reale et al. [27], the large-scale structure of the T511 NR is very realistic. In some cases, smaller scale structures in the T511 NR are more realistic than in the

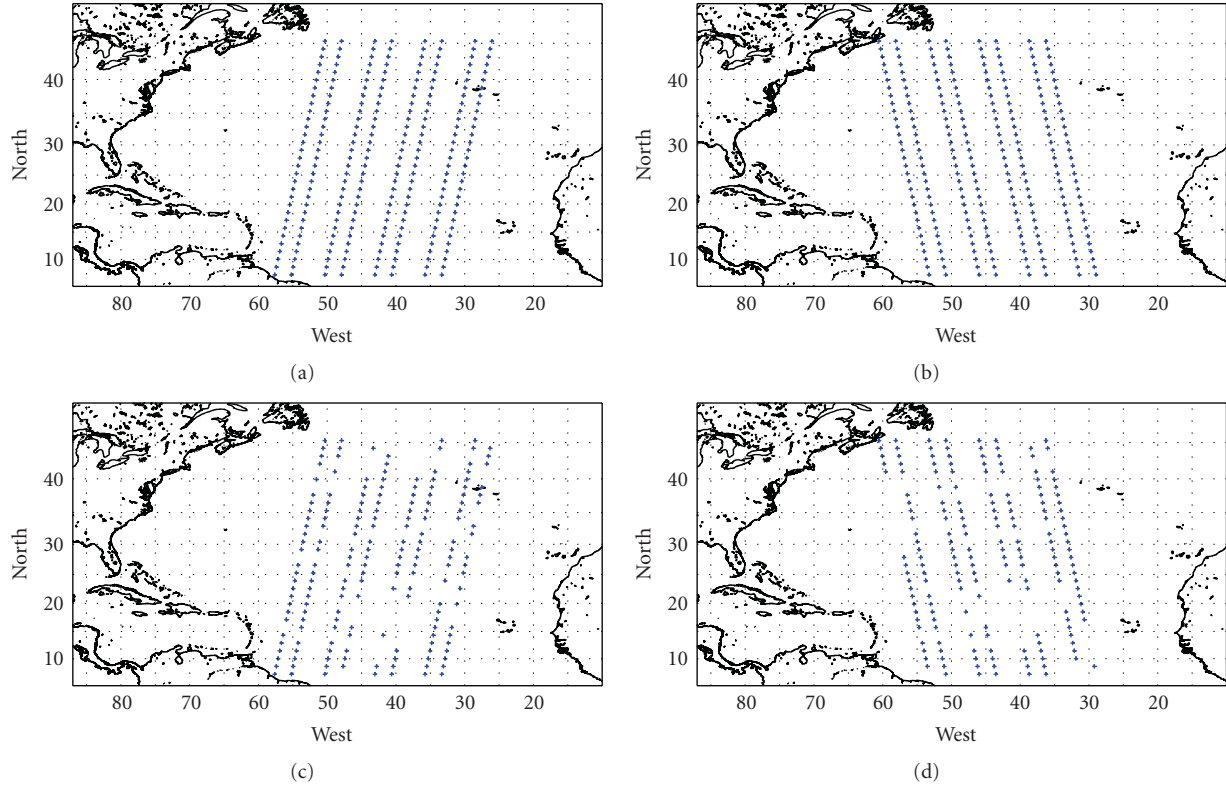


FIGURE 1: Simulated DWL observation locations at 0600 UTC ((a) and (c)) and 1800 UTC 01 October 2005 ((b) and (d)). (a), (b), (c), and (d) are simulated observation sampling for data assimilation Experiment 1 and Experiment 2, respectively.

reanalysis, which is processed by a much lower resolution model.

Since we intend to evaluate the data impact on tropical cyclone forecasts with a mesoscale model, we choose to use the T799 NR. From the T799 NR, a tropical storm, which occurred over the Atlantic Ocean during the period from 27 September to 11 October 2005, was arbitrarily selected for this study. The simulation period is from 0600 UTC 01 to 0600 UTC 03 October 2005.

3.2. Experimental Design. A two-way nested interactive simulation was conducted for all experiments. The model horizontal resolutions were 27 km for outer domain and 9 km for inner domain, respectively. In total there were 31 vertical model levels from the surface up to 50 hPa. Various model physics options were used in the different experiments.

Four experiments were conducted:

- (i) a regional nature run to generate the “truth” field;
- (ii) a control run to generate a reference field;
- (iii) two data assimilation experiments with different observational sampling strategies to investigate the potential impact of the simulated DWL wind profiles on the storm track and intensity forecasts. Results were compared against the regional nature run and control run.

Differences in the model setups and configurations for all above experiments are summarized in Table 1.

3.2.1. Regional Nature Run. In this paper, we mainly focus on the regional numerical model prediction problems. Pu et al. [28] has commented that the ECMWF nature runs are sufficiently accurate in describing the tropical cyclone track and intensity at an intermediate model resolution. However, they are not good enough in representing the tropical cyclone inner-core structures. Thus, it is necessary to generate regional nature runs for regional verification purposes. In this study, the WRF model was nested inside of the ECMWF nature run to generate a set of regional nature runs. The model was initialized using the T799 NR and then integrated forward for 78 hours starting at 0000 UTC 30 September 2005. The domain sizes are 377×259 and 646×583 for the outer and inner domain, respectively. The horizontal grid spacing is 27 km for the outer domain and 9 km for the inner domain, respectively, as mentioned above. The model physics parameterizations include: the Lin microphysics scheme, Mellor-Yamada-Janjic planetary boundary layer model (MYJ), Betts-Miller-Janjic cumulus parameterization scheme, RRTM longwave, and Dudhia shortwave radiation model. Detailed descriptions of each physical parameterization scheme can be found in Skamarock et al. [29].

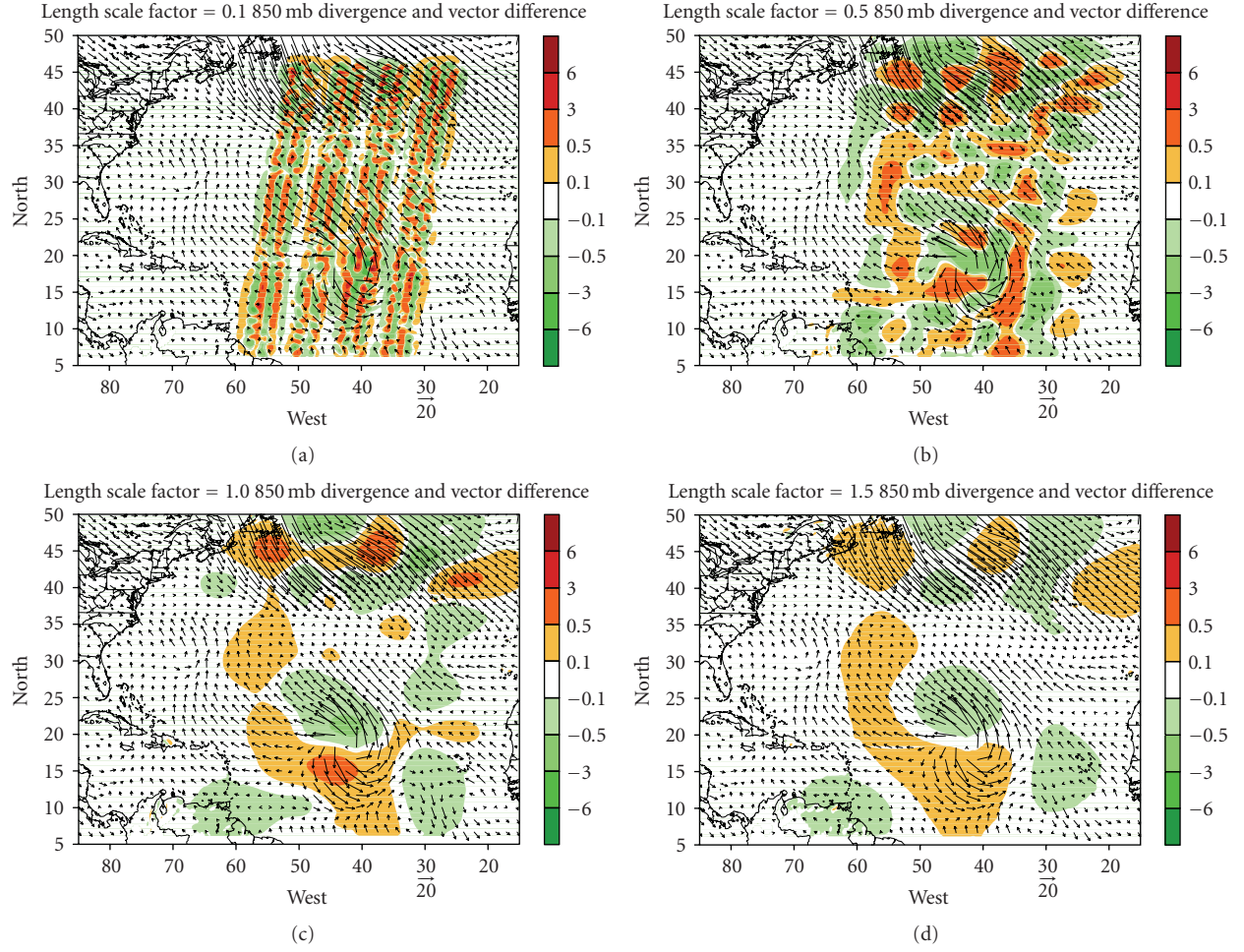


FIGURE 2: Horizontal wind and divergence increments at 850 hPa for length scale factor of 0.1 (a), 0.5 (b), 1.0 (c), and 1.5 (d) at 0600 UTC 01 October 2005.

TABLE 1: Summary of model set up for all experiments.

		Regional nature run	Control run	DA Exp1	DA Exp2
Time period		00Z 30 September	06Z 01 October	06Z 01 October	06Z 01 October
		2005–00 Z 05 October	2005–06Z 03 October	2005–06Z 03 October	2005–06Z 03 October
Size of domain		2005	2005	2005	2005
		377×259	307×217	307×217	307×217
Physics scheme		646×583	406×349	406×349	406×349
	Microphysics scheme	Lin	WSM-6	WSM-6	WSM-6
	PBL scheme	MYJ	YSU	YSU	YSU
	Cumulus scheme	Betts-Miller	Grell	Grell	Grell
Initialization	Initial /first guess fields	T799 NR	T511 NR	T511 NR	T511 NR
	Boundary conditions	T799 NR	T799 NR	T799 NR	T799 NR

3.2.2. Control Run. The control run was a 48-hour free forecast. Unlike the regional nature run, the model integration started at 0600 UTC 01 October 2005, instead of at 0000 UTC 30 September in the regional nature run, and ended at 0600 UTC 03 October 2005. The initial conditions were obtained by interpolating the ECMWF coarser resolution T511 NR into the WRF model domains. The boundary

conditions were provided by the T799 NR. The model domains were set within the domains of the regional nature run but were smaller in size. The domain sizes were 307×217 and 406×349 for the outer and inner domains, respectively. In order to take into account the model errors in OSSEs, model physics options that were deployed in the control run were different from these used in the regional nature

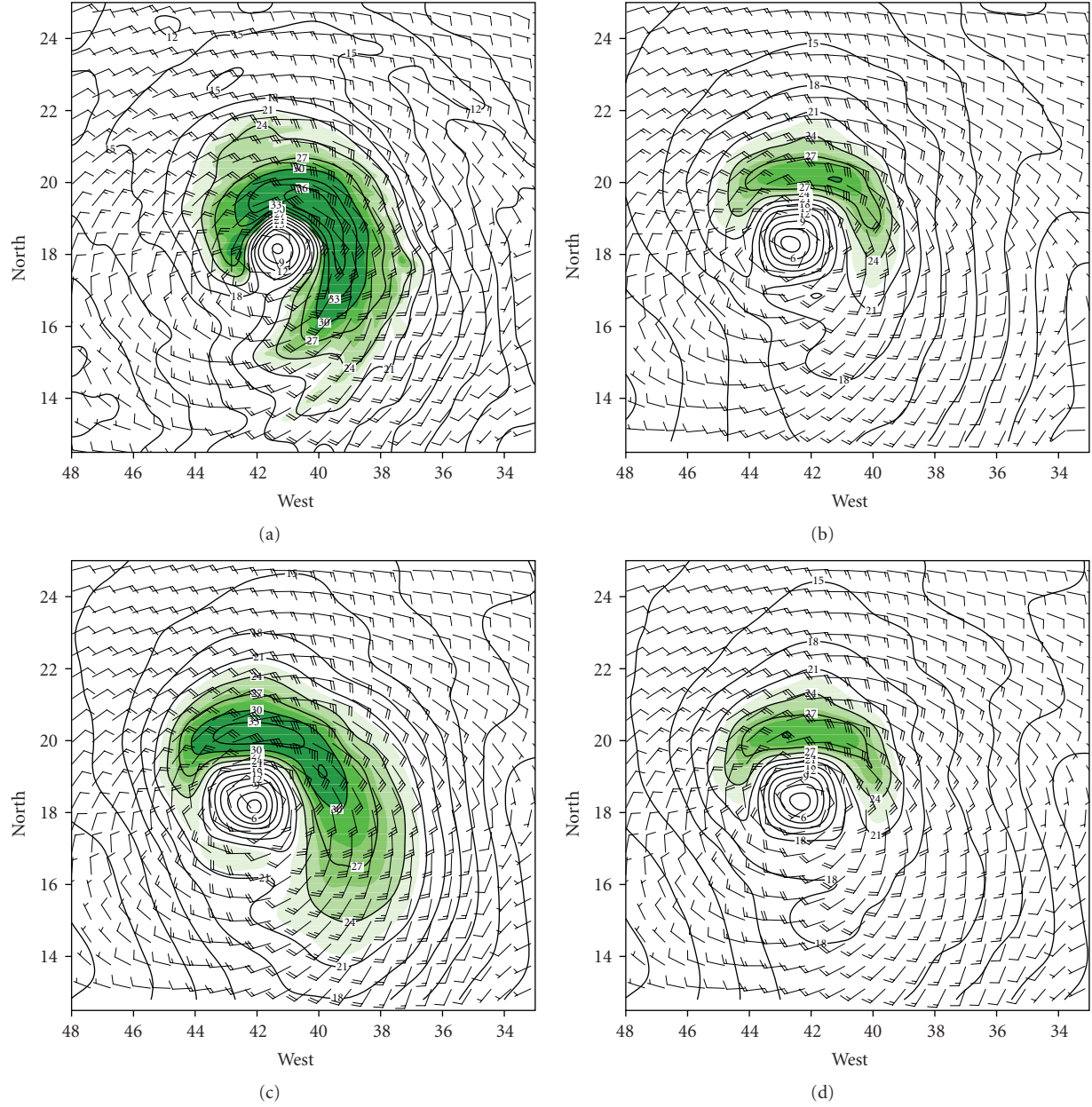


FIGURE 3: Horizontal wind structure (wind speed contour and wind vector) at the storm center at 850 hPa from (a) regional nature run, (b) control run, (c) data assimilation Experiment 1, and (d) data assimilation Experiment 2 at 0600 UTC 01 October 2005. The contour interval of wind speed is 3 m s^{-1} , the areas with wind speed exceeding 20 m s^{-1} are shaded.

run. Thus, the physics options include: the WRF Single-Moment 6-class microphysics scheme (WSM-6), the Yonsei University planetary boundary layer model (YSU PBL), and the Grell-Devenyi ensemble cumulus parameterization scheme. Other parameters are same as in the regional nature run.

3.2.3. Simulation of Observations. According to Marseille et al. [12, 13], the DWL was assumed to be aboard on a given polar-orbiting satellite. This means that the wind measurements are available only twice daily over the same region. An idealized distribution of observations is used

following an early suggestion from D. Emmitt (personal communication). Considering the influence of clouds, two configurations of the observations sampling are simulated. Figures 1(a) and 1(b) show the distributions of the simulated DWL observations in data assimilation Experiment 1 (DA Exp1) at 0600 UTC and 1800 UTC 01 October 2005, respectively. In this observational configuration, cloud effect is not taken into account. Wind observations are available from near the surface up to 18 km. To simulate the DWL sampling in cloudy atmospheres, we used the realistic atmospheric conditions extracted from the regional nature run dataset. Figures 1(c) and 1(d) represent the simulated observation

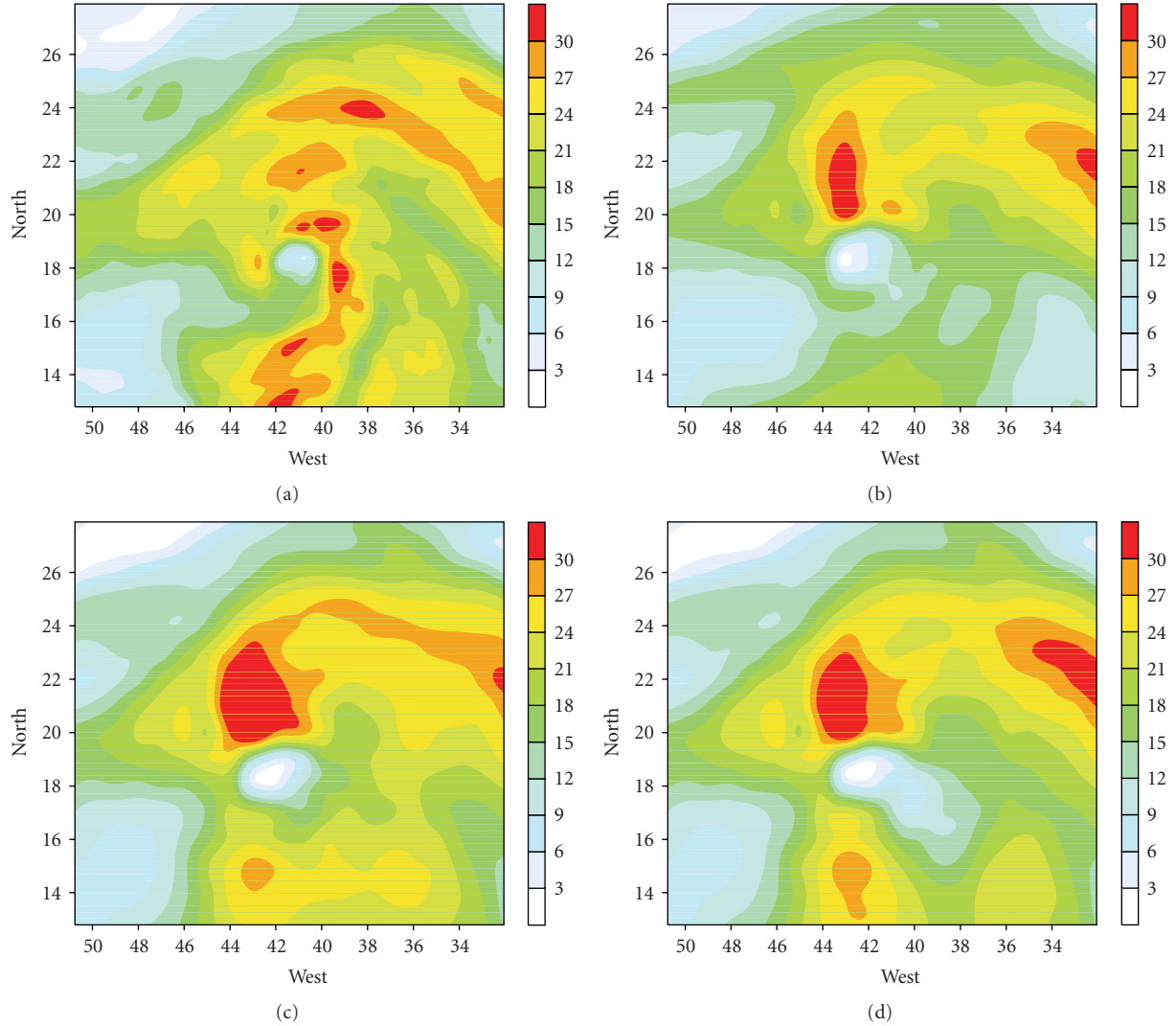


FIGURE 4: The wind shear (units: m s^{-1}) between 850 hPa and 200 hPa at 0600 UTC 01 October 2005 from (a) regional nature run, (b) control run, (c) data assimilation Experiment 1, and (d) data assimilation Experiment 2.

configurations with consideration of the cloud effect and are used in data assimilation Experiment 2 (DA Exp2). Since the cloud effect is taken into account in this case, wind profiles are not available in areas with cloud contamination. In both DA Exp1 and DA Exp2, the observations used for data assimilation experiments are generated by interpolating the “truth” field (regional nature run) both horizontally and vertically from the model grids onto the simulated observational locations and by superimposing random noises. The vertical resolution of the measurements is 250 m below and 1 km above the 2 km level. Typical values for the standard deviation of DWL wind errors are 2 m s^{-1} below 2 km and 3 m s^{-1} above the 2 km level [30]. No bias has been assumed for the simulated DWL wind errors.

3.2.4. Data Assimilation Experiments. The WRF 3DVAR system was used to assimilate DWL wind profiles. Corresponding to the two configurations of the simulated

observations mentioned in Section 3.2.3, two data assimilation experiments are performed: the first is an ideal experiment that does not consider cloud influence. The observational samplings are shown in Figures 1(a) and 1(b) for 0600 UTC and 1800 UTC, respectively. For simplification, in this paper it is referred as DA Exp1. The other one is a more realistic experiment. As shown in Figures 1(c) (for 0600 UTC) and 1(d) (for 1800 UTC), the observations contaminated by clouds are eliminated. For simplification it is referred as DA Exp2. Similar to the control run, the model domain configuration and physics options for both of these two experiments are the same as those used in the control run. The first guess field was initialized at 0600 UTC 01 October 2005 from the T511 NR. A cycled data assimilation was carried out to assimilate simulated DWL wind profiles between 0600 UTC and 1800 UTC 01 October 2005. The data assimilation was conducted between 0600 UTC 01 October 2005 and 1800 UTC 01 October 2005. After that, the model

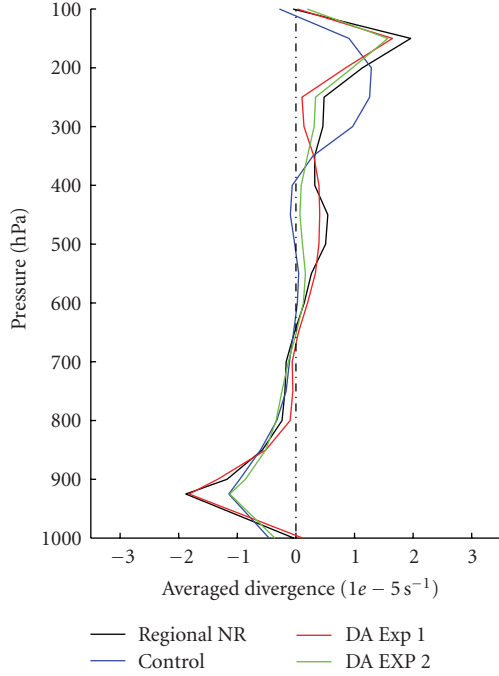


FIGURE 5: Area-averaged divergence vertical profiles over the area with radius of 250 km around the storm center at 0600 UTC 01 October 2005 (black line: regional nature run; blue line: control run; red line: data assimilation Experiment 1; green line: data assimilation Experiment 2).

initial condition was replaced by the analysis from data assimilation experiments and then a 36-hour forecast was conducted from 1800 UTC 01 October to 0600 UTC 03 October 2005. All results presented in this paper use the results from the 9 km grid domain.

4. Results and Discussion

4.1. Sensitivity of DWL Data Assimilation to Background Error Correlations. The basic goal of the 3DVAR is to find an optimal estimate of the model initial conditions at analysis time through the minimization of a cost function J :

$$J = J_b + J_o, \quad (1)$$

$$J_b = \frac{1}{2}(x - x_b)^T \mathbf{B}^{-1}(x - x_b), \quad (2)$$

$$J_o = \frac{1}{2}(H(x) - y_o)^T \mathbf{O}^{-1}(H(x) - y_o). \quad (3)$$

The cost function J is a combination of a background term J_b and an observation term J_o (1). Here J_b is the background term that measures the distance between analysis and background (2), J_o is the observation term that measures the distance between observations and model-simulated observations (3). The superscripts -1 and T denote the inverse and adjoint of a matrix or a linear operator, respectively. \mathbf{B} is the background error covariance matrix. In this study, the \mathbf{B}

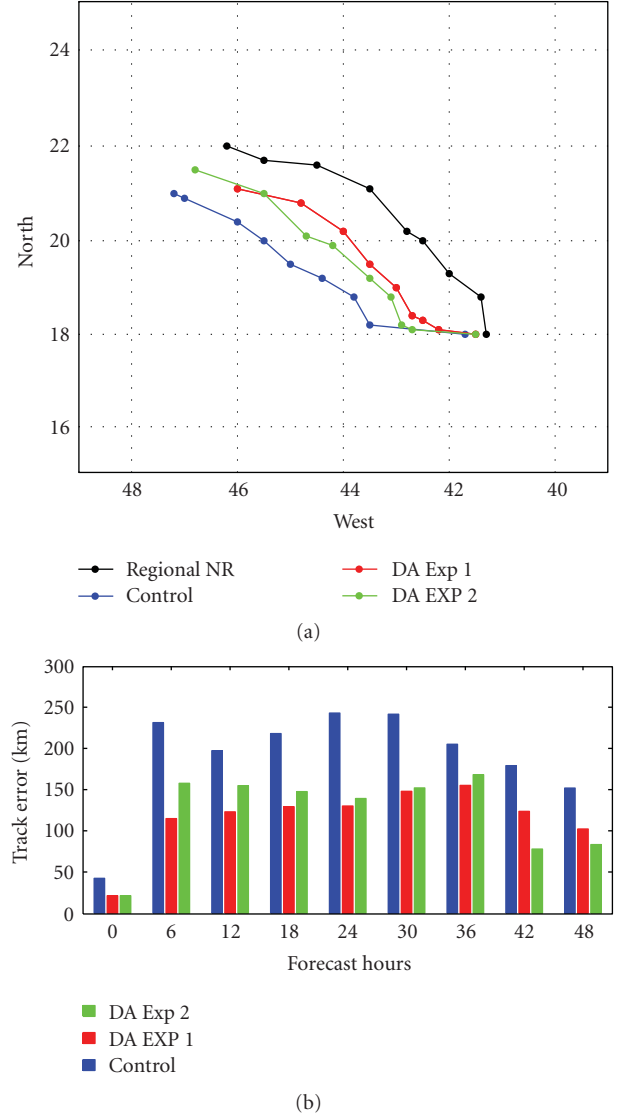


FIGURE 6: Time series of the tropical cyclone (a) track and (b) track error during 48-hour simulations for different experiments (black line: regional nature run; blue line: control run; red line: data assimilation Experiment 1; green line: data assimilation Experiment 2) from 0600 UTC 01 to 0600 UTC 03 October 2005.

matrix was generated using the NMC-method [23], which is a popular method used for background error estimation. \mathbf{O} is the observation error covariance matrix. x_b is the first guess field, usually it is a short-range forecast or from an analysis. H is the observation operator that transforms model variables from model physical space to the observation space. y_o is the observation at the analysis time.

The background error covariance matrix (\mathbf{B} matrix) plays an important role in a 3DVAR system. It influences the analysis fit to observations and also define the influencing distance of the analysis response from the observations. In the horizontal direction, the background error correlations are assumed to be a Gaussian probability density function (4). The observational information is spread using a

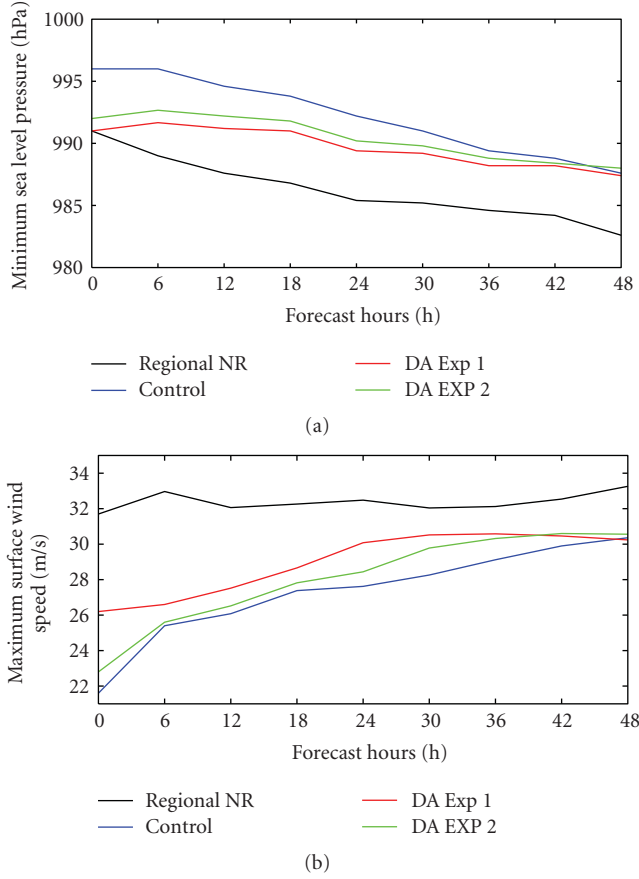


FIGURE 7: Time series of (a) minimum Sea Level Pressure (SLP) at the storm center and (b) maximum surface wind speed from different experiments (black line: regional nature run; blue line: control run; red line: data assimilation Experiment 1; green line: data assimilation Experiment 2) from 0600 UTC 01 to 0600 UTC 03 October 2005.

recursive filter, while the vertical relation is represented by applying the empirical orthogonal decomposition technique:

$$B(r) = B(0) \exp\left(-\frac{r^2}{s^2}\right). \quad (4)$$

In (4), r is the distance between the model grid point and the observation location, s is the length scale of the Gaussian function, and it determines how far the observation information can be spread spatially. $B(0)$ is the background covariance at observation location and $B(r)$ is the background error covariance at the model grid point away from the observation location with distance r .

Since the B matrix is based on climatological statistics, in order to specify it for the DWL data and grid resolution used in this particular study, four experiments were conducted to examine the impact of different length scales on the analysis results of wind fields where the length scales were set to 0.1, 0.5, 1.0, and 1.5 times of the original values (which uses statistics from the NMC method). The data assimilated in

all of these four experiments are the DWL wind profiles from Figure 1(a). Figure 2 shows the horizontal wind vectors and divergence increments (i.e., 3DVAR analysis minus first guess) from these four experiments at 850 hPa at analysis time 0600 UTC 01 October 2005. It shows that the horizontal distributions of the analysis increments from assimilation of DWL data were significantly different among these four experiments. If a small length scale (such as 0.1 times of the original values) was used, the observations only influenced the areas surrounding its locations. This implies that, in this situation, the observation information cannot be used optimally and that areas far away from the observation locations cannot benefit from the observations. If a large length scale (such as 1.5 times of the original values) was employed, although the observation information was spread to the areas far away from the observation locations, the relations were not always realistic for practical applications. Therefore, in practical applications, determining a reasonable horizontal correlation length scale for various kinds of observations, model resolutions, and observation density is still a challengeable question for a 3DVAR method. Comparing the analysis results from all four experiments, a length scale of 1.0 seems to be optimal for the analysis of the DWL data in this study. Therefore, a length scale factor of 1.0 was adapted for all experiments.

4.2. Data Impact on Initial Conditions

4.2.1. Horizontal Wind Structures. Figure 3 shows the horizontal winds at 850 hPa from the regional nature run, the control run, DA Exp1, and DA Exp2 at 0600 UTC 01 October 2005, respectively. In Figure 3, the shaded areas indicate regions with wind speed exceeding 20 m s^{-1} . Compared with the regional nature run simulation, both the control run and data assimilation experiments are able to reproduce the basic structures of the storm wind field. However, the simulated wind speed from the control run was weaker than that from the data assimilation experiments. After data assimilation, a more intensive wind structure was found near the storm center. In DA Exp1, the wind field in the southeast of the storm center was strengthened and the location of the regions with wind speed exceeding 20 m s^{-1} agreed well with the regional nature simulation. The maximum surface wind speed near the storm center reached 26.3 m s^{-1} . This indicates that assimilation of DWL wind profiles enhanced the wind field around storm center. In DA Exp2, the wind field around the storm center was not enhanced as in DA Exp1. This could be mainly attributed to the fact that there are fewer observations available over the storm center in DA Exp2.

4.2.2. Wind Shear. Wind shear, which is the change in wind speed or direction with height in the atmosphere, is one of the most critical factors controlling tropical cyclone formation and destruction [31]. Figure 4 illustrate the wind shear between 850 hPa and 200 hPa at 0600 UTC 01 October 2005 from the regional nature run, the control run, DA Exp1 and DA Exp2, respectively. The wind shear structures

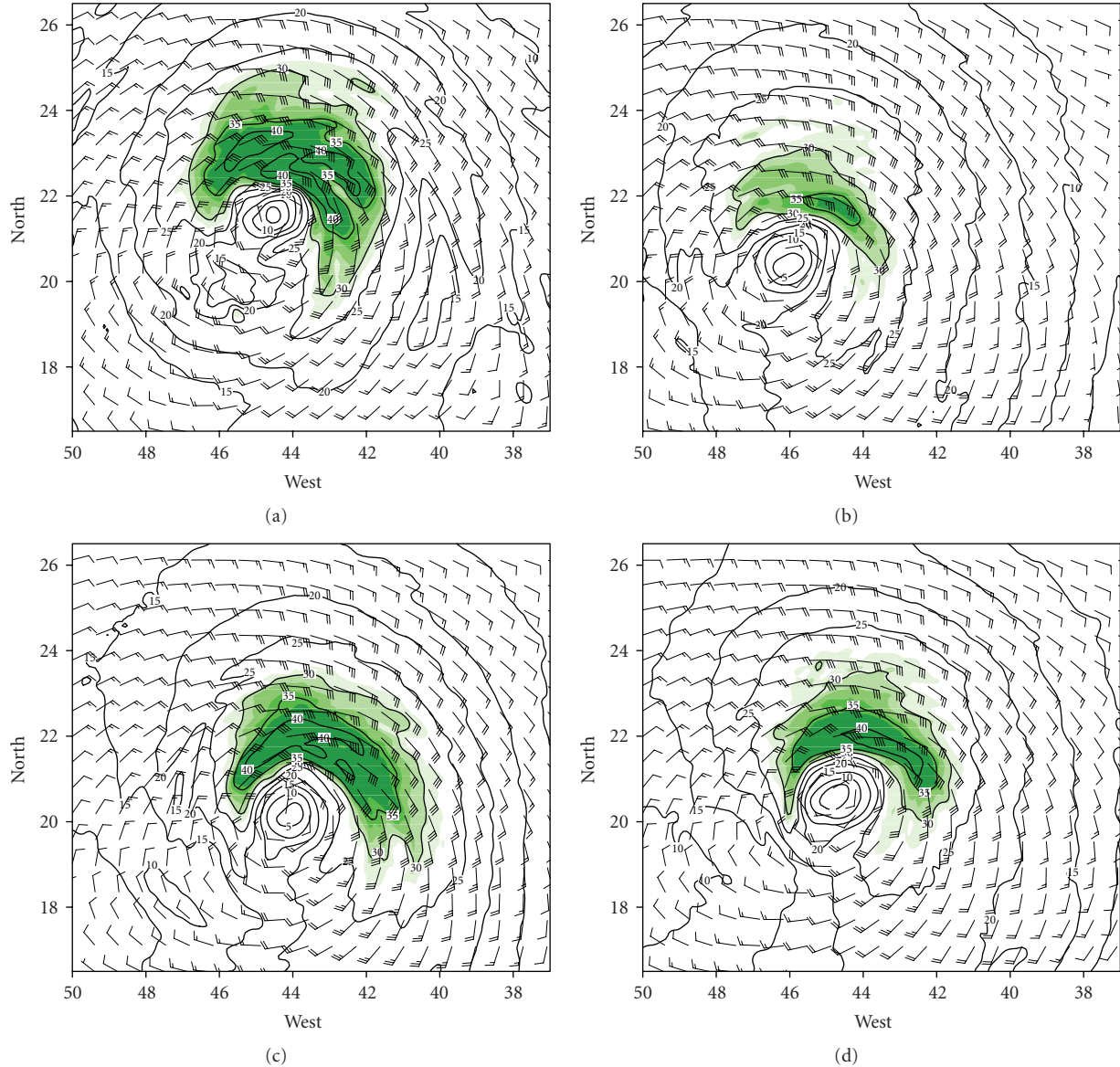


FIGURE 8: Same as Figure 3 but at 1800 UTC 02 October 2005. The contour interval of wind speed is 5 m s^{-1} , the areas with wind speed exceeding 26 m s^{-1} are shaded.

were well reproduced after assimilating DWL wind profiles as simulated structural features was much closer to that of the regional nature run. In both the control run and data assimilation experiments, the simulated maximum wind shear appears in the north of the storm center. It is a little farther to the west compared to the regional nature run. But in the control run, in the south of the storm center the wind shear from the control run was weaker than those from DA Exp1 and DA Exp2. This indicates that assimilation of 3D wind profiles has the potential to adjust the vertical structures of the wind field to some extent. In addition, since the observations over the storm center were available and were assimilated in DA Exp1, the structure of the wind shear around the storm center is much closer to that of the regional nature run, compared with the DA Exp2 analysis results.

4.2.3. Divergence Fields. Figure 5 shows the area-averaged divergence vertical profiles within a radius of 250 km around the storm center for these four experiments at 0600 UTC 01 October 2005. Compared to the results from the data assimilation experiments, in the control run, the divergence variation with height showed a larger difference from the regional nature run simulation. For data assimilation experiments, in DA Exp1, from the surface to 400 hPa, the area-averaged divergence was very close to that of the regional nature run; above 400 hPa, the divergence profile did not keep close to the nature run simulations. But, it kept the same tendency. DA Exp2 did not behave as good as DA Exp1, but it still performed better than the control run. A possible explanation for this is the fact that more observations over the storm center were included in DA Exp1.

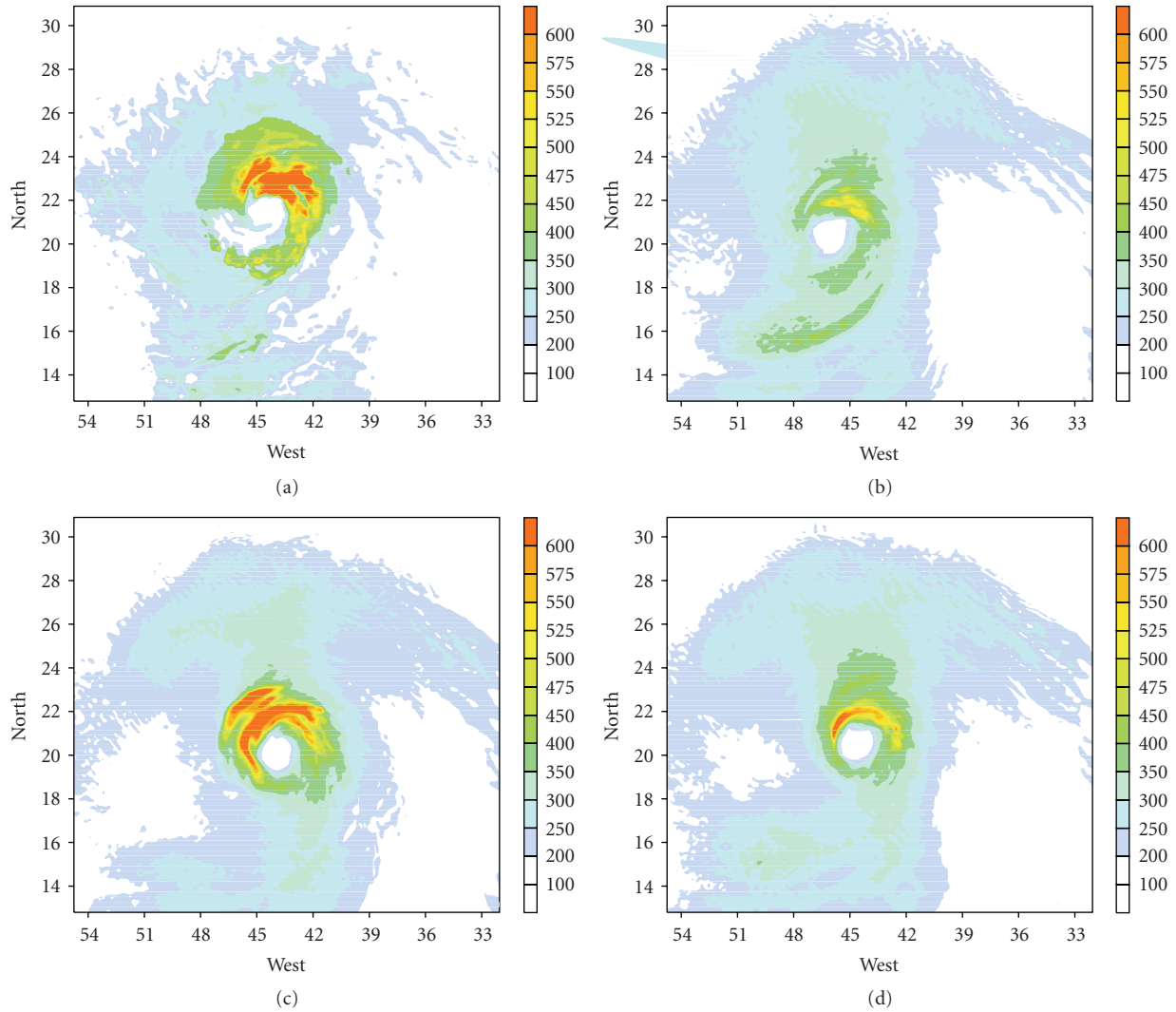


FIGURE 9: The surface latent heat flux (W m^{-1}) from (a) regional nature run, (b) control run, (c) data assimilation Experiment 1, and (d) data assimilation Experiment 2 at 1800 UTC 02 October 2005.

4.3. Impact on Forecasts

4.3.1. Track and Intensity. Figures 6 and 7 show the time evolution of the simulated track and minimum central sea level pressure (SLP) and maximum surface wind speed for different experiments.

From Figure 6, the simulated storm track in the control run was farther to the west and the storm moved slightly quicker compared to the regional nature run. After assimilating the DWL 3D wind profiles, the storm track forecast was improved and the predicted storm track error was reduced compared to the control run. Compared with the results from DA Exp2, the simulated storm track in DA Exp 1 is much closer to the nature run simulations (“truth”) in the first 24-h simulation. The track errors are smaller than those from DA Exp2. The advantages from DA Exp1 can be attributed to including the observations over cloudy areas (most of them over the storm center). After 36

hours simulation, the DA Exp2 performed better in track simulation.

In the regional nature run (“truth”), the minimum central SLP was 991 hPa and steadily dropped to 983 hPa within the first 36-hour simulation. It then deepened slowly during the following 12 hours (Figure 7). Accordingly, the maximum surface wind intensified gradually in the first 36 hours and then increased slowly in the following 12 hours. The simulated minimum central SLP of the storm from the control run showed the same tendency during the 48-hour simulation but it was weaker than that from the regional nature run. The maximum surface wind was also weaker than that from the regional nature run. In DA Exp1, both the minimum SLP and the maximum surface wind were improved significantly during the first 36 hours, and then the improvements decreased slightly over the next 12 hours. In DA Exp2, the storm intensity was also improved after

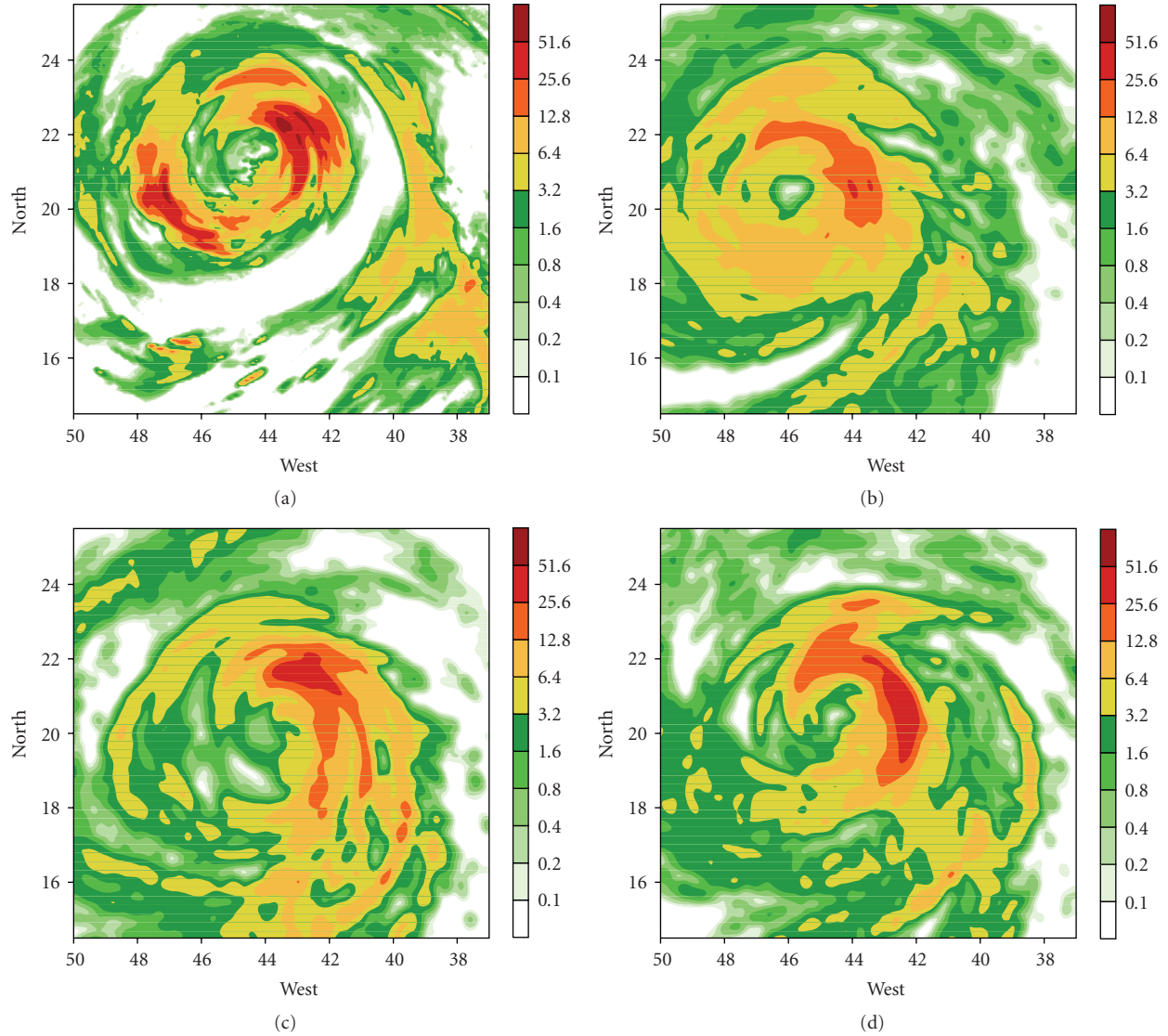


FIGURE 10: The simulated accumulated 3 hours rainfall (mm) from (a) regional nature run, (b) control run, (c) data assimilation Experiment 1, and (d) data assimilation Experiment 2 at 1800 UTC 02 October 2005.

data assimilation, but the improvements were a little weaker compared to that of DA Exp1.

In order to further examine the impact of DWL data on the simulation and prediction of tropical cyclones, diagnoses were also conducted for several other parameters as follows.

4.3.2. Horizontal Wind Structures. As discussed in Section 4.2.1, assimilation of DWL wind profiles enhanced the wind field at the initial time. It also made improvements in the wind simulations during the following forecast period. Figure 8 is the same as Figure 3 but for 1800 UTC 02 October 2005 (36 hours forecast). The shaded areas indicate the regions with wind speed exceeding 26 m s^{-1} . Although both the control run and data assimilation experiments are able to produce the basic structure of the horizontal wind field, the simulated locations of the storm center are different. In the control run, the simulated storm center was farther to the

west compared with the regional nature run simulation. In the data assimilation experiments (DA Exp1 and DA Exp2), the simulated storm centers are much closer to these from the regional nature run. In addition, the simulated wind field in the control run was much weaker than those from the data assimilation experiments. Compared with the regional nature run simulation, the horizontal wind intensity was better represented after data assimilation.

4.3.3. Surface Latent Heat Fluxes. Surface latent heat flux is the flux of heat from the Earth's surface to the atmosphere that is, associated with evaporation or transportation of water from the surface and subsequent condensation of water vapor in the troposphere. The heating at low-levels from the surface can substantially modify the temperature field thereby enhancing or destroying the baroclinic environment. In addition, the latent heat release, derived from

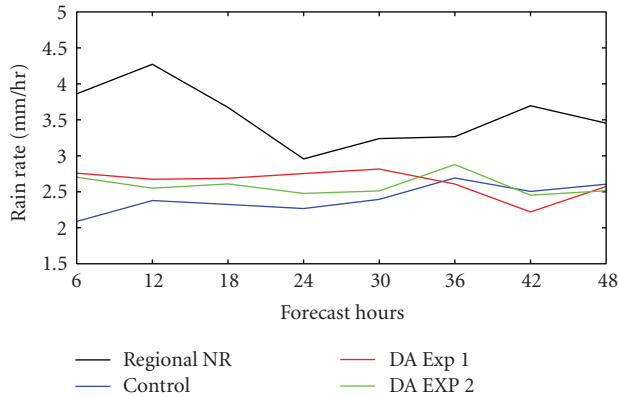


FIGURE 11: The time series of area-averaged rain rate (mm/hr) over the area with radius of 250 km around the storm center between 1200 UTC 01 and 0600 UTC 03 October 2005. (Black line: regional nature run; blue line: control run; red line: data assimilation Experiment 1; green line: data assimilation Experiment 2).

condensation throughout the troposphere can also be a crucial factor determining the vertical extent of the intense deepening of tropical cyclones. The influence of the latent heat flux over oceanic cyclones has been studied in many previous studies [32–36]. It was shown that the latent heat flux plays an important role in hurricane formation and intensification [15]. The study by Papasimakis et al. [37] indicates that hurricane development is heavily related to latent heat release. It was also pointed out that latent heat release had positive impacts on hurricane development and intensification. Figure 9 shows the latent heat flux from these four experiments at 1800 UTC 02 October 2005. In the regional nature run (Figure 9(a)), the maximum latent heat release occurred mainly in the northeast of the storm center, while the simulated latent heat flux was too weak in the control run (Figure 9(b)). The locations of maximum latent heat flux in the data assimilation experiments are farther to the west of these from the regional nature run simulation; but the assimilations of the DWL wind profiles (Figures 9(c) and 9(d)) produced a larger latent heat flux around the storm center that was helpful for storm development. As a result, the wind field was strengthened in the simulations with data assimilation.

4.3.4. Rainfall Simulation. Figure 10 compares the accumulated 3-hour precipitation around the storm center at 1800 UTC 02 October 2005. It shows that the precipitation near the region of 22N and 43W (northeast of the storm center) was well simulated in the experiments with data assimilation (DA Exp 1 and 2), compared to the control run results. Both the simulated quantity and location of the maximum rainfall are similar to the regional nature run. For the control run simulation, the simulated rainfall surrounding the storm center is relatively weak compared to the regional nature run.

To further examine the impact of the assimilation of DWL wind profiles on precipitation forecasts, the area-averaged, storm-induced rainfall rates from different experiments were compared. Figure 11 illustrates the time series

of the rainfall rate averaged in the region within a radius of 250 km from the storm center in different experiments compared with the results from the regional nature run between 1200 UTC 01 and 0600 UTC 03 October 2005. As shown in the figure, both the control run and the data assimilation experiments underestimated the rainfall rate as produced in the regional nature run. However, the data assimilation experiments (DA Exp1 and DA Exp2) improved the rainfall forecasts in the first 36 hours, although they did not perform well in the last 12 hours of the simulations.

5. Summary and Discussions

The potential impact of simulated Doppler Wind Lidar (DWL) wind profiles on the numerical simulation and prediction of tropical cyclones has been investigated using the WRF model and its 3DVAR data assimilation system by means of Observing System Simulation Experiments (OSSEs). Results indicated that, for this particular case, the assimilation of DWL wind profiles had the potential to improve both the horizontal and vertical wind structures and hence we could simulate stronger wind circulation. The simulated storm track and intensity were also improved after assimilation of DWL wind profiles during the 48-hour simulation. Results from the two data assimilation experiments with different observation sampling strategies have shown that assimilating the wind observations around the storm center is useful for improving storm track and intensity simulations.

Future studies will be performed to evaluate the DWL wind observation impact with different sampling strategies, such as different horizontal and vertical resolutions of the measurements. A more comprehensive evaluation of the impacts of the DWL data on operational tropical cyclone forecasts will also be assessed using operational models and integrating the DWL data with all other conventional and satellite data available.

Acknowledgments

The computer time for this study was provided by NASA High-End Computing System and the Center for High Performance Computing (CHPC) at the University of Utah. Authors are grateful to Drs. Lars Peter Riishojgaard and Michiko Masutani for providing ECMWF nature run data through a joint OSSE effort. The second author would like to thank Drs. G. David Emmitt, Bruce Gentry and Robert Atlas for useful discussion. This study is supported by NASA Grant no. NNX08AH88G.

References

- [1] W. E. Baker, G. D. Emmitt, F. Robertson, et al., "Lidar-measured winds from space: a key component for weather and climate prediction," *Bulletin of the American Meteorological Society*, vol. 76, no. 6, pp. 869–888, 1995.
- [2] W. A. Lahoz, R. Brugge, D. R. Jackson, et al., "An observing system simulation experiment to evaluate the scientific merit of wind and ozone measurements from the future SWIFT

- instrument,” *Quarterly Journal of the Royal Meteorological Society*, vol. 131, no. 606, pp. 503–523, 2005.
- [3] A. Stoffelen, J. Pailleux, E. Källén, et al., “The atmospheric dynamics mission for global wind field measurement,” *Bulletin of the American Meteorological Society*, vol. 86, no. 1, pp. 73–87, 2005.
 - [4] C. S. Velden, T. L. Olander, and S. Wanzong, “The impact of multispectral GOES-8 wind information on Atlantic tropical cyclone track forecasts in 1995. Part I: dataset methodology, description, and case analysis,” *Monthly Weather Review*, vol. 126, no. 5, pp. 1202–1218, 1998.
 - [5] J. S. Goerss, C. S. Velden, and J. D. Hawkins, “The impact of multispectral GOES-8 wind information on Atlantic tropical cyclone track forecasts in 1995. Part II: NOGAPS forecasts,” *Monthly Weather Review*, vol. 126, no. 5, pp. 1219–1227, 1998.
 - [6] I. Szunyogh, Z. Toth, R. E. Morss, S. J. Majumdar, B. J. Etherton, and C. H. Bishop, “The effect of targeted dropsonde observations during the 1999 Winter Storm Reconnaissance Program,” *Monthly Weather Review*, vol. 128, no. 10, pp. 3520–3537, 2000.
 - [7] P. M. Boorman, R. Swinbank, and D. A. Ortland, “Assimilation of directly measured stratospheric winds into the Unified Model,” Forecasting Research Technical Report 332, Met Office, 2000.
 - [8] L. Isaksen and A. Stoffelen, “ERS scatterometer wind data impact on ECMWF’s tropical cyclone forecasts,” *IEEE Transactions on Geoscience and Remote Sensing*, vol. 38, no. 4, pp. 1885–1892, 2000.
 - [9] L. Isaksen and P. A. E. M. Janssen, “Impact of ERS scatterometer winds in ECMWF’s assimilation system,” *Quarterly Journal of the Royal Meteorological Society*, vol. 130, no. 600, pp. 1793–1814, 2004.
 - [10] S. M. Leidner, L. Isaksen, and R. N. Hoffman, “Impact of NSCAT winds on tropical cyclones in the ECMWF 4DVAR assimilation system,” *Monthly Weather Review*, vol. 131, no. 1, pp. 3–26, 2003.
 - [11] N. Žagar, “Assimilation of equatorial waves by line-of-sight wind observations,” *Journal of the Atmospheric Sciences*, vol. 61, no. 15, pp. 1877–1893, 2004.
 - [12] G. J. Marseille and A. Stoffelen, “Simulation of wind profiles from a space-borne Doppler wind lidar,” *Quarterly Journal of the Royal Meteorological Society*, vol. 129, no. 594, pp. 3079–3098, 2003.
 - [13] G.-J. Marseille, A. D. Stoffelen, and J. A. N. Barkmeijer, “Impact assessment of prospective spaceborne Doppler wind lidar observation scenarios,” *Tellus A*, vol. 60, no. 2, pp. 234–248, 2008.
 - [14] G.-J. Marseille, A. D. Stoffelen, and J. Barkmeijer, “A cycled sensitivity observing system experiment on simulated Doppler wind lidar data during the 1999 Christmas storm ‘Martin’,” *Tellus A*, vol. 60, no. 2, pp. 249–260, 2008.
 - [15] S.-H. Chen, “The impact of assimilating SSM/I and QuikSCAT satellite winds on Hurricane Isidore simulations,” *Monthly Weather Review*, vol. 135, no. 2, pp. 549–566, 2007.
 - [16] Z. Pu, X. Li, C. Velden, S. Abernson, and W. T. Liu, “Impact of aircraft dropsonde and satellite wind data on the numerical simulation of two landfalling tropical storms during TCSP,” *Weather and Forecasting*, vol. 23, pp. 62–79, 2008.
 - [17] D. G. H. Tan and E. Andersson, “Simulation of the yield and accuracy of wind profile measurements from the Atmospheric Dynamics Mission (ADM-Aeolus),” *Quarterly Journal of the Royal Meteorological Society*, vol. 131, no. 608, pp. 1737–1757, 2005.
 - [18] M. Weissmann and C. Cardinali, “Impact of airborne Doppler lidar observations on ECMWF forecasts,” *Quarterly Journal of the Royal Meteorological Society*, vol. 133, no. 622, pp. 107–116, 2007.
 - [19] C. J. Grund, R. M. Banta, J. L. George, et al., “High-resolution doppler lidar for boundary layer and cloud research,” *Journal of Atmospheric and Oceanic Technology*, vol. 18, no. 3, pp. 376–393, 2001.
 - [20] C. P. Arnold Jr. and C. H. Dey, “Observing-systems simulation experiments: past, present and future,” *Bulletin of the American Meteorological Society*, vol. 67, no. 6, pp. 687–695, 1986.
 - [21] R. M. Atlas, “Observing system simulation experiments: methodology, examples and limitations,” in *CGC/WMO Workshop*, Geneva, Switzerland, April 1997, WMO TD No. 868.
 - [22] S. J. Lord, E. Kalnay, R. Daley, G. D. Emmitt, and R. Atlas, “Using OSSEs in the design of future generation integrated observing systems,” in *Proceedings of the 1st Symposium on Integrated Observing Systems*, pp. 45–47, AMS, Long Beach, Calif, USA, 1997, preprints.
 - [23] D. F. Parrish and J. C. Derber, “The National Meteorological Center’s spectral statistical-interpolation analysis system,” *Monthly Weather Review*, vol. 120, no. 8, pp. 1747–1763, 1992.
 - [24] D. M. Barker, W. Huang, Y.-R. Guo, A. J. Bourgeois, and Q. N. Xiao, “A three-dimensional variational data assimilation system for MM5: implementation and initial results,” *Monthly Weather Review*, vol. 132, no. 4, pp. 897–914, 2004.
 - [25] D. M. Barker, M. S. Lee, Y.-R. Guo, W. Huang, Q.-N. Xiao, and R. Rizvi, “WRF variational data assimilation development at NCAR,” in *Proceedings of the 5th WRF/14th MM5 Users’ Workshop*, p. 5, NCAR, Boulder, Colo, USA, 2004.
 - [26] M. Masutani, J. S. Woollen, S. J. Lord, et al., “Observing system simulation experiments at the National Centers for Environmental Prediction,” *Journal of Geophysical Research D*, vol. 115, no. 7, Article ID D07101, 2010.
 - [27] O. Reale, J. Terry, M. Masutani, E. Andersson, L. P. Riishojgaard, and J. C. Jusem, “Preliminary evaluation of the European Centre for Medium-Range Weather Forecasts’ (ECMWF) Nature Run over the tropical Atlantic and African monsoon region,” *Geophysical Research Letters*, vol. 34, no. 22, Article ID L22810, 6 pages, 2007.
 - [28] Z. Pu, L. Zhang, B. Gentry, and B. Demoz, “Potential impact of lidar wind measurements on high-impact weather forecasting: a regional OSSEs study,” in *Proceedings of the 13th AMS Conference on Integrated Observing Systems for Atmosphere, Ocean, and Land Surface (IOAS-AOLS ’09)*, Phoenix, Ariz, USA, January 2009.
 - [29] W. C. Skamarock, J. B. Klemp, J. Dudhia, et al., “A description of the advanced research WRF version 2,” NCAR Technical Note NCAR/TN-468+STR, NCAR, Boulder, Colo, USA, 2005.
 - [30] W. Baker, “Concept for a US space-based wind lidar: status and current activities,” in *Joint Center for Satellite Data Assimilation (JCSDA) Seminar*, July 2009.
 - [31] W. M. Frank and E. A. Ritchie, “Effects of vertical wind shear on the intensity and structure of numerically simulated hurricanes,” *Monthly Weather Review*, vol. 129, no. 9, pp. 2249–2269, 2001.
 - [32] W. A. Nuss and R. A. Anthes, “A numerical investigation of low-level processes in rapid cyclogenesis,” *Monthly Weather Review*, vol. 115, pp. 2728–2743, 1987.
 - [33] E. Rogers and L. F. Bosart, “A diagnostic study of two intense oceanic cyclones,” *Monthly Weather Review*, vol. 119, no. 4, pp. 965–996, 1991.

- [34] G. H. Crescenti and R. A. Weller, "Analysis of surface fluxes in the marine atmospheric boundary layer in the vicinity of rapidly intensifying cyclones," *Journal of Applied Meteorology*, vol. 31, no. 8, pp. 831–848, 1992.
- [35] P. J. Neiman and M. A. Shapiro, "The life cycle of an extratropical marine cyclone. Part I: frontal-cyclone evolution and thermodynamic air-sea interaction," *Monthly Weather Review*, vol. 121, no. 8, pp. 2153–2176, 1993.
- [36] D.-L. Zhang, E. Radeva, and J. Gyakum, "A family of frontal cyclones over the western Atlantic Ocean. Part II: parameter studies," *Monthly Weather Review*, vol. 127, no. 8, pp. 1745–1760, 1999.
- [37] N. Papasimakis, G. Cervone, F. Pallikari, and M. Kafatos, "Multifractal character of surface latent heat flux," *Physics A*, vol. 372, no. 2, pp. 703–718, 2006.

Research Article

Impacts of Oceanic Preexisting Conditions on Predictions of Typhoon Hai-Tang in 2005

Akiyoshi Wada and Norihisa Usui

Meteorological Research Institute, 1-1 Nagamine, Tsukuba, Ibaraki 305-0052, Japan

Correspondence should be addressed to Akiyoshi Wada, awada@mri-jma.go.jp

Received 31 December 2009; Revised 13 April 2010; Accepted 27 May 2010

Academic Editor: Zhaoxia Pu

Copyright © 2010 A. Wada and N. Usui. This is an open access article distributed under the Creative Commons Attribution License, which permits unrestricted use, distribution, and reproduction in any medium, provided the original work is properly cited.

We investigated the impact of variations in oceanic preexisting conditions on predictions of Typhoon Hai-Tang (2005) by using a coupled atmosphere-ocean model with 6-km horizontal resolution and providing the oceanic initial conditions on 12 July from 1997 to 2005 to the model. Variations in oceanic preexisting conditions caused variation in predicted central pressure of nearly 18 hPa at 72 h, whereas sea-surface cooling (SSC) induced by Hai-Tang caused a predicted central pressure difference of about 40 hPa. Warm-core oceanic eddies up to a few hundred kilometers across and a deep mixed layer climatologically distributed in the western North Pacific led to high mixed-layer heat potential, which increased latent heat flux, water vapor, and liquid water contents around Hai-Tang's center. These increases were closely associated with Hai-Tang's intensification. SSC negatively affected the eyewall, whereas variations in oceanic preexisting conditions remarkably affected spiral rainbands and the magnitude of SSC.

1. Introduction

Advances in ocean data assimilation systems have enabled us to further understand tropical cyclone (TC) activity and the ocean response at weather-forecasting as well as seasonal to climate time scales. The relationships between TC activity and variations in the global ocean are of growing interest on seasonal to climate time scales. In contrast, TC-induced sea-surface cooling (SSC), the decrease in sea-surface temperature (SST) during and after the passage of a TC in general, is a well-known ocean response to a TC on a weather-forecasting scale. Previous studies reported that SSC varied depending on oceanic preexisting conditions [1] as well as on TC intensity and translation speed [2]. However, the dynamic and thermodynamic processes associated with SSC remain controversial [1, 3, 4] although vertical turbulent mixing and upwelling are known to be important [2]. According to our current understanding of the relationship between TC activity and ocean thermal forcing, not only SST but also temperature and salinity profiles in the upper ocean are important for determining TC intensity, whereas SSC slightly affects TC track prediction [5].

TC heat potential (TCHP), a measure of the oceanic heat content from the surface to the 26°C isotherm depth (Z26), is highly correlated with TC intensity in the western North Pacific (WNP) on seasonal to climate time scales [6, 7]. TCs tend to rapidly intensify in the WNP when they pass over a region with a high TCHP and a deep Z26. Providing accurate oceanic preexisting conditions as oceanic initial conditions to a coupled atmosphere-ocean model used for typhoon prediction is thus important if the model is to predict TCs precisely, particularly their intensity, but how oceanic preexisting conditions affect TC predictions is still unclear.

On a weather-forecasting scale, idealized numerical experiments have demonstrated that TC-induced SSC substantially affects TC intensity during its intensification phase but not during its mature phase [8]. Rapid TC intensification during its intensification phase is caused by mesovortices, filamentation, and vortex Rossby waves enhanced by TC-scale cyclonic circulation. SSC in Wada [8], defined as a decrease in computed SST from the initial SST, plays a role in weakening mesovortices, which suppresses lower-tropospheric cooling by evaporation along spiral rainbands

and the associated local anticyclonic flow around the mesovortices. The resulting relatively high central pressure then weakens the TC-scale cyclonic circulation. This negative feedback [9] reduces TC intensification.

The purpose of the present study was to quantitatively evaluate the impact of oceanic preexisting conditions on predictions of a TC during its intensification phase on a weather-forecasting time scale. We performed several numerical prediction experiments for Typhoon Hai-Tang (2005) by providing nine different oceanic initial conditions to a coupled atmosphere-ocean model. The initial conditions were determined from daily oceanic reanalysis data for 1997 to 2005 calculated by the North Pacific version of the Meteorological Research Institute (MRI) ocean variational estimation (MOVE) system [10].

This paper consists of five sections. Section 2 describes the model and the experiment design. Section 3 describes the results of numerical prediction experiments. Section 4 discusses the role of variation in oceanic preexisting conditions on predictions of TC intensity and the sensitivity of predictions of Hai-Tang's intensity to upper-ocean variations on seasonal to climate time scales. Section 5 is the conclusion.

2. Model and Experiment Design

This section consists of four subsections. Section 2.1 explains the best-track data used in this study. Section 2.2 presents a summary of each component of the coupled atmosphere-ocean model. Section 2.3 outlines the experiment design. Section 2.4 defines mixed-layer heat potential.

2.1. Best-Track Data. To validate the results of the numerical prediction experiments described below, the best-track data of Hai-Tang's positions and central pressures, archived by the Regional Specialized Meteorological Center [6], were used. Best-track data are defined as the sustained 10-min means. We used predicted central pressure to represent Hai-Tang's predicted intensity.

2.2. Coupled Model. The nonhydrostatic atmosphere model coupled with the ocean model (NCM) consists of a nonhydrostatic atmosphere model (NHM) [11] and a mixed-layer ocean model [2, 8]. An oceanic sublayer scheme for calculating an increase in temperature in the upper-ocean skin layer [12] is included in the mixed-layer ocean model for calculating diurnally varying SST.

2.2.1. NHM. The NHM used in the present study is an older version of the nonhydrostatic mesoscale model developed for operational use at the Japan Meteorological Agency in collaboration with the MRI. Physical schemes incorporated into the NHM and NCM are an explicit three-ice bulk microphysics scheme [13] in conjunction with the Kain-Fritsch convective parameterization scheme [14], a resistance law assumed for sensible and latent heat fluxes and wind stress in the surface boundary layer; exchange coefficients for sensible and latent heat fluxes and wind stress over the sea, determined using Kondo's [15] bulk formulas, a turbulent

closure model in the atmospheric-boundary layer [16, 17], and an atmospheric radiation scheme [18].

2.2.2. Mixed-Layer Ocean Model. The mixed-layer ocean model is a reduced gravity model developed at the MRI [2, 8]. In the present study, the ocean model consists of three layers and four levels. The uppermost layer is a mixed layer with vertically uniform density. The middle layer is a seasonal thermocline and shows the largest vertical temperature gradient among the three layers. The bottom layer is assumed to be undisturbed by entrainment. Four levels consist of the surface, the base of the mixed layer/top of the thermocline, the base of the thermocline/top of the bottom layer, and the sea floor. Temperature and salinity are calculated only at the surface and at the base of the mixed layer, whereas layer thickness and oceanic flows are calculated for all layers. The water depth is limited to 2000 m. The mixed-layer depth is determined from oceanic reanalysis data by assuming a difference in density from the surface of no more than 0.25 g m^{-3} and it is limited to 200 m. The base of the thermocline is limited to 600 m.

2.2.3. Oceanic Sublayer Scheme. The specifications of the mixed-layer ocean model described in Section 2.2.2 are insufficient for realistic simulation of the amplitude of diurnal SST variations because of the thickness ($>1 \text{ m}$) of the mixed layer. To improve the simulation of diurnally varying SST, we incorporated into the mixed-layer ocean model an oceanic sublayer scheme that we developed following Schiller and Godfrey [19], but with short-wave absorption/penetration calculated using the formulation of Ohlmann and Siegel [20].

According to the algorithm of Schiller and Godfrey's [19] scheme, a skin layer forms in the uppermost layer when short-wave radiation warms the sea surface. The thickness of the skin layer is determined from the total amount of short-wave radiation and the cumulative wind stress from sunrise to sunrise. Short-wave radiation and wind stress are provided by the NHM to the mixed-layer ocean model at every time step, but short-wave radiation and wind stress accumulate between sunrises only in the oceanic sublayer scheme. The thinner the skin layer is, the larger the amplitude of diurnal SST variation becomes. After sunset, the skin layer vanishes and its depth is reset to the reference depth (5 m in the present study). The total amounts of short-wave radiation and wind stress then remain constant within the oceanic sublayer scheme until next sunrise.

Ohlmann and Siegel [20] derived the formulas associated with short-wave absorption/penetration by multiple regression analysis. Short-wave absorption/penetration is a function of the chlorophyll-*a* concentration (mg m^{-3}), the cloud index under cloudy conditions, and the solar zenith angle under clear-sky conditions. When the chlorophyll-*a* concentration is high, the amplitude of diurnal SST variations tends to be large [12].

2.3. Experiment Design. NHM and the mixed-layer ocean model each contain 721×421 horizontal grids and the

horizontal grid spacing is 6 km. NHM has 40 vertical levels, and the interval between levels varies from 40 m near the surface to 1180 m for the uppermost layer. The top height is nearly 23 km. The time step of the NHM is 12 s, and that of the mixed-layer ocean model is 72 s. Atmospheric and oceanic data are exchanged between the NHM and mixed-layer ocean model every 72 s as follows: the SST calculated in the mixed-layer ocean model is provided to the NHM as the surface boundary condition, and wind stress, short-wave and long-wave radiation, sensible and latent heat fluxes, and precipitation accumulated by the NHM during the time step of the ocean model (72 s) are provided to the mixed-layer ocean model as atmospheric forcing data.

To set the initial and boundary atmospheric conditions for the NHM and NCM, we first ran hydrostatic global spectral model (GSM) version T213L40 for 72 h. The horizontal resolution of GSM T213L40 is nearly 60 km. To avoid gaps in the horizontal resolution of downscale calculations, we next ran a hydrostatic regional spectral typhoon model (TYM) with a horizontal grid spacing of nearly 20 km at Hai-Tang's initial position for 72 h. The TYM provided initial and boundary atmospheric conditions every 3 h based on the output of the GSM [5] to both the NHM and NCM. It should be noted that a bogus typhoon was incorporated only into the numerical prediction by the TYM, and that the effect of the bogus typhoon must be considered in the numerical prediction experiments of the NHM and NCM, because the initial atmospheric conditions for the NHM and NCM runs were based on the output of the TYM. Lateral boundary conditions created from the TYM output were also provided to NHM and NCM every 3 h. The integration time of GSM, TYM, NHM, and NCM was 72 h, starting from 1200 UTC 12 July 2005.

Oceanic initial conditions were obtained from daily oceanic reanalysis data with a horizontal grid spacing of 0.5° from 1997 to 2005. Daily oceanic reanalysis data were calculated by the MOVE system [10]. Table 1 lists the numerical prediction experiments conducted in the present study. We ran nine experiments with the NCM and another nine experiments with the NHM, not being coupled with the mixed-layer ocean model.

To investigate the impact of variations in oceanic preexisting conditions on predictions of Hai-Tang, nine separate sets of oceanic initial conditions were created from the daily oceanic reanalysis data of 12 July during 1997–2005 (Table 1). The nine oceanic initial conditions include some remarkable oceanic variations at seasonal to climate time scales: for example, 12 July 1999 was during a mature La Niña event, whereas 12 July 2002 was during a mature El Niño event; 12 July 2005 fell at the end of a central Pacific warming event during the transition to La Niña.

Hai-Tang was a super-typhoon, defined as a typhoon with maximum sustained 1-min-mean surface winds of 67 m s^{-1} or greater. According to the best-track data, Hai-Tang formed near 22.9° N , 149.2° E at 0000 UTC on 13 July 2005. Hai-Tang initially moved northwestward; then, after it entered the tropical cyclogenesis phase, it turned to move southwestward to westward while rapidly intensifying. Hai-Tang attained a central pressure of 920 hPa

TABLE 1: Designations of the numerical-prediction experiments, the year used for the oceanic preexisting conditions, and the model, NCM and NHM, used to conduct the experiments. El Niño years are followed by (E) and La Niña years by (L).

Experiment	Year	Model
NCM97	1997 (E)	NCM
NCM98	1998	NCM
NCM99	1999 (L)	NCM
NCM00	2000	NCM
NCM01	2001	NCM
NCM02	2002 (E)	NCM
NCM03	2003	NCM
NCM04	2004	NCM
NCM05	2005	NCM
NHM97	1997 (E)	NHM
NHM98	1998	NHM
NHM99	1999 (L)	NHM
NHM00	2000	NHM
NHM01	2001	NHM
NHM02	2002 (E)	NHM
NHM03	2003	NHM
NHM04	2004	NHM
NHM05	2005	NHM

at 0600 UTC on 16 July. This study investigated Hai-Tang's rapid-intensification phase, starting with the tropical cyclogenesis phase. Therefore, we set the initial integration time to 1200 UTC on 12 July 2005. We could not, however, reproduce the tropical cyclogenesis phase realistically in the present numerical prediction experiments because the bogus typhoon included in the initial atmospheric conditions negatively affected the prediction of Hai-Tang's track, as described in Section 3.1. Therefore, we focused on the impact of variations in the oceanic preexisting conditions on predictions of Hai-Tang's rapid intensification.

Hai-Tang passed over two warm-core eddies, characterized by a high sea-surface height (SSH) with a positive SSH anomaly (SSHA), a high TCHP, and a deep Z26, in the WNP as it rapidly intensified (Figure 1). Conversely, as it passed over the cold wake, it ceased to intensify and its best-track central pressure remained constant (Figure 1(a)). The warm-core eddy at around 22° N , 148° E (Figure 1(b)), where the SSH was high, was a few hundred kilometers across. The MOVE system reproduced this warm-core eddy (W1, Figure 1(c)) reasonably well, as well as the high SSH associated with the other warm-core eddy (W2, Figures 1(a) and 1(c)). Hai-Tang's intensification was thus associated with these warm-core eddies.

2.4. Mixed-Layer Heat Potential. Here, we defined the mixed-layer heat potential (MLHP: kJ cm^{-2}) [8] as

$$Q_{\text{MLHP}} = \rho C_p (T_1 - 26) h_1, \quad (1)$$

where ρ is the density of sea water in the mixed layer underneath a TC, which is assumed to be constant; C_p is the

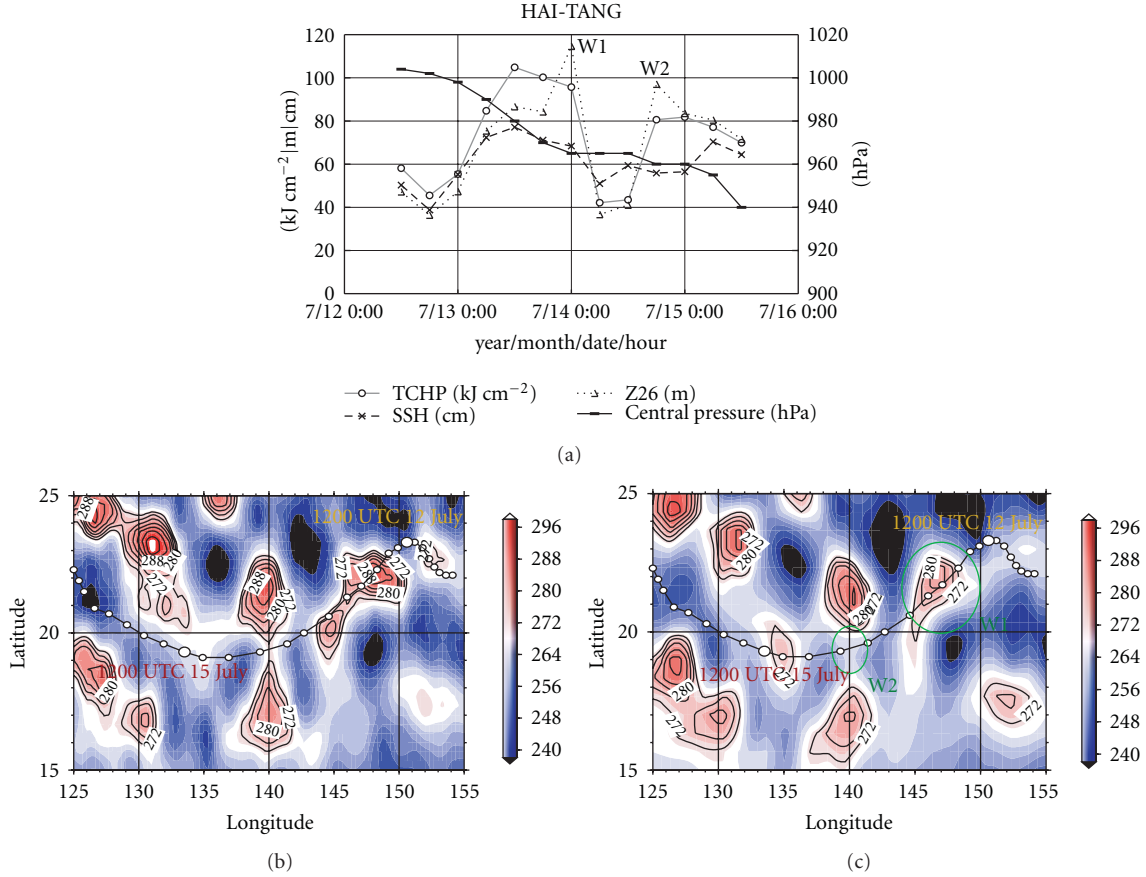


FIGURE 1: (a) Time series of best-track central pressure, tropical-cyclone heat potential (TCHP), 26°C isotherm depth (Z26), and sea surface height (SSH) from 1200 UTC 12 July to 1200 UTC 15 July 2005. (b) Horizontal distribution of the 7-day mean SSH (cm) obtained from the Archiving and Validating Interpretation of Satellite Oceanographic (AVISO) data product (<ftp://ftp.aviso.oceanobs.com/pub/oceano/AVISO/SSH/duacs/global/dt/ref/madt/merged/h/>) for 13 July 2005. (c) Horizontal distribution of daily SSH (cm) calculated by the MOVE system and corrected to make the 7-day spatial mean of the daily MOVE SSH equal to that of the AVISO SSH. W1 and W2 in part (a) and the green circles in part (c) indicate the warm-core eddies. The large circles along Hai-Tang's track in parts (b) and (c) indicate the start and end positions of the numerical integration.

specific heat at constant pressure; T_1 is the SST underneath a TC; h_1 is the mixed-layer depth (MLD) underneath a TC. The variables ρ , T_1 , and h_1 were obtained from daily oceanic reanalysis data.

2.5. Tropical-Cyclone Heat Potential. TCHP (kJ cm⁻²) is defined as

$$Q_{\text{TCHP}} = \sum_{z=0}^H \rho_h C_p (T_h - 26.) \Delta Z_h, \quad (2)$$

where ρ_h is the density of the sea water at each layer, T_h is the sea temperature (°C) at each layer, ΔZ_h is the thickness at each layer, H is the vertical level of depth corresponding to Z26, and h is the variable number of vertical levels based on the configuration of the ocean data reanalysis system described in Section 3. When T_h is below 26°C, TCHP at the layer is assumed to be zero.

3. Results

3.1. Track and Intensity Prediction. We first investigated the impact of variations in oceanic preexisting conditions on predictions of Hai-Tang's track. Figure 2 depicts Hai-Tang's best-track positions and the mean positions predicted by NHM and NCM (Table 1). Both predicted tracks show a marked northwestward bias during the early integration period, and they both subsequently turn southwestward. Thus, the track predictions did not significantly differ between NHM and NCM. At 72 h, the predicted tracks approach Hai-Tang's best-track position. Table 2 lists the mean predicted positions for every 24 h and their standard deviations. The maximum standard deviation at 72 h, 0.27° of longitude, is comparable to the difference of center position at 72 h between NHM and NCM, nearly 0.3° of latitude (Table 2). Thus, variations in oceanic preexisting conditions had no significant impact on predictions of Hai-Tang's track as well as a difference in predicted SSTs between NHM and NCM.

TABLE 2: Mean longitude and latitude and standard deviations of the predicted position every 24 h and best-track longitude and latitude.

Experiment		lon(24 h)	lat(24 h)	lon(48 h)	lat(48 h)	lon(72 h)	lat(72 h)
NHM	MEAN (°)	145.21	22.51	139.49	19.83	133.42	18.72
	STD (°)	0.05	0.08	0.14	0.09	0.26	0.12
NCM	MEAN (°)	145.27	22.61	139.67	19.86	133.69	19.02
	STD (°)	0.04	0.11	0.10	0.08	0.27	0.20
Best track	(°)	147.1	21.7	141.4	19.6	133.5	19.3

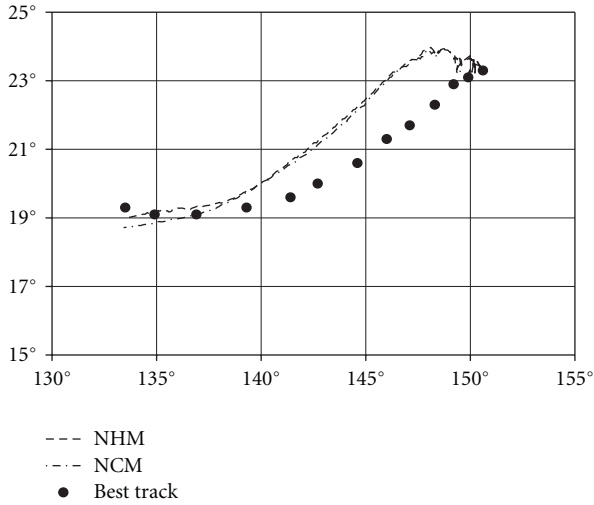


FIGURE 2: Hai-Tang's best-track positions from 1200 UTC 12 July (23.3° N, 150.6° E) to 1200 UTC 15 July 2005 (19.3° N, 133.5° E) and the mean predicted positions of the nine NHM and nine NCM experiments. Longitude is shown on the horizontal axis and latitude on the vertical axis.

The impact of SSC on predictions of TC central pressure was remarkable, particularly during the later period of numerical integration [5]. We investigated the evolution of the central pressures predicted by NCM (Figure 3(a)) and NHM (Figure 3(b)) along with their mean difference and standard deviations (Figure 3(c)). All of the central pressures predicted by NCM were higher than the best-track central pressure after 18 h (Figure 3(a)), whereas most central pressures predicted by NHM were lower (Figure 3(b)). The difference in predicted central pressure between NHM and NCM became significant after 24 h and small after 48 h (Figure 3(c)). The twofold standard deviation of the predicted central pressure difference was nearly 18 hPa at 72 h (Figure 3(c)). This value represents the amplitude of the variation in the predicted central pressure due to the variation in oceanic preexisting conditions. The amplitude of 18 hPa is less than the difference in predicted central pressure between NHM and NCM, which increased to more than 40 hPa at 72 h, suggesting that the impact of oceanic preexisting conditions on predictions of Hai-Tang's intensity was smaller than the impact of the difference between NHM and NCM in the SST decrease caused by Hai-Tang's passage.

3.2. Oceanic Responses. We defined SST as temperature at the first level of the mixed-layer model plus skin temperature calculated in the oceanic sublayer scheme and SSC as the decrease in predicted SST from the initial SST due to Hai-Tang's passage hereafter. It should be noted that the initial SST does not change during the integration in the experiments by NHM. Therefore, the magnitude of SSC at a certain integration time was equal to the difference in SST at a certain integration time between NHM and NCM. We investigated the evolution of mean SST and SSC underneath Hai-Tang and their standard deviations to determine the impact of the variations in oceanic preexisting conditions on SSC (Figure 4). Mean SST was calculated as the average SST underneath Hai-Tang's center position among the nine predictions by NCM. Each SSC value was calculated as the difference in predicted SST underneath Hai-Tang's center position from the initial SST. Mean differences in both SST and SSC were calculated as the averaged differences between NHM and NCM in the predictions of the nine experiments. The minimum mean SST and the maximum mean decrease in SST became significant at around 18 h, when the difference in the predicted central pressures between NHM and NCM also became apparent. The twofold standard deviation associated with the variations in SST underneath Hai-Tang was nearly 0.7°C, and the standard deviation associated with the variations in SSC was nearly 0.5°C. The standard deviation was large from the initial time to 18 h as predicted Hai-Tang rapidly intensified. After 18 h, the rate of intensification decreased and SST underneath Hai-Tang began to increase; however, it remained lower than the initial SST underneath Hai-Tang even though it did not decrease monotonically during the passage. The trend of predicted SST underneath Hai-Tang obtained here differed from the result of an idealized numerical experiment [8] because SSC was sensitive to the variations in the oceanic preexisting conditions such as the spatial and temporal variations in the preexisting warm-core eddy.

To investigate the relationships between the preexisting warm-core eddies and the climatologically deep mixed layer and Hai-Tang's intensification, we calculated MLHP underneath Hai-Tang every hour using (1) and investigated the evolution of mean central pressure and mean MLHP averaged over the nine NCM predictions and their standard deviations (Figure 5). Mean MLHP was calculated as the average in a 1° grid box at Hai-Tang's center. The trend of mean central pressure was negatively correlated with the trend of mean MLHP, implying that high MLHP underneath Hai-Tang was associated with Hai-Tang's intensification.

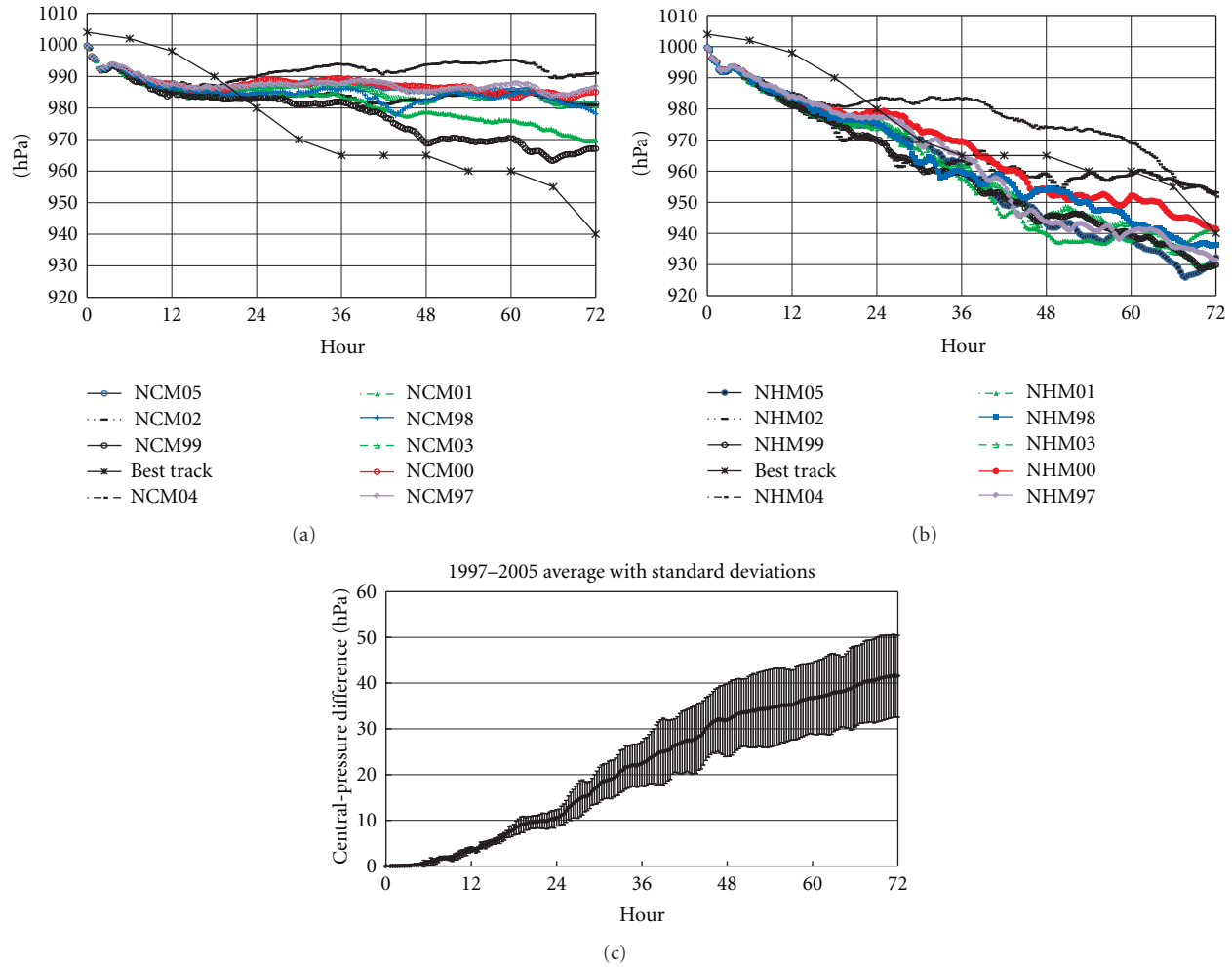


FIGURE 3: Time series of best-track central pressures (hPa) and central pressures predicted in each of the nine experiments by (a) NCM and (b) NHM. (c) Time series of the mean differences in central pressure between NCM and NHM values averaged over the nine experiments and their standard deviations.

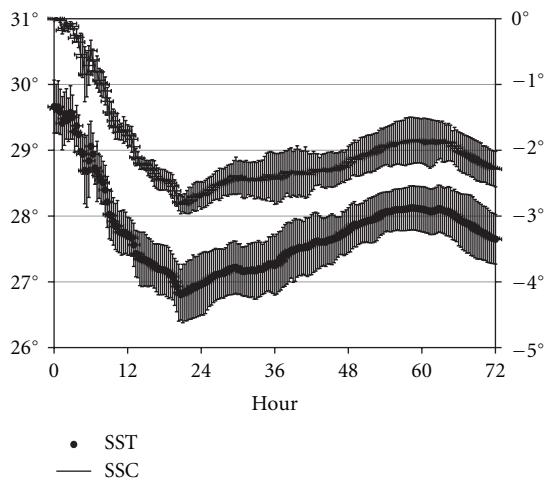


FIGURE 4: Time series of the mean differences in SST (°C; left axis) and SSC (°C; right axis) between NCM and NHM values averaged over the nine experiments and their standard deviations.

However, Hai-Tang's predicted track bypassed the warm-core eddy where MLHP was relatively high. In other words, Hai-Tang passed over a relatively low MLHP area because of the significant northwestward track-prediction error. This track-prediction error led to an intensity-prediction error caused by the predicted passage over an area with different MLHP. This difference in MLHP caused the standard deviation of predicted central pressure to increase (Figure 5) as the integration time progressed.

We have already mentioned in Section 3.1 that the northwestward track-prediction error during the early integration, which was closely related to the bogus typhoon used in the TYM calculation, caused the predicted Hai-Tang to travel where MLHP was relatively low. In contrast, the best-track data indicated that Hai-Tang passed over the warm-core eddy between 12 h to 36 h (Figure 1). In fact, NCM and NHM predicted that Hai-Tang would pass over the warm area north of warm-core eddy W1 (Figure 1(c)) between 0 h and 24 h (Figure 5). The amplitude of the variations in MLHP (Figure 5) was relatively high compared with that of

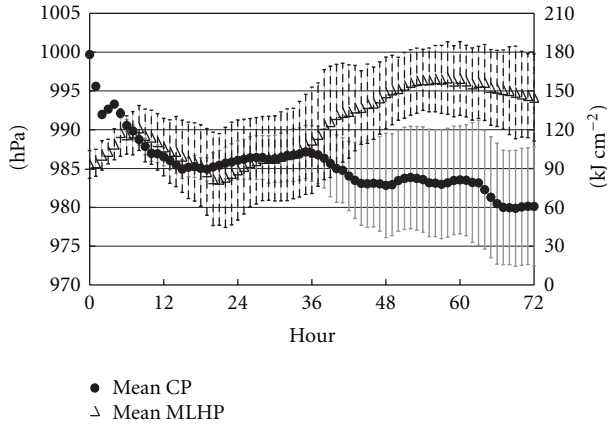


FIGURE 5: Time series of mean central pressure (CP, left axis) and mean mixed-layer heat potential (MLHP, right axis) predicted by NCM (averages of nine experiments) and their standard deviations.

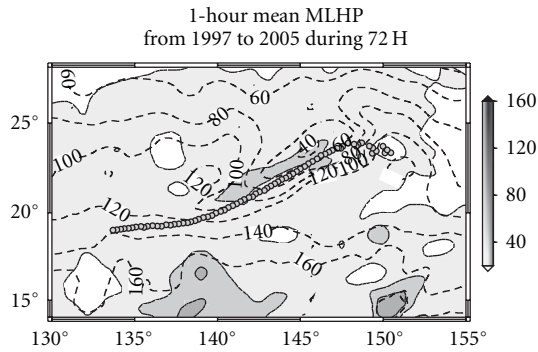


FIGURE 6: Horizontal distributions of mean MLHP (kJ cm^{-2}) averaged during 72 h among the nine NCM predictions (contours), and of the standard deviation of MLHP (shading). MLHP values instantaneously calculated every hour were used. Hai-tang's best track is also shown.

the analyzed TCHP variation, even though the high TCHP at 1800 UTC on 14 July (Figure 1) was reproduced by NCM. The overestimation of MLHP caused by the track-prediction error led to prediction of an excessive reintensification of Hai-Tang. This overestimation of MLHP affected Hai-Tang's predicted central pressure continuously, not temporarily during the integration.

The horizontal distribution of mean MLHP averaged over the nine NCM predictions during 72 h and that of the standard deviation are shown in Figure 6. MLHP was significantly lower on the north side of Hai-Tang's track, where the standard deviation was relatively high, implying that SSC was highly sensitive to variations in oceanic preexisting conditions. The standard deviation was high not only on the north side of Hai-Tang's track but also around 15°N , 138°E and 15°N , 150°E . The high standard deviation in these areas away from Hai-Tang's track can be explained by seasonal to climate time scale variations of oceanic conditions. Figure 6 also indicated that Hai-Tang entered a high-MLHP area during the later integration, and, in fact, the time series of best-track central pressure shows

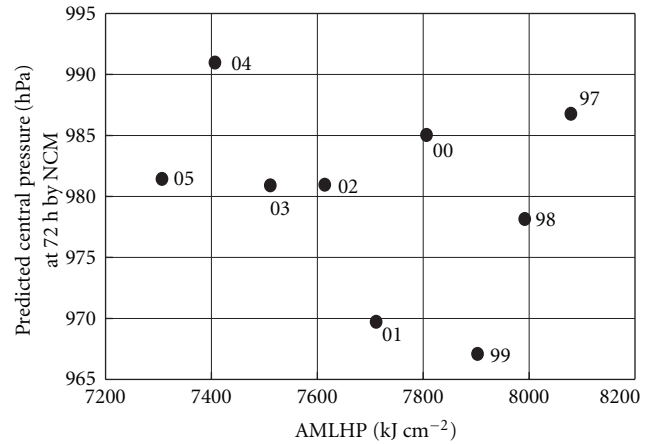


FIGURE 7: Scatter diagram of central pressure (hPa) versus accumulated MLHP (AMLHP) during 72 h (kJ cm^{-2}) from 1997 to 2005. The numbers by each point indicate which year's daily oceanic reanalysis data on 12 July were used by NCM.

remarkable intensification during this later integration time (Figures 3 and 5).

According to Wada and Usui [6], accumulated TCHP (ATCHP) was highly correlated with the minimum central pressure of TCs occurring from 1998 to 2004. ATCHP is defined as the summation of TCHP within a 1.5° square around the TC center from the genesis to the phase first reaching the minimum central pressure every six hours, corresponding to the interval of TC best track data. Here, instead of ATCHP, we calculated accumulated MLHP (AMLHP) from the initial time to 72 h. We then investigated the relationship between AMLHP and predicted central pressure at 72 h among the nine NCM predictions (Figure 7). Interestingly, AMLHP underneath Hai-Tang decreased monotonically from 1997 to 2005, however, predicted minimum central pressure did not increase monotonically during the period. In particular, predicted minimum central pressure markedly decreased during the strong El Niño Southern Oscillation (ENSO) event from 1997 to 1999. In addition, the predicted minimum central pressure was relatively low in 2005 even though AMLHP was also low. Therefore, a high linear correlation between minimum central pressure and AMLHP cannot be assumed, a result that is not consistent with the findings of Wada and Usui [6]. Thus, whether AMLHP and predicted minimum central pressure are correlated may depend on the oceanic preexisting conditions (Figure 7).

3.3. Atmospheric Impact. The energy source for TC genesis and intensification is moisture provided from the ocean to the atmosphere through latent heat flux. Thus, latent heat flux is an important metric for TC intensification. We investigated the horizontal distribution of the mean latent heat flux averaged over 72 h among the NCM experiments and that of its standard deviation (Figure 8). Note that the NCM outputs latent heat flux every hour. Mean latent heat flux was relatively small during the early integration

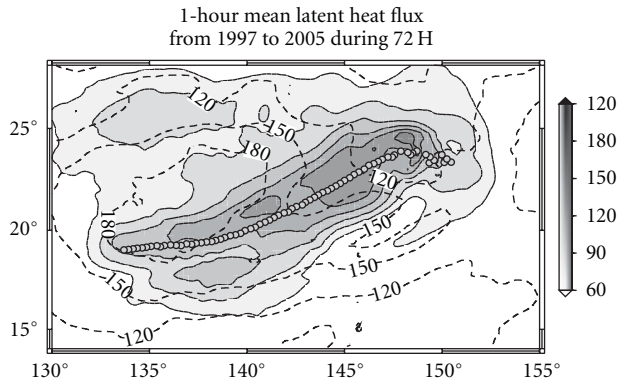


FIGURE 8: Horizontal distributions of mean latent heat flux (W m^{-2}) during 72 h among the nine NCM predictions (contours) and of its standard deviation (shading). Latent heat flux values instantaneously calculated every hour were used. Hai-tang's best track is also shown.

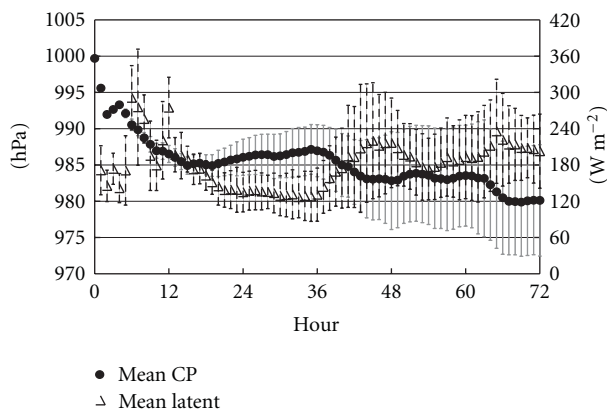


FIGURE 9: Time series of mean central pressure (CP, left axis) and mean latent heat flux (W m^{-2} , right axis) and their standard deviations.

owing to the relatively weak intensity of Hai-Tang, but the standard deviation was relatively high at around 25°N , 148°E because of the uncertainty of Hai-Tang's predicted central position. The standard deviation became small as integration progressed, whereas the mean latent heat flux became high as Hai-Tang intensified. Figure 9 depicts time series of mean central pressure and mean latent heat flux and their standard deviations, with mean latent heat flux calculated as the average in a 1° grid box at Hai-Tang's center. The two trends are negatively correlated, similar to the trends of mean central pressure and mean MLHP (Figure 5), implying that the variation in latent heat flux is closely related to that in MLHP, although surface wind velocity is another important metric for estimating latent heat flux when Kondo's [15] bulk formulas are used.

Next, we investigated the effect of variations in oceanic preexisting conditions on the horizontal distribution of mean latent heat flux at 72 h, averaged over the nine NCM and NHM predictions. The NCM result shows a wave-1 asymmetric distribution pattern of mean latent heat flux

(Figure 10(a)), whereas NHM produced an axisymmetric distribution pattern (Figure 10(c)). The area of high mean latent heat flux west of the mean center position of predicted Hai-Tang corresponds to Hai-Tang's mean direction of travel as predicted by NCM (Figure 2). The standard deviation of the latent heat flux predictions by NCM was high inside Hai-Tang's eyewall, where the horizontal gradient of surface wind velocity was variable ahead of Hai-Tang's direction of travel (Figure 10(b)), whereas the standard deviation of the NHM predictions was high behind Hai-Tang's direction of travel (Figure 10(d)). The difference in the horizontal distributions of mean latent heat flux between NCM (Figure 10(a)) and NHM (Figure 10(c)) resulted from SSC. In fact, mean latent heat flux was remarkably reduced behind Hai-Tang in NCM (Figure 10(a)) where atmospheric conditions had stabilized (not shown). High latent heat flux can be attributed to both the high-velocity surface winds associated with Hai-Tang's intensification (Figure 9) and high SST or mixed-layer temperature associated with high MLHP (Figure 5). This result suggests that not atmospheric thermostatics but atmospheric dynamics and oceanic preexisting conditions determined the distribution and amplitude of latent heat flux around Hai-Tang.

We then examined the horizontal distributions of mean hourly precipitation averaged over 72 h among the nine NCM experiments and of the standard deviation (Figure 11). Heavy precipitation was concentrated along Hai-Tang's predicted track. High mean precipitation and larger standard deviations tended to be on the south side of Hai-Tang's track. Thus, precipitation was high on the opposite side of Hai-Tang's track to high MLHP standard deviations (Figure 6). Figure 12 depicts time series of mean central pressure and mean precipitation and their standard deviations. Mean precipitation was calculated as the average in a 1° grid box at Hai-Tang's center. Mean precipitation tended to increase as Hai-Tang intensified. We can infer that high MLHP led to increases in latent heat flux (Figures 5 and 9), which caused the enhanced release of latent in the troposphere and heavy precipitation (Figure 12). The impact of the variations in oceanic preexisting conditions on MLHP predicted by NCM can be widely seen not only around 15°N , 138°E and 15°N , 150°E but also around the area where MLHP decreased as a result of the SSC induced by Hai-Tang (Figure 6), whereas their impact on precipitation was mainly limited to the south side of Hai-Tang.

The horizontal distribution of mean precipitation at 72 h (Figure 13(a)) successfully captures its wave-1 asymmetric pattern, which is similar to the precipitation pattern observed by satellite (Figure 14). In contrast, the axisymmetric pattern near Hai-Tang's center (Figure 14) is similar to the horizontal distribution of mean precipitation at 72 h predicted by NHM (Figure 13(c)). The heavy precipitation near Hai-Tang's center (Figure 14) is not reproduced well (Figure 13(a)) owing to the weak intensity of Hai-Tang predicted by NCM (Figure 3(a)), but it is reproduced to some extent in the NHM prediction (Figure 13(c)). The standard deviation of predicted mean precipitation was high in both NCM (Figure 13(b)) and NHM (Figure 13(d)) where mean precipitation was also high. The impact of variations in

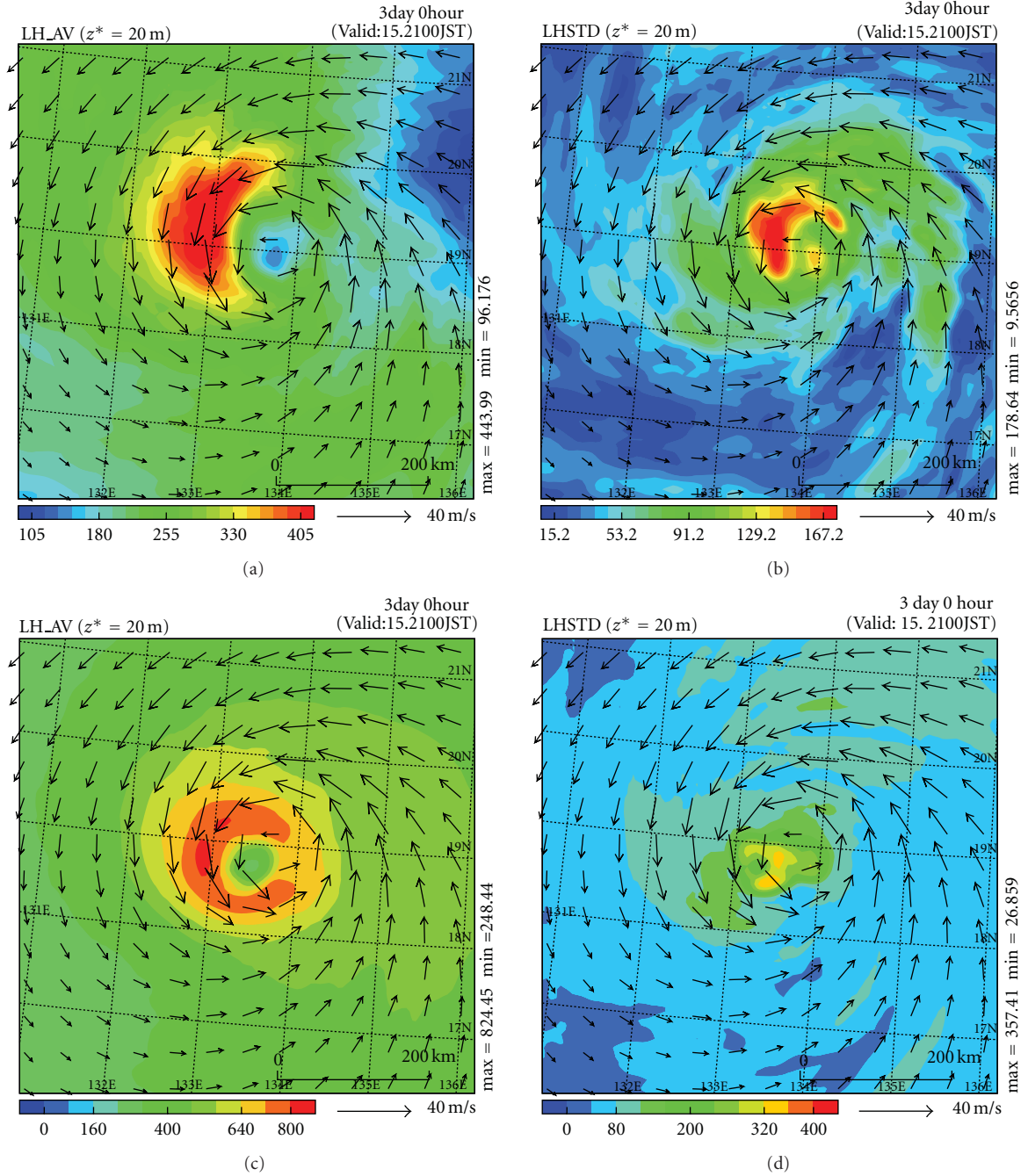


FIGURE 10: (a) Horizontal distribution of mean latent heat flux (W m^{-2}) at 72 h averaged over the nine NCM predictions and (b) that of the standard deviation at 72 h in NCM; (c) and (d) are the same as (a) and (b), respectively, except that they show the NHM results. Mean horizontal wind field vectors at 72 h averaged over the nine NCM (in parts (a) and (b)) and NHM (in parts (c) and (d)) predictions are also shown in each panel.

oceanic preexisting conditions on precipitation was significant around the spiral rainband southeastward of Hai-Tang's center. In contrast, the axisymmetric pattern of precipitation vanished as a result of SSC (Figure 13(a)), suggesting that the variation in oceanic preexisting conditions directly affected the intensity of precipitation over the spiral rainbands, and then the variation over the spiral rainbands affected in turn the intensity prediction. Although Wada [8] studied

intensification caused by mesovortices on spiral bands, this study demonstrated for the first time that the intensification process is influenced by variations in oceanic preexisting conditions.

To investigate the impact of variations in oceanic preexisting conditions on precipitation and Hai-Tang's intensification, we focused on the variations in mean specific humidity averaged from the surface to nearly 14 km height

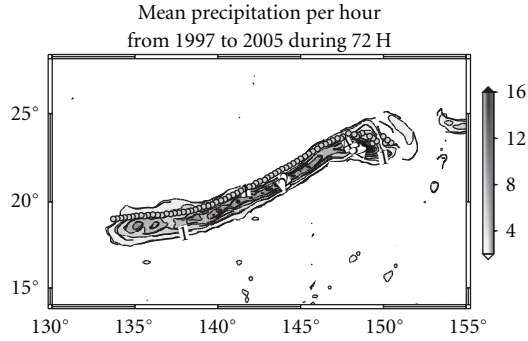


FIGURE 11: Horizontal distributions of mean hourly precipitation (mm) during 72 h among the nine NCM predictions (contours) and of the standard deviation (shading). Cumulative hourly precipitation was used to calculate the mean value.

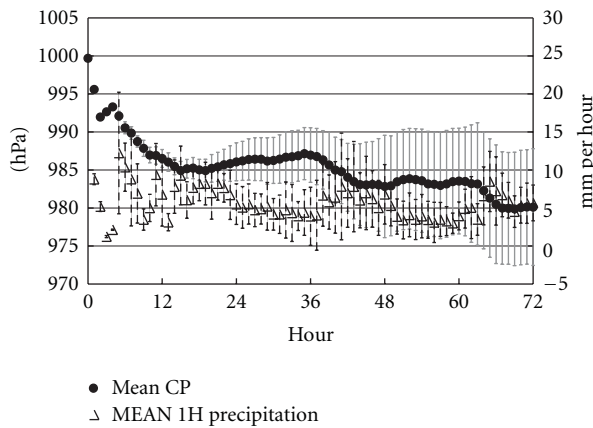


FIGURE 12: Time series of mean central pressure (CP, left axis) and mean hourly precipitation (mm, right axis) and their standard deviations.

(Figure 15(a)), mean specific cloud plus specific rain averaged from the surface to nearly 6.5 km height (Figure 15(b)), and the mean hourly change in potential temperature caused by radiation averaged from nearly 6.5 km height to 14 km height (Figure 15(c)). These mean values were also averaged within a radius of 300 km from Hai-Tang's predicted center and also over the nine NCM predictions. Figure 15 also depicts the variations in mean specific humidity, mean specific cloud plus specific rain, and mean hourly change in potential temperature caused by radiation in 1999, 2004, and 2005. Here, we consider specific humidity to represent the water vapor content, and specific cloud plus rain to represent the liquid water content.

Variations in oceanic preexisting conditions began to cause significant variation in the water vapor content around predicted Hai-Tang at 12 h. The standard deviation increased during the early integration and reached a maximum at around 30 h. After 36 h, the standard deviation of the liquid water content around predicted Hai-Tang increased rapidly. Both water vapor and liquid water contents increased around predicted Hai-Tang as the predicted Hai-Tang intensified, suggesting that they can be regarded as the energy source

for TC intensification. The impact of variations in oceanic preexisting conditions on the hourly change in potential temperature caused by radiation became significant after 36 h (Figure 15(c)), corresponding in timing to Hai-Tang's intensification, as a result of variations in Hai-Tang's atmospheric warm-core temperature caused by latent heat release. The difference in predicted central pressures among the nine NCM predictions became large at 24 h (Figure 3(a)) when the difference in hourly change in potential temperature caused by radiation began to appear significantly (Figure 15(c)). Predicted central pressure tended to be lower when the amplitude of diurnal variations in the hourly change in potential temperature caused by radiation was larger. The relationship was particularly marked when the oceanic preexisting conditions in 1999 were used as the initial oceanic conditions in NCM (NC99 in Table 1).

In contrast, water vapor content was markedly lower when oceanic preexisting conditions in 2004 were used as the initial oceanic conditions in NCM (NC04 in Table 1) compared with when the preexisting conditions of other years were used (Figure 15(a)). AMLHP predicted by NCM was lower in 2004 than that in any other year except 2005 (Figure 7). Liquid water content was also low at around 30 h and from 45 to 54 h in NC04 (Figure 15(b)). Lower water vapor and liquid water contents were associated with less variation in the hourly change in potential temperature caused by radiation. Thus, Hai-Tang's central pressures predicted by NHM and NCM were particularly high when the oceanic preexisting conditions in 2004 were used as the initial oceanic conditions in the models. Therefore, the oceanic preexisting conditions associated with high MLHP around Hai-Tang's track were more favorable for Hai-Tang's intensification, because both MLHP and Hai-Tang's surface winds played a crucial role in enhancing water vapor and liquid water contents around Hai-Tang as well as latent heat release in the upper troposphere, which resulted in high value of the hourly change in potential temperature caused by radiation.

4. Discussion

4.1. The Effect of Cumulus Parameterization. We clarified the uncertainty in TC intensity predictions caused by variations in oceanic preexisting conditions for Typhoon Hai-Tang (2005). We first demonstrated that Hai-Tang's predicted intensity was closely related to the variation in MLHP. Warm-core eddies and the climatologically deep mixed layer in the WNP played a crucial role in the intensification of Hai-Tang. We next demonstrated that water vapor and liquid water contents around Hai-Tang's center increased when predicted Hai-Tang intensified over high MLHP areas, indicating a close relationship between MLHP and water vapor and liquid water contents. However, the Kain-Fritsch cumulus parameterization scheme [14] incorporated into the NHM and NCM might have contributed to these results, even though similar results were obtained by experiments with NHM and NCM when the Kain-Fritsch's cumulus parameterization scheme was not used (not shown). Hai-Tang's central pressures predicted by the NHM and NCM

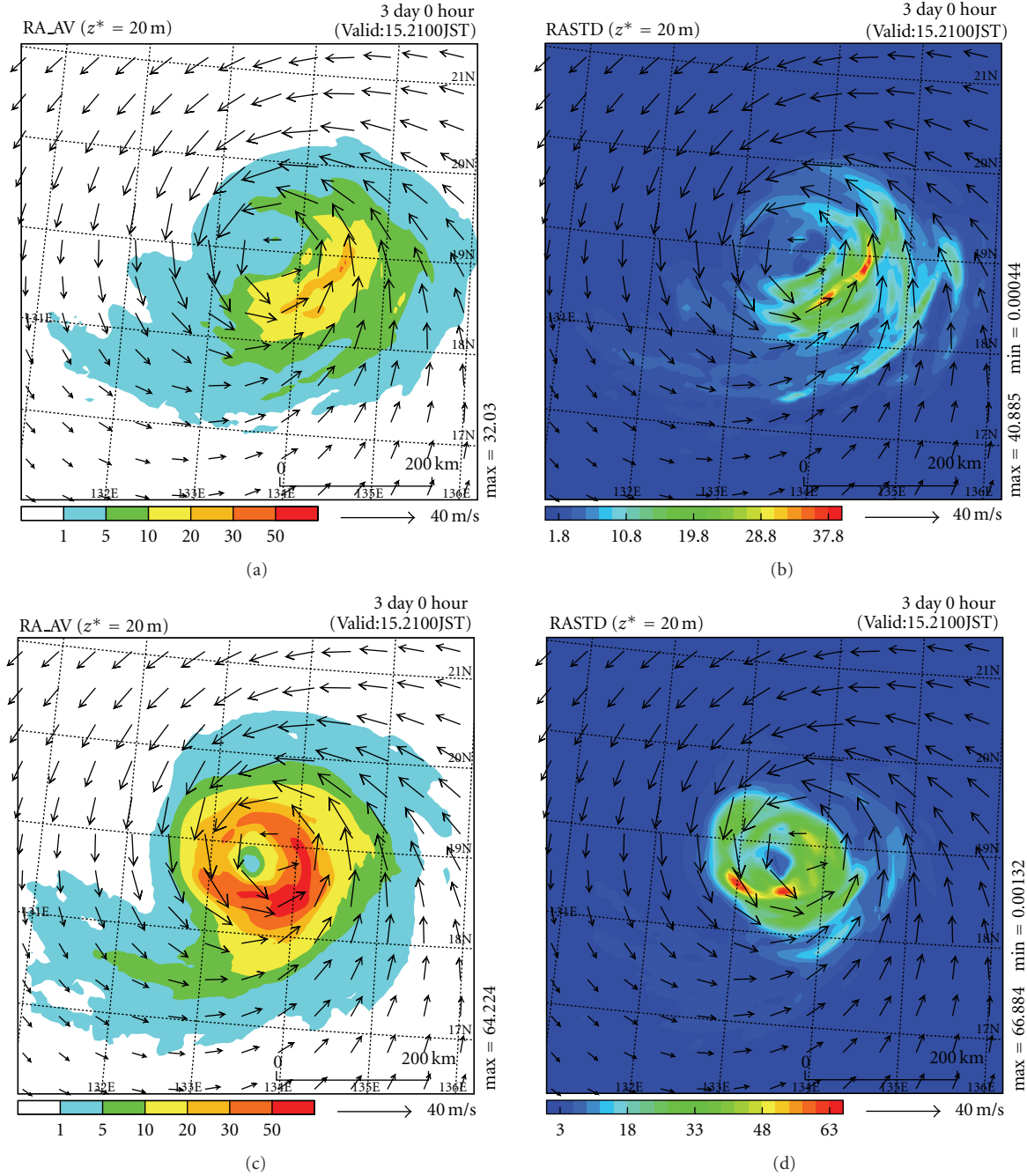


FIGURE 13: Horizontal distribution of mean hourly precipitation (mm per hour) at 72 h averaged over the nine NCM predictions and (b) that of the standard deviation at 72 h; (c) and (d) are the same as (a) and (b), respectively, except that they show the NHM results. Mean horizontal wind field vectors at 72 h averaged over the nine NCM (in parts (a) and (b)) and NHM (in parts (c) and (d)) predictions are also shown in each panel.

without using the Kain-Fritsch's cumulus parameterization scheme were higher at the 6-km horizontal resolution than those predicted with the use of the Kain-Fritsch scheme (not shown) and far from the best-track central pressures. Therefore, in the present study we concluded that cumulus parameterization is required even at the 6-km resolution to reproduce Hai-Tang's intensity realistically. In fact, the Kain-Fritsch's cumulus parameterization scheme is closely

associated with the local Convective Available Potential Energy (CAPE). CAPE is sensitive to the local thermodynamic profile in the atmospheric boundary layer, enthalpy flux, and thus SST. Thus, cumulus convection as calculated by Kain-Fritsch's cumulus parameterization is sensitive to SST. This implies that the Kain-Fritsch's cumulus parameterization possibly changes not only central pressure predictions but also the distribution patterns of latent heat flux and

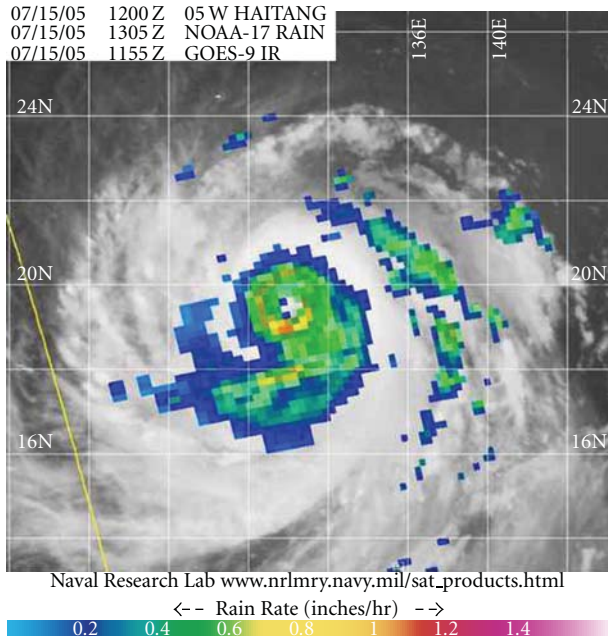


FIGURE 14: Advanced Microwave Sounding Unit-B (AMSUB)-sensor observed rain at 1305 UTC on 15 July 2005 (color shading) superimposed on the GOES-9 IR image obtained at 1155 UTC on 15 July 2005 (gray shading) (from http://www.nrlmry.navy.mil/tc-pages/tc_home.html).

precipitation intensity at around Hai-Tang's predicted center. This study does not explore the sensitivity any further.

The impact in variations in oceanic preexisting conditions on precipitation intensities on the spiral rainbands of the typhoon (Figure 13) is qualitatively consistent with the results of cloud-resolving numerical experiments [8] that SSC suppresses mesovortices along the spiral bands. This suggests that precipitation intensities on the spiral rainbands around Hai-Tang are sensitive to variations in oceanic preexisting conditions. However, the impact of oceanic preexisting conditions on precipitation intensities on the spiral rainbands still requires quantitative evaluation because of the uncertainties associated with the cumulus parameterization. To explore the relationships among MLHP, water vapor plus liquid water contents, and Hai-Tang's intensity, another numerical-prediction experiment with a grid spacing of 1 to 2 km, should be performed with a coupled atmosphere-ocean model that does not include cumulus parameterization. Although such experiments would improve TC intensity prediction, many computational resources would be needed to carry them out.

The evolution of SST, and SSC in particular, was associated with the variations in oceanic preexisting conditions [1] as well as with Hai-Tang's intensity and translation [2]. The magnitude of SSC in this study tended to be larger than that obtained in the previous study [1], partly because of the northwestward track error. In addition, we must pay attention to the possibility that the tuning parameter associated with breaking surface waves in the mixed-layer formulation [2, 8] may be too high. High tuning parameter

values lead to excessive vertical turbulent mixing near the surface because of breaking surface waves, which enhances SSC [2]. We thus need to improve the tuning parameter associated with breaking surface waves in the entrainment formulation [2] using the result of a coupled atmosphere-wave-ocean model.

The results of the numerical experiments of this study include the impact of diurnally varying SST in the upper-ocean skin layer on TC intensity prediction, but we could not separate the impact of sea-surface skin temperature variations on TC intensity prediction from that of oceanic preexisting conditions. Another numerical-prediction experiment without the upper-ocean skin-temperature scheme is needed to determine the separate impact of diurnally varying SST in the upper-ocean skin layer on TC intensity prediction. Previous study recently reported that sea-surface skin temperature variations may affect maximum hourly precipitation over the western Pacific in boreal summer and in the seasonal climatology [21]. However, the impact of diurnally varying SST on TC intensity prediction on a weather-forecasting time scale is not well understood. Moreover, the sensitivity of diurnally varying SST to oceanic preexisting conditions and to cumulus parameterization should be considered. Determination of whether oceanic preexisting conditions or sea-surface skin temperature variations significantly affect TC intensity prediction on a weather-forecasting time scale is, however, beyond the scope of this study.

4.2. Upper-Ocean Variability on Seasonal to Climate Scales.

Here, we discuss the relationship between TC intensity prediction on a weather-forecasting time scale and upper-ocean variability on seasonal to climate time scales. Even though the time scales are different, initial oceanic conditions for predicting Hai-Tang can indeed be determined by analysis of the oceanic field, including oceanic variations on both weather-forecasting and seasonal to climate time scales. Wada and Chan [7] investigate upper-ocean variability in the North Pacific on seasonal to climate time scales in the North Pacific by using monthly oceanic reanalysis data sets calculated by MOVE. Table 3 lists the correlation coefficients between the nine NHM and NCM predicted central pressures at 72 h and the normalized amplitudes in July from 1997 to 2005. Wada and Chan [7] already derived the normalized amplitudes by Empirical Orthogonal Function analysis (EOF) of the 44-year monthly North Pacific TCHP data set. The central pressures predicted by the NCM at 72 h were significantly correlated with the normalized amplitudes of EOF first mode (EOF1) at a 90% significance level (Table 3), indicating a significant relationship between predicted central pressures at 72 h around 19° N, 134° E, and ENSO events [7]. In contrast, central pressures predicted by the NHM were significantly correlated with the normalized amplitudes of EOF second mode (EOF2) at the 80% significance level. In fact, the region with remarkable SSC around Hai-Tang's predicted track corresponds to that where TCHP remained high. The high TCHP is associated with ENSO Modoki event, when all of the North Pacific except its eastern tropical part was

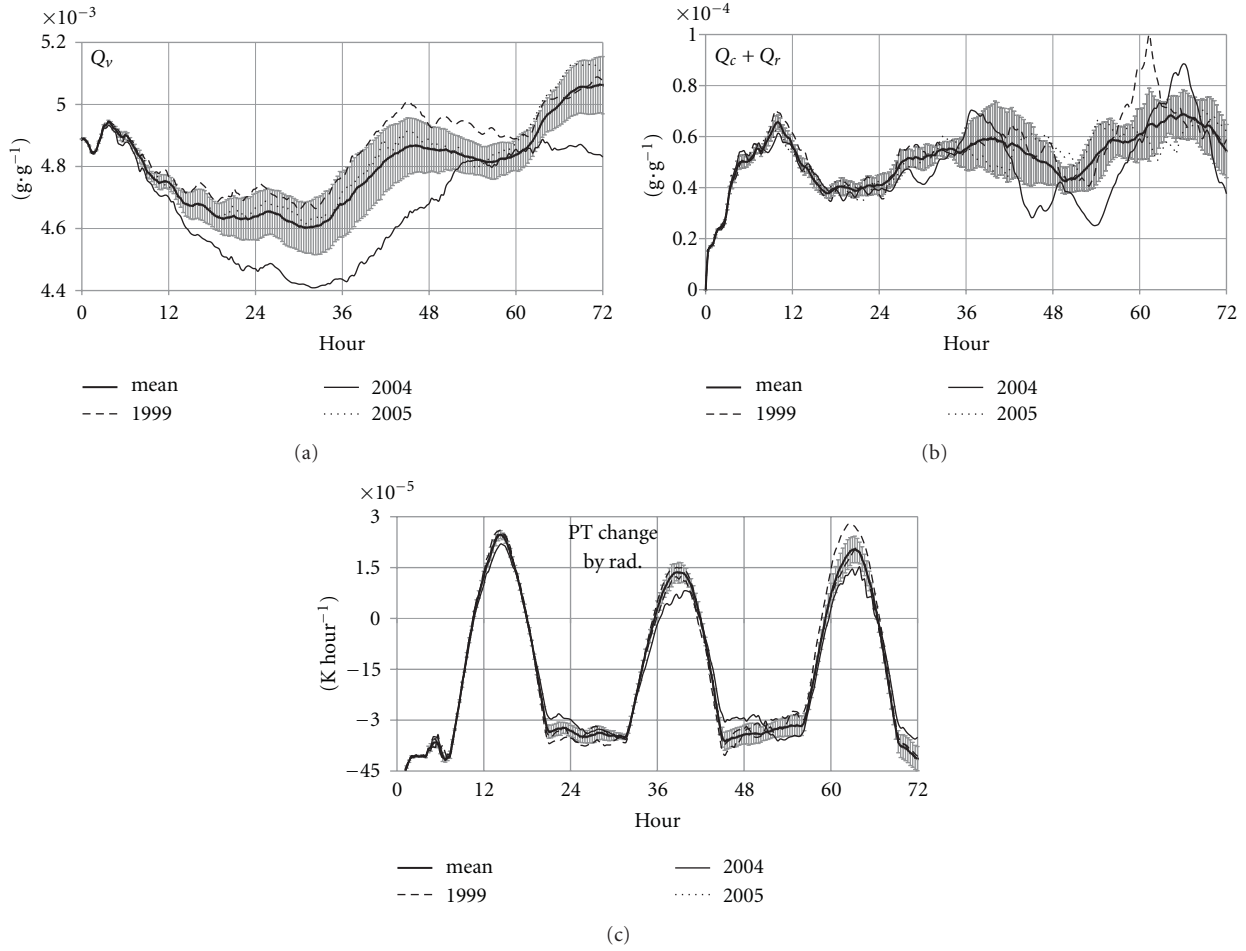


FIGURE 15: (a) Time series of mean specific humidity (Q_v , $\text{g} \cdot \text{g}^{-1}$) averaged over the nine NCM predictions within a radius of 300 km from the predicted Hai-Tang's center, along with time series of specific humidity in 1999, 2004, and 2005 predicted by NCM, also averaged within a radius of 300 km from the predicted Hai-Tang's center; (b) same as Figure 15(a) except for mean specific cloud (Q_c) plus specific rain (Q_r , $\text{g} \cdot \text{g}^{-1}$); and (c) same as Figure 15(a) except for mean hourly change in potential temperature caused by radiation (K per hour).

TABLE 3: Correlation coefficients between predicted central pressures and normalized EOF amplitudes (calculated by Wada and Chan [7]).

Experiment	EOF1(ENSO)	EOF2(ENSO MODOKI)	EOF3
NHM	0.27	-0.60**	0.39
NCM	0.61*	0.00	0.38

Significance levels: * $\alpha = 0.1$, ** $\alpha = 0.2$.

relatively warm [7]. In contrast, the region with remarkable SSC corresponds to that where TCHP decreased owing to the passage of the TC during El Niño. Conversely, predicted central pressure was lowest in 1999 during the transition to a mature La Niña event, implying that a climatologically deep mixed layer in the WNP during La Niña events may cause TCs to intensify.

Chia and Ropelewski [22] reported that the climatological mean location of TC formation varies in relation to ENSO. In that sense, certain oceanic preexisting conditions matched the certain atmospheric conditions to produce

reasonable atmospheric and oceanic environmental fields, which are necessary for tropical cyclogenesis and intensification in the case of super-typhoon Hai-Tang. In other words, the atmospheric thermodynamics conditions favorable to tropical cyclogenesis and intensification are associated with the oceanic preexisting conditions. Here we take as an example a typhoon generated in July 2004 in the area where Hai-Tang was generated and intensified in 2005. A tropical storm was generated at around 19.1°N , 136.3°E at 0600 UTC on 11 July 2004, and it became a tropical cyclone, named Typhoon Kompasu, at 0000 UTC on 14 July 2004 in a location near Hai-Tang's track. The minimum central pressure of Kompasu was 992 hPa. Thus, Kompasu did not show remarkable intensification in 2004 even though in 2005 Hai-Tang was generated and intensified in the same location. Oceanic preexisting conditions in 2004 led to the weak intensity of Kompasu, consistent with the weak intensity of predicted Hai-Tang under the initial oceanic conditions of 12 July 2004 (Figures 3(a) and 3(b)). Thus, certain large-scale atmospheric forcing must accompany the certain oceanic preexisting conditions to cause the tropical

cyclogenesis and intensification of a super-typhoon such as Hai-Tang.

5. Conclusion

We qualitatively evaluated the impact of variations in oceanic preexisting conditions on predictions of Typhoon Hai-Tang in 2005 by a coupled atmosphere-ocean model to which we provided nine initial oceanic conditions obtained from daily oceanic reanalysis data for 12 July from 1997 to 2005. Our conclusions are as follows.

- (1) The amplitude of the impact of the variations in oceanic preexisting conditions on predicted Hai-Tang's central pressure was nearly 18 hPa at 72 h, compared with a predicted central pressure difference of about 40 hPa at 72 h, predicted from the difference in sea-surface temperature (SST) between the nonhydrostatic atmospheric model (NHM) and the nonhydrostatic atmosphere model coupled with the ocean model (NCM). The marked difference between the predicted SST and the initial SST is the sea-surface cooling (SSC) caused by the passage of Hai-Tang. The impact of SSC was more remarkable than that of variations in oceanic preexisting conditions on Hai-Tang's intensity prediction. However, to evaluate the impact of the variation in oceanic preexisting conditions on predicted Hai-Tang's central pressure quantitatively, the effect of cumulus parameterization should be considered. Numerical-prediction experiments with NCM at horizontal resolutions of 1–2 km will be needed in the future because of the poor intensity prediction by even the NHM at the 6-km horizontal resolution.
- (2) Warm-core oceanic eddies and a climatologically deep mixed layer led to a high mixed-layer heat potential, which increased the latent heat flux and enhanced the water vapor and liquid water contents, leading to increases in Hai-Tang's atmospheric warm-core temperature owing to latent heat release and thus intensification of Hai-Tang. The difference in the intensity predictions of Hai-Tang among the nine NCM predictions accompanied that in the hourly changes in potential temperature caused by radiation. Variations in oceanic preexisting conditions were sensitive to precipitation intensities along the spiral rainbands and thus affected Hai-Tang's intensity, whereas SSC negatively affected the formation of an axisymmetric precipitation pattern near Hai-Tang's center.

We discussed the requirement that certain large-scale atmospheric forcing must accompany the certain oceanic preexisting conditions to cause the tropical cyclogenesis and intensification of a super-typhoon such as Hai-Tang. Chan [23] also reported that locations of TC genesis varied depending on the atmospheric dynamic forcing. However, it is not well understood how the atmospheric thermodynamic field and associated oceanic preexisting conditions

affect TC intensity. In this study, we successfully evaluated uncertainties in predictions of Hai-Tang's intensity related to variations in oceanic preexisting conditions. This is the first step to understanding the impact of the atmospheric thermodynamic field and its associated oceanic preexisting conditions on TC intensity and to making TC intensity prediction more precise. To explore this further, a more sophisticated oceanic data assimilation system and coupled atmosphere(-wave)-ocean model are needed. In addition, the results of the coupled model suggest that we should consider seasonal to climate variations in oceanic conditions to improve the intensity predictions on a weather-forecasting scale.

Acknowledgments

A. Wada is grateful to Dr. Y. Kawai for developing the oceanic sublayer scheme. This work was supported by the Japan Society for the Promotion of Science (JSPS), Grant-in-Aid for Scientific Research (C) (19612005 and 22540454). The authors thank Dr. T. Kato of the Meteorological Research Institute, Japan Meteorological Agency, for the use of his plotting tools. General Mapping Tools (GMT) were also used to draw figures.

References

- [1] Z.-W. Zheng, C.-R. Ho, and N.-J. Kuo, "Importance of pre-existing oceanic conditions to upper ocean response induced by Super Typhoon Hai-Tang," *Geophysical Research Letters*, vol. 35, no. 20, Article ID L20603, 2008.
- [2] A. Wada, H. Niino, and H. Nakano, "Roles of vertical turbulent mixing in the ocean response to Typhoon Rex (1998)," *Journal of Oceanography*, vol. 65, no. 3, pp. 373–396, 2009.
- [3] A. Wada, K. Sato, N. Usui, and Y. Kawai, "Comment on 'Importance of pre-existing oceanic conditions to upper ocean response induced by Super Typhoon Hai-Tang' by Z.-W. Zheng, C.-R. Ho, and N.-J. Kuo," *Geophysical Research Letters*, vol. 36, no. 9, Article ID L09603, 2009.
- [4] C.-R. Ho, Q. Zheng, Z.-W. Zheng, N.-J. Kuo, C.-K. Tai, and F.-C. Su, "Reply to comment by A. Wada et al. on 'Importance of pre-existing oceanic conditions to upper ocean response induced by Super Typhoon Hai-Tang,'" *Geophysical Research Letters*, vol. 36, no. 9, Article ID L09604, 2009.
- [5] A. Wada, "Numerical problems associated with tropical cyclone intensity prediction using a sophisticated coupled typhoon-ocean model," *Papers in Meteorology and Geophysics*, vol. 58, pp. 103–126, 2007.
- [6] A. Wada and N. Usui, "Importance of tropical cyclone heat potential for tropical cyclone intensity and intensification in the Western North Pacific," *Journal of Oceanography*, vol. 63, no. 3, pp. 427–447, 2007.
- [7] A. Wada and J. C. L. Chan, "Relationship between typhoon activity and upper ocean heat content," *Geophysical Research Letters*, vol. 35, no. 17, Article ID L17603, 2008.
- [8] A. Wada, "Idealized numerical experiments associated with the intensity and rapid intensification of stationary tropical-cyclone-like vortex and its relation to initial sea-surface temperature and vortex-induced sea-surface cooling," *Journal*

- of Geophysical Research*, vol. 114, no. 18, Article ID D18111, 2009.
- [9] I. Ginis, "Ocean response to tropical cyclone," in *Global Perspective on Tropical Cyclones*, R. L. Elsberry, Ed., pp. 198–260, WMO/TD-No. 693, Geneva, Switzerland, 1995.
 - [10] N. Usui, S. Ishizaki, Y. Fujii, H. Tsujino, T. Yasuda, and M. Kamachi, "Meteorological Research Institute multivariate ocean variational estimation (MOVE) system: some early results," *Advances in Space Research*, vol. 37, no. 4, pp. 806–822, 2006.
 - [11] K. Saito, T. Fujita, Y. Yamada et al., "The operational JMA nonhydrostatic mesoscale model," *Monthly Weather Review*, vol. 134, no. 4, pp. 1266–1298, 2006.
 - [12] A. Wada and Y. Kawai, "The development of diurnally-varying sea-surface temperature scheme. Part I. Preliminary numerical experiments," *CAS/JSC WGNE, Research Activities in Atmospheric and Ocean Modelling*, vol. 39, no. 4, pp. 0907–0908, 2009.
 - [13] Y.-L. Lin, R. D. Farley, and H. D. Orville, "Bulk parameterization of the snow field in a cloud model," *Journal of Climate & Applied Meteorology*, vol. 22, no. 6, pp. 1065–1092, 1983.
 - [14] J. S. Kain and J. M. Fritsch, "A one-dimensional entraining/detraining plume model and its application in convective parameterization," *Journal of the Atmospheric Sciences*, vol. 47, no. 23, pp. 2784–2802, 1990.
 - [15] J. Kondo, "Air-sea bulk transfer coefficients in diabatic conditions," *Boundary-Layer Meteorology*, vol. 9, no. 1, pp. 91–112, 1975.
 - [16] J. B. Klemp and R. Wilhelmson, "The simulation of three-dimensional convective storm dynamics," *Journal of the Atmospheric Sciences*, vol. 35, pp. 1070–1096, 1978.
 - [17] J. W. Deardorff, "Stratocumulus-capped mixed layers derived from a three-dimensional model," *Boundary-Layer Meteorology*, vol. 18, no. 4, pp. 495–527, 1980.
 - [18] M. Sugi, K. Kuma, and K. Tada, "Description and performance of the JMA operational global spectral model (JMA-GSM88)," *Geophysical Magazine*, vol. 43, pp. 105–130, 1990.
 - [19] A. Schiller and J. S. Godfrey, "A diagnostic model of the diurnal cycle of sea surface temperature for use in coupled ocean-atmosphere models," *Journal of Geophysical Research*, vol. 110, no. 11, Article ID C11014, 2005.
 - [20] J. C. Ohlmann and D. A. Siegel, "Ocean radiant heating. Part II: parameterizing solar radiation transmission through the upper ocean," *Journal of Physical Oceanography*, vol. 30, no. 8, pp. 1849–1865, 2000.
 - [21] M. A. Brunke, X. Zeng, V. Misra, and A. Beljaars, "Integration of a prognostic sea surface skin temperature scheme into weather and climate models," *Journal of Geophysical Research*, vol. 113, no. 21, Article ID D21117, 2008.
 - [22] H. H. Chia and C. F. Ropelewski, "The interannual variability in the genesis location of tropical cyclones in the northwest Pacific," *Journal of Climate*, vol. 15, no. 20, pp. 2934–2944, 2002.
 - [23] J. C. L. Chan, "Thermodynamic control on the climate of intense tropical cyclones," *Proceedings of the Royal Society A*, vol. 465, no. 2110, pp. 3011–3021, 2009.

Research Article

Towards Direct Simulation of Future Tropical Cyclone Statistics in a High-Resolution Global Atmospheric Model

Michael F. Wehner,¹ G. Bala,² Phillip Duffy,³ Arthur A. Mirin,⁴ and Raquel Romano⁵

¹Lawrence Berkeley National Laboratory, 1 Cyclotron Rd. MS50F, Berkeley, CA 94720, USA

²Divecha Center for Climate Change, Center for Atmospheric and Oceanic Sciences, Indian Institute of Science, Bangalore 560 012, India

³Climate Central, Inc., 895 Emerson St., Palo Alto, CA 94301, USA

⁴Lawrence Livermore National Laboratory, Livermore, 94551-0808, USA

⁵Google, Inc., 1600 Amphitheatre Parkway, Mountain View, CA 94043, USA

Correspondence should be addressed to Michael F. Wehner, mfwehner@lbl.gov

Received 31 December 2009; Revised 14 April 2010; Accepted 22 April 2010

Academic Editor: Song Y. Hong

Copyright © 2010 Michael F. Wehner et al. This is an open access article distributed under the Creative Commons Attribution License, which permits unrestricted use, distribution, and reproduction in any medium, provided the original work is properly cited.

We present a set of high-resolution global atmospheric general circulation model (AGCM) simulations focusing on the model's ability to represent tropical storms and their statistics. We find that the model produces storms of hurricane strength with realistic dynamical features. We also find that tropical storm statistics are reasonable, both globally and in the north Atlantic, when compared to recent observations. The sensitivity of simulated tropical storm statistics to increases in sea surface temperature (SST) is also investigated, revealing that a credible late 21st century SST increase produced increases in simulated tropical storm numbers and intensities in all ocean basins. While this paper supports previous high-resolution model and theoretical findings that the frequency of very intense storms will increase in a warmer climate, it differs notably from previous medium and high-resolution model studies that show a global reduction in total tropical storm frequency. However, we are quick to point out that this particular model finding remains speculative due to a lack of radiative forcing changes in our time-slice experiments as well as a focus on the Northern hemisphere tropical storm seasons.

1. Introduction

Hurricanes and tropical cyclones are arguably the most devastating meteorological events in both loss of human life as well as financial costs. Following the most active Atlantic hurricane season ever recorded in 2005, the debate as to the influence a warmer climate might have on the statistics of tropical cyclones has become more urgent. If the frequency or intensity of such storms were to change, the impacts could be severe. The number of tropical cyclones has been remarkably stable since 1970 averaging about ninety storms globally per year [1, 2]. No statistically significant trend in this number of tropical cyclones has been observed in the period 1970 to present [1]. However, there is evidence of significant trends in tropical cyclone intensity and duration over this period. Holland and Webster [3] found that the number of Atlantic tropical cyclones has increased in a

statistically significant sense and Emanuel [4] has correlated increases in a hurricane power index with increases in North Atlantic sea surface temperatures. Elsner et al. [5] have found a twenty-six year positive trend in the maximum wind speeds of Atlantic storms in the 70th percentile and greater by an analysis of satellite records.

A causal connection between warming in the main cyclogenesis regions and human activities has been established to a high degree of statistical certainty [6, 7]. Future warming in these regions where most tropical cyclones form is virtually certain. However, sea surface temperature is only one of several factors determining tropical cyclone formation and development. Vorticity, humidity, wind shear and moist instability conditions must also be satisfied in the cyclogenesis region [8, 9]. Additionally, a disturbance such as an easterly wave must pass through the cyclogenesis region at a moment when all these conditions are satisfied

for a tropical cyclone to form. Detection and attribution of changes in cyclogenesis factors other than sea surface temperatures have not been presently attained in a formal statistical sense. Progress in this regard is limited not only by climate model characteristics, including resolution, but also by long high quality observational records. Our confidence in climate models' ability to model future changes in these other factors is substantially lower than it is for temperatures [10].

The current generation of coupled global ocean atmosphere models prepared for the Fourth Assessment Report (AR4) of the Intergovernmental Panel on Climate Change (IPCC) are too coarsely resolved to directly simulate tropical cyclones. Nonetheless, some models produce vortices resembling tropical cyclones and have been interpreted in that light [11–13]. The number of high-resolution simulations of tropical cyclone statistics is limited. An innovative approach to reduce the computational burden uses a limited area north Atlantic basin hurricane prediction system forced with the output from coarser global climate models [14–16]. However, computational capabilities have increased to the point where it is feasible to run global models at resolutions high enough to directly simulate some aspects of tropical cyclones. Oouchi et al. [17] integrated an atmospheric model at high-resolution (a spectral truncation of T959, approximately 20 km at the equator) and found that the model could simulate some aspects of tropical cyclone behavior realistically and ran it long enough to generate robust statistical information. Zhao et al. [18] integrated a four member ensemble of a 50 km global atmospheric model finding a strong correlation between north Atlantic sea surface temperature (SST) and tropical cyclone count consistent with observations. They also found that future north Atlantic tropical cyclone frequency was more dependent on changes in a relative SST index rather than on changes in SST itself. In this paper, we present results from another high horizontal resolution atmospheric general circulation model (AGCM) that we find realistically simulates some aspects of individual tropical cyclones.

The model used in this paper is the finite volume dynamics form of the Community Atmospheric Model version 2.2 (fvCAM2.2). The ability of the model to simulate tropical cyclones is dependent on horizontal resolution. Most of the results presented here are at a horizontal resolution of $0.5^\circ \times 0.625^\circ$, which is about 50 km at the equator. At this resolution, we performed a simulation of the period 1979–1996 to compare the model's tropical cyclone statistics with observations. We have also performed a short integration at $0.25^\circ \times 0.375^\circ$ and find that details of the individual tropical cyclones produced are yet more realistic than they are at the coarser resolution. A lower resolution simulation of the period 1979–1994 at $1.0^\circ \times 1.25^\circ$ was also performed further demonstrating the effect of resolution on tropical cyclones. At all three horizontal resolutions, the vertical structure of the model is identical to the 26 layers as in the standard NCAR release of $2.0^\circ \times 2.5^\circ$ horizontal resolution. Also, in all experiments described here no tuning or other modifications to the physics parameterizations were imposed.

In Section 2, we present results from a model simulation of the recent past and compare model tropical cyclone statistics with observations. In Section 3, we present results from the model forced under a future climate change scenario to investigate the sensitivity of the model's tropical cyclone statistics to increases in sea surface temperature (SST). In the future scenario experiments, we alter only SST and do not alter the atmospheric greenhouse gas concentrations or other radiative forcing agents. One study [19] has examined this issue and found that both increases in SST and atmospheric CO_2 concentration independently cause a reduction in total tropical storm frequency in a different model. The direct radiative forcing effect is not included in our experimental design. In Section 4, we conclude with a discussion of these results and comparison to other estimates of the changes in possible future tropical cyclone activity.

2. fvCAM2.2: A Present Day Simulation

fvCAM2.2 is an intermediate release version of the Community Atmospheric Model developed at the National Center for Atmospheric Research (NCAR). This particular version shares many similarities to the atmospheric component of the Community Climate System Model (CCSM3.0). The principal difference is that the solution of the dynamics equations is performed using a finite volume approach [20–23]. Significant differences in the parameterization of sub-grid scale processes include cloud microphysics and radiation processes (Collins, et al. 2006). We performed a simulation of the recent past following the standard Atmospheric Model Intercomparison Project (AMIP2) protocol [24] over the period 1979 to 1996. The ocean and sea ice in the AMIP2 protocol is treated as a lower boundary condition with specified time varying values and distributions. Monthly varying sea surface temperatures and sea ice extent fields were generated by the Program for Climate Model Diagnosis and Intercomparison (PCMDI) with their standard algorithm for this study [25]. Simulations were integrated at three different horizontal resolutions, $1.0^\circ \times 1.25^\circ$, $0.5^\circ \times 0.625^\circ$ and $0.25^\circ \times 0.375^\circ$. The standard vertical resolution of 26 vertical layers in the public release version of the model was retained [26], as was the hydrostatic approximation. The actual code was closely related to the publicly released version of CAM2.2, with significant changes only to the parallel computing domain decomposition strategies [27]. These changes were necessary to permit the usage of large number of processors allowing the numerical integration to proceed in a tolerable amount of time.

2.1. Ability of fvCAM2.2 to Capture the Dynamical Features of Tropical Cyclones. At moderate to high horizontal resolutions, the model produces many incidences of high local vorticity. Many of these events are identified to have characteristics of tropical depressions, tropical cyclones, and even hurricanes. These events are self-initializing from the numerical algorithm itself without any artificial stimulus or external forcing and vary considerably in maximum wind

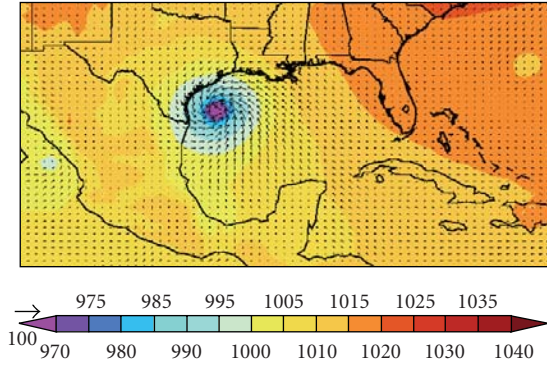


FIGURE 1: Instantaneous mean sea level pressure (in color) and surface wind (10 meter) vectors (as arrows) of the strongest Atlantic tropical cyclone in the $0.5^\circ \times 0.625^\circ$ horizontal resolution AMIP simulation. Pressure in hPa, the wind vector scale in miles per hour is to the left of the color bar.

speed, local pressure minima, vertical structure, and trajectory. In a lengthy climate simulation, it is not appropriate to attempt a comparison to any specific observed tropical storm, as individual weather events are not predictable after a few weeks due to the chaotic nature of the atmosphere [28]. Nonetheless, analysis of individual simulated events can reveal if the model produces some of the typical behaviors associated with real storms.

In Figure 1, the strongest Atlantic storm simulated at the $0.5^\circ \times 0.625^\circ$ horizontal resolution is shown just before it makes landfall. At the time shown, this storm is at its greatest intensity. The maximum surface wind speed (at 10 meters) is 116 knots (133 miles per hour) and the surface pressure at the vorticity center is 945 hPa, which occurred just prior to landfall. On the Saphir-Simpson scale, these values would categorize this simulated storm as a category 4 hurricane. Over the course of the event, it maintained category 1 hurricane status or greater for 5 days. The storm quickly lost strength as it crossed into Texas and dissipated in a few simulated days.

In addition to the high winds and low pressure centers, other features of the simulated storms offer additional realism. In Figure 2, the scalar surface (10 m) wind speed and surface pressure isobars of this same simulated storm are shown 12 hours prior to that shown in Figure 1. Also, the trajectory of the storm up until landfall is shown by the thick dashed line. When this storm passed over the Yucatan Peninsula, it weakened somewhat. Later as it passed into the middle of the Gulf of Mexico, it reorganized and became more symmetric in its surface pressure structure. Real tropical cyclones and hurricanes often exhibit stronger winds along the leading edge of the storm and weaker winds along the trailing edge. This is also evident in this and other simulated storms that are far from land. Note the asymmetry of the colors representing scalar wind speed but the symmetry of the isobars. Wind speed asymmetry of this sort is a dynamical consequence as the storm's rotational velocity and its translational velocity add to produce the net wind speed. It is reassuring that the model maintains this

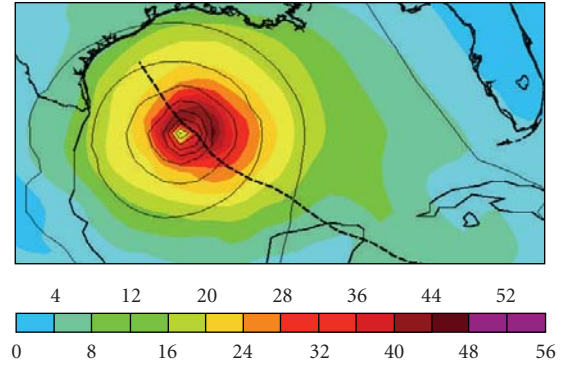


FIGURE 2: Instantaneous surface (10 meter) wind speeds (in color) and surface pressure (as isobars) for the same storm twelve hours earlier than in Figure 1. The storm center trajectory is shown as a thick dotted line. Units of wind speeds are m/s.

dynamical consistency. Note also that a hurricane eye (in velocity) is simulated although only a single velocity point on this Arakawa B-mesh [29] has near zero winds at this resolution.

The ability of the model to simulate tropical cyclones and hurricanes depends greatly on horizontal resolution. In general, as grid spacing is reduced, the strength of the most intense simulated storms increases. Hence, for a given magnitude, the number of simulated storms increases as horizontal resolution is increased. A twelve month simulation at a $0.25^\circ \times 0.375^\circ$ horizontal resolution was also performed. Although it is difficult to quantify how many more storms of a given intensity are simulated per year in this simulation due to the short integration period, several interesting storms of hurricane class are produced. Because of the higher fidelity, additional realism along with greater intensities is seen in these simulated storms. In Figure 3, the instantaneous precipitation is shown for a category 4 storm in September off the coast of the Bahamas simulated at the $0.25^\circ \times 0.375^\circ$ horizontal resolution. At the moment shown in Figure 3, the storm's maximum winds are 100 knots and the low pressure is 963 hPa. In this figure, the spiral and banded nature of intense precipitation exhibit some realism. Note especially the two intense precipitation bands exceeding 90 mm/day on either side of the hurricane center. Also note the long arms of precipitation extending towards the southeast and southwest. These features trail and rotate about the overall motion of the storm. However, even at this resolution there is no suppression of precipitation in the center of the eye of the storm. Although this storm is more compact than the less finely resolved storm in Figure 1, other storms at this resolution need not be so.

Strong tropical cyclones transport large amounts of heat energy from the ocean surface to high altitudes. Such an upper air temperature positive anomaly is one of the signatures of these events. In Figure 4, a vertical cross section of the air temperature of the storm in Figure 3 is shown at a slightly later time. This east-west cross section is a slice at 34.25°N across longitude lines intersecting the center of

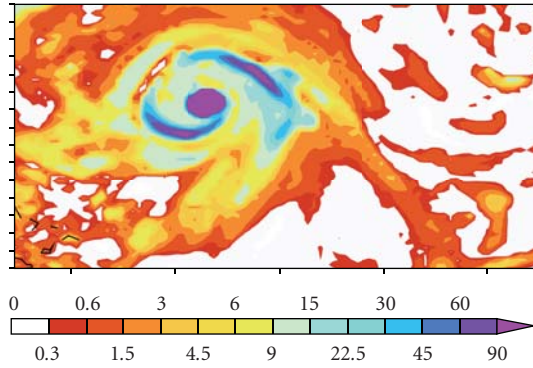


FIGURE 3: Instantaneous precipitation rates during an intense simulated North Atlantic hurricane at the $0.25^\circ \times 0.375^\circ$ horizontal resolution. Units are mm/day.

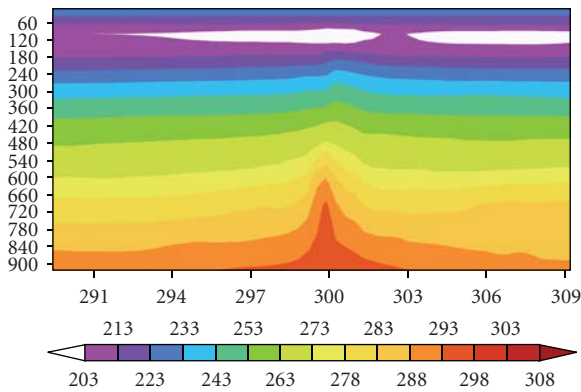


FIGURE 4: Vertical cross section of the air temperature at 34.25°N through the center of a simulated Atlantic tropical cyclone. Warm air is advected upwards inside the region of high vorticity. Air temperature units are Kelvin. Units of the vertical axis are hPa. The horizontal axis spans $290^\circ\text{--}309^\circ\text{W}$.

the storm. The model exhibits realistic upwelling of heat from the ocean surface to higher altitudes as seen by the elevated temperatures near the storm center at 300°W . The air temperature anomaly at 500 hPa is up to 10 K. At this point in time, the storm's northwestwards motion slightly tilts the tower of warm air to the east at the higher elevations.

2.2. Ability of fvCAM2.2 to Capture the Statistical Features of Tropical Atlantic Cyclones. Simulated storms such as the ones considered in the previous section occur spontaneously in the course of the integration long after any memory of the initial conditions is lost. Thus there is no direct relationship between these simulated storms and actual storms. However, data collected from the seventeen-year $0.5^\circ \times 0.625^\circ$ fvCAM2.2 AMIP simulation do permit a statistical comparison with actual storms. Identification of simulated tropical cyclones in this dataset was made by possible by running it through a tropical cyclone tracking program [15]. Developed at the Geophysical Fluid Dynamics Laboratory (GFDL), it produces storm tracks as well as summary statistics describing storm intensity by first finding

colocated vorticity centers and local pressure minima, then identifying if the 300 mb to 500 mb average temperature is anomalously high relative to the surroundings and if the 1000 mb to 200 mb thickness is anomalous in that region. The tracking program was confined to ocean points to between 40°S and 40°N . All other parameters used in the tracking program were the same as described in Appendix B of Knutson et al. [15].

In the AMIP simulation, the $0.5^\circ \times 0.625^\circ$ fvCAM2.2 produced over the entire globe 165 ± 8 tropical storms per year of which 97 were of hurricane strength or greater and 23 were of intense hurricane strength. The model is overactive in its simulation of tropical storms when compared to the observational estimate of Frank and Young [2]. In that study, they estimate 87 ± 8 tropical storms of which 49 ± 7 are of hurricane strength and 16 ± 5 are of intense hurricane strength. As is discussed in more detail below the model actually produces too few storms in the Atlantic basin. Hence, most of the tropical storms and nearly all of the simulated intense hurricanes were produced in the Pacific basin with these numbers significantly exceeding the observations. This overprediction of the ratio of Pacific to Atlantic tropical storms has been documented in a few other models [18].

A fifteen-year (1979–1994) AMIP-type simulation of fvCAM2.2 at $1.0^\circ \times 1.25^\circ$ permits a statement about the effect of horizontal resolution on tropical cyclone statistics. At this coarser resolution, the model produced a global average of only 52 tropical storms per year of which 25 were of hurricane strength. Although, the tropical storms are weaker than at the finer resolutions in general, the strongest storm in this simulation experienced maximum winds of 111 knots and a pressure minimum of 935 mb. However, only 11 tropical storms were produced in the north Atlantic basin over the entire simulation period.

Tropical storms in the North Atlantic basin are generally better observed than elsewhere with routine flights directly into them. This permits a much more detailed comparison in the North Atlantic of tropical cyclone statistics. The North Atlantic storm tracks produced from 1979 through 1996 by the model in the $0.5^\circ \times 0.625^\circ$ configuration are shown in upper panel of Figure 5. The observed storm tracks in this region over this period are shown for comparison in lower panel of Figure 5. The source of the observed storm data is the UNISYS Best Track database (available at <http://weather.unisys.com/hurricane/>). There are 173 actual storms and 83 simulated storms of tropical storm strength or greater identified by the tracking algorithm during this period in the North Atlantic basin. Most of the simulated storm tracks follow realistic paths despite biases in the mean atmospheric state (see the discussion in Section 4). However, we note that the model initiates too many tropical cyclones in the Caribbean and too few in the Eastern Atlantic.

Professor Gray and his team at Colorado State University have been statistically forecasting North Atlantic hurricane activity for many years [30, 31]. The standards that the group applies to their forecast to measure success are also useful in assessing the ability of the model integration in this study to simulate tropical cyclone statistics. Professor Gray's

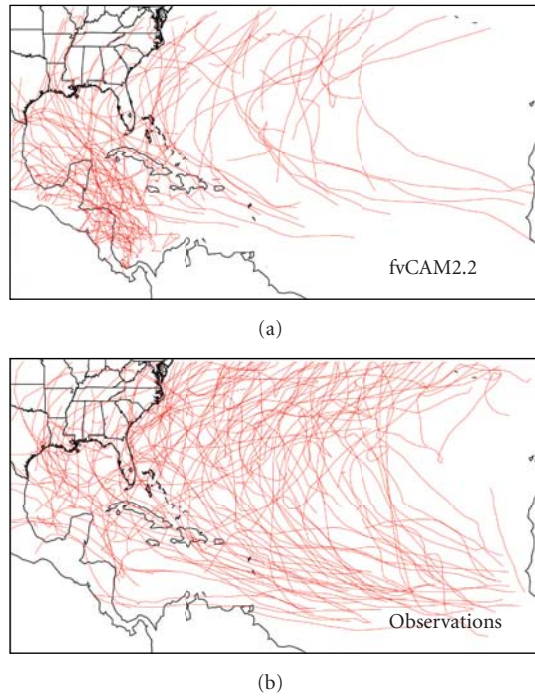


FIGURE 5: Simulated (a) and observed (b) tropical Atlantic cyclone storm tracks. The period is 1979 to 1996 and the model resolution is $0.5^\circ \times 0.625^\circ$.

group defines seven simple numbers describing the Atlantic hurricane season shown in Table 1. The first four of them are easily comparable between the model and observations.

At the $0.5^\circ \times 0.625^\circ$ resolution, the model produced about half as many named tropical storms and a little less than half as many hurricanes in the north Atlantic basin than the observations as shown in Table 2. The total duration of the simulated named storms were shorter than the actual storms but the average simulated storm lasted about two days longer than the average real storm. At hurricane intensity, the model produced less total storm days with the average storm about half as long as the real storms over the 1979–1996 period.

As mentioned before, the ability to simulate high vorticity and associated winds is quite dependent on the model's horizontal resolution. Only three intense hurricanes (Category 3 or larger) in the north Atlantic basin were simulated over the seventeen-year simulation period. It is likely that a long simulation at higher horizontal resolution would produce a greater number of storms of hurricane intensity. Our simulation of fvCAM2.2 at the $0.25^\circ \times 0.375^\circ$ resolution could only be integrated for twelve months due to constraints on computer time allocations. However, two category 3 north Atlantic hurricanes were produced at this higher resolution with minimum pressures of 946 and 966 mb with each storm exceeding 105 knots despite the relatively short integration period. The $0.5^\circ \times 0.625^\circ$ configuration of the model produced multiple storms of Category 3 and 4 in the Pacific basin in every simulated year of the AMIP integration. It never produced a category 5 storm in any ocean basin.

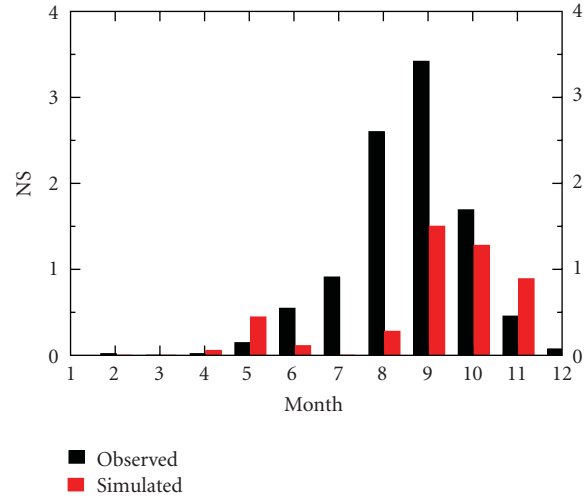


FIGURE 6: The average number of named Atlantic tropical storms per month in $0.5^\circ \times 0.625^\circ$ fvCAM2.2 and observed.

Tropical storms in the Atlantic basin follow a distinct seasonal cycle dictated both by sea surface temperature and wind shear conditions. A comparison in Figure 6 of the seasonality of Atlantic tropical storms in the $0.5^\circ \times 0.625^\circ$ version of fvCAM2.2 and in the real world reveals that model is a bit late in its timing of the hurricane season. The period shown here is 1979 to 1996. The model produces a few weak storms in months when there are practically no observed tropical cyclones (December through May). None of these form into hurricane strength.

Tropical cyclones exhibit significant interannual variability. Although the AMIP protocol specifies realistic monthly averaged sea surface temperatures for each year of the simulation, one should not expect the modeled tropical cyclone activity to agree with observations on a yearly basis because of the other factors important to cyclogenesis that are not constrained. In fact, the model does exhibit substantial interannual variability in the number of North Atlantic tropical storms as shown in Figure 7. Although the standard deviation of the observed and simulated annual storm counts are similar, the two-time series are not highly correlated (correlation factor ~ 0.4). Other models have exhibited a stronger relationship between interannual temperature variability and tropical storm count in the North Atlantic [18, 32].

3. Future Changes in Simulated Tropical Cyclone Activity

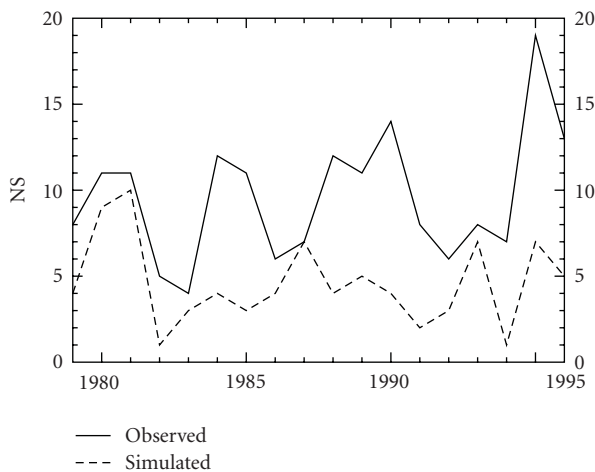
Historical changes in the intensity of tropical cyclones and hurricanes are strongly correlated with sea surface temperature (SST) changes in the cyclogenesis regions. While factors such as wind shear, moisture availability, and atmospheric stability also influence tropical cyclone genesis and evolution, there is emerging evidence that SSTs may play a dominant role in the late 20th century increase in intense hurricanes [4, 33]. Attribution of recent increases in

TABLE 1: Professor Gray's seven hurricane summary statistics.

NS	Named Storms	Number of storms with winds exceeding 35 knots
NSD	Named Storm Days	Number of storm days with winds exceeding 35 knots
H	Hurricanes	Number of storms with winds exceeding 64 knots
HD	Hurricane Days	Number of storm days with winds exceeding 64 knots
IH	Intense Hurricanes	Number of storms with winds exceeding 96 knots
IHD	Intense Hurricane Days	Number of storm days with winds exceeding 96 knots
NTC	Net Tropical Cyclone Activity	A relative measure of a given year's tropical cyclone activity.

TABLE 2: North Atlantic values of the first four of Professor Gray's hurricane summary statistics for the model and observations for the period 1979–1996.

	NS	NSD	H	HD
Observations	9.6	54.1	5.6	21.5
fvCAM2.2 $0.5^\circ \times 0.625^\circ$	4.8	34.5	2.4	4.5

FIGURE 7: The annual number of named Atlantic tropical storms (NS) per year produced by $0.5^\circ \times 0.625^\circ$ fvCAM2.2 compared to observations. The model and observed mean values are 4.6 and 9.6 and their standard deviations are 2.4 and 2.9, respectively.

cyclogenesis region SSTs to human-induced changes to the atmospheric composition suggests that future increases are highly likely [6, 7].

Three future scenarios defined in the IPCC “Special Report on Emissions Scenarios” were widely simulated by the global climate modeling community [34]. These scenarios span the range from minimal (A2), to moderate (A1B) and to aggressive efforts (B1) to reduce greenhouse gas emissions and are well represented in the publically accessible CMIP3 database of climate model integration [35].

In Figure 8, the predicted annual mean sea-surface temperature anomalies in the Atlantic Cyclogenesis Region (ACR) over the 21st century are shown. The ACR is the main development region for tropical cyclogenesis in the North Atlantic and spans 6° – 18° N by 300° – 340° W. Results from simulations of 20th century climate change experiment (20c3m) are also given. All modeled SST changes are

the averages of multimodel ensembles. Observational SST changes are shown from two independent sources: ERSST, Extended Reconstructed SST data set [36] and HadISST, the Hadley Centre Sea Ice and SST data set [37]. Anomalies were calculated with respect to climatological annual means over 1900–1909, and spatially averaged over 6° N– 18° N, 60° W– 20° W. Uncertainty in the model results is represented by the shaded envelopes, which are the 1σ confidence intervals calculated across the ensemble of different models.

The prediction envelope encompasses a wide range of possibilities. The upper boundary, with SST increases of nearly 4.0° C by 2100, is set by models with high climate sensitivities run with the A2 scenario. The lower boundary of the envelope, which is dictated by low-sensitivity models driven by the low emission rate B1 scenario, yields an SST increase of about 1.5° C by the end of the 21st century. To put this increase in historical perspective, note that observed SST changes in the ACR range from 0.41 to 0.67° C over the 20th century. Thus, even the lower boundary of the changes predicted to occur by 2100 represents an approximate doubling of the 20th century warming. Such an increase is well outside the range of model-based estimates of natural climate variability [6]. Similar behavior is seen in the main development region (5° N– 15° N, 180° E– 130° E designated below as PCR) for north Pacific tropical cyclones as well.

Note that the model-average SST changes in the A2, A1B, and B2 scenarios are virtually identical until roughly 2030, and begin to diverge thereafter. The model-average warming over the next 20–30 years is nearly as large as the warming over the entire 20th century. By the end of the 21st century, the uncertainties associated with future greenhouse-gas emission rates are the largest contributor to the total prediction uncertainty, and there are large and statistically significant differences between the SST changes in the three scenarios. The ensemble-mean SST changes in 2100 range from 2.0 to 3.5 Kelvin. Such large increases would be truly unprecedented if realized.

In view of the historical relationship between cyclogenesis region temperatures and hurricane intensity [38], these projections of future cyclogenesis region SST changes motivate an investigation of potential changes in future tropical cyclone statistics by direct simulation. To investigate the sensitivity of the tropical cyclone statistics to increases in SST, we performed a second numerical experiment of two ensembles. In this set of simulations, we integrated an ensemble of fifteen simulations of the late 20th century

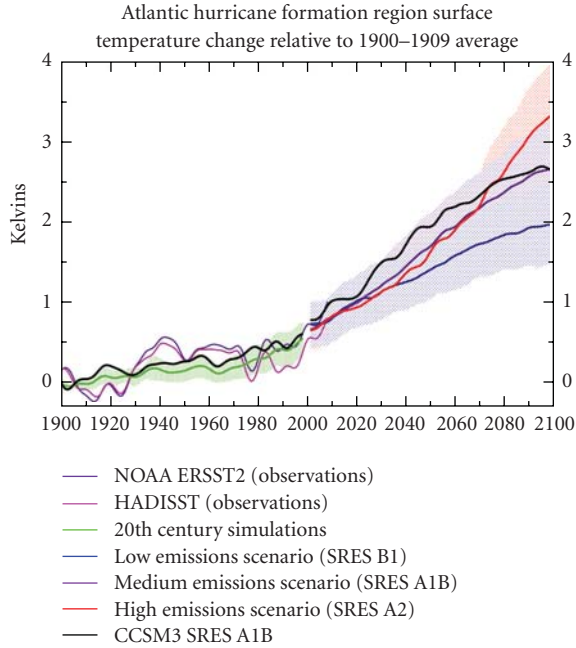


FIGURE 8: Modeled and observed annually averaged SST changes over the Atlantic cyclogenesis region. Model results are multi-model averages for the 20th and 21st centuries. Observed changes are for the 20th century only. All anomalies were defined relative to climatological means over 1900–1909. The shaded envelopes are the 1σ confidence intervals calculated across the ensemble of simulated SST changes from different models. All data were smoothed by application of a 13-point binomial filter. The amplitude of simulated and observed SST variability over the 20th century is not directly comparable because simulated changes are averaged over realizations and models, thus damping climate noise. The CCSM3.0 result is shown for reference.

using the 1990–1999 climatological monthly SST values. The annual cycle was retained in this averaged surface forcing. A second ensemble of fifteen integrations was completed with only the SSTs changed to represent a future climate state. The SST change was constructed by adding the monthly average SST change predicted over 2090–2098 from an ensemble of eight realizations of CCSM3.0 forced under the A1B future scenario to the 1990–1999 climatological monthly SST. CCSM3.0 was chosen as the closest related model to fvCAM2.2 and its 2090–2098 average change over the Atlantic cyclogenesis region is 2.65 Kelvin. The solid black curve in Figure 8 shows the ACR response of CCSM3.0 relative to the other CMIP3 models. The spatial structure of the predicted SST change was retained in the construction of the future temperature forcing. Each member of the ensemble was initialized with slightly different initial conditions leading to statistically identical but randomly distributed realizations of the model climate. Also, as our original intent was to focus on the Atlantic basin, the simulations spanned a six-month period from July 1 to December 31, in order to increase the number of Atlantic hurricanes produced. However, the results found are interesting for other ocean basins and we will discuss them here as well.

The initial conditions for both the future and past ensembles were chosen from the AMIP simulation described in the previous section. To remove the effect of these initial conditions, we discarded the first simulated month (July) from our analysis allowing the model to generate statistically identical independent realizations [28]. We also discarded the last month (December) of each simulation to ensure a uniformity of the output data, as a few runs did not complete the last few days due to computer hardware issues. In the AMIP experiment, the model averaged 66.8 tropical storms across the globe with winds exceeding 33 knots during the August through November period. The 1990–1999 ensemble of this sensitivity experiment averaged 62.7 such storms during these months. This difference is within both the interannual standard deviation of the AMIP simulation and the interrealization standard deviation of the 1990–1999 ensemble of the sensitivity experiment. Hence, we are comfortable that the choice of the time averaged surface forcing in the sensitivity experiment produces representative tropical cyclone statistics.

A comparison of the 1990–1999 ensemble with the A1B 2090–2099 ensemble reveals a dramatic increase in the number of tropical storms with winds in excess of 33 knots. Figure 9 shows this increase globally, hemispherically and in the ocean basins with tropical cyclone activity. Because the analysis is confined to the August through November period, most of the storms are located in the Northern Hemisphere. Statistical confidence in these changes is high both in the Northern Pacific and in the North Atlantic basins. Changes in tropical storm count are also statistically significant in the Southern Hemisphere, although the analysis period is out of phase with most of the tropical storms over this part of the ocean. A summary of the tropical storm counts represented by Figure 9 is shown in Table 3. The null hypothesis that there is no difference between the number of “named” tropical storms in the two ensembles may be rejected with a confidence level of 99.9% or higher in all basins based on Student’s test statistic.

Not only does the number of “named” storms increase when the model is forced with the higher A1B emissions scenario SSTs, the strongest storms get stronger. The average maximum wind speed of the strongest storm in each realization increases from 113 knots to 119 knots while the average minimum pressure in those storms decreases from 938 mb to 931 mb. Figure 10 shows an increase in each category of the Saffir-Simpson Hurricane Scale when the SSTs are increased. The null hypothesis of no change in the number of storms in each of these categories may be rejected with high confidence except for that of Category 2 hurricane intensity. Table 4 summarizes the changes in tropical storm number as a function of intensity.

4. Discussion

4.1. The Relationship of Simulated Future Tropical Cyclone Statistics to Large-Scale Climatological Features. We have demonstrated that the simulated tropical cyclones statistics produced by one particular model, fvCAM2.2, exhibit a

TABLE 3: Average number of tropical storms with wind in excess of 33 knots during the August–November period simulated in fvCAM2.2 as shown in Figure 9. Percent change is shown in the 4th column relative to the 1990–1999 ensemble average. Student’s test statistic, calculated with 14 degrees of freedom is shown in the 5th column. The last column shows the level of confidence for the rejection of the null hypothesis of no change in the number of tropical storms.

	Present no. of tropical storms	Future no. of tropical storms	Percent change	Student’s test statistic	Statistical significance of change
Global	62.7	87.7	40%	11.5	>99.9%
Northern Hemisphere	51.9	71.6	38%	11.5	>99.9%
Southern Hemisphere	10.7	16.1	51%	4.7	>99.9%
North Pacific	40.0	51.2	28%	7.5	>99.9%
North Atlantic	5.1	8.6	70%	5.6	>99.9%
South Pacific	0.7	2.6	250%	4.9	>99.9%
Indian Ocean	12.5	18.3	47%	5.0	>99.9%

TABLE 4: The average number of tropical storms across the globe during the August–November period as characterized by the Saffir–Simpson scale simulated by fvCAM2.2 as shown in Figure 10. Percent change is shown in the 4th column relative to the 1990–1999 ensemble average. Student’s test statistic, calculated with 14 degrees of freedom is shown in the 5th column. The last column shows the level of confidence for the rejection of the null hypothesis of no change in the number of tropical storms. The “present” ensemble is forced with 1990–1999 sea surface conditions. The “future” ensemble is forced with sea surface conditions representative of the SRES A1B scenario at the end of the 21st century.

	Present no. of tropical storms	Future no. of tropical storms	Percent change	Student’s test statistic	Statistical significance of change
All named storms	62.7	87.7	40%	11.5	>99.9%
Tropical storm	25.8	40.9	59%	6.7	>99.9%
Category 1	20.1	24.3	21%	3.04	>99.5%
Category 2	8.3	9.5	15%	1.09	<90%
Category 3	7.9	10.3	29%	2.24	>97.5%
Category 4	0.5	2.6	387%	3.76	~99.9%

pronounced sensitivity to changes in sea surface temperature. Forced by SSTs typical of a mid-range global warming scenario (SRES A1B), the strongest storms produced in the model became more intense (Figure 10). This is in agreement with independent studies from three other groups that have explored this issue using relatively high-resolution models [13, 16, 17, 39] Bengtsson 2007. Such intensification is also consistent with the theoretical notion of tropical cyclones as giant heat engines [40] and the changes in the model’s climatology. An examination of the changes in large-scale features of the atmosphere relevant to tropical cyclones is revealing. The monthly mean windshear in the ACR and PCR (Figure 11) does not change significantly in the ensemble of future scenario runs compared to the AMIP simulation. Note that modeled wind shear is substantially higher than ERA40 reanalysis in the Atlantic hurricane season. Hence, the chances of the low wind shear conditions in the cyclogenesis regions necessary for intense storms do not change much in the future simulation. The total column water vapor (Figure 12) increases in the warmer integration, a consequence of the ability of warmer air to hold more water [6]. This implies that more latent heat energy would

be available for tropical cyclones also supporting the notion that stronger storms are possible in the future simulation. Emanuel’s [40] thermodynamical description of tropical cyclones as Carnot heat engines transporting energy from the surface to higher altitudes can be expressed by a maximum potential intensity (MPI) of surface winds and is straightforwardly calculated assuming ideal wind shear conditions. In Figure 13, the average July through November change in the maximum potential intensity (MPI) of tropical storm winds per degree warming is shown for the ensemble of climate change experiments and is comparable to the multi-model ensemble result calculated by Vecchi and Soden [41]. Changes in MPI are principally driven by changes in future SSTs which can vary a great deal between models. fvCAM2.2 exhibits an increase in MPI across most of the Northern Pacific similar in magnitude and pattern to the Vecchi and Soden multi-model average. In the small area of the northwestern Pacific where the multi-model average shows little change, fvCAM2.2 exhibits a decrease similar to another model as detailed by Xie et al. [42] but smaller in extent and magnitude. In the north Atlantic, a band of MPI decrease extending from Gibraltar towards the southwest

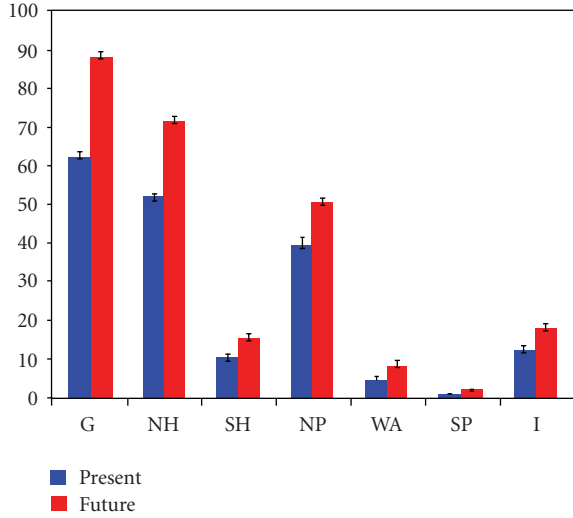


FIGURE 9: Average number of tropical storms with wind in excess of 33 knots during the August–November period simulated in fvCAM2.2. The “present” ensemble is forced with 1990–1999 sea surface conditions. The “future” ensemble is forced with sea surface conditions representative of the SRES A1B scenario at the end of the 21st century. The error bars represent the inter-realization standard error for each ensemble. G: global, NH: Northern Hemisphere, SH: Southern Hemisphere, NP: North Pacific basin, NA: North Atlantic basin, SP: South Pacific basin, I: Indian Ocean.

divides two areas of MPI increase. This region of MPI decrease is similar in its east-west extent to the multi-model average but narrower in its north-south extent. In this regard, the present result resembles that of Xie et al. [42]. Because of these climatological changes in MPI, tropical storms forming under near ideal conditions of low wind shear and high moist instability would more likely undergo the rapid and explosive intensification typical of major storms in fvCAM2.2.

Unlike previous studies [13, 16, 17, 39] Bengtsson, 2007, fvCAM2.2 produced a larger total number of named tropical storms rather than less in every ocean basin with significant tropical cyclone activity when driven by warmer SSTs (Figure 9). In the Table 4 of the present paper, percent increases in the numbers of storms were greatest for the most intense storms produced (category 4) followed by the smallest storms tracked (tropical storm strength). Percent increases in the numbers of category 2 storms were the smallest and not as statistically significant. In the prior studies just cited, the calculations with warmer surface temperatures exhibited a reduction in the number of tropical storms. However, Kusunoki et al. [43] and Sugi et al. [44] find that despite a global decrease in the number of tropical cyclones, the number of tropical cyclones increases in the North Atlantic basin. Bengtsson et al. [13] suggests that a reduction in tropical cyclone number might be due to a slowing down of the large-scale tropical circulation and a resultant decrease in the number of initial disturbances capable of developing into full-scale tropical cyclones. Figure 14 shows the potential temperature for the tropical region 30S–30N averaged over August through November in the $0.5^\circ \times 0.625^\circ$

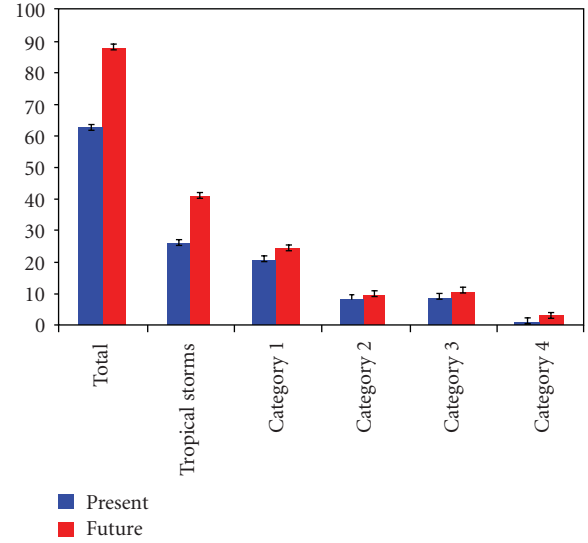


FIGURE 10: The average number of tropical storms across the globe during the August–November period as characterized by the Saffir–Simpson scale simulated by fvCAM2.2. The “present” ensemble is forced with 1990–1999 climatological sea surface conditions. The “future” ensemble is forced with sea surface conditions representative of the SRES A1B scenario at the end of the 21st century. The error bars represent the inter-realization standard error for each ensemble.

configuration of fvCAM2.2. A less steep lapse rate in the simulation of the warmer future atmosphere, evident from the difference in the slopes of the two curves in Figure 14, indicates a more statically stable atmosphere than in the present day simulation. This figure is comparable to Figure 17 in Bengtsson et al. [13] and suggests that the change in static stability in fvCAM2.2 is similar to that seen in the ECHAM5 model, especially above 500 mb.

Zhao et al. [18, 45] show that in a different 50 km model that the difference between SSTs in the cyclogenesis regions and across the entire tropics controls the interannual variations in North Atlantic tropical storms. They also suggest that relative warming defined by this difference could be a factor in the number of future tropical storms. However, for this experiment, the August–September–October average “Atlantic relative SST, Φ_{NA} ” is 1.9 K in the present day configuration and 1.8 K in the end of 21st century configuration. This small negative change in relative warming does not explain the North Atlantic tropical storm response of fvCAM2.2.

4.2. Comments on Future Directions. Both the model and the experimental design are flawed in a number of ways, undermining the confidence in these projections of future tropical cyclone activity. These flaws are not unique to this study and a frank discussion of them can guide future work in this important activity. The integration period for the climate change experiment was chosen to double the number of Atlantic hurricane seasons available for analysis. In hindsight, it would be interesting to include the complete

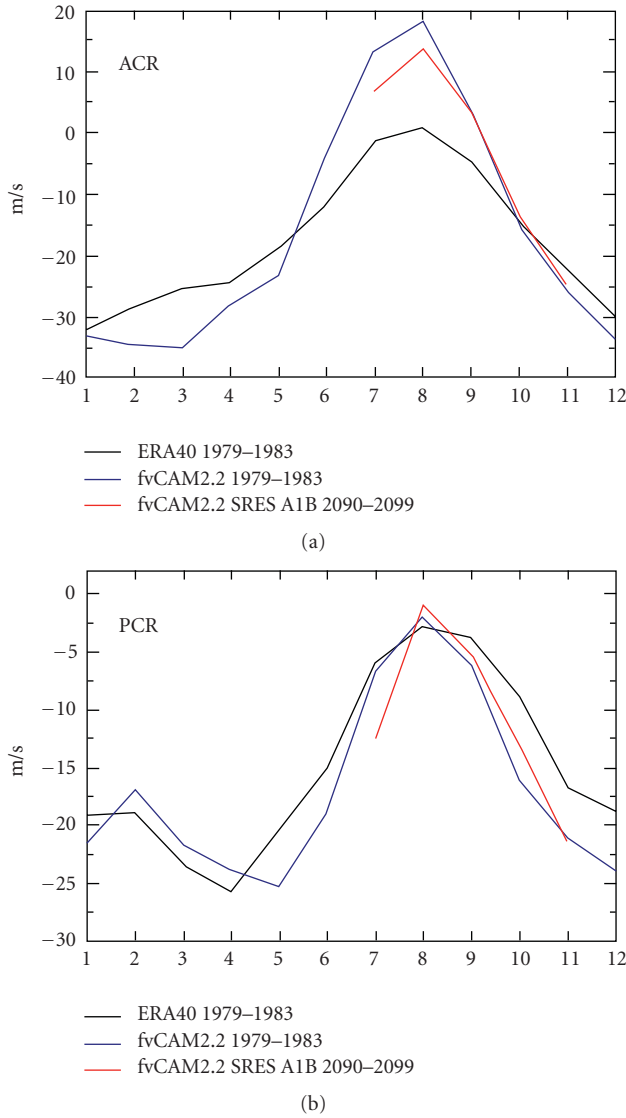


FIGURE 11: The monthly average wind shear (m/s) in the Atlantic (ACR) and Pacific (PCR) Cyclogenesis Regions. Wind shear is defined as the difference between zonal wind speed at 200 mb and 850 mb. Black line: ERA40 reanalysis. Blue line: fvCAM2.2 ($0.5^\circ \times 0.625^\circ$) 1979–1983 average. Red line: fvCAM2.2 ($0.5^\circ \times 0.625^\circ$) 2090–2099 July–November conditions (SRES A1B).

annual cycle so that southern hemisphere tropical cyclones were included in the study. Also, we feel that time slices of selected past and future periods would be more interesting than climatologically averaged integrations in that changes in interannual variability could be studied provided large enough ensembles could be generated.

The AMIP-style integration of fixed SST is a more significant limitation. Intense tropical storms can noticeably reduce the upper ocean temperatures. The infinite heat capacity ocean of the experiments discussed here cannot replicate this effect. A mixed layer ocean model coupled to the AGCM would be an improvement but a coupled ocean-atmosphere general circulation model could capture

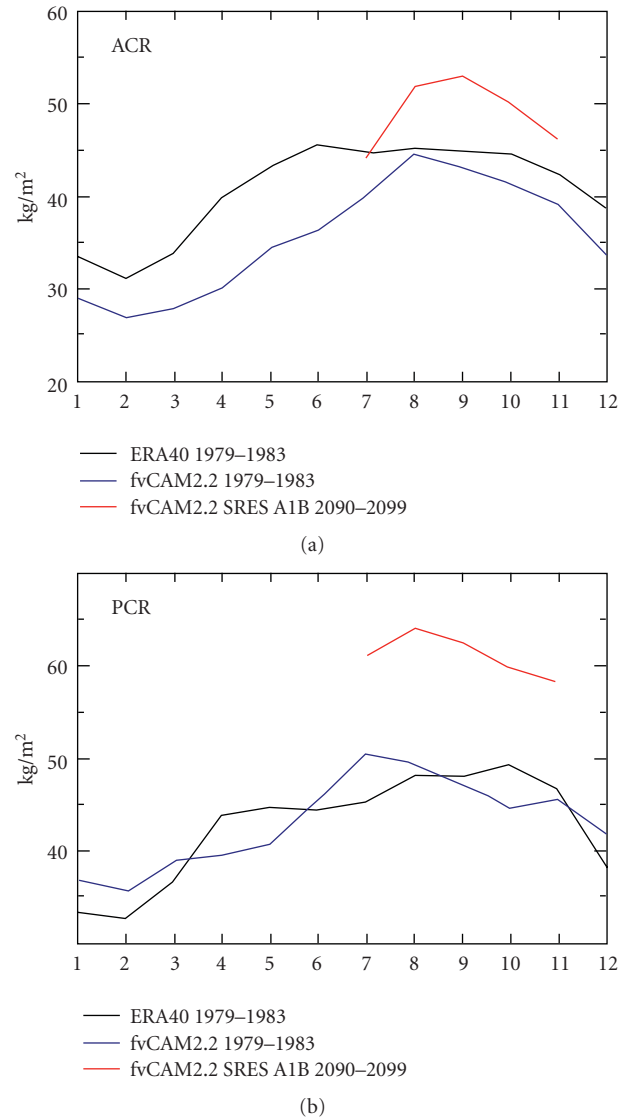


FIGURE 12: The monthly average total column integrated water vapor (kg/m^2) in the Atlantic (ACR) and Pacific (PCR) Cyclogenesis Regions. Black line: ERA40 reanalysis. Blue line: fvCAM2.2 ($0.5^\circ \times 0.625^\circ$) 1979–1983 average. Red line: fvCAM2.2 ($0.5^\circ \times 0.625^\circ$) 2090–2099 July–November conditions (SRES A1B).

the upper ocean layers even more realistically. Spin-up of initial ocean conditions is made somewhat simpler than for typical century-scale integrations as the deep ocean layers do not play as large a role in decadal scale simulations.

The AMIP protocol defines transient forcing only at the surface. However, human induced changes to trace pollutants have a detectable *in situ* influence on the vertical structure of the atmosphere [46]. Single forcing couple climate model runs indicate that stratospheric ozone depletion tends to cool the stratosphere and heat the troposphere. This human induced effect tends to raise the tropopause height, effectively cooling the air temperature at this boundary. In Emanuel's idealized Carnot heat engine model of a perfect

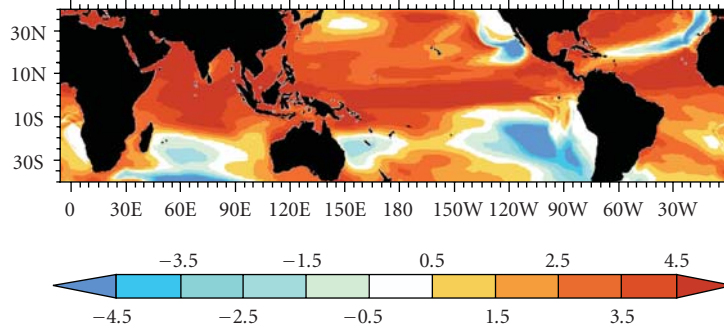


FIGURE 13: The change in maximum potential intensity (MPI) of surface (10 meter) winds (knots/°C) calculated by Emanuel's Carnot heat engine theory in the fvCAM2.2 ($0.5^\circ \times 0.625^\circ$) climate change experiment (SRES A1B). The results are averaged from July 1 to November 30 (JASON) to be comparable to Vecchi and Soden [41].

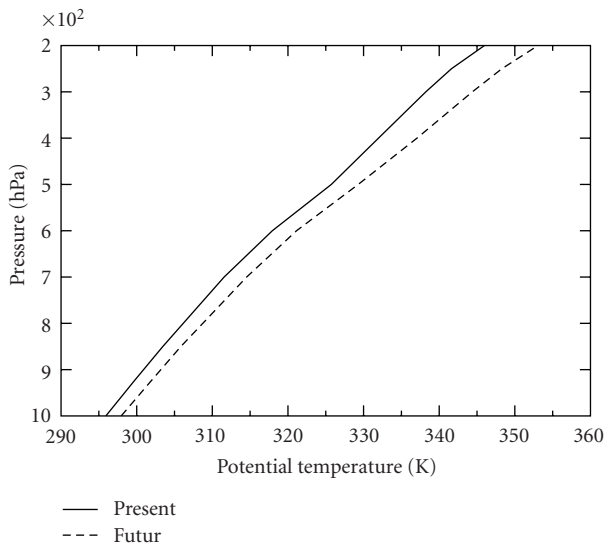


FIGURE 14: Potential temperature in the $0.5^\circ \times 0.625^\circ$ configuration of fvCAM2.2 ($0.5^\circ \times 0.625^\circ$) for the tropical region 30S-30N averaged over August through November illustrating a change in the static stability of the simulated atmosphere.

hurricane [40], such a reduction in top of storm temperature raises the maximum potential wind intensity by making the engine more thermodynamically efficient. Greenhouse gas concentration changes have a similar effect on the vertical temperature profile that is even larger. Conversely, sulfate aerosols tend to increase the temperature of the stratosphere and decrease the temperature in the troposphere, lowering the tropopause height. Hence, increases in atmospheric sulfate aerosols have the opposite effect of stratospheric ozone depletion by lowering Emanuel's maximum potential intensity. The *in situ* change in the atmosphere's vertical structure due to trace pollutants also plays a role in the atmosphere's vertical static stability. The lack of changes in these pollutants in our climate change experiment and the associated change in radiative forcing may be a possible explanation for the increase in the number of weaker

tropical cyclones compared to the decreases seen in other studies. An attempt to investigate the role of this radiative forcing by calculating the change in MPI in an ensemble of SRES A1B and twentieth century CCSM3.0 simulations was inconclusive. Despite more realistic radiative forcing, the CCSM3.0 MPI change does not resemble similar calculations from either the GFDL AM2.1 [42] or the multi-model average [41]. In fact, the fvCAM2.2 MPI change in Figure 13 shares more in common with these two previously published results than does the fully coupled model. However, MPI is not a measure of cyclogenesis and this exercise does not rule out the possibility that future changes in radiative forcing suppress the number of tropical cyclones. A related study by Yoshimura and Sugi [19] varied changes in greenhouse gas forcing and SST independently and found that each reduced the global number of tropical cyclones. Our results, which are similar to the SST variation half of the Yoshimura and Sugi [19] experiment, are at odds with their result. We did not explore the radiative forcing changes directly in this study.

The horizontal resolution necessary to capture the finest details of intense hurricanes in a global climate model is well beyond current computing capabilities. This study focused on a model with a grid spacing of about 50 km at the equator. Consistent with a conjecture by Bengtsson et al. [13], this resolution captured enough of the coarser characteristics of tropical cyclones to permit a reasonable description of storm statistics. However, the strongest storms in the simulation do not exceed Category 4 on the Saffir-Simpson intensity scale and are definitely weaker than the strongest storms in the real world. It is also likely that convergence of strong tropical storm intensity with resolution increases has not completed at 50 km. Fortunately, computing technology continues to progress. We estimate that the fidelity of fvCAM could be doubled to approximately 25 km at the equator yet model integration time could be simulated 350 times faster than real time on 2048 processors of a CRAY XT4 [47]. A fully coupled version of CCSM with a 0.1° ocean and sea ice model would require about twice as many processors and run at half the rate. For comparison, execution speeds of the numerous CCSM3.0 simulations prepared for the IPCC

AR4 report averaged around 1600 times faster than real time. This would be a significant investment in computer resources but is certainly possible on existing and future machines.

There are large model dependencies in the literature regarding tropical cyclone simulation, especially in the ability to simulate intense storms [13, 16–18, 39, 45]. Comparing these studies, it is clear that high horizontal resolution is not the only factor controlling tropical cyclone genesis and development in climate models [18]. A systematic investigation of parameterization differences would be another useful investment in computer resources and could lead to better simulation of tropical cyclone statistics.

5. Conclusions

We demonstrate that fvCAM2.2, a finite volume version of the Community Atmospheric Model, produces surprisingly realistic tropical cyclone statistics with essentially no tuning. In a $0.5^\circ \times 0.625^\circ$ configuration (approximately 50 km at the equator), the model has no difficulty producing Category 4 storms on the Saffir-Simpson intensity scale. The number and distribution of tropical cyclones is sensitive to horizontal resolution and has probably not converged at this grid size. A climate change experiment, based on an IPCC SRES A1B end of 21st century projection of sea surface temperatures, reveals that the change in Emanuel's Maximum Potential Intensity index (MPI) is consistent with other studies [40, 41], Xie et al. 2010. As in similar high-resolution climate change studies [13, 16, 17, 39], an increase in the number of intense tropical cyclones is projected by fvCAM2.2 with the strongest storms becoming more intense. This is expected based on thermodynamic considerations [4]. In contrast to these similar high-resolution studies, fvCAM2.2 produced more overall tropical cyclones, not less as the climate warms. The biggest percent increase occurred in the number of category 4 storms followed by the number of weak named tropical cyclones (wind speeds less than Category 1). The mechanisms for this difference in model behavior are unclear and further numerical experimentation is required. It is also clear that in order to have confidence in projections of future tropical cyclone activity, more high-resolution modeling studies must be performed by independent groups.

Acknowledgments

This work was performed under the auspices of the U.S. Department of Energy (DOE) by the Lawrence Berkeley National Laboratory (LBNL) under Contract no. DE-AC03-76SF00098 (LBNL) and by the Lawrence Livermore National Laboratory under Contract DE-AC52-07NA27344 and with support from the DOE Earth System Modeling Program. The authors are grateful for advice from Joseph Sirutis (GFDL), Michael Fiorino (NOAA), and Benjamin Santer (LLNL). The authors thank the National Center for Energy Research (NERSC) for a generous preacceptance allocation of computational resources.

References

- [1] P. J. Webster, G. J. Holland, J. A. Curry, and H.-R. Chang, "Atmospheric science: changes in tropical cyclone number, duration, and intensity in a warming environment," *Science*, vol. 309, no. 5742, pp. 1844–1846, 2005.
- [2] W. M. Frank and G. S. Young, "The interannual variability of tropical cyclones," *Monthly Weather Review*, vol. 135, no. 10, pp. 3587–3598, 2007.
- [3] G. J. Holland and P. J. Webster, "Heightened tropical cyclone activity in the North Atlantic: natural variability or climate trend?" *Philosophical Transactions of the Royal Society A*, vol. 365, no. 1860, pp. 2695–2716, 2007.
- [4] K. Emanuel, "Increasing destructiveness of tropical cyclones over the past 30 years," *Nature*, vol. 436, no. 7051, pp. 686–688, 2005.
- [5] J. B. Elsner, J. P. Kossin, and T. H. Jagger, "The increasing intensity of the strongest tropical cyclones," *Nature*, vol. 455, no. 7209, pp. 92–95, 2008.
- [6] B. D. Santer, T. M. L. Wigley, P. J. Gleckler et al., "Forced and unforced ocean temperature changes in Atlantic and Pacific tropical cyclogenesis regions," *Proceedings of the National Academy of Sciences of the United States of America*, vol. 103, no. 38, pp. 13905–13910, 2006.
- [7] N. P. Gillett, P. A. Stott, and B. D. Santer, "Attribution of cyclogenesis region sea surface temperature change to anthropogenic influence," *Geophysical Research Letters*, vol. 35, no. 9, Article ID L09707, 2008.
- [8] W. M. Gray, "Hurricanes: their formation, structure and likely role in the tropical circulation," in *Meteorology over the Tropical Oceans*, Royal Meteorological Society, Bracknell, UK, August 1979.
- [9] S. J. Camargo, A. H. Sobel, A. G. Barnston, and K. A. Emanuel, "Tropical cyclone genesis potential index in climate models," *Tellus, Series A*, vol. 59, no. 4, pp. 428–443, 2007.
- [10] C. Covey, K. M. AchutaRao, S. J. Lambert, and K. E. Taylor, "Intercomparison of present and future climates simulated by coupled ocean-atmosphere GCMs," Program for Climate Model Diagnosis and Intercomparison Report 66, 2000, Lawrence Livermore National Laboratory UCRL-ID-140325.
- [11] L. Bengtsson, M. Botzet, and M. Esch, "Hurricane-type vortices in a general circulation model," *Tellus, Series A*, vol. 47, no. 2, pp. 175–196, 1995.
- [12] L. Bengtsson, M. Botzet, and M. Esch, "Will greenhouse gas-induced warming over the next 50 years lead to higher frequency and greater intensity of hurricanes?" *Tellus, Series A*, vol. 48, no. 1, pp. 57–73, 1996.
- [13] L. Bengtsson, K. I. Hodges, M. Esch et al., "How may tropical cyclones change in a warmer climate?" *Tellus, Series A*, vol. 59, no. 4, pp. 539–561, 2007.
- [14] T. R. Knutson and R. E. Tuleya, "Impact of CO₂-induced warming on simulated hurricane intensity and precipitation: sensitivity to the choice of climate model and convective parameterization," *Journal of Climate*, vol. 17, no. 18, pp. 3477–3495, 2004.
- [15] T. R. Knutson, J. J. Sirutis, S. T. Garner, I. M. Held, and R. E. Tuleya, "Simulation of the recent multidecadal increase of Atlantic hurricane activity using an 18-km-grid regional model," *Bulletin of the American Meteorological Society*, vol. 88, no. 10, pp. 1549–1565, 2007.
- [16] M. A. Bender, T. R. Knutson, R. E. Tuleya, et al., "Modeled impact of anthropogenic warming on the frequency of intense Atlantic hurricanes," *Science*, vol. 327, no. 5964, pp. 454–458, 2010.

- [17] K. Oouchi, J. Yoshimura, H. Yoshimura, R. Mizuta, S. Kusunoki, and A. Noda, "Tropical cyclone climatology in a global-warming climate as simulated in a 20 km-mesh global atmospheric model: frequency and wind intensity analyses," *Journal of the Meteorological Society of Japan*, vol. 84, no. 2, pp. 259–276, 2006.
- [18] M. Zhao, I. M. Held, S.-J. Lin, and G. A. Vecchi, "Simulations of global hurricane climatology, interannual variability, and response to global warming using a 50-km resolution GCM," *Journal of Climate*, vol. 22, no. 24, pp. 6653–6678, 2009.
- [19] J. Yoshimura and M. Sugi, "Tropical cyclone climatology in a high-resolution AGCM—impacts of SST warming and CO₂ increase," *Scientific Online Letters on the Atmosphere*, vol. 1, pp. 133–136, 2.
- [20] S.-J. Lin and R. B. Rood, "Multidimensional flux-form semi-Lagrangian transport schemes," *Monthly Weather Review*, vol. 124, no. 9, pp. 2046–2070, 1996.
- [21] S.-J. Lin and R. B. Rood, "An explicit flux-form semi-Lagrangian shallow-water model on the sphere," *Quarterly Journal of the Royal Meteorological Society*, vol. 123, no. 544, pp. 2477–2498, 1997.
- [22] S.-J. Lin, "A finite-volume integration method for computing pressure gradient force in general vertical coordinates," *Quarterly Journal of the Royal Meteorological Society*, vol. 123, no. 542, pp. 1749–1762, 1997.
- [23] S.-J. Lin, "A 'vertically Lagrangian' finite-volume dynamical core for global models," *Monthly Weather Review*, vol. 132, no. 10, pp. 2293–2307, 2004.
- [24] W. L. Gates, "AMIP: the Atmospheric Model Intercomparison Project," *Bulletin—American Meteorological Society*, vol. 73, no. 12, pp. 1962–1970, 1992.
- [25] K. Taylor, D. Williamson, and F. Zwiers, "The sea surface temperature and sea-ice concentration boundary conditions for AMIP II simulations," PCMDI Report 60, 2000, Lawrence Livermore National Laboratory Report UCRL-MI-123395.
- [26] W. D. Collins, P. J. Rasch, B. A. Boville et al., "The formulation and atmospheric simulation of the Community Atmosphere Model version 3 (CAM3)," *Journal of Climate*, vol. 19, no. 11, pp. 2144–2161, 2006.
- [27] A. A. Mirin and W. B. Sawyer, "A scalable implementation of a finite-volume dynamical core in the community atmosphere model," *International Journal of High Performance Computing Applications*, vol. 19, no. 3, pp. 203–212, 2005.
- [28] C. E. Leith, "Climate response and fluctuation dissipation," *Journal of the Atmospheric Sciences*, vol. 32, no. 10, pp. 2022–2026, 1975.
- [29] A. Arakawa and V. R. Lamb, "Computational design of the basic dynamical processes of the UCLA general circulation model," in *Methods in Computational Physics*, J. Chang, Ed., vol. 17, pp. 173–265, Academic Press, New York, NY, USA, 1977.
- [30] P. J. Klotzbach and W. M. Gray, "Twenty-five years of Atlantic basin seasonal hurricane forecasts (1984–2008)," *Geophysical Research Letters*, vol. 36, Article ID L09711, 5 pages, 2009.
- [31] P. J. Klotzbach and W. M. Gray, "The Tropical Meteorology Project," <http://hurricane.atmos.colostate.edu/Forecasts/>.
- [32] T. E. Larow, Y.-K. Lim, D. W. Shin, E. P. Chassignet, and S. Cocke, "Atlantic basin seasonal hurricane simulations," *Journal of Climate*, vol. 21, no. 13, pp. 3191–3206, 2008.
- [33] C. D. Hoyos, P. A. Agudelo, P. J. Webster, and J. A. Curry, "Deconvolution of the factors contributing to the increase in global hurricane intensity," *Science*, vol. 312, no. 5770, pp. 94–97, 2006.
- [34] N. Nakicenovic and R. Swart, Eds., *IPCC Special Report on Emissions Scenarios*, 2000, <http://www.grida.no/climate/ipcc/emission/>.
- [35] G. A. Meehl, C. Covey, T. Delworth et al., "The WCRP CMIP3 multimodel dataset: a new era in climatic change research," *Bulletin of the American Meteorological Society*, vol. 88, no. 9, pp. 1383–1394, 2007.
- [36] T. M. Smith and R. W. Reynolds, "A global merged land-air-sea surface temperature reconstruction based on historical observations (1880–1997)," *Journal of Climate*, vol. 18, no. 12, pp. 2021–2036, 2005.
- [37] N. A. Rayner, P. Brohan, D. E. Parker et al., "Improved analyses of changes and uncertainties in sea surface temperature measured in Situ since the mid-nineteenth century: the HadSST2 dataset," *Journal of Climate*, vol. 19, no. 3, pp. 446–469, 2006.
- [38] K. A. Emanuel, "The dependence of hurricane intensity on climate," *Nature*, vol. 326, no. 6112, pp. 483–485, 1987.
- [39] T. R. Knutson, J. J. Sirutis, S. T. Garner, G. A. Vecchi, and I. M. Held, "Simulated reduction in Atlantic hurricane frequency under twenty-first-century warming conditions," *Nature Geoscience*, vol. 1, no. 6, pp. 359–364, 2008.
- [40] K. A. Emanuel, "Sensitivity of tropical cyclones to surface exchange coefficients and revised steady-state model incorporating eye dynamics," *Journal of the Atmospheric Sciences*, vol. 52, no. 22, pp. 3969–3976, 1995.
- [41] G. A. Vecchi and B. J. Soden, "Effect of remote sea surface temperature change on tropical cyclone potential intensity," *Nature*, vol. 450, no. 7172, pp. 1066–1070, 2007.
- [42] S.-P. Xie, C. Deser, G. A. Vecchi, J. Ma, H. Teng, and A. T. Wittenberg, "Global warming pattern formation: sea surface temperature and rainfall," *Journal of Climate*, vol. 23, no. 4, pp. 966–986, 2010.
- [43] S. Kusunoki, J. Yoshimura, H. Yoshimura, R. Mizuta, K. Oouchi, and A. Noda, "Global warming projection by an atmospheric global model with 20-Km grid," *Journal of Disaster Research*, vol. 3, pp. 4–14, 2008.
- [44] M. Sugi, H. Murakami, and J. Yoshimura, "A reduction in global tropical cyclone frequency due to global warming," *Scientific Online Letters on the Atmosphere*, vol. 5, pp. 164–167, 2009.
- [45] M. Zhao, I. M. Held, and G. A. Vecchi, "Retrospective forecasts of the hurricane season using a global atmospheric model assuming persistence of SST anomalies," *Monthly Weather Review*. In press.
- [46] B. D. Santer, M. F. Wehner, T. M. L. Wigley et al., "Contributions of anthropogenic and natural forcing to recent tropopause height changes," *Science*, vol. 301, no. 5632, pp. 479–483, 2003.
- [47] L. Oliker, J. Carter, M. Wehner et al., "Leading computational methods on scalar and vector HEC platforms," in *Proceedings of the ACM/IEEE Supercomputing Conference (SC '05)*, pp. 62–74, November 2005.

Research Article

Numerical Modeling of the Severe Cold Weather Event over Central Europe (January 2006)

D. Hari Prasad,¹ Joanna Wibig,² and Marcin Rzepa²

¹ Centro de Geofísica (CG/UE), University of Evora, 7000 Evora, Portugal

² Department of Meteorology and Climatology, University of Lodz, 90-131 Lodz, Poland

Correspondence should be addressed to D. Hari Prasad, dasarihariprasad@rediffmail.com

Received 23 January 2010; Revised 26 April 2010; Accepted 15 June 2010

Academic Editor: Zhaoxia Pu

Copyright © 2010 D. Hari Prasad et al. This is an open access article distributed under the Creative Commons Attribution License, which permits unrestricted use, distribution, and reproduction in any medium, provided the original work is properly cited.

Cold waves commonly occur in higher latitudes under prevailing high pressure systems especially during winter season which cause serious economical loss and cold related death. Accurate prediction of such severe weather events is important for decision making by administrators and for mitigation planning. An Advanced high resolution Weather Research and Forecasting mesoscale model is used to simulate a severe cold wave event occurred during January 2006 over Europe. The model is integrated for 31 days starting from 00UTC of 1 January 2006 with 30 km horizontal resolution. Comparison of the model derived area averaged daily mean temperatures at 2m height from different zones over the central Europe with observations indicates that the model is able to simulate the occurrence of the cold wave with the observed time lag of 1 to 3days but with lesser intensity. The temperature, winds, surface pressure and the geopotential heights at 500 hPa reveal that the cold wave development associates with the southward progression of a high pressure system and cold air advection. The results have good agreement with the analysis fields indicates that the model has the ability to reproduce the time evolution of the cold wave event.

1. Introduction

Advance information of extreme weather phenomena such as cold waves is very important to avert their adverse impact on the life and economy of a given region. Prediction of the cold weather events in advance of 15 to 30 days is a challenging issue for the researchers and is useful for the administrators to minimize the damage and for adopting necessary mitigation measures. Cold waves belong to the weather phenomenon which occurs when marked cooling of the air persists for a period of at least few days [1, 2]. Cold waves generally occur with an advection of cold air mass over a large area associated with radiative cooling when a blocking anticyclone develops and persists for at least few days.

Several studies have reported observed strong warming in the end of the nineteen century, with an evident increase in minimum and maximum temperatures in Central and Eastern Europe [3, 4] and in the whole Baltic region [5] indicating that mortality risk increases every winter in Central and Eastern Europe [6]. Though the rise in mean

daily and mean minimum temperatures does not necessarily affect the frequency of extreme cold weather [7]; however it exerts a strong impact on the environment and society.

Numerical simulation of cold waves requires incorporation of the various atmospheric processes in the model such as the interaction of the large-scale atmospheric flow with the local-scale circulation, interaction of the surface and planetary boundary layer (PBL) with the free atmosphere and vice versa, and radiation transfer. In numerical models the subgrid scale processes are parameterized to define their interaction with grid-resolvable prognostic variables. The application of recently developed high resolution atmospheric models like the Advanced Research Weather Forecasting Model (ARW) is expected to improve the prediction of extreme weather events as the regional models are based on more advanced dynamical and physical processes. However, an important aspect of high resolution models is their spin-up time. When operated in climate mode they require simulation lengths exceeding the spin-up time which is of the order of several days [10–16] for

TABLE 1: Details of the ARW model.

Model Name	NCEP/NCAR ARW
Model type	Primitive equation, Non- hydrostatic
Vertical resolution	28 sigma levels 1.000, 0.990, 0.978, 0.964, 0.946, 0.922, 0.894, 0.860, 0.817, 0.766, 0.707, 0.644, 0.576, 0.507, 0.444, 0.380, 0.324, 0.273, 0.228, 0.188, 0.152, 0.121, 0.093, 0.069, 0.048, 0.029, 0.014, 0.000
Horizontal resolution	30 km
Time step	180 Seconds
Domain of integration	6.7624E - 37.2992E; 42.605N - 61.1074N
Short wave radiation scheme	Dudhia scheme
Long wave radiation scheme	Rapid Radiative Transfer Model for long wave radiation
Surface scheme	5-layer thermal diffusion scheme
Convection scheme	Kain- Fritsch (KF) [8, 9].
PBL scheme	YSU scheme
Explicit moisture scheme	WSM 3-class Simple Ice
Initial and boundary conditions	NCEP reanalysis data available at 2.5 degree and boundary conditions are updated every 6-hour interval

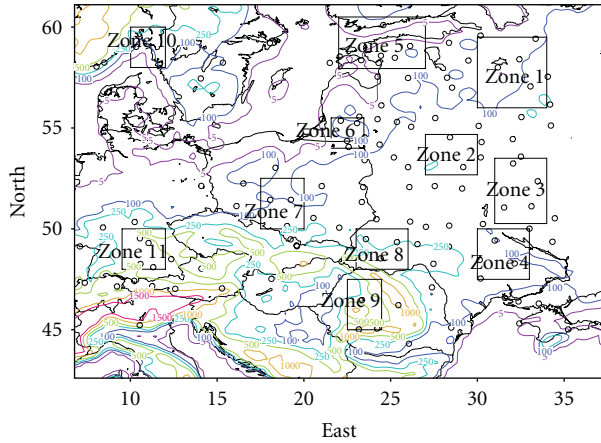


FIGURE 1: Model chosen domain along with the topography. The circles indicate the available station observation over the domain during 1–31 January 2006. The boxes indicate different zones chosen for analysis.

the atmospheric component, and even much longer for the surface component. A typical threshold length for a climate mode run using regional models is 1 month [11, 17].

Weather and climate forecasting is usually done following statistical, synoptic, and numerical techniques. The statistical methods depend on the interrelationships between observable atmospheric variables and their influence on the climatic behavior. Though statistical methods provide certain broad trends of weather and climate systems, they find limited use as the climate system is highly nonlinear and simple correlations between any two variables may not always provide estimate of any variable especially over long periods like seasons. The synoptic methods bank upon systematic analysis of large-scale trends of the dynamical systems based on a series of observation charts called the synoptic charts. However this method is subject to the skill of the interpreter and cannot be applied for time periods

beyond a few days due to the inherent variability of the atmospheric system. Atmospheric dynamical models are based on the physical and dynamical processes of the atmosphere and hence provide the basis for objective predictions of the ever-changing atmospheric conditions quantitatively; however their success depends on the accuracy of the initial and boundary conditions and the appropriateness of the physics used in the model. Atmospheric General Circulation models (AGCMs) are used to simulate the trends in climate patterns over the globe. The GCM simulations provide the information on the movement of the large scale pressure systems, air masses, and associated climate over various parts of the globe. However, the GCMs have a limitation of predicting the regional characteristics due to coarse resolution. The GCMs find a limited application when it comes to the disaster mitigation and decision making aspects where much finer quantitative predictions along with precise time of occurrence of a weather event is the necessary key information required by the administrators. The availability of regional models with horizontal resolutions of 30–50 km permits simulating the fine scale seasonal weather patterns to study the regional climatic characteristics more precisely. The theoretical limit for the useful daily weather forecast is about 10–14 days, but in practical application, the current limit is about 5–7 days. For longer periods of about months or seasons average temperature and precipitation can only be assessed; however the skill of such forecasts is low. The developments of numerical models provide the basis for an improved understanding of monthly and seasonal weather variation and for an enhanced ability to predict them with reasonable skill. Even a small improvement in the skill of extended range forecasting of extreme weather events may be helpful to take necessary precautions and to minimize weather-related losses or deaths and is important for substantial economic benefit.

In this study the objective is to examine the WRF ARW model capability for extended range seasonal prediction by simulating the extreme cold weather event that occurred

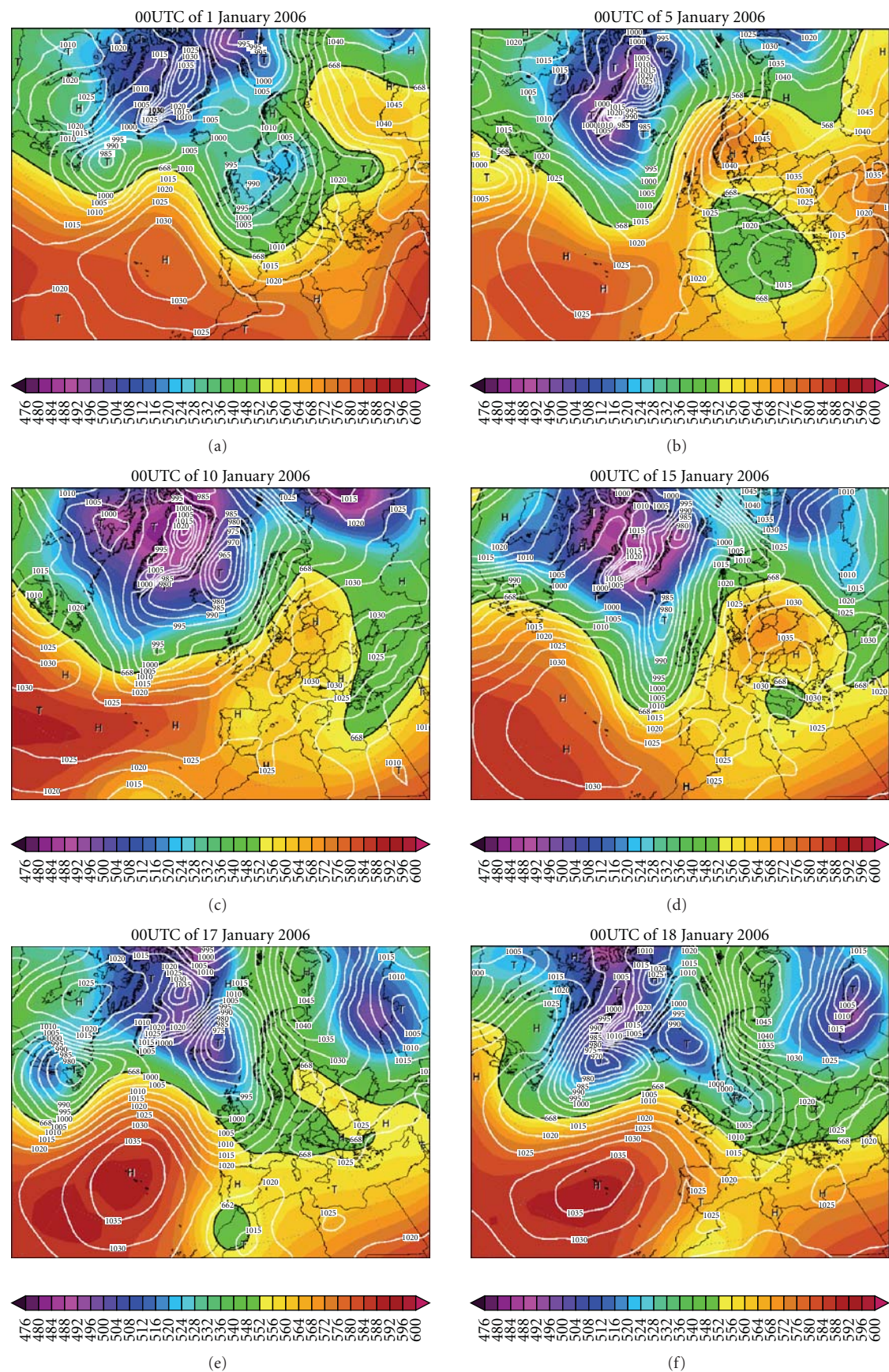


FIGURE 2: Continued.

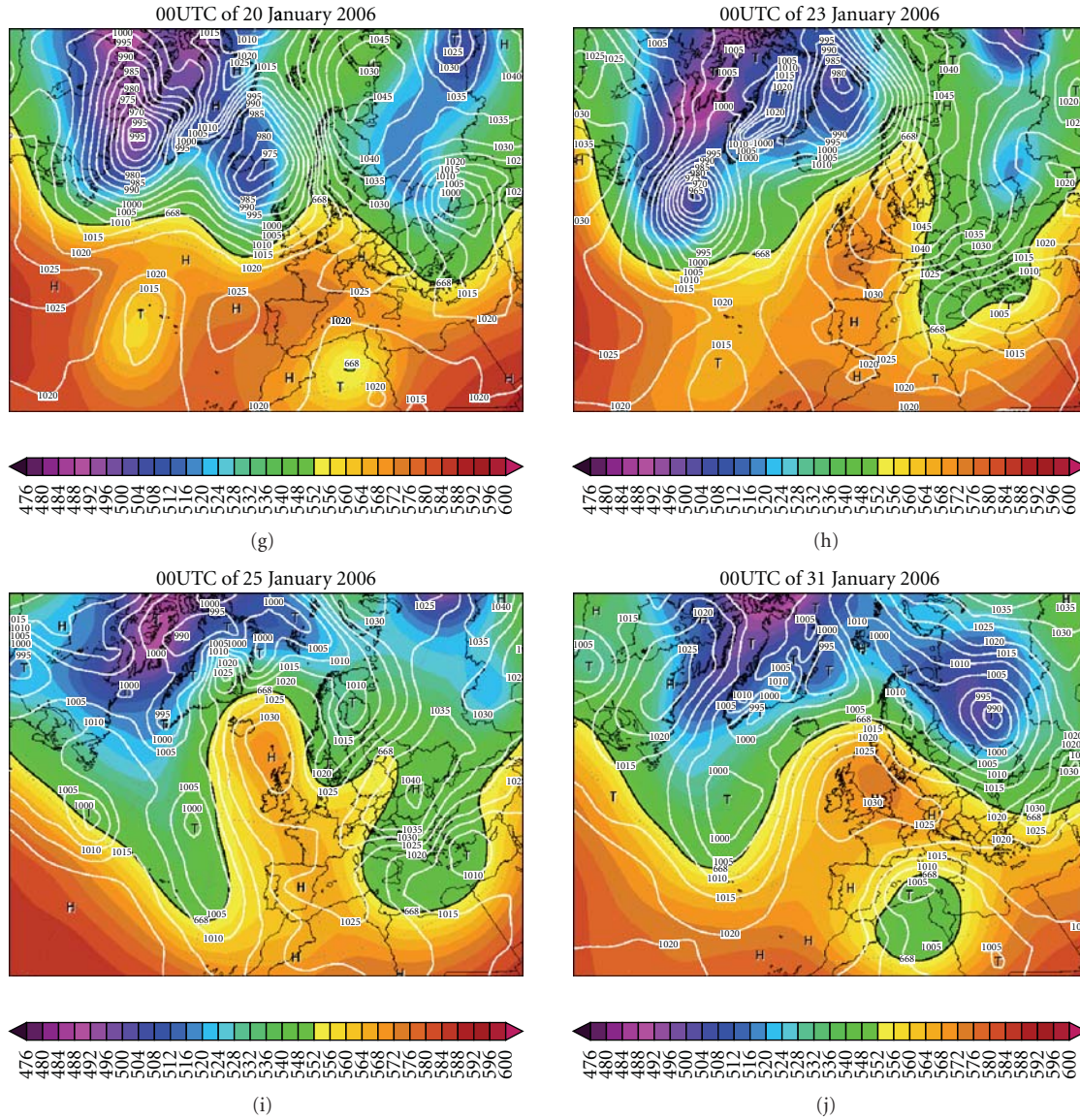


FIGURE 2: Geopotential height (shaded) at 500 hPa level (gpdm) and mean seal level pressure (contours) during the period 1-31 January 2006 from NCEP 2.5 degree reanalysis data.

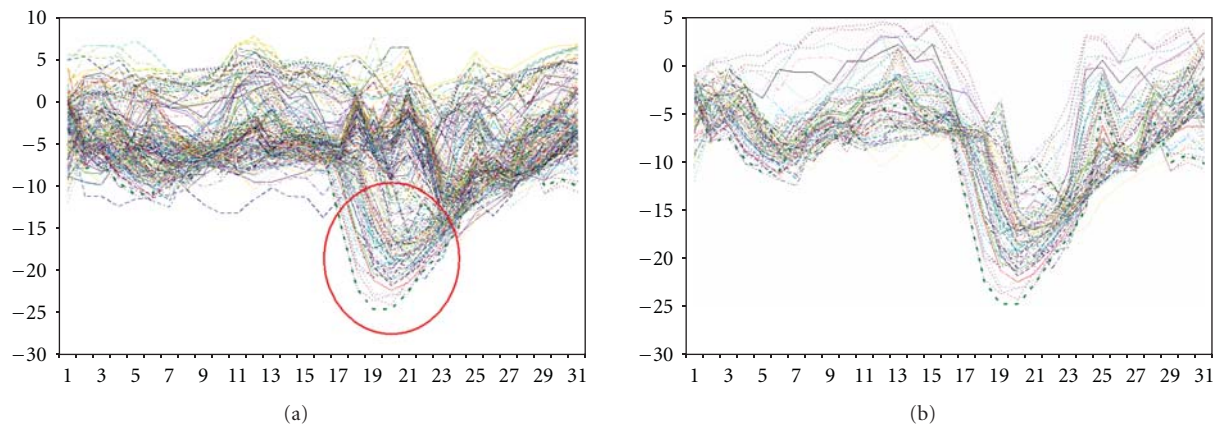


FIGURE 3: (a) The time series of the temperature at 2 m (C) at different grid points located over model domain. (b) The time series of the temperatures at different grid points with the fall in temperatures less than -20°C during one-month period separated from Figure 3(a).

over Central Europe during January 2006 with the WRF model. The model-derived intensity and development of the cold wave analyzed by comparing temperature at 2 m height, surface pressure, low level wind flow, and geopotential height at 500 hPa. The paper is organized as follows. A brief description of the cold wave in Central Europe is given in Section 2, the details of the model configuration and initialization are presented in Section 3, the results of the simulations are discussed in Section 5, and the summary and conclusions are presented in Section 6. Finally, the applicability of this study is discussed in Section 7.

2. Description of Cold Wave during January 2006

Cold waves at higher latitudes belong to the class of extreme weather conditions during winter. The observations show a severe cold wave occurred in January 2006 in Central Europe. This winter was extremely cold with snowy conditions observed over a vast area of Central, Eastern, and Southern Europe and relatively mild winter observed in Northern Norway. The phenomenon started in the European part of Russia, where a severe cold wave occurred between January 17–18 with a temperature drop up to about -30°C in Moscow, the coldest situation ever since the winter of 1978–1979. On 20 January 2006 temperatures lower than -40°C occurred in European Russia where the lowest temperature on record was about -42.1°C in 1940. The cold wave extended to Central European parts of Poland, Slovakia, and Austria with the recorded low temperatures below -30°C , and snow and cold weather penetrated to the south in Eastern Europe with heavy snowfalls over Acropolis in Athens, Greece on the 25th of January. The abnormal conditions gradually abated towards the end of the month, when temperatures dropped to -38°C . There were numerous cold-related deaths reported, primarily in Russia (50 people), Ukraine (181), Romania (27), Poland (25), Czech Republic (10), and Bulgaria (3) (Reuters). Heavy snowfalls were attributed for an avalanche near Dushanbe in Tajikistan. The cold weather in Southern Central and Eastern Europe has spread from Italy to the Urals. As January 2006 is one of the reported extreme cold weather over European region, this event is taken as a case study to simulate and also to understand the probable causes for its occurrence.

The synoptic situation of the cold wave during 1–31 January 2006 is depicted in Figure 2 using NCEP reanalysis data for surface pressure and geopotential at 500 hPa level. The analysis shows that at 00UTC of 1 January 2006, a low-pressure system is located over Central Europe. The trough is elongated from the head of the Baltic Sea to the south. The thickness of the atmospheric layer (i.e., geopotential difference) from surface to 500 hPa is seen to increase from Northern Europe to Southern Europe. After five days, that is, at 00UTC of 5 January, the whole region is completely replaced with high pressure system, and the low pressure is limited to a small region over east of Iceland. Over that region thickness of the geopotential is high and moved toward south of the region and with encircled lower

thickness of geopotential observed over Central Europe and neighbor hood. The thickness of the geopotential increased over entire region, and it last up to 14 January with minor day-by day variations. The synoptic flow pattern was more or less constant during this whole period. At 00UTC of 15 January the weather map show well-defined low pressure systems observed over south of Iceland, north-eastern parts of Green land, and north-eastern parts of Central Europe. A well-defined high-pressure system with high geopotential thickness is located over Central Europe. A well-defined trough region is observed at west of Central Europe and also over North eastern parts of the Central Europe. From this day onwards the thickness of the height contours slowly started decreasing over Central Europe, and after two days the weather map showed that the axis of the trough is extended from the East of the Iceland to Central Europe also another trough region developed from north-eastern parts of Central Europe. Well-defined low-and-high pressure systems are observed, and the southward progress of the cold wave is observed. This type of weather pattern is almost observed up to 18 January. After this day onwards the low pressure system moved towards Iceland, and high pressure system started moving towards the Central Europe and was sustained up to 26 January and then it started moves towards west and then north. This narrow zone of high pressure system is associated with low pressure systems in both east and west. During this period another branch of cold wave also slowly developed and started progressing from North east of the Central Europe towards Europe and that was sustained up to 26 January and then slowly disappeared.

3. Model Configuration and Initialization

A nonhydrostatic primitive equation ARW model developed by the National Center for Atmospheric Research (NCAR) was used in the present study. The ARW is a flexible state-of-the-art mesoscale atmospheric simulation system that is portable and efficient on a range of parallel computing platforms [18, 19]. The model has higher-order numerics and mass conservation characteristics [20]. For the present study the model was designed with a single domain of 30 km horizontal resolution. As the extratropical weather systems are relatively slow moving systems and large in size, the domain area was chosen to be about $3000 \times 3000 \text{ sq-km}$ ($6.7624\text{E}-37.2992\text{E}$; $42.605\text{N}-61.1074\text{N}$) which covers most of Central European and adjacent regions (Figure 1). The model physics used for the simulation included Kain-Firstch scheme for convection, Rapid Radiative Transfer Model for long wave radiation, Yonsei University scheme for planetary boundary layer turbulence, and the WSM 3-class Simple Ice scheme for explicit moisture processes (Table 1). The model was integrated for 31 days starting from 00 UTC of 1 January, 2006 to study the movement of the cold wave front.

Our first objective was to test whether the 31-day model simulations provide reasonable agreement with observations on this timescale, so that a strategy for real-time forecasts could be devised later using the larger-scale model forecasts like GFS or other global models that provide seasonal

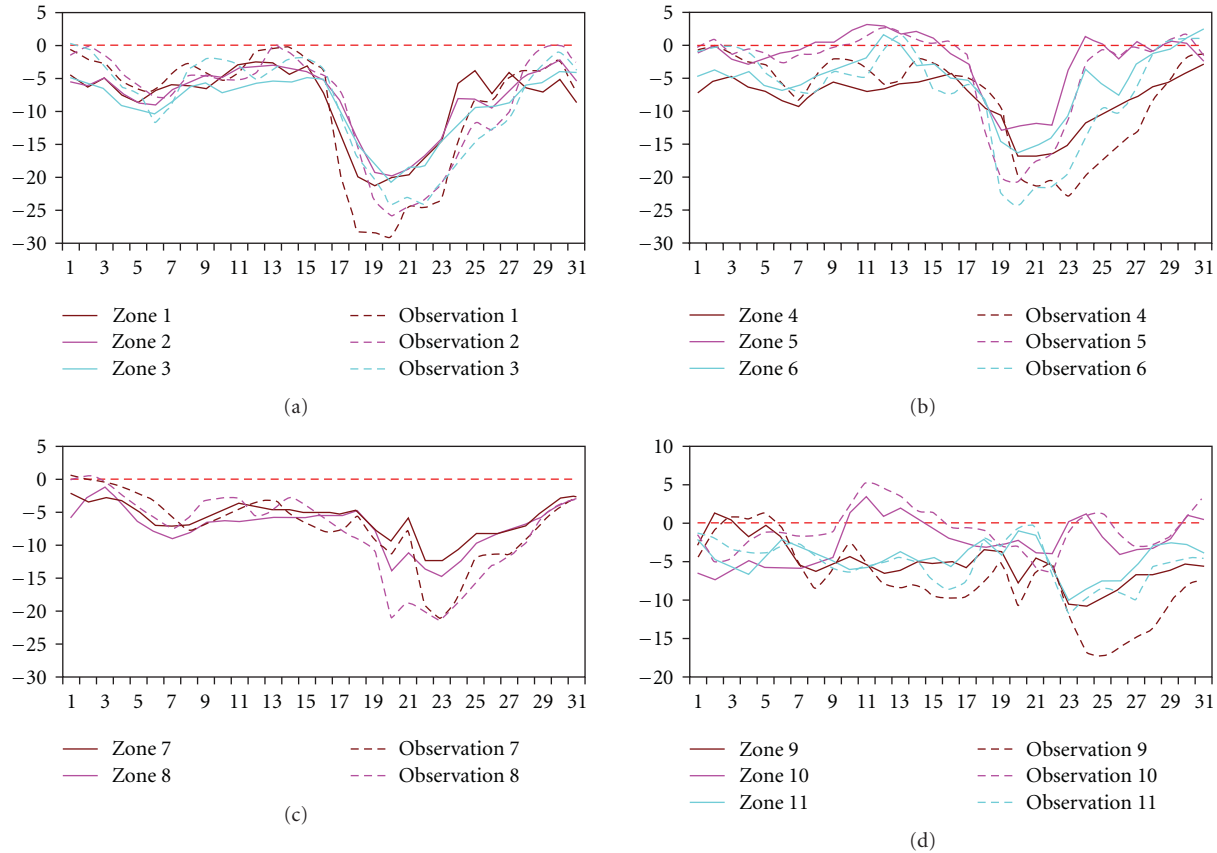


FIGURE 4: Time series of the daily mean area averaged temperature (C) at 2 m height for different zones along with the averaged station daily mean surface temperature for corresponding zone.

forecasts. Hence in the present study, the initial conditions for the model were given from NCEP reanalysis data [21] available at 2.5×2.5 degree resolution corresponding to 00 UTC 1 Jan 2006. The terrain, land cover, and soil types data over the region of study are obtained from the USGS topography data with a resolution of 10 minutes (roughly 18 km). The time-varying lateral boundary conditions are provided at every 6 hours interval during the entire period from NCEP reanalysis data.

4. Observational Data

The daily mean temperatures from 106 meteorological stations collected from different parts of Europe for the period 1–31 January 2006 were used for comparison. Out of 106 stations 85 records were taken from European Climate Assessment and Dataset [22], and 21 Polish records were taken from Institute of Meteorology and Water Management.

The intensity of the simulated cold wave was studied on the basis of a comparison of the observed surface temperatures with the model results. The movement of the pressure systems which caused the cold wave during that period was discussed from model fields for surface pressure and 500 hPa geopotential height. The above fields from WRF model were compared with the high-resolution NCEP

Final analysis (FNL) data available at 1 degree horizontal resolution to assess the skill of the model in capturing the time and intensity of the cold weather event.

5. Results and Discussions

Unlike global models, numerical simulations using limited area models require specification of atmospheric variables at the lateral boundaries at regular time intervals to represent the time-varying large scale weather condition across the boundaries of the domain and to permit the outside flow in to the model domain. The specification of time varying lateral boundary conditions will also influence the model atmosphere evolution, which is due to the model dynamics. The mesoscale model ARW described in the previous section provides the option to use either a single domain or nested multiple domains with one-way or two-way interaction. The general practice is to use as much as possible higher resolution which is constrained by computational resources. For this study, the simulation was conducted to examine the performance of the model on the prediction of the cold wave passage over Central Europe region with a single domain of 30 km resolution and updating the lateral boundary conditions once every 6 hours to represent the change in the outer atmospheric condition at that interval. The model

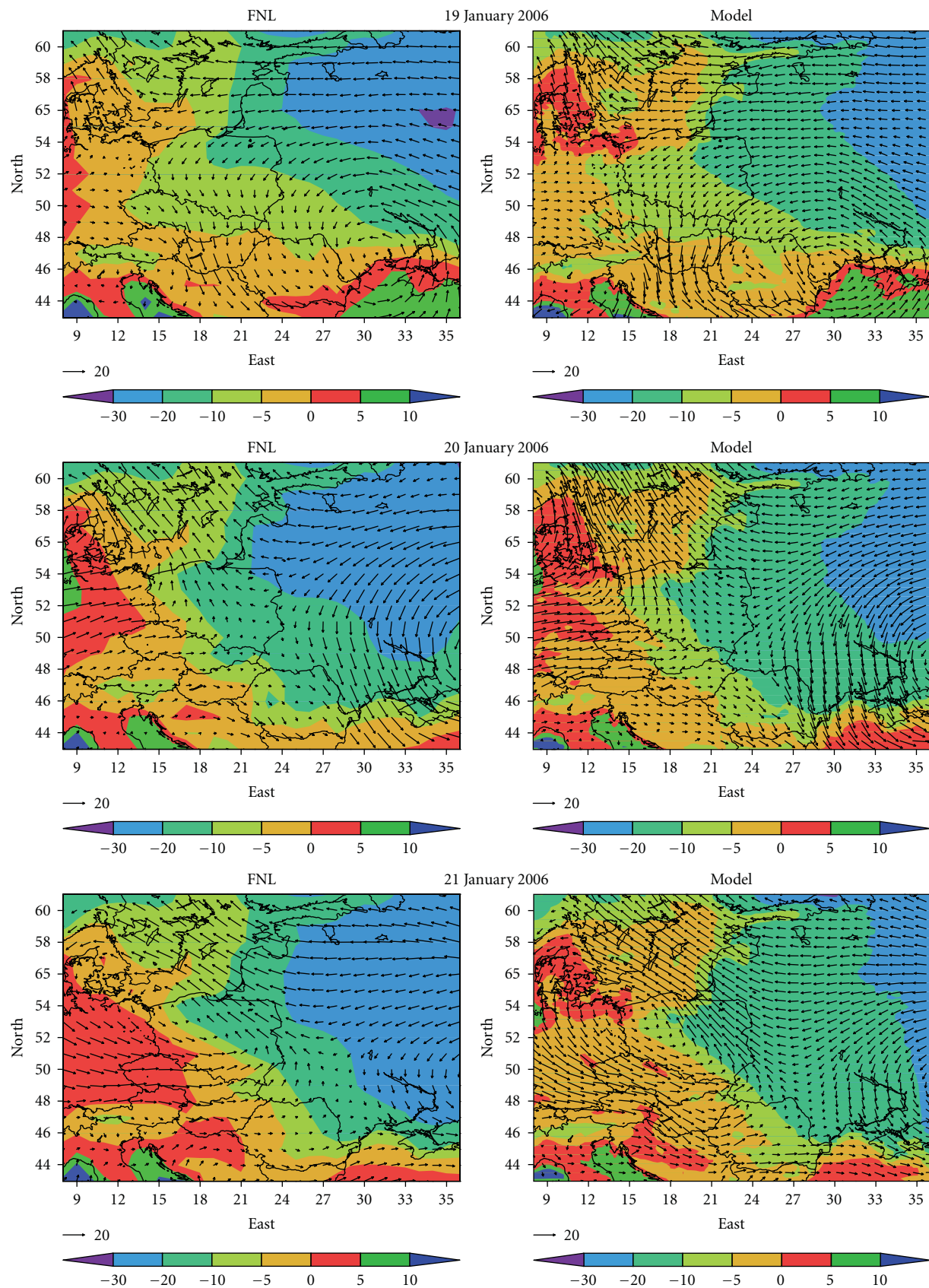


FIGURE 5: Continued.

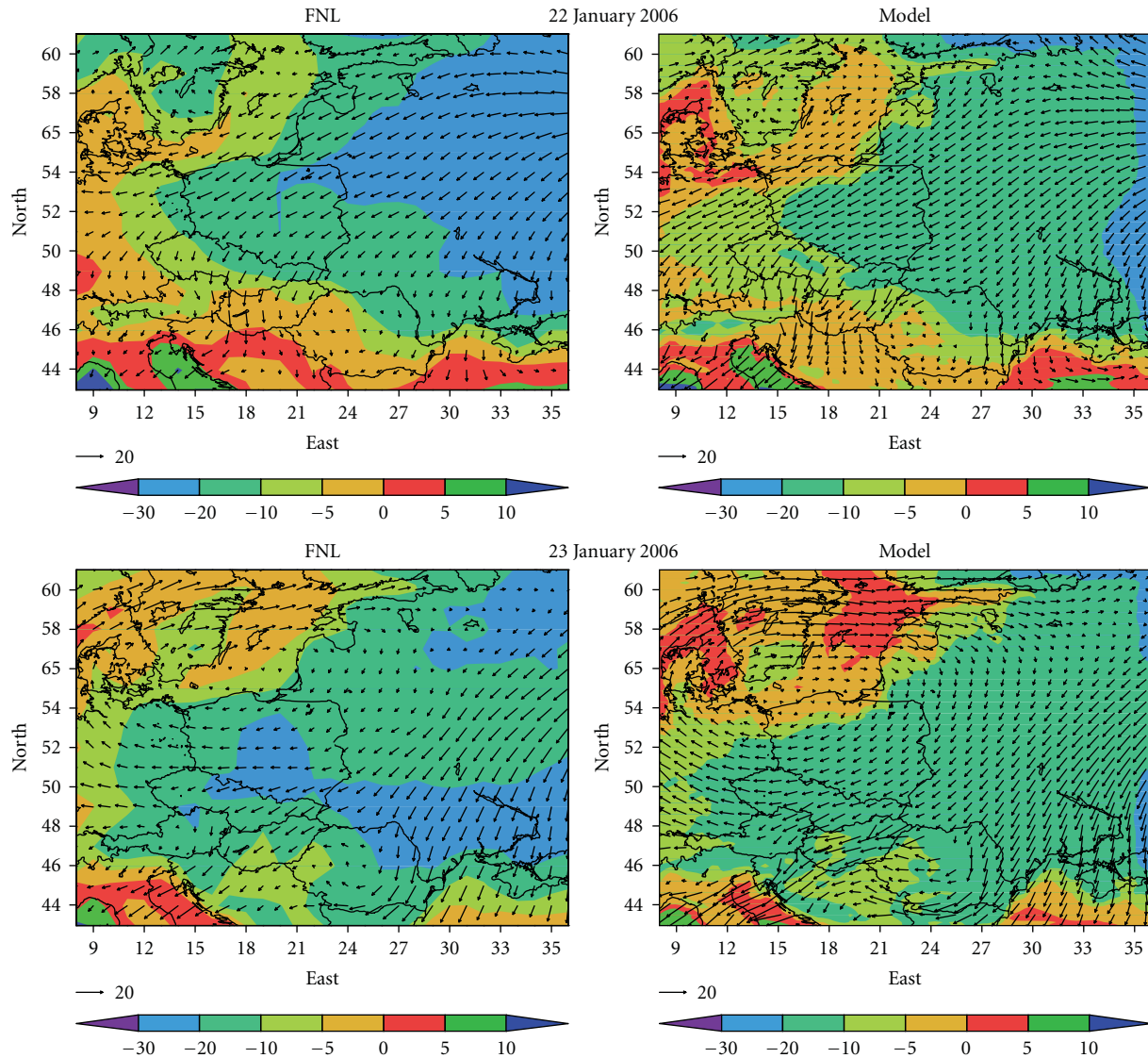


FIGURE 5: Daily mean temperature (C) at 2m (shaded) along with winds at 925 hPa for FNL (left panel) and ARW model (right panel) at different times.

evolution of cold wave, in terms of intensity and movement, was analyzed and discussed by a comparison with the available observations. The model predicted intensification of cold wave during the period 1 to 31 January 2006 was analyzed in terms of the model-simulated daily averaged air temperature at 2m height and the comparison with corresponding observations.

As the first step, the variations of model-derived daily mean temperatures at 2m above ground level (AGL) were analysed over the entire domain, and a set of zones are identified based on the differences in the topography. Figure 3(a) shows the daily mean temperatures at 2m AGL for different grid points during entire January. It shows a fall of about -10°C (sometimes even below -20°C) in daily mean temperatures for a period of 2 to 5 days at some grid points. This trend is not found uniformly at all grid points

indicating that the simulated temperature fields drastically varied at regional scale. The variation in the temperature field is probably due to the variations in elevation, land use category, and so forth in different parts of the modeling domain. Figure 3(b) shows the time series of temperature for those grid points at which temperature had fallen below -10°C . From these two pictures, it is understandable that the model is able to predict the cold wave scenario over some area and not over the entire domain. This was analyzed by observational comparison further. Based on results from Figures 3(a) and 3(b) a few areas were identified and categorized as zones. Accordingly zone 1 to zone 8 represent areas with mean daily temperatures below -10°C for few days (boxes in Figure 1) and zone 9, 10, and 11 correspond to areas where the fall in temperature is not below -10°C . Out of all these 11 zones, the zones from 1 to 8 have elevations less

than 150 m, and the other three zones have relatively higher elevation. Zone 5 has both ocean and land and represents coastal region. Zone 10 is a coastal region and also has higher elevation. The area averaged temperatures for the above zones for each day in January 2006 were compared with the observed daily mean surface temperature for the stations (shown circles in Figure 1) located within and very close to the selected zones. The model diagnostic statistics of area averaged temperature were computed between ARW-derived daily mean temperatures and the observations (correlation, standard deviation, bias, RMSE) and presented in Table 2. It is observed that in all zones the simulated temperature correlated well with observations in the range of 0.765 to 0.953 with a negative bias for zones 3, 4, and 10 and with positive bias for the remaining zones. The results indicate the model showed positive and negative bias over different zones. A strong positive bias (2.4651) is observed at zone 9 which is a mountain region with correlation coefficient of 0.8835. The next positive bias maxima of 1.79 are found for zone 6 located close to coast with correlation of 0.898 followed by zone 5 (land and ocean) with a bias of 1.3872 and with highest correlation of 0.95. This indicates that the simulated air temperature has strong positive bias over mountain and coastal regions. A strong negative bias (−1.621) and low correlation (0.7659) are observed over zone 10 which is a coastal and mountainous area. Thus the ARW has reasonably simulated temperature at all zones except the mountainous and coastal regions. Positive correlations above 0.76 at all zones and at 95% significance indicate ARW model skill for quantitative temperature simulations.

5.1. Model-Derived Temperatures at 2 m Height. The time series of the area averaged daily mean temperatures at 2 meter height from zones 1, 2, and 3 located in the eastern parts of the domain are presented in Figure 4(a) along with the station averaged daily mean surface temperatures. Results clearly show that the model is able to pick up the day-to-day variation of temperature over the eastern parts of the domain but with a slight underestimation during the intense cold wave period. The difference between the model and observations is not much at the onset of the cold wave conditions but very significant during the intense cold wave period. The difference in model temperature and observations is about 3–5°C in the onset phase and about 10°C during the peak cold wave period. The variation of simulated temperature in January 2006 is well matched with the observations is a correlation coefficient of 0.944 and with positive bias of 0.81 in zone 1 where the cold wave appeared around 17 January, intensified, and sustained for 2 to 3 days by 19 January and gradually disappeared thereafter. A similar situation was also observed over zone 2 with correlation coefficient 0.940 (bias of 0.495) but with a lag of one day and over zone 3 (with correlation coefficient 0.953 and a negative bias of −0.204) and with a lag of 2 days. Similarly over zone 4 (the southeastern parts of the domain) the model values matched well with the averaged station observations with a correlation of 0.900 (Figure 4(b)), but model temperatures were slightly underestimated with a negative bias of −0.236.

The decrease in temperature started from 19 of January, attained minimum value by 21 January and the very cold weather situation sustained up to the 24 of January. It is evident that the model well simulated the passage of the cold wave from zone 1 (from north east) to zone 4 (to the south east) closely following the observations. The mean daily temperature plots for zone 5 and 6 indicate that the cold conditions are simulated by the model from 18 to 23 of January. The temperature in zone 5 was slightly higher than that in zone 6, which is expected as part of zone 5 covers the ocean and land parts. The correlation coefficient between the modeled and observed temperature for zones 5 and 6 was 0.950 and 0.899 with a positive bias of 1.3871 and 1.79, respectively. From Figures 4(a) and 4(b) it is noted clearly that the time difference in the drop of temperature is about 1 to 2 days. This delay in the temperature drop at different zones is due to the slow movement of the cold wave from the northeastern part (Zone 1, 2, and 3) of the domain towards the central parts (Zone 6). The extreme cold condition was sustained for three to four days causing very cold temperatures in these areas.

The model-derived area averaged 2 m daily mean temperature over zone 7 (central part of domain) is noted to agree well with the observations up to 21 January thereafter the model indicated overestimation of temperature (Figure 4(c)), with a correlation of 0.930 and bias of 1.16. The model-predicted minimum temperature was evidently higher than the observed one; however the trends were reproduced reasonably well. The model simulated a fall in temperature and persistence of cold conditions for 2–3 days in the southern parts of the domain, that is, zone 8 with correlation of 0.9 reasonably agreeing well with observations but with an underestimation of low temperature by 7°C.

The zones 9 and 11 are located in mountainous area. The time series of temperature from these zones shows that the time of occurrence minimum temperature (drop) is well simulated. However a strong positive bias of 2.465 is noted for zone 9, where the lowest temperatures were evidently higher than the observed ones (Figure 4(d)). The model temperature evolution in these zones may have been influenced by the land surface processes as represented by the model topography, land cover, and soil conditions which need to be examined further. Also the physical parameterizations used for the treatment of the surface energy and boundary layer turbulence need to be investigated for their application over these mountainous regions. The correlation between the simulated and observed temperatures is 0.884 and 0.783 for zones 9 and 11. The simulated temperature over the northwestern parts (zone 10) showed relatively higher daily mean temperatures than all other zones. This area is situated close to the mountains and to the Atlantic Ocean (Figure 4(d)). For this zone the model simulated temperature evolution of the area averaged daily mean temperature at 2 m height was in good agreement with the averaged daily mean station observations with a correlation of 0.766, which is slightly lower than the correlation of all the other zones and with a strong negative bias of −1.621.

From the above analysis of mean daily temperature evolution it is evident that the model is able to simulate the

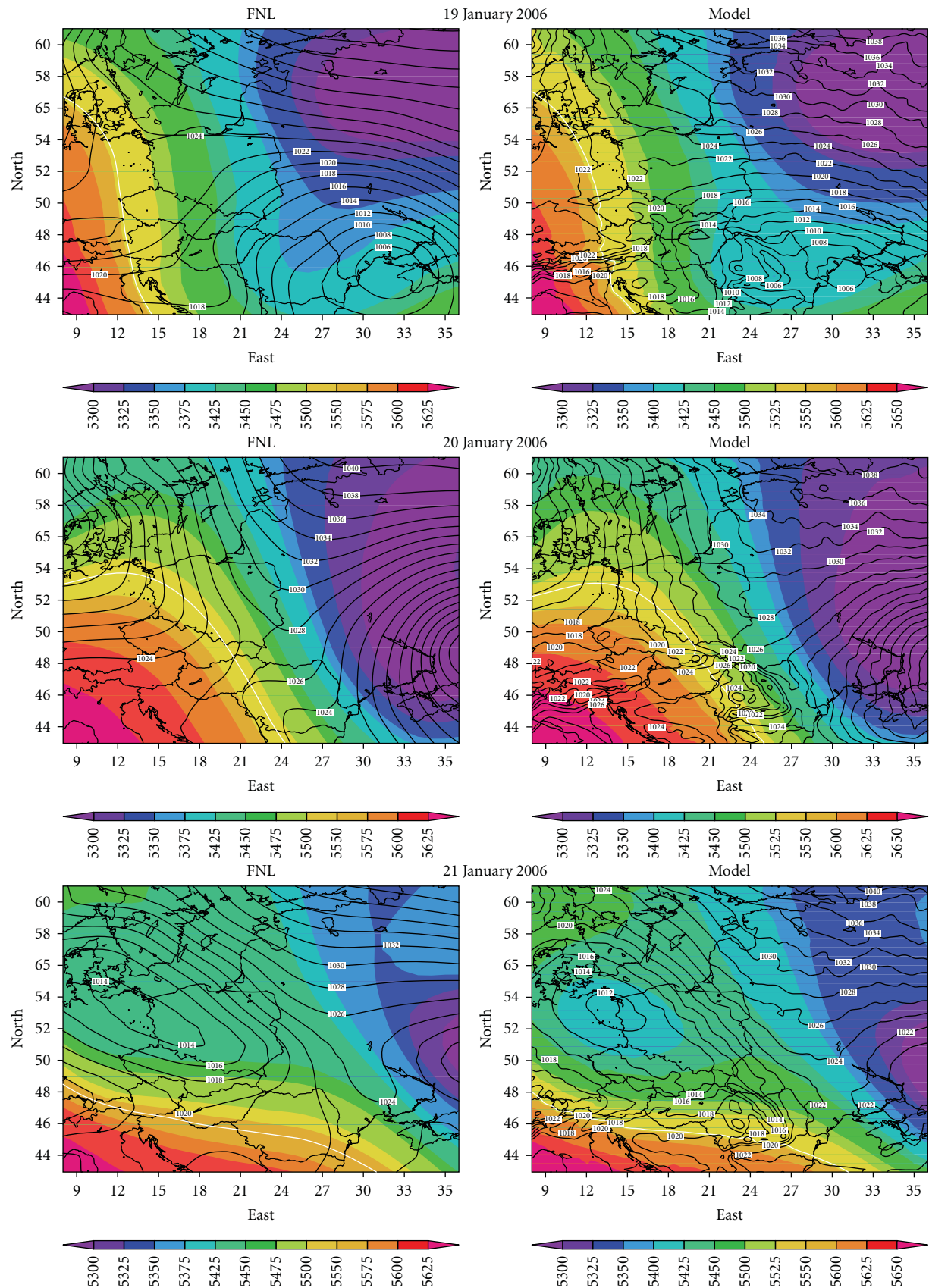


FIGURE 6: Continued.

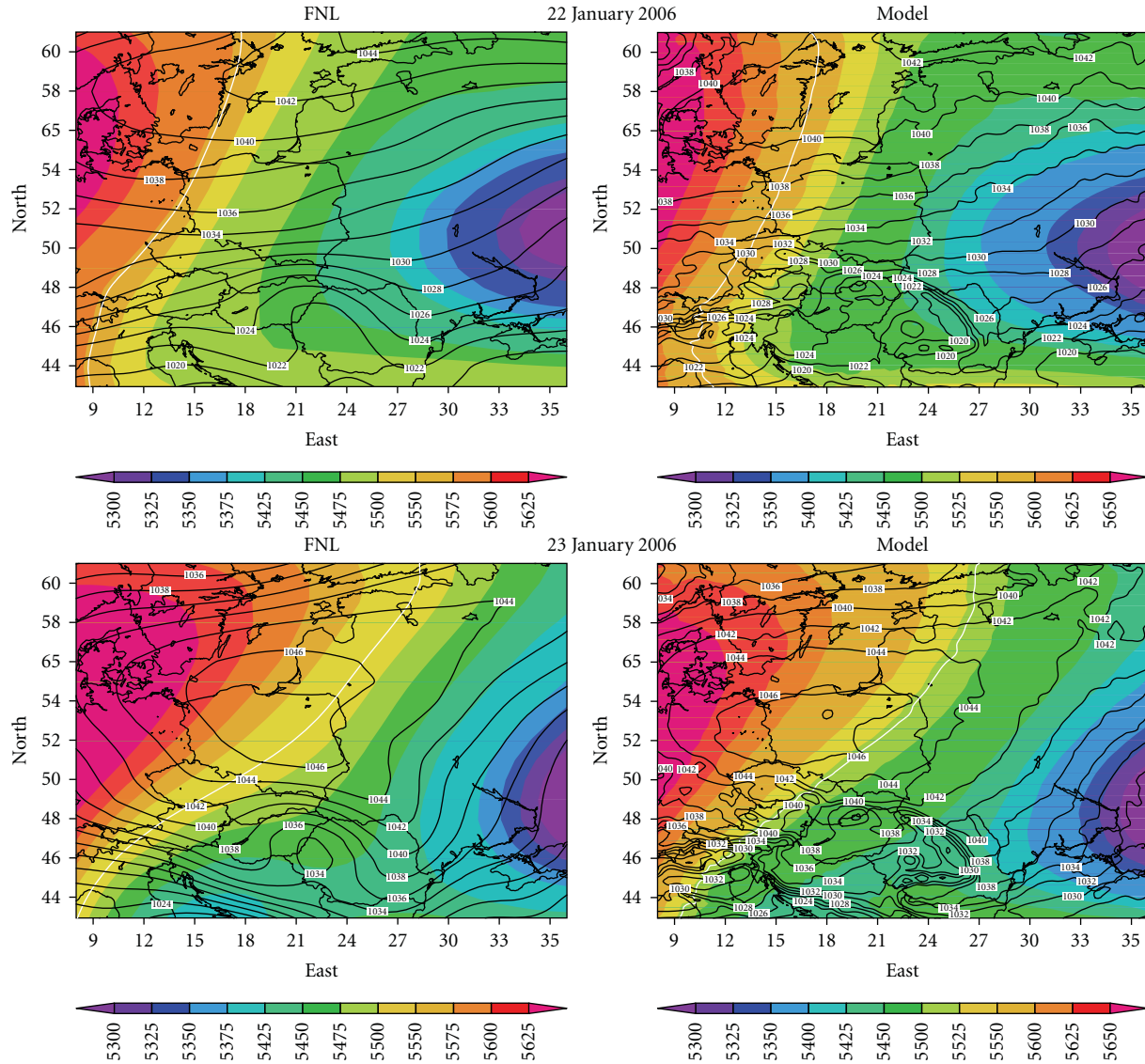


FIGURE 6: Daily mean geopotential height (gpm) at 500 hPa level (shaded) along with Surface pressure (hPa) (contours) for FNL (left panel) and ARW model (right panel) at different times.

intensity of the cold wave with a time lag of 1 to 3 days and its migration from north-eastern to the south-western parts of the domain. The model derived area averaged daily mean temperatures at 2 m height for different zones are found to match well with the averaged station daily mean temperature observations but with slight underestimation of about 5 to 10 degrees in temperature during the period of the intensive cold wave. A few exceptions are found for zones comprising ocean and adjoining land portions and for zones covering mountainous regions. Duration of the cold wave period is well agreeing with the observation but the model gets warmer one to two days before than the observations. Thus in general the ARW model seems to prove a useful modeling tool to simulate the seasonal climate with reasonable skill over extended range time scale and hence can be used to obtain an indication or a signal of the forthcoming extreme weather events such as cold wave conditions.

5.2. Model-Derived 2 m Air Temperature and Wind Flow at 925hPa. A detailed comparative analysis is made between FNL analysis data available at 1 degree resolution and model simulated products of the 2 m air temperature and winds at 925 hPa level to assess how well the spatial trends of temperature and horizontal advective motion are simulated by ARW. The daily mean values for extreme cold days are computed for both temperature at 2 m and winds at 925 hPa for both FNL and model outputs and presented in Figure 5. The spatial distribution of the wind flow on 19 January shows the presence of a strong cyclonic circulation over south-eastern parts of the domain in both model and FNL data and a strong easterly flow in the northern parts of the domain. These circulation features are well simulated by ARW model as seen from FNL data. The temperature pattern is almost the same in both model and FNL data except for the area under higher temperature contours relatively

larger in the ARW simulation. This indicates that the model has produced a slightly warmer atmosphere than the FNL data. The FNL data indicated strong cold temperatures in the northeastern part which was not simulated by the model. The model showed a relatively warmer region in the northwestern part of the domain than the FNL data. On 20 January the cyclonic circulation has moved toward east, and an anticyclonic circulation is observed over north western parts of the domain in both model and FNL data. The simulated temperature pattern agrees with the FNL data but the area under higher temperature contours are relatively larger thus indicating a warm bias in model temperature. In the next 24 hours the cyclonic circulation has moved to west of Poland in both model and FNL. On 21 January the model temperatures are seen to be roughly 5 to 10°C lower over western part of the domain than the values from the FNL data. In all three days (19-21 Jan) westerly flow is noticed over western parts of the domain especially in the central and lower latitudes in both model and FNL data, and the wind is gradually intensified from 19 to 21 January. The simulated flow patterns are noted to agree well with the FNL but with little higher intensity. Also the fine-scale features are well resolved in the simulation which may be because of the model higher resolution than FNL. On 22 January the flow pattern was altered to easterly/northeasterly over much of the domain except for a small region in the northwestern portion where the flow had changed to southwesterly indicating the onset of an anticyclone. In the next day, that is, on 23 Jan the anticyclonic circulation was fully established over the whole Baltic Sea and neighborhood regions. These flow features are well simulated by the model. The simulated spatial temperature distribution also agreed well with FNL data but with a warm bias (about 5 to 10°C) indicating less intensity of the simulated cold wave.

From the above discussions it is clear that the model could simulate most of the regional scale climate features comparable with FNL. The model is able to simulate the progression of the cyclonic and anti cyclonic circulations and trough and ridge regions with little higher intensity than those found in the FNL data. The model-derived temperature pattern agreed well with the FNL temperature distribution but with underestimation of cold conditions. The model simulated relatively higher temperatures at the colder region during extreme cold days and also relatively higher temperature in the warmer regions indicating a warm bias which needs to be examined further.

5.3. Model Derived Surface Pressure along with Geopotential at 500 hPa Level. To understand the role of the pressure systems over the central Europe during the event of the extreme cold wave, the daily mean sea level pressure (SLP) along with the daily mean geopotential height at 500 hPa level (500GH) is examined from the model and FNL data (Figure 6). The temporal sea level pressure and geopotential height patterns serve to describe the onset time and period of intensification of the cold wave between 18 to 24 January 2006.

On 18 of January 2006, a low-pressure system was located over the southwestern parts of Poland and the adjacent areas,

and a high-pressure system (not shown) was located over the northeastern parts of the domain observed in FNL. This pattern was well simulated by the model, but with the low pressure system located over the Czech Republic and high pressure located over the northeastern parts of the domain. The high pressure system which caused the low temperatures over this area was evidently lower than the other parts of the domain. On the 19th of January, 2006 the low pressure system moved to the southeastern part of the domain in both FNL data and the simulation. Also, at the same time the high-pressure systems started moving towards the southwest portion of the domain. The thickness of the geopotential decreased over the entire region of the central Europe but was relatively higher over a small region of south western parts. These features would cause the air temperature over those areas to consistently decrease towards the minimum as seen from discussions in the previous sections. On 20 January, the low and high pressure systems sustained with small tilt towards the Southeast and Northwest, respectively, and a new low pressure system appeared over the northwestern part of the domain in both the model and the FNL. The geopotential height pattern indicates that the contours of higher geopotential height are concentrated over southwest part of the domain and all the other remaining area is with lower thickness. As the high-pressure system remained for a long duration over the central parts of Europe and north and northeastern parts of the domain, the air temperature in those areas dropped significantly. The temperature reached below -20°C which was the monthly minimum in most of the central region. On the 21st of January 2008, the low pressure system from the northwestern part moved towards the South West and was located over the coastal parts of Denmark and the central part of Poland. At the same time, the high-pressure system was still dominating over the northeastern part of the domain. The thickness of the geopotential height further decreased over the entire region except the southern part of the domain. These features are well simulated by the model and agree well with FNL data. However, the intensity of the simulated low pressure system was slightly lower, and the location of the center of low pressure system was simulated over southern part of Poland and its adjacent parts. On 22 January, the low pressure system disappeared from the domain, and the high-pressure system occupied the entire domain. On this day the geopotential pattern indicated higher thickness over northwestern part of the domain and lower thickness over remaining parts. Under this high pressure system the central part of the domain recorded very low temperatures which were simulated well by the model. On 23 January, a well-established high pressure system was located over the central part of the domain and remained over Poland for the next 48 hours. The geopotential pattern is almost similar to that of the previous day but with slightly higher thickness and a shift towards the east. Under this stable high pressure system especially over Poland the temperatures reached their monthly minimum values in those two days as low record. This prolonged cold wave situation could be simulated by the model. After 23 January the temperatures increased gradually in the northeastern part of the domain, and the

TABLE 2: Number of the station observations considered for the average surrounded by the corresponding zones and the correlation coefficient values between the areas averaged daily mean temperatures at 2 m height from model and station observations.

S. No	Name of the Zone	Number of stations (observations) considered for comparison	BIAS	RMSE	Standard deviation	Correlation coefficient
1	Zone 1	7	0.8105	4.543	7.7829	0.9439
2	Zone 2	6	0.4971	3.733	6.7153	0.9398
3	Zone 3	8	-0.204	3.5012	6.3889	0.9530
4	Zone 4	7	-0.236	4.0652	5.6857	0.8996
5	Zone 5	6	1.3872	3.1706	5.8532	0.9504
6	Zone 6	7	1.7921	4.3078	6.4188	0.8987
7	Zone 7	10	1.166	3.1988	4.2399	0.9303
8	Zone 8	11	0.8273	3.8727	5.1576	0.9004
9	Zone 9	5	2.4651	3.7733	4.2653	0.8835
10	Zone 10	8	-1.621	2.5082	2.9767	0.7659
11	Zone 11	14	0.6357	1.8848	2.5269	0.7824
12	TOTAL	89	0.6836	2.71	4.248	0.9447

high pressure system disappeared slowly. By 25 January, 2006 the temperature increased and reached its normal value over entire Europe.

The model results suggest that it could simulate the passage of high and low pressure systems comparing closely with the trends from FNL data. The time series of simulated air temperature is found to match with the observed temperature time series in different zones. The model is able to resolve the regional scale features of the pressure systems which caused the spread of cold wave in the study domain.

6. Summary and Conclusions

A numerical modeling of extreme cold weather event over Europe during January 2006 was performed using the high-resolution ARW model to examine the performance of the model for the seasonal climate simulation and to understand the probable causes of the cold wave formation.

The simulated daily mean 2 m air temperatures were analyzed and compared with the observed station surface temperatures. The model simulated winds at 925 hPa, 2 m air temperatures, surface pressure, and geopotential height at 500 hPa are compared with FNL data. Eight zones were identified on the basis of drop in mean daily temperatures below -10°C and three zones based on the lowest temperatures above -10°C . The area averaged daily mean temperatures were computed from the model 2 m air temperature which were then compared with the averaged station surface temperatures from the respective zones.

The model-derived products showed a fall of temperatures starting from zone 1 located over northeastern parts to zone 11 located over the south western parts of the domain along with the passage of the high and low pressure systems in agreement with the station observations. The model is able to simulate the occurrence of the extreme cold situation at different zones and its temporal passage

was reasonably well agreeing with observations but with lesser intensity. The model temperatures indicated a good correlation with observations above 0.76 at 95% significance. The simulated flow patterns during the passage of the cold wave are found to agree well with the FNL data which indicates that the model is able to capture the advection of cold temperatures associated with the high pressure systems. The lower atmospheric temperature could be simulated well by the model but with higher temperatures than observed. The model results show warmer bias in extreme cold days. The persistent cold condition spanning 3 to 5 days over different zones could be captured by the model. This cold condition is known from its impact on economy and the death rate, especially in Russia, Ukraine, Poland, and some parts of the adjacent regions.

The present study attempted to simulate one extreme cold event due to the availability of limited computational resources. In order to assess the skill of the model for extended range seasonal climate forecasting it would be desirable to examine the model performance for a series of events over past few years. However, the results from the present study provide an indication of skill of the ARW model for its application for the extended range weather forecasting for Central Europe region during the winter season which may help to give an indication of the extreme events like cold waves for use by the public as well as the policy makers to take disaster mitigation measures. In the present study the ARW model is run with the initial and boundary conditions adopted from the NNRP data. In order to use the ARW model for near-real time applications of regional climate forecasting it would be necessary to run the model with a global domain initialized once with either GFS or other global analyses and thus provides the time-varying lateral boundary conditions from the global domain to a regional domain for region-specific climate forecasting, which would be tested in the future studies.

7. Application of Dynamical Models in Disaster Mitigation

The ARW model (as well as other dynamical mesoscale models) has been routinely applied for weather forecasting and as a part of a disaster mitigation tool in many countries. In this present study, the ARW model was used to study the regional climate feature over Central Europe with 30 km resolution during the period from 1st to 31st January 2006. The real-time integrations require large scale lateral boundary conditions and initial conditions that are now available in a near-real time basis from global operational forecast centers over different parts of the globe. The global products are available at a coarse resolution of 150 to 300 km. High-resolution mesoscale models are required to study and understand the intensity and its passage or movement of the extreme events like cold waves, heat waves, and flash floods and so forth, which are orographically and convectively driven. Mesoscale models with regional analysis and better representation of the initial conditions and local forcing have to be adopted when applying for specific regions.

The regional climate models are useful to give a better forecast for planners in advance to implement disaster mitigation measures over particular regions in such aspects as agricultural operations, food storage, and energy storage, to improve public transportation facilities and so forth, which may be useful to save large economy and death rates, especially during cold and heat wave conditions.

Acknowledgments

This paper was supported by an STATME project within the 6th European Community Framework Programme through contract MTKD-CT-2004-014222 and the Polish Ministry of Science and Higher Education under Grant K 091/Po4/2004/11. The data for this study are from the Research Data Archive (RDA) which is maintained by the Computational and Information Systems Laboratory (CISL) at the National Center for Atmospheric Research (NCAR). NCAR is sponsored by the National Science Foundation (NSF). The original data are available from the RDA (<http://dss.ucar.edu/>) in dataset number ds090.0

References

- [1] A. M. G. Klein Tank and G. P. Können, "Trends in indices of daily temperature and precipitation extremes in Europe, 1946–99," *Journal of Climate*, vol. 16, no. 22, pp. 3665–3680, 2003.
- [2] A. Moberg and P. D. Jones, "Trends in indices for extremes in daily temperature and precipitation in central and western Europe, 1901–99," *International Journal of Climatology*, vol. 25, no. 9, pp. 1149–1171, 2005.
- [3] R. Heino, R. Brázdil, E. Førland et al., "Progress in the study of climatic extremes in Northern and Central Europe," *Climatic Change*, vol. 42, no. 1, pp. 151–181, 1999.
- [4] J. Wibig and B. Glowicki, "Trends of minimum and maximum temperature in Poland," *Climate Research*, vol. 20, no. 2, pp. 123–133, 2002.
- [5] The BACC Author Team, *Assessment of Climate Change for the Baltic Sea Basin*, Springer, Berlin, Germany, 2008.
- [6] M. M. Huynen, P. Martens, D. Schram, M. P. Weijenberg, and A. E. Kunst, "The impact of heat waves and cold spells on mortality rates in the Dutch population," *Environmental Health Perspectives*, vol. 109, no. 5, pp. 463–470, 2001.
- [7] J. E. Walsh, A. S. Phillips, D. H. Portis, and W. L. Chapman, "Extreme cold outbreaks in the United States and Europe, 1948–99," *Journal of Climate*, vol. 14, no. 12, pp. 2642–2658, 2001.
- [8] J. S. Kain and J. M. Fritsch, "Convective parameterization for mesoscale models: the Kain-Fritsch scheme," in *The Representation of Cumulus Convection in Numerical Models*, K. A. Emanuel and D. J. Raymond, Eds., Amer. Meteor. Soc., 1993.
- [9] J. S. Kain and J. Kain, "The Kain-Fritsch convective parameterization: an update," *Journal of Applied Meteorology*, vol. 43, no. 1, pp. 170–181, 2004.
- [10] R. E. Dickinson, R. M. Errico, F. Giorgi, and G. T. Bates, "A regional climate model for the western United States," *Climatic Change*, vol. 15, no. 3, pp. 383–422, 1989.
- [11] F. Giorgi and G. T. Bates, "The climatological skill of a regional model over complex terrain," *Monthly Weather Review*, vol. 117, no. 11, pp. 2325–2347, 1989.
- [12] F. Giorgi, C. Shields Brodeur, and G. T. Bates, "Regional climate change scenarios over the United States produced with a nested regional climate model," *Journal of Climate*, vol. 7, no. 3, pp. 375–399, 1994.
- [13] H. Hirakuchi and F. Giorgi, "Multiyear present-day and 2×CO₂ simulations on monsoon climate over eastern Asia and Japan with a regional climate model nested in a general circulation model," *Journal of Geophysical Research*, vol. 100, no. D10, pp. 21,105–21,125, 1995.
- [14] R. G. Jones, J. M. Murphy, and M. Noguer, "Simulation of climate change over Europe using a nested regional-climate model. I: assessment of control climate, including sensitivity to location of lateral boundaries," *Quarterly Journal of the Royal Meteorological Society*, vol. 121, no. 526, pp. 1413–1449, 1995.
- [15] R. G. Jones, J. M. Murphy, M. Noguer, and A. B. Keen, "Simulation of climate change over Europe using a nested regional-climate model. II: comparison of driving and regional model responses to a doubling of carbon dioxide," *Quarterly Journal of the Royal Meteorological Society*, vol. 123, no. 538, pp. 265–292, 1997.
- [16] J. H. Christensen, B. Machenhauer, R. G. Jones et al., "Validation of present-day regional climate simulations over Europe. LAM simulations with observed boundary conditions," *Climate Dynamics*, vol. 13, no. 7–8, pp. 489–506, 1997.
- [17] F. Giorgi and L. O. Mearns, "Regional climate modeling revisited: an introduction to the special issue," vol. IC/98/191, 1–44, 1998, http://www.ictp.trieste.it/~pub_off.
- [18] W. Wang, D. Barker, C. Bruyère, J. Dudhia, D. Gill, and J. Michalakes, "WRF Version 2 modeling system user's guide," 2004, <http://www.mmm.ucar.edu/wrf/users/docs/user-guide/>.
- [19] J. Michalakes, J. Dudhia, D. Gill, et al., "The weather research and forecast model: software architecture and performance," in *Proceeding of the 11th ECMWF Workshop on the Use of High Performance Computing in Meteorology*, G. Mozdzynski, Ed., Reading, UK, October 2004.
- [20] W. C. Skamarock, J. B. Klemp, J. Dudhia, et al., "A description of the Advanced Research WRF Version 3," Technical Note TN-475+STR, NCAR, 2008.

- [21] E. Kalnay, M. Kanamitsu, R. Kistler et al., “The NCEP/NCAR 40-year reanalysis project,” *Bulletin of the American Meteorological Society*, vol. 77, no. 3, pp. 437–471, 1996.
- [22] A. M. G. Klein Tank, J. B. Wijngaard, G. P. Können et al., “Daily dataset of 20th-century surface air temperature and precipitation series for the European Climate Assessment,” *International Journal of Climatology*, vol. 22, no. 12, pp. 1441–1453, 2002.

Research Article

Orography-Induced Gravity Wave Drag Parameterization in the Global WRF: Implementation and Sensitivity to Shortwave Radiation Schemes

Hyeyum Hailey Shin,¹ Song-You Hong,¹ Jimmy Dudhia,² and Young-Joon Kim³

¹ Department of Atmospheric Sciences and Global Environment Laboratory, Yonsei University, Seoul 120-749, Republic of Korea

² Mesoscale and Microscale Meteorology Division, National Center for Atmospheric Research, Boulder, CO 80305, USA

³ Marine Meteorology Division, Naval Research Laboratory, Monterey, CA 93943, USA

Correspondence should be addressed to Song-You Hong, shong@yonsei.ac.kr

Received 24 December 2009; Accepted 24 March 2010

Academic Editor: Hann-Ming Henry Juang

Copyright © 2010 Hyeyum Hailey Shin et al. This is an open access article distributed under the Creative Commons Attribution License, which permits unrestricted use, distribution, and reproduction in any medium, provided the original work is properly cited.

This paper describes the implementation of the orographic gravity wave drag (GWDO) processes induced by subgrid-scale orography in the global version of the Weather Research and Forecasting (WRF) model. The sensitivity of the model simulated climatology to the representation of shortwave radiation and the addition of the GWDO processes is investigated using the Kim-Arakawa GWDO parameterization and the Goddard, RRTMG (Rapid Radiative Transfer Model for GCMs), and Dudhia shortwave radiation schemes. This sensitivity study is a part of efforts of selecting the physics package that can be useful in applying the WRF model to global and seasonal configuration. The climatology is relatively well simulated by the global WRF; the zonal mean zonal wind and temperature structures are reasonably represented with the Kim-Arakawa GWDO scheme using the Goddard and RRTMG shortwave schemes. It is found that the impact of the shortwave radiation scheme on the modeled atmosphere is pronounced in the upper atmospheric circulations above the tropopause mainly due to the ozone heating. The scheme that excludes the ozone process suffers from a distinct cold bias in the stratosphere. Moreover, given the improper thermodynamic environment conditions by the shortwave scheme, the role of the GWDO process is found to be limited.

1. Introduction

The Weather Research and Forecasting (WRF) model has been evaluated in terms of regional modeling for both research and operational applications since it was first released in 2000. The capability of the regional WRF model is established over a wide temporal range; from short-range forecasts such as simulations of localized heavy rainfall and snowfall within a couple of days over Korea (i.e., [1, 2]), 36-h real time forecasts in the United States [3], and simulations of typhoon and hurricane that affect synoptic fields for several days (i.e., [4, 5]), to regional climate simulations of such as U.S. warm-season precipitation and East-Asia summer monsoon circulations (i.e., [6, 7]). These studies support the satisfactory performance of the WRF model in various regions over the globe.

With the verification of the regional WRF model performance, National Center for Atmospheric Research (NCAR) researchers tested the ability of the WRF model to cover the global domain. It is noticed that a global version of WRF was first developed to study atmospheres on Mars and other planets by Mark Richardson and colleagues at California Institute of Technology, and researchers in NCAR Mesoscale and Microscale Meteorology (MMM) Division extended that version of the WRF-ARW model to forecast weather on Earth (NCAR articles on 9 November 2007, available in http://www.ncar.ucar.edu/index.php/ncar/articles/weather_forecast_goes_global). The regional WRF model was extended with a latitude-longitude grid system to cover the global domain, based on the Advanced Research WRF (ARW) version 3.0 that was released in April 2008. The global WRF shares the same dynamic core with the regional WRF

except that a polar filter is applied in the global version [8]. In addition, the physics options and behavior should be examined separately from the regional configuration because the intrinsic requirements for global circulation modeling, such as higher model top, and coarser resolution require further validation.

The advancement of human knowledge continues together with increasing computing resources; the cutting-edge numerical weather prediction (NWP) and climate models, however, cannot resolve all relevant scales of atmospheric phenomena. Global numerical prediction models are typically run with horizontal resolutions that cannot capture atmospheric processes smaller than about 10–100 km. Gravity wave is an unresolved process in coarse resolution models, playing an important role in transporting momentum from source regions to regions where gravity waves are dissipated or absorbed during their propagation, producing synoptic scale body forces [9]. Palmer et al. [10] and McFarlane [11] noted that unresolved mountain gravity wave drag was one of the most critical causes of the systematic biases in seasonal simulations—excessive surface westerlies and a too cold pole—and suggested a GWDO parameterization for large-scale models. Since then, this subgrid-scale process of gravity waves has been an essential physical process that should be parameterized in global models to represent global circulations realistically. However, the global WRF, which is a spatial extension of the original regional WRF, currently does not include any orography-induced gravity wave drag (GWDO) parameterization. It is noted that the GWDO parameterization is not included in most regional models including the WRF since horizontal resolutions of regional models are considered to be sufficiently high to resolve gravity waves. Moreover, global models include much of stratosphere, whereas the model top is lower (i.e., typically lower than 50 hPa) for regional models. Thus, most regional models do not typically include the GWDO parameterization.

The purpose of this study is to describe the implementation of the GWDO parameterization based on Kim and Arakawa [12] (hereafter, KA GWDO) into the global WRF model and evaluate the performance of the model in simulating general features of the boreal winter climate with the KA GWDO. The KA GWDO includes the enhanced low-tropospheric gravity wave drag in addition to the upper-level wave breaking that is traditionally incorporated into GWDO schemes. The KA GWDO was earlier implemented into the National Centers for Environmental Prediction (NCEP) Global Spectral Model (GSM) successfully and its performance was later reported by Hong et al. [13]. The KA GWDO scheme went into operation at the NCEP global forecast system in 2000. Sensitivity of the simulated climatology to shortwave radiation schemes is also investigated in order to re-evaluate present physics options in the WRF model in global and seasonal configuration, which have been evaluated only in regional configuration. Section 2 describes the experimental setup and implementation of the KA GWDO parameterization, and results are discussed in Section 3. Concluding remarks are given in the final section.

2. Experimental Design

2.1. The Advanced Research WRF (ARW) Model. The Advanced Research WRF (ARW; [14]) is a community model designed for both research and forecasting, which is a fully compressible nonhydrostatic model with the Arakawa-C grid system. The model performs reasonably well for detailed numerical weather prediction (NWP) cases with real-data initial and boundary conditions. The WRF model became available with the global coverage starting from WRF version 3.0, which was released in April 2008. The model used in this study is a beta version of the ARW version 3.1 with the global domain. The global WRF utilizes the latitude-longitude grid system and then a polar filter is used to filter out small-scale waves and avoid the singularity problem at the poles.

2.2. Implementation of the KA GWDO Parameterization Scheme. The KA GWDO scheme [12] includes the lower-tropospheric enhancement of GWDO due to selective low-level wave breaking mainly in downstream regions with the aid of additional subgrid-scale orographic statistics: the orographic asymmetry (OA) and orographic convexity (OC). The OA measures the asymmetry and location of subgrid-scale orography relative to the model grid box and it distinguishes between the upstream and downstream regions. The OC measures how convex or sharp the subgrid-scale orography is by statistically relating the characteristics of the mountain waves to the subgrid-scale orography.

The KA GWDO parameterization is implemented in the WRF model following Hong et al. [13]; in Hong et al. [13] the reference level is determined as the larger value between the PBL height and $2\sigma_h$ following Kim and Doyle [15], where σ_h is the standard deviation of subgrid-scale terrain heights. Kim and Hong [16] demonstrated that this method in determining the reference level greatly improves the climate simulations compared with the previous method that employs the PBL height as the reference level height; we note that the new method generally elevates the reference level height. The mechanism behind the improvement is explained in Kim and Hong [16].

For utilizing the KA GWDO in the WRF model, the necessary input to the KA GWDO scheme (i.e., mean, variance, asymmetry, and convexity) is derived from a 30-arcsecond resolution topography dataset [17] for global domains with 10 min., 20 min., 30 min., 1 deg., and 2 deg. resolutions. These orographic statistics are interpolated to the model grid points using one of the five-resolution datasets in the WRF Preprocessing System (WPS); prepared statistics of a comparable resolution to model grid size are used.

2.3. Experimental Setup. Seasonal simulations are conducted for three boreal winters in December, January, and February (DJF) of 1996/1997, 1997/1998, and 1999/2000. For each winter, five ensemble runs are conducted with different initialization times of 00UTC 1–5 November to average out the unpredictable parts of the flow. Thus, one experiment

TABLE 1: A summary of the physics options used in the numerical experiments. “—” denotes the same option as that in the Gsw_nGWD experiment.

	GWDO	SW	LW	PBL	LSM	CPS	MPS
Gsw_nGWD	None	Goddard	RRTMG	YSUPBL	NOAH	Grell-Devenyi	WSM3
Rsw_nGWD	None	RRTMG	—	—	—	—	—
Dsw_nGWD	None	Dudhia	—	—	—	—	—
Gsw_GWD	KA GWDO	Goddard	—	—	—	—	—
Rsw_GWD	KA GWDO	RRTMG	—	—	—	—	—
Dsw_GWD	KA GWDO	Dudhia	—	—	—	—	—

consists of 15 runs. Initial conditions are forced by the NCEP-Department of Energy (DOE) (NCEP-DOE) Reanalysis II (R2) data on the $2.5^\circ \times 2.5^\circ$ global grid. The National Oceanic and Atmospheric Administration (NOAA) Optimal Interpolation Sea Surface Temperature (OISST) is used as the surface boundary conditions every 24 hours. The horizontal resolution of $1.875^\circ \times 1.875^\circ$ is used, which is comparable to the 200 km resolution along the equator. The 38-layer Eta level system is used with the model top at 10 hPa. Intervals between the adjoining vertical levels are determined not to exceed 1 km or to be comparable to 1 km.

The physics package includes the RRTMG scheme [18] for longwave radiation, the Yonsei University Planetary Boundary Layer (YSU PBL) [19] for vertical diffusion process, the Noah land surface model [20], the Grell-Devenyi ensemble scheme [21] for cumulus parameterization, and the WSM3 (WRF Single-Moment 3-class) scheme [22] for microphysics. In the YSU PBL, the vertical diffusion coefficients in the stable boundary layer (SBL) conditions are calculated as in the case of the unstable conditions; the coefficients are parabolic functions of heights as in the mixed layer, and the SBL top is determined by the bulk Richardson number. Kim and Hong [16] demonstrated that the interaction between the KA GWDO and YSU PBL processes is improved with the SBL parameterization mentioned above. For shortwave radiation, three different shortwave schemes are used to observe the sensitivity of the simulated climate associated with the GWDO to the shortwave radiation processes in the modeled atmosphere: the Goddard [23], RRTMG, and Dudhia [24] schemes. The physics options used for the numerical experiments are summarized in Table 1.

3. Results

In this study, the results are obtained from and discussed based on the composite of 3-year simulations (i.e., ensemble averages of the 15 simulations). The simulated zonal wind and temperature structures are evaluated in comparison with the reanalysis (R2) data. The shortwave process in R2 is based on Chou [25] and Chou and Lee [26], and the GWDO scheme used in the R2 is described by Alpert et al. [27]. In precipitation analysis, the daily Global Precipitation Climatology Project (GPCP) data with a $1^\circ \times 1^\circ$ spatial resolution are used for the evaluation. Hereafter, to make a

clear distinction, the global WRF without the KA GWDO implementation is designated the earlier version.

3.1. Wind and Temperature Structures. Figure 1 compares the three-winter ensemble averages of the zonal-mean zonal wind and temperature structures simulated with the Goddard (Figures 1(a) and 1(d)), RRTMG (Figures 1(b) and 1(e)) and Dudhia (Figures 1(c) and 1(f)) shortwave parameterizations in the earlier version of the global WRF that includes no effect of the GWDO (denoted by Gsw_nGWD, Rsw_nGWD, and Dsw_nGWD, resp.). The contours in each figure represent the 3-year averaged fields from the 15 ensemble members, and the color shades denote their deviations from the reanalysis fields. As can be expected and as the results show, the earlier version of the global WRF cannot reasonably represent the typical boreal winter climatology. The model clearly shows the systematic errors in the simulated climatology—too cold pole and excessively strong westerlies over the northern hemisphere (cf. Figure 1), which is typical when GWDO is not included in general circulation models. There is no separation between the tropospheric subtropical jet and stratospheric polar night jet and also the polar night jet is overly strong due mainly to the lack of GWDO. The thermodynamic structure shows too strong meridional temperature gradient in balance with the improper wind structure; the simulated temperature of the Arctic polar stratosphere is almost about 40 K colder than that of the reanalysis. Thus, it is obvious that the earlier version of the global WRF has a systematic problem due to a missing critical process; that is, orographically induced gravity wave drag. Note that the three nGWD experiments are conducted in parallel with the three GWD experiments (i.e., Gsw_GWD, Rsw_GWD, and Dsw_GWD) to validate the implementation of the KA GWDO in the global WRF model, and thus the sensitivity to shortwave process schemes is not discussed for these nGWD experiments.

With the KA GWDO implemented, the global WRF is able to reproduce the general mean structures of both the zonal-mean zonal wind (Figures 2(a)–2(c)) and temperature (Figures 2(d)–2(f)) in the troposphere. All three experiments simulate the subtropical jet in the northern hemisphere with realistic intensity, which is comparable to 45 m s^{-1} of the reanalysis data, as well as the overall mean wind state of the troposphere (Figures 2(a)–2(c)). This reasonable representation of the wind fields including the mid-latitude jet in the northern troposphere is attributed to the implementation of

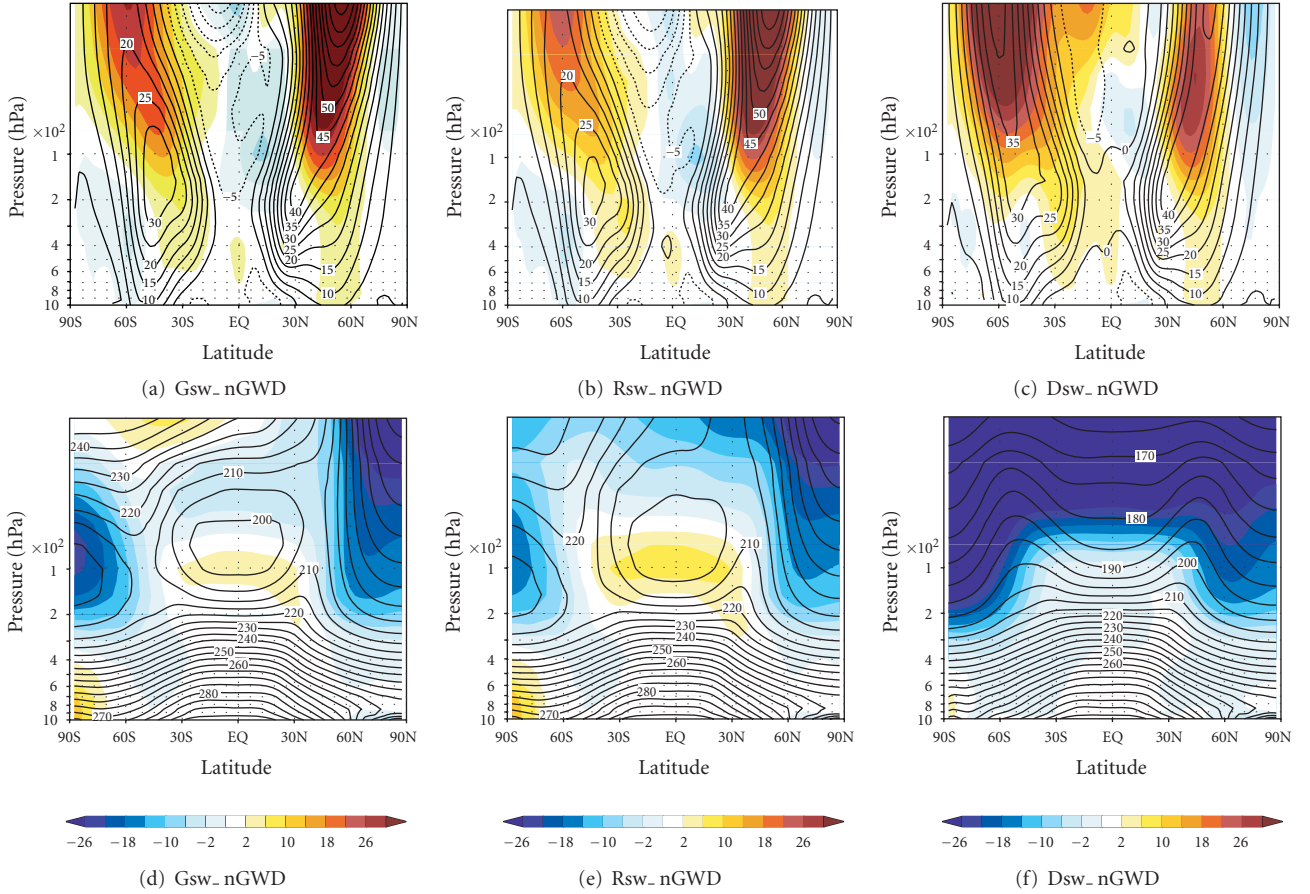


FIGURE 1: Three-winter ensemble averages (contours) of the zonal-mean zonal wind (upper panels) and temperature (lower panels) structures simulated from the (a), (d) Gsw_nGWD, (b), (e) Rsw_nGWD, and (c), (f) Dsw_nGWD experiments with the earlier version of global WRF without the KA GWDO implementation. Differences from the NCEP reanalysis (R2) are color shaded.

the GWDO. Associated with these improvements in the wind fields, the cold bias of the thermodynamic structures is also reduced. In the troposphere, the simulated results are less sensitive to the shortwave schemes than those in the upper atmosphere. On the other hand, clear differences among the shortwave radiation parameterizations exist in upper levels. The subtropical jet and stratospheric polar night jet in the northern hemisphere are reasonably separated with the Goddard and RRTMG shortwave radiation processes while the two jets are unrealistically bonded to each other with the Dudhia scheme; the westerly continuously decreases as the height increases such that the magnitude of the wind is evidently underestimated at the location of the observed polar-night jet, which is entirely missing in the simulation (cf. Figure 2(c)). Moreover, in the southern hemisphere, the tropospheric westerly jet is erroneously extended into the stratosphere in the Dsw_GWD experiment.

This radical difference in simulating the wind structure in the middle atmosphere among the three experiments (Gsw_GWD, Rsw_GWD, and Dsw_GWD) is related to the different thermodynamic structures that heavily rely on the shortwave heating processes. The Goddard and RRTMG shortwave schemes include ozone effects that are

responsible for the typical thermodynamic structure of the stratosphere; an ozone-absorption coefficient profile is specified in the Goddard scheme according to an observed climatology, and the RRTMG scheme includes tropical/mid-latitude/polar and summer/winter ozone profiles. The simulated temperature-profile inversion near the tropical and southern-hemispheric polar tropopause is shown with these two shortwave schemes due to the ozone heating effects (Figures 2(d) and 2(e)). Because of this temperature inversion, there exists meridional temperature gradient in the middle stratosphere over high latitudes, which is responsible for the presence of the northern polar night jet in the two experiments (i.e., Gsw_GWD and Rsw_GWD). In the Gsw_nGWD and Rsw_nGWD experiments, there is significant cold bias related to the extremely overestimated temperature gradient in the lower stratospheric regions associated with the excessive westerlies caused by the missing drag, as shown previously, this cold bias is alleviated by its balance with the wind reduction due to the GWDO in the two GWD experiments.

On the other hand, the Dudhia scheme does not consider the ozone effects [28] and thus cannot simulate the temperature inversion; the strong cold bias is induced throughout

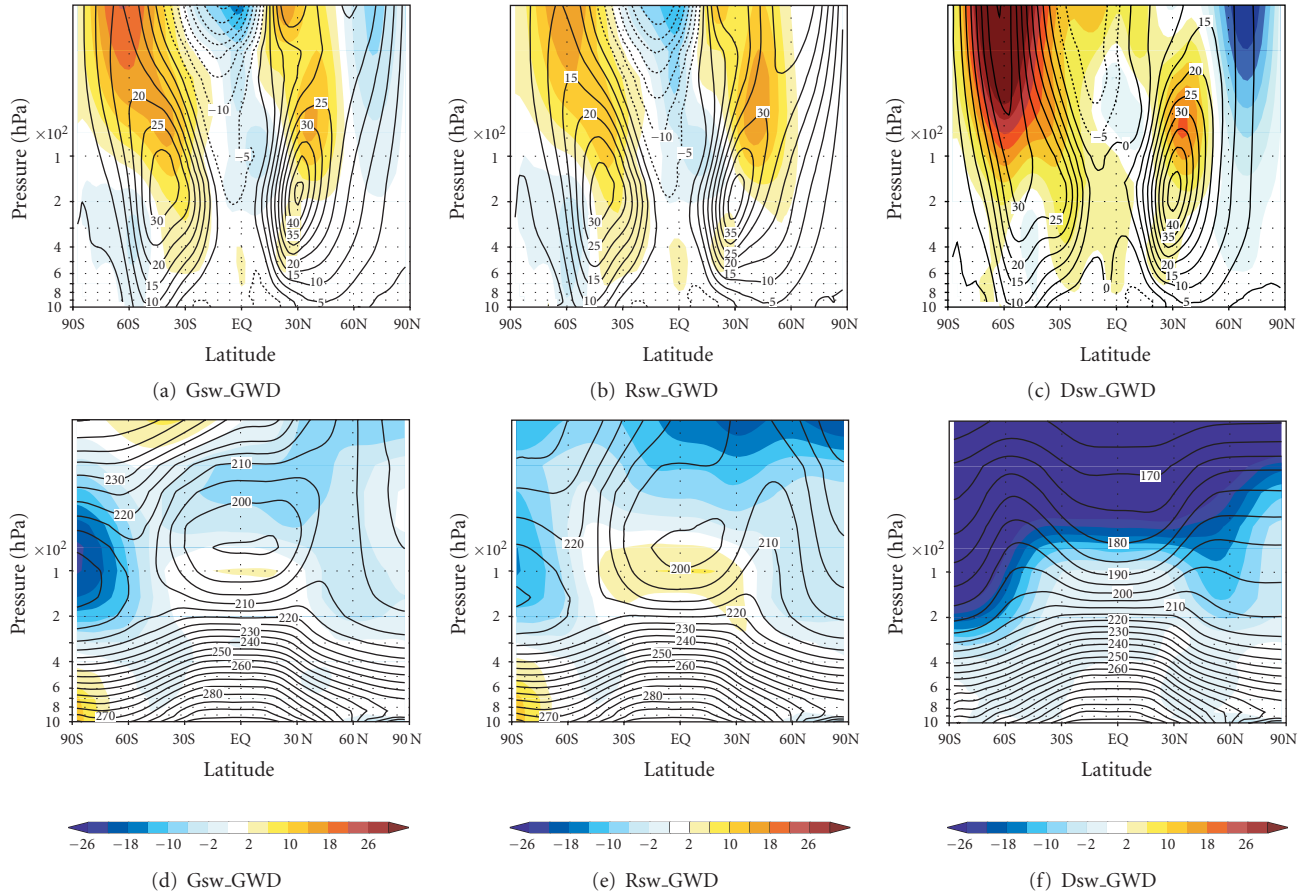


FIGURE 2: As in Figure 1, but with the new version of global WRF including the KA GWDO parameterization.

the stratosphere (Figure 2(f)) (note that the cold bias in the Dsw_nGWD experiment is due to the absence of both the ozone heating and GWDO). Moreover, given the highly-unrealistic thermodynamic structure, the GWDO process does not improve but continues to force the unrealistic system. We note that similar results were previously reported by Kim et al. [29]. They demonstrated that the underestimated ozone mixing ratio inducing an underestimation of shortwave heating can result in significant bias in zonal-mean temperature and wind structures; the impact of the low ozone mixing ratio is the largest in the lower polar stratosphere, which leads to the overly strong polar night jet in the northern hemisphere and unrealistically strong extension of the tropospheric westerly jet into the stratosphere in the southern hemisphere. Consequently, when the GWDO parameterization is given wrong information from other physical process, including GWDO does not improve the simulated results even though the GWDO process itself is a critical component in climate models. The Dudhia shortwave scheme shows good performance, that is, without large systematic bias, in regional weather prediction models since the model top is usually lower than 50 hPa in the regional model application, so that the simulated results do not suffer from the absent ozone effects.

In summary, shortwave radiation significantly impacts the modeled atmosphere, especially on the upper atmospheric circulations above the tropopause mainly due to the ozone heating. The heating scheme without the ozone process undergoes a distinct cold bias in the stratosphere, which in turn results in improper wind fields balancing with the cold bias. Under the unreasonable environmental conditions, the GWDO process continuously forces the system toward an unrealistic state.

3.2. Tropical Precipitation. In Figure 3, the simulated 3-year mean daily precipitation is compared with the daily GPCP data with a $1^\circ \times 1^\circ$ spatial resolution. The pattern correlation (PC), biases, and Root Mean Square Error (RMSE) between each simulation and GPCP data are presented at the top of each panel. The overall performance of the global WRF model in simulating the precipitation is acceptable in the three GWD experiments regardless of the shortwave processes (e.g., Figures 3(e)–3(g)). As seen in Shimpo et al. [30], the distribution of global precipitation from the global WRF is comparable, even though the integration period differs from one to another. The model produces tropical rainfall distributions quite reasonably, compared with the observations showing the double rainbelts along the double intertropical convergence zone (ITCZ) and precipitation

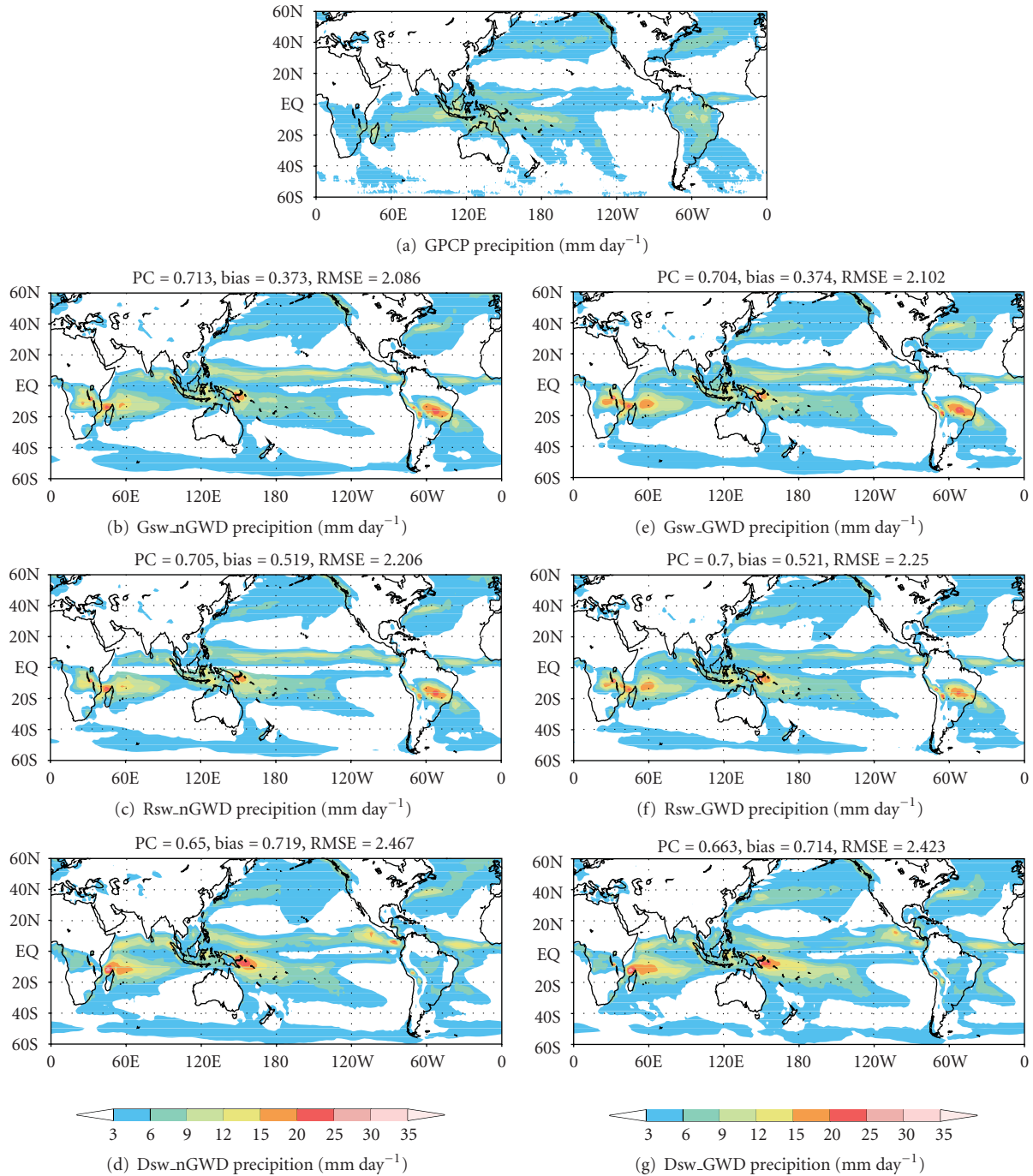


FIGURE 3: Comparison of 3-year averaged daily precipitation (mm day^{-1}) obtained from (a) observations, (b), (c), (d) the experiments without the KA GWDO scheme and with three different shortwave radiation processes, and (e), (f), (g) the experiments including the KA GWDO scheme and with three different shortwave radiation processes.

maximum regions over South America and South Africa. However, the model generally tends to overestimate the local rainfall maximum values over tropical regions (e.g., central South America, the northwestern ocean of Madagascar, near Sumatra, and western equatorial Pacific near the maritime continent), while it underestimates the rainfall around middle latitudes. Compared with the nGWD experiments, the inclusion of the GWDO neither significantly changes the

distribution, nor improves the distribution of the precipitation. With the Goddard and RRTMG shortwave processes the statistics are slightly worse in the GWDO experiments while the GWDO experiment shows slightly better statistics with the Dudhia shortwave. The simulated hydroclimate shows the best results—although not significant—with the Goddard shortwave scheme in this study both with and without GWDO.

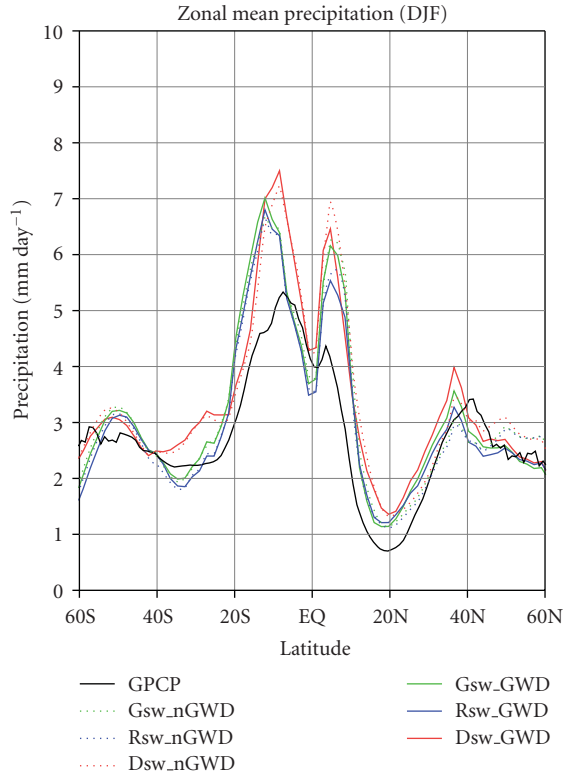


FIGURE 4: The zonal-mean of the 3-year mean daily precipitation (mm day^{-1}) obtained from the three nGWD (dotted lines) and three GWD (solid lines) experiments with the Goddard (green lines), RRTMG (blue lines), and Dudhia (red lines) shortwave radiation schemes, respectively.

Figure 4 shows the zonal mean of the 3-year mean daily precipitation from 60°S to 60°N . The model is successful in representing meridional distributions of the zonal-mean precipitation, but tends to overestimate the precipitation over the tropics, regardless of the shortwave scheme. Near the equator, the simulated daily precipitation patterns from the experiments with the shortwave schemes including ozone effects (i.e., the Goddard and RRTMG) are similar to each other while the experiment with the Dudhia scheme shows somewhat different behaviors, both with and without the KA GWDO. In other words, the experiments with the Goddard and RRTMG schemes commonly produce less rainfall than the experiment with the Dudhia scheme so that the amounts are closer to observations than that with the Dudhia scheme.

4. Concluding Remarks

The orographic gravity-wave drag (GWDO) process induced by subgrid scale orography is implemented in the global version of Weather Research and Forecasting (WRF) model. The sensitivity of the simulated climatology to the representation of shortwave radiation with the GWDO process in the modeled atmosphere is investigated using the Kim-Arakawa

GWDO (KA GWDO) parameterization and the Goddard, RRTMG, and Dudhia shortwave radiation schemes.

With the KA GWDO parameterization implemented, the climatology from the global WRF is relatively well simulated in the troposphere; the zonal-mean zonal wind and temperature structures are realistically represented. In the stratosphere, however, the performance of the model widely varies according to the representations of shortwave processes mainly due to the ozone heating. The scheme that excludes the ozone process induces a distinct cold bias in the stratosphere, and modeled wind fields balance with the unreasonable thermodynamic fields. The already unrealistic system due to the deficiency in the heating scheme is continuously impelled by the GWDO process. This result supports the notion that the success of a particular physics parameterization scheme in atmospheric models depends not only on the accuracy of the particular scheme itself but also on the success of other physical processes [16]. In view of the precipitation, the global WRF also well represents the overall patterns of the tropical precipitation but the model tends to overestimate (underestimate) the precipitation at the tropical (mid-latitude) regions. It is found that the simulated meridional precipitation distributions differ according to the shortwave schemes depending on the presence of ozone effects.

The KA GWDO is implemented in the WRF model based on this study and became available starting from the WRF version 3.1, which was released in April 2009.

Acknowledgments

This paper was supported by the Basic Science Research Program through the National Research Foundation of Korea (NRF) funded by the Ministry of Education, Science and Technology (2010-0000840), and by the Korean Foundation for International Cooperation Science & Technology (KICOS) 21 through a grant provided by the Korean Ministry of Science & Technology (MOST).

References

- [1] S.-Y. Hong and J.-W. Lee, "Assessment of the WRF model in reproducing a flash-flood heavy rainfall event over Korea," *Atmospheric Research*, vol. 93, no. 4, pp. 818–831, 2009.
- [2] K.-S. Lim and S.-Y. Hong, "Numerical simulation of heavy snowfall over the Ho-Nam province of Korea in December 2005," *Journal of the Korean Meteorological Society*, vol. 43, no. 2, pp. 161–173, 2007.
- [3] M. L. Weisman, C. Davis, W. Wang, K. W. Manning, and J. B. Klemp, "Experiences with 0-36-h explicit convective forecasts with the WRF-ARW model," *Weather and Forecasting*, vol. 23, no. 3, pp. 407–437, 2008.
- [4] G. Jianfeng, Q. Xiao, Y.-H. Kuo, D. M. Barker, X. Jishan, and M. Xiaoxing, "Assimilation and simulation of typhoon Rusa (2002) using the WRF system," *Advances in Atmospheric Sciences*, vol. 22, no. 3, pp. 415–427, 2005.
- [5] X. Li and Z. Pu, "Sensitivity of numerical simulation of early rapid intensification of Hurricane Emily (2005) to cloud

- microphysical and planetary boundary layer parameterizations," *Monthly Weather Review*, vol. 136, no. 12, pp. 4819–4838, 2008.
- [6] M. S. Bukovsky and D. J. Karoly, "Precipitation simulations using WRF as a nested regional climate model," *Journal of Applied Meteorology and Climatology*, vol. 48, no. 10, pp. 2152–2159, 2009.
 - [7] S.-R. Ham, S.-J. Park, C.-H. Bang, B.-J. Jung, and S.-Y. Hong, "Intercomparison of the East-Asian summer monsoon on 11–18 July 2004, simulated by WRF, MM5, and RSM models," *Atmosphere*, vol. 15, no. 2, pp. 91–99, 2005.
 - [8] W.-C. Skamarock, "Global WRF development," in *Proceedings of the 9th WRF User's Workshop*, Boulder, Colo, USA, June 2008.
 - [9] Y.-J. Kim, S. D. Eckermann, and H.-Y. Chun, "An overview of the past, present and future of gravity-wave drag parametrization for numerical climate and weather prediction models," *Atmosphere-Ocean*, vol. 41, no. 1, pp. 65–98, 2003.
 - [10] T. N. Palmer, G. J. Shutts, and R. Swinbank, "Alleviation of a systematic westerly bias in general circulation and numerical weather prediction models through an orographic gravity wave drag parameterization," *Quarterly Journal of the Royal Meteorological Society*, vol. 112, no. 474, pp. 1001–1039, 1986.
 - [11] N. A. McFarlane, "The effect of orographically excited gravity wave drag on the general circulation of the lower stratosphere and troposphere," *Journal of the Atmospheric Sciences*, vol. 44, no. 14, pp. 1775–1800, 1987.
 - [12] Y.-J. Kim and A. Arakawa, "Improvement of orographic gravity wave parameterization using a mesoscale gravity wave model," *Journal of the Atmospheric Sciences*, vol. 52, no. 11, pp. 1875–1902, 1995.
 - [13] S.-Y. Hong, J. Choi, E.-C. Chang, H. Park, and Y.-J. Kim, "Lower-tropospheric enhancement of gravity wave drag in a global spectral atmospheric forecast model," *Weather and Forecasting*, vol. 23, no. 3, pp. 523–531, 2008.
 - [14] W. C. Skamarock, J.-B. Klemp, J. Dudhia, et al., "A description of the advanced research WRF version 3," Tech. Rep. NCAR/TN-475+STR, 2008.
 - [15] Y.-J. Kim and J. D. Doyle, "Extension of an orographic-drag parametrization scheme to incorporate orographic anisotropy and flow blocking," *Quarterly Journal of the Royal Meteorological Society*, vol. 131, no. 609, pp. 1893–1921, 2005.
 - [16] Y.-J. Kim and S.-Y. Hong, "Interaction between the orography-induced gravity wave drag and boundary layer processes in a global atmospheric model," *Geophysical Research Letters*, vol. 36, Article ID L12809, 2009.
 - [17] S.-Y. Hong, "New global orography data sets," Office Note 424, NCEP, Camp Springs, Md, USA, 1999.
 - [18] E. J. Mlawer, S. J. Taubman, P. D. Brown, M. J. Iacono, and S. A. Clough, "Radiative transfer for inhomogeneous atmospheres: RRTM, a validated correlated-k model for the longwave," *Journal of Geophysical Research*, vol. 102, no. 14, pp. 16663–16682, 1997.
 - [19] S.-Y. Hong, Y. Noh, and J. Dudhia, "A new vertical diffusion package with an explicit treatment of entrainment processes," *Monthly Weather Review*, vol. 134, no. 9, pp. 2318–2341, 2006.
 - [20] F. Chen and J. Dudhia, "Coupling and advanced land surface-hydrology model with the Penn State-NCAR MM5 modeling system. Part I: model implementation and sensitivity," *Monthly Weather Review*, vol. 129, no. 4, pp. 569–585, 2001.
 - [21] G. A. Grell and D. Dévényi, "A generalized approach to parameterizing convection combining ensemble and data assimilation techniques," *Geophysical Research Letters*, vol. 29, no. 14, 1693, 2002.
 - [22] S.-Y. Hong, J. Dudhia, and S.-H. Chen, "A revised approach to ice microphysical processes for the bulk parameterization of clouds and precipitation," *Monthly Weather Review*, vol. 132, no. 1, pp. 103–120, 2004.
 - [23] M.-D. Chou and M. J. Suarez, "A solar radiation parameterization for atmospheric studies," Technical Report Series on Global Modeling and Data Assimilation 104606, 1999.
 - [24] J. Dudhia, "Numerical study of convection observed during the winter monsoon experiment using a mesoscale two-dimensional model," *Journal of the Atmospheric Sciences*, vol. 46, no. 20, pp. 3077–3107, 1989.
 - [25] M.-D. Chou, "A solar radiation model for use in climate studies," *Journal of the Atmospheric Sciences*, vol. 49, no. 9, pp. 762–772, 1992.
 - [26] M.-D. Chou and K.-T. Lee, "Parameterizations for the absorption of solar radiation by water vapor and ozone," *Journal of the Atmospheric Sciences*, vol. 53, no. 8, pp. 1203–1208, 1996.
 - [27] J. C. Alpert, M. Kanamitsu, P. M. Caplan, J. G. Sela, G. H. White, and E. Kalnay, "Mountain induced gravity wave drag parameterization in the NMC medium-range forecast model," in *Proceedings of the 8th Conference on Numerical Weather Prediction*, pp. 726–733, American Meteorological Society, Baltimore, Md, USA, 1988.
 - [28] R. J. Zamora, S. Solomon, E. G. Dutton, et al., "Comparing MM5 radiative fluxes with observations gathered during the 1995 and 1999 Nashville southern oxidants studies," *Journal of Geophysical Research*, vol. 108, no. D2, 4050, 2003.
 - [29] Y.-J. Kim, J. D. Farrara, and C. R. Mechoso, "Sensitivity of AGCM simulations to modifications in the ozone distribution and refinements in selected physical parameterizations," *Journal of the Meteorological Society of Japan*, vol. 76, no. 5, pp. 695–709, 1998.
 - [30] A. Shimpo, M. Kanamitsu, S. F. Iacobellis, and S.-Y. Hong, "Comparison of four cloud schemes in simulating the seasonal mean field forced by the observed sea surface temperature," *Monthly Weather Review*, vol. 136, no. 7, pp. 2557–2575, 2008.

Research Article

Evaluation of the WRF Double-Moment 6-Class Microphysics Scheme for Precipitating Convection

Song-You Hong,¹ Kyo-Sun Sunny Lim,¹ Yong-Hee Lee,² Jong-Chul Ha,² Hyung-Woo Kim,³ Sook-Jeong Ham,³ and Jimmy Dudhia⁴

¹ Department of Atmospheric Sciences and Global Environment Laboratory, Yonsei University, Seoul 120-749, Republic of Korea

² Forecast Research Laboratory, National Institute of Meteorological Research, Korea Meteorological Administration, Seoul 156-010, Republic of Korea

³ 73rd Weather Group, Korea Air Force, Chungnam 321-923, Republic of Korea

⁴ Mesoscale and Microscale Meteorology Division, National Center for Atmospheric Research, Boulder, CO 80305, USA

Correspondence should be addressed to Song-You Hong, shong@yonsei.ac.kr

Received 24 December 2009; Revised 23 February 2010; Accepted 8 April 2010

Academic Editor: Zhaoxia Pu

Copyright © 2010 Song-You Hong et al. This is an open access article distributed under the Creative Commons Attribution License, which permits unrestricted use, distribution, and reproduction in any medium, provided the original work is properly cited.

This study demonstrates the characteristics of the Weather Research and Forecasting (WRF) Double-Moment 6-Class (WDM6) Microphysics scheme for representing precipitating moist convection in 3D platforms, relative to the WSM6 scheme that has been widely used in the WRF community. For a case study of convective system over the Great Plains, the WDM6 scheme improves the evolutionary features such as the bow-type echo in the leading edge of the squall line. We also found that the WRF with WDM6 scheme removes spurious oceanic rainfall that is a systematic defect resulting from the use of the WSM6 scheme alone. The simulated summer monsoon rainfall in East Asia is improved by weakening (strengthening) light (heavy) precipitation activity. These changes can be explained by the fact that the WDM6 scheme has a wider range in cloud and rain number concentrations than does the WSM6 scheme.

1. Introduction

The Weather Research and Forecasting (WRF) model [1] is a community numerical weather prediction (NWP) model that is applicable to various scales of weather phenomena. Application of the WRF model has recently been extended to resolving regional details embedded within climate signals from the general circulation model [2]. As computer resources become available, the use of high-resolution WRF with a horizontal grid spacing of less than 5 km will improve forecasts for convective-scale phenomena, including explicit information about the timing, intensity, and mode of convection (e.g., [3, 4]). These previous reports demonstrate a 4-km resolution in WRF forecasts, which explicitly resolves convection yields for better guidance in precipitation forecasts, in comparison to 12-km resolution. Microphysical schemes are explicit, whereas convective parameterizations are implicit. As grid spacings decrease, convective parameterizations become more inappropriate (and scientifically

questionable given the underlying assumptions), whereas the explicit representation of microphysical processes can be computed for increasingly small clouds, cloud particles, water droplets, and so forth.

In the WRF model, there are multiple choices for each physical component; for example, there are ten algorithms for the cloud microphysics scheme, as of August 2009. Among the microphysics packages for clouds and precipitation, the series of the WRF single-moment (WSM) schemes (WSM3, WSM5, and WSM6 [5, 6]) has been widely used. As of June 2009, there are about 50 institutions across the globe running the WRF model on a real-time basis, and many of these institutions chose the WSM scheme for the microphysics option. As an example, the WRF model with the WSM6 microphysics has provided useful information on high-resolution weather phenomena over the Great Plains in the US [7, 8]. The Korean Meteorological Administration (KMA) and Korean Air Force (KAF) have also chosen the WSM6 scheme for real-time forecasts over East Asia, as noted

by Ha et al. [9] and Byun et al. [10]. There are numerous reports evaluating the performance of the WRF with WSM microphysics on various weather phenomena, including over the US [11], for a hurricane over the Atlantic [12], heavy rainfall over East Asia [13] and polar weather [14]. Huang et al. [15] used the WSM5 scheme to develop an advanced data assimilation system. Otkin and Greenwald [16] evaluated the WSM6 scheme using the MODIS-derived cloud data.

These studies demonstrated that the WSM schemes are competitive options in WRF by reproducing precipitating convection and associated meteorological phenomena. However, some systematic deficiencies have been reported, such as too much light precipitation activity [17] and an excessive amount of graupel, as compared to snow [18]. Spurious light precipitation was a systematic problem in the KMA forecast systems, as noted by Jo et al. [19]. A further revision to the WSM6 scheme employing a combined sedimentation velocity for graupel and snow [20] helped to alleviate the problem of excessive graupel, but weak radar reflectivity remained a systematic problem (personal communication with J. Kain).

The WRF Double-Moment 6-class (WDM6) scheme [21] was announced to the WRF community in April 2009. The WDM6 scheme enables the investigation of the aerosol effects on cloud properties and precipitation processes with the prognostic variables of cloud condensation nuclei (CCN), cloud water and rain number concentrations. The WDM6 scheme has been evaluated on an idealized two-dimensional thunderstorm testbed [21], but its overall characteristics relative to the WSM6 scheme for 3D real cases has not been provided. For these reasons, it is crucial to provide physical reasons for the differences in simulated precipitation and clouds between the WDM6 and WSM6 schemes.

A squall-line case over the Great Plains in the US will be simulated with both WSM6 and WDM6 microphysics schemes. In Lim and Hong [21], the fundamentals in the WDM6 were described in detail, but the differences in the simulated convection were demonstrated only for an idealized 2D storm. The purpose of a specific squall-line simulation is to evaluate the basic differences in convective activities between the WSM6 and WDM6 schemes in a real 3D model framework, prior to a robust evaluation of the hydrometeors and investigation studies on associated dynamics. Experimental evaluations of the WDM6 scheme over the WSM6 scheme at a real-time forecast platform at KMA have not shown distinct discrepancy in the predicted precipitation, but at times there have been cases that the WDM6 scheme is superior to the WSM6 scheme. A reduction of spurious precipitation in the case of the WSM6 scheme was systematically alleviated by the WDM6 scheme. We will demonstrate a mid-latitude cyclogenesis in East Asia as an example. As another evaluation tool, a regional climate modeling approach is adapted to examine the characteristics of a summer monsoon precipitation in East Asia. We focus on differences in the simulated precipitation with a possible physical reasoning on the fundamental differences in microphysics between the WSM6 and WDM6 schemes. The causes for the different model performances in the

underlying assumptions of WSM6 and WDM6 schemes will be investigated. In addition, a statistical measure of skill in precipitation forecasts over South Korea in summer 2008 will be shown in the final section.

2. Model Setup

2.1. Overview of the WDM6 Scheme. Prognostic water substance variables include water vapor, clouds, rain, ice, snow, and graupel for both the WDM6 [21] and WSM6 [5] schemes. Additionally, the prognostic number concentrations of cloud and rain waters, together with the CCN, are considered in the WDM6 scheme. The number concentrations of ice species such as graupel, snow, and ice are diagnosed following the ice-phase microphysics of Hong et al. [6]. This simplicity is theoretically based on the fact that the prediction of ice-phase number concentrations has significantly less impact on the results than the prediction of warm-phase concentrations in deep convective cases [22]. The activated CCN number concentration is predicted and formulated using the drop activation process based on Twomey's relationship between the number of activated CCN and supersaturation [23, 24], which enables a level of complexity to be added to the traditional bulk microphysics schemes through the explicit CCN-cloud drop concentration feedback. The complete evaporation of cloud drops is assumed to return corresponding CCN particles to the total CCN count. The CCN number concentration can be regulated under the forced large-scale environment, even for the seasonal climate cases. Any other CCN sink/source terms, except for CCN activation and droplet evaporation, are ignored in the WDM6 scheme. Further details on the CCN activation process are described in appendix A of Lim and Hong [21]. Accurate 3D CCN information is an important aspect of model simulations. However, obtaining real-time CCN information in both the horizontal and vertical directions is difficult. Thus, we chose an initial value of 100 cm^{-3} for the CCN number concentration in this study, as in Lim and Hong [21].

The formulation of warm-rain processes such as auto-conversion and accretion in the WDM6 scheme is based on the studies of Cohard and Pinty [25]. For other source and sink terms in warm-rain processes, the formulas in the WSM6 scheme were adopted. However, the microphysics processes in the WDM6 scheme, even if the same formula is applied, work differently from those in the WSM6 scheme due to the predicted number concentrations of cloud water and rain, which in turn indirectly influence the ice processes. Lim and Hong [21] demonstrated that, compared to the simulation of an idealized 2D thunderstorm with the WSM6 scheme, the higher drop concentrations in the convective core versus lower drop concentrations in the stratiform region are distinct in the WDM6. A marked radar bright band near the freezing level was produced with the WDM6 microphysics scheme. Meanwhile, the WSM6 scheme extended strong reflectivity to the ground level over the stratiform region. The aerosol effects on the cloud/rain properties and surface precipitation were also investigated by

varying the initial CCN number concentration. Varying the CCN number concentration had a nonmonotonic impact on rainfall amount.

2.2. Experimental Setup. The model used in this study is the Advanced Research WRF version 3.1 [1]. The physics packages, other than the microphysics, included the Kain-Fritsch cumulus parameterization scheme [26], the unified Noah land-surface model [27], a simple cloud-interactive shortwave radiation scheme [28], the Rapid Radiative Transfer Model (RRTM) longwave radiation scheme [29], and the Yonsei University planetary boundary layer (PBL) scheme, for vertical diffusion [30]. The PBL scheme was replaced with the Mellor-Yamada-Janjic (MYJ) scheme [31, 32] for the squall line case over US. The MYJ scheme has been widely evaluated for convective systems over the Great Plains in the US (e.g., [3, 4]).

The model configuration consisted of a nested domain defined on a Lambert conformal projection for all the selected cases. For a squall-line case over the US Great Plains, we followed the same model configuration of Shi et al. [17]. They investigated the impact of microphysical schemes on the IHOP_2002 case. From the comparison between the results from this study and those from Shi et al. [17], we can easily examine the advantage of the WDM6 scheme. A 1-km model covering Oklahoma (Domain 3, 540×465) was surrounded by a 3-km grid model (Domain 2, 480×351), which in turn was nested by a 9-km grid model (Domain 1, 300×201) using a two-way interaction. Model integration was conducted during a 36-hour period, from 0000 UTC June 12 to 1200 UTC June 13, 2002. The cumulus parameterization was applied, except for the 1-km and 3-km grid models for this case. A 30-km model covered the East Asia region (199×189) for a mid-latitude cyclogenesis case. This model configuration is identical to the model setup for operational forecasts at KMA, as of summer 2008. The experiments were performed for 36 hours, from 0000 UTC February 23 to 1200 UTC February 24, 2008. For a summer monsoon case in East Asia, a 50-km WRF was nested using analyzed data from the month of July 2006. The domain covers the East Asian monsoon regions (109×86) centered over the Korean peninsula. This configuration is identical to the model setup for several regional climate studies over East Asia (e.g., [33]). Koo and Hong [33] demonstrated that the WRF model is capable of reproducing the climatology and precipitation embedded within the summer monsoon over East Asia with the same model configuration of this study. The whole grid systems had 27 vertical layers, and the model top was located at 10 hPa for all the simulated cases. Initial and boundary conditions were generated by the National Centers for Environmental Prediction (NCEP)-Final Analysis (FNL) data on $1^\circ \times 1^\circ$ global grids, every six hours.

The Tropical Rainfall Measuring Mission (TRMM) TRMM Multisatellite Precipitation Analysis (TMPA; [34]) data on a $0.25^\circ \times 0.25^\circ$ were used for an evaluation of the simulated precipitation. In addition, simulated reflectivities were verified against observed ones, which were obtained from the WSI IHOP Sector Mosaic Reflectivity Imagery

(2-km) provided by the NCAR/EOL across the United States [35, 36] for the squall-line case.

3. Results and Discussion

3.1. Squall Line Case over the US Great Plains. Thompson et al. [37] and Weisman et al. [38] recognized that the WSM6 scheme tends to produce isolated intense convective cores compared to other schemes, such as that of Thompson [39]. This defect in the WSM6 scheme often failed to produce radar reflectivity and the associated mesoscale features of squall lines. The International H₂O project (IHOP_2002) was conducted over southern Kansas, Oklahoma, and northern Texas for six weeks during May and June of 2002 (13 May to 25 June 2002). A detailed summary of the physical processes (i.e., mesoscale convergence lines and gust fronts) associated with convective storm initiation and evolution for IHOP cases can be found in Wilson and Roberts [40].

Figure 1 compares the radar reflectivity and numbered gust fronts associated with a squall line that developed on 12 June in Kansas and moved southeastward. The WRF was initialized at 00 UTC 12 June 2002, and the simulation results at the 24-hr, 27-hr, and 30-hr forecast times are shown. Here, we focus on the evolutionary feature of the squall line passed Oklahoma between 0000 UTC 13 June and 0600 UTC 13 June, which can be evaluated though the comparisons with the available observations.

The observed data at 00 UTC 13 (Figure 1(a)) exhibits a line type convection core stretching from the Texas panhandle northeastward to the border between Kansas and Oklahoma. Wilson and Roberts [40] demonstrated that gust fronts 3 and 4 initiate many more storms than gust fronts 1 or 2. With time gust fronts 3 and 4 merge and a continuous squall line results in Figure 1(d). The storms associated with gust front 2 soon die, as does the gust front. The storms associated with gust front 1 live longer but never organize into a significant squall line. They also discovered that the most important factor for storm initiation and longevity is the gust front differential wind velocity. Generally, upward motion beginning in the boundary layer near the gust front extends up through the convective region, and slops more gently into the base of the trailing stratiform cloud. This descending current passes through the melting level, and finally enters the back of the convective region at low levels where it reinforces convergence at the leading gust front. Thus, the near-surface wind, normal to gust fronts, can enhance the convergence and organize a strong squall line.

The WSM6 run shows ambiguous separation of the two storms associated with gust fronts 3 and 4, showing larger convective areas than the observed areas data at 00 UTC 13 (Figure 1(b)). These storms do not develop into a continuous squall line after 3 hours. The storms associated with gust fronts 3 and 4 are well organized in the WDM6 run. After 3 hours, these storms are combined and the squall line traveled southeastward in central Oklahoma. However, the strength of reflectivity from the WDM6 run is systematically higher in a broad region compared to the WSM6 run and observations. In addition, the WDM6 run shows narrowed

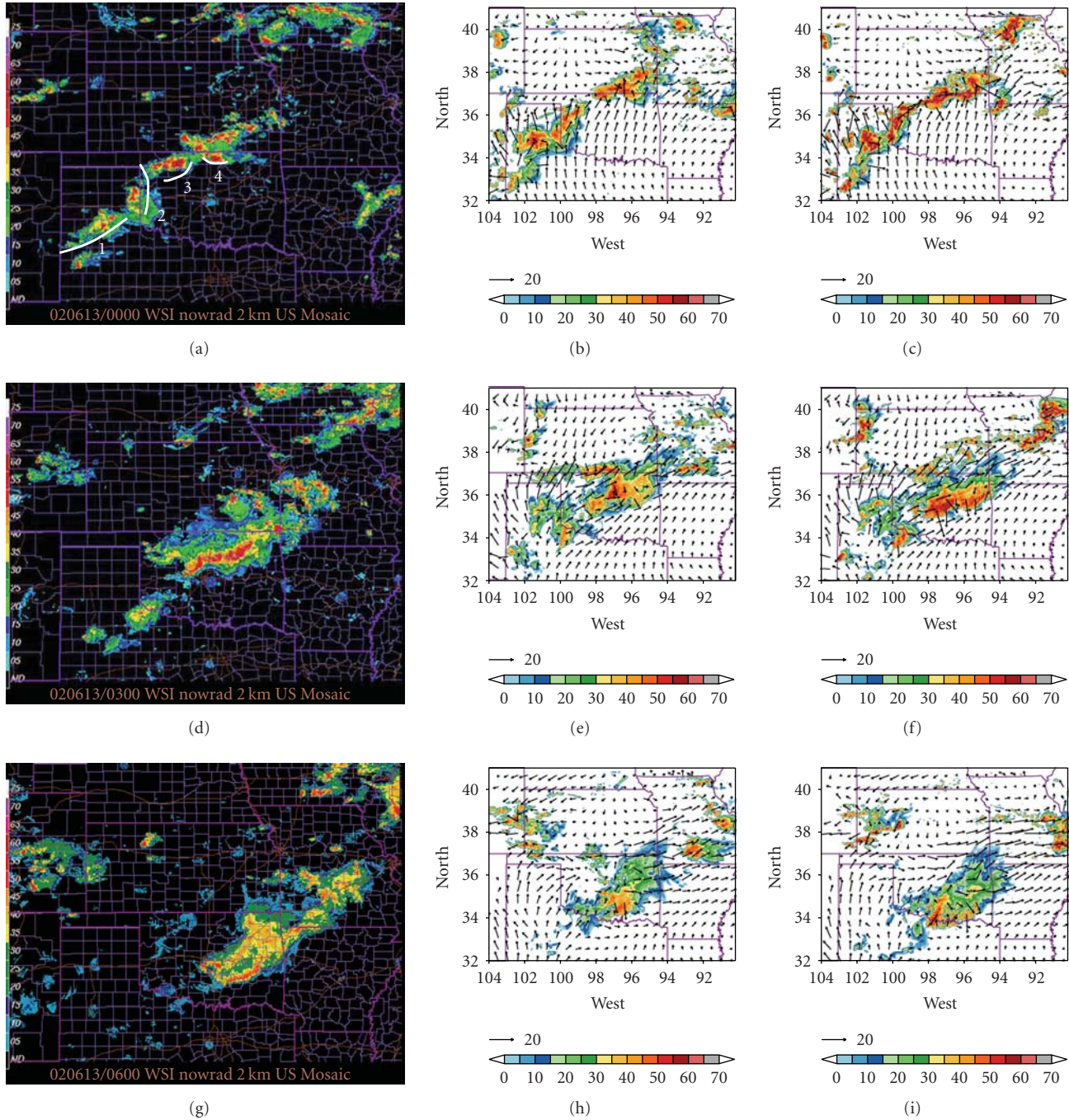


FIGURE 1: Radar reflectivity (in dBZ) and numbered gust fronts for a squall line case over the US. (a) The observed WSI IHOP Sector Mosaic reflectivity (2-km) at 00UTC 13 June 2002 (URL: <http://data.eol.ucar.edu/codiac/dss/id=77.091>). Note that these images are a vertical composite of reflectivity and depict the highest reflectivity measured over each point on the Earth's surface. (b) and (c) are from the WSM6 and WDM6 experiments, respectively. The reflectivities were calculated from model-simulated precipitation particles (rain, snow, and graupel). The plotted results are from the second domain (i.e., 3-km resolution). Three figures in the second row are the same as (a), (b), and (c), except they were observed at 03UTC 13 June 2002. Figures in the third row represent same fields at 06UTC 13 June 2002. Here, the vectors denote the 850-hPa wind (ms^{-1}).

areas of convection and the line-type band (Figure 1(c)). A reduction in light precipitation is noted in the Oklahoma panhandle at 0300 UTC in the WDM6 compared to the WSM6, as well as northeast Kansas and western Missouri at 0000 UTC. Convection in Missouri looks overdone at 0300

UTC in the WDM6 run. However, not much improvement is seen in Texas with the WDM6 microphysics scheme. During the weakening and dissipating stages (Figures 1(g), 1(h), and 1(i)), both experiments fail to simulate strong convection in the leading edge of a squall line, but with a better

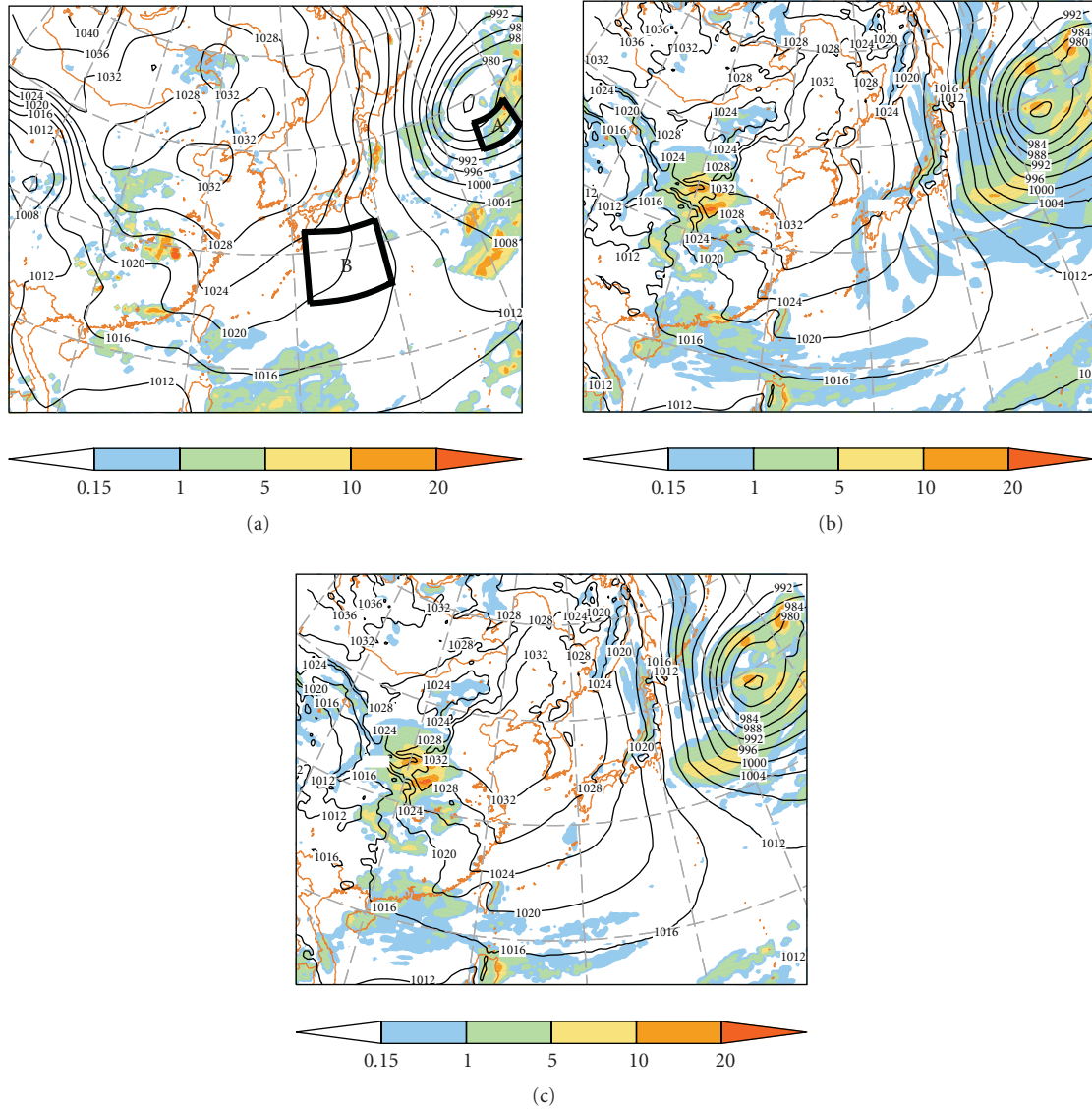


FIGURE 2: The 6 hours accumulated rainfall amount (mm) and averaged sea level pressure (SLP) from 0600 UTC to 1200 UTC 24 February 2008, obtained from the (a) TMPA observation for the rainfall and FNL data for the SLP, (b) WSM6, and (c) WDM6 experiments. Model integrations were conducted during the 36-h from 0000 UTC 23 February 2008. The marks “A” and “B” in Figure 2(a) designate the precipitating and nonprecipitating areas.

organized lined-up convection by the WDM6 experiment. This precipitating storm soon dissipates in both simulations at 1100 UTC, which is agreement with the observation (not shown).

The relatively narrower area of stratiform rain in the WDM6 run results from a larger number of rain number concentrations having smaller size, which causes rain to fall slowly on the ground, compared with the WSM6 run. Lim and Hong [21] noted that the WDM6 run shows well organized downdrafts with a strengthened cold pool, leading a slightly faster movement of the convective system, as compared to the WSM6 run within an idealized 2D thunderstorm testbed. Therefore, a possible reason for the faster movement of the squall line in the WDM6 run than in the WSM6 run in Figure 1 can be deduced from a

strengthened cold pool. Further study on the impact of microphysics on the evolutionary features of the convective storms and associated cloud dynamics is needed. In addition, it is no doubt that the more realistic squall-line evolution might not be achieved with other cases under different thermodynamic condition.

3.2. Oceanic Cyclogenesis. At KMA, the WRF model was run with 10-km resolution centered over South Korea, which is nested by a 30-km coarse mesh model from May 2007. The WRF model outperformed the operational regional model, which is based on the PSU/NCAR MM5 [41], in terms of statistical skill score for forecasted rainfall. However, it was often observed that the WRF with the WSM6 scheme produced spurious precipitation over the

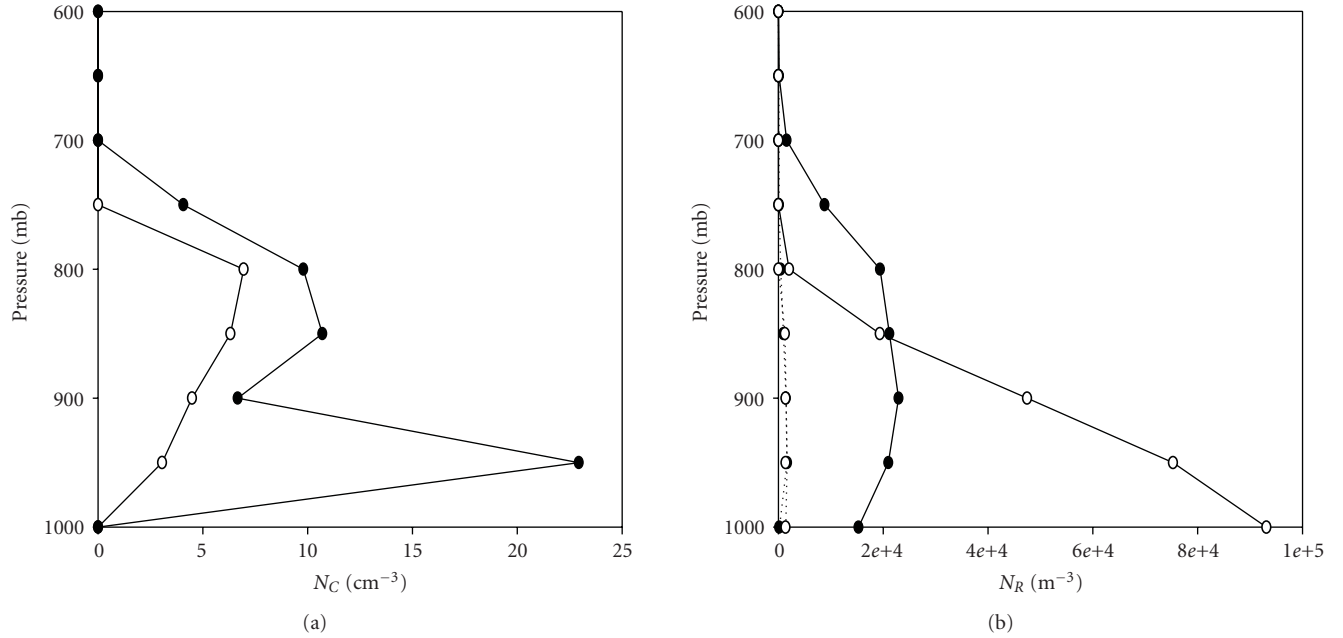


FIGURE 3: Modeled number concentrations of (a) cloud droplets and (b) raindrops over the regions “A” (closed circles) and “B” (open circles), as marked in Figure 2(a). The region “A” represents a relatively heavy rainfall region near the center of a cyclone, whereas a non-precipitating cloud region is observed in region “B.” The values are obtained from the cloud area averaged values during the six hours from 0600 UTC to 1200 UTC 24 February 2008. Solid lines indicate the results from the WDM6 scheme and dotted lines are from the WSM6 scheme. The number concentration for raindrops can be calculated using the slope of rain size distribution and intercept parameter of rain in the WSM6 microphysics scheme. A cloudy area is defined as either $q_c > 0.01 \text{ g kg}^{-1}$ or $q_R > 0.01 \text{ g kg}^{-1}$.

oceans (e.g., Figure 2). The modeled precipitation with the WSM6 scheme exhibits banded precipitation activity over the southern part of Japan, which is absent in the TMPA observation (cf. Figures 2(a) and 2(b)). Precipitation over the subtropics near the southern boundary of the model domain and near the center of the cyclone is excessive. Such an excessively light precipitation is greatly reduced when the WDM6 scheme is employed. The KAF real-time forecasts verified that occasional spurious light precipitation over South Korea in the case of a WSM6 run was also removed by employing the WDM6 scheme, as shown by Byun et al. [10].

Figure 3 shows the modeled cloud droplets and raindrop concentrations averaged over the regions “A” ($34^\circ\text{--}37.5^\circ\text{N}$, $154.5^\circ\text{--}160^\circ\text{E}$) and “B” ($26^\circ\text{--}32^\circ\text{N}$, $132^\circ\text{--}140^\circ\text{E}$), as marked in Figure 2(a). The region “A” represents a relatively heavy rainfall region near the center of a cyclone, whereas a non-precipitating cloud region is observed in region “B.” The number concentrations of cloud droplets from the WDM6 scheme vary according to the convective activity and reveal larger values over region “A” than over region “B.” A direct comparison of cloud droplet number concentrations between the WDM6 and WSM6 schemes is less meaningful since the CCN interacts explicitly with cloud droplets, and the cloud droplet number concentrations, which is predicted from the governing equation including the 3D advection and the source/sink of the number concentration in the WDM6 scheme, can be modulated according to the environmental features. Nevertheless, the comparison of cloud number

concentration in Figure 3 shows that the constant value of 300 cm^{-3} for the cloud water number concentration in the WSM6 scheme is not an appropriate representation of various types of clouds.

In terms of the number concentration of raindrops, the WSM6 scheme produces a rather uniform distribution in the vertical direction, and the differences in number concentration of raindrops between the regions “A” and “B” are not significant, with a constant intercept parameter value of $8 \times 10^6 \text{ m}^{-4}$ for rain. Meanwhile, the WDM6 scheme shows a large variation in rain number concentration in both the horizontal and vertical directions with a flexible size distribution of rain, which is modulated with different microphysical processes according to the precipitation type and the characteristics of convection. A relatively larger number of rain drops over the region “B” implies the existence of nonsedimenting small raindrops. As a result, the WDM6 scheme effectively suppresses the spurious light precipitation through the enhanced evaporation of small droplets. A more realistic distribution of particle sizes for clouds and raindrops and associated microphysics would provide a physical feedback to the convective environment.

3.3. Monsoonal Rainfall in July 2006. The regional climate simulation by analyzed large-scale forcing is an efficient way to evaluate model performance [42]. The WRF model with the WSM6 scheme is capable of reproducing two major rain bands, one over the subtropics covering South China and the

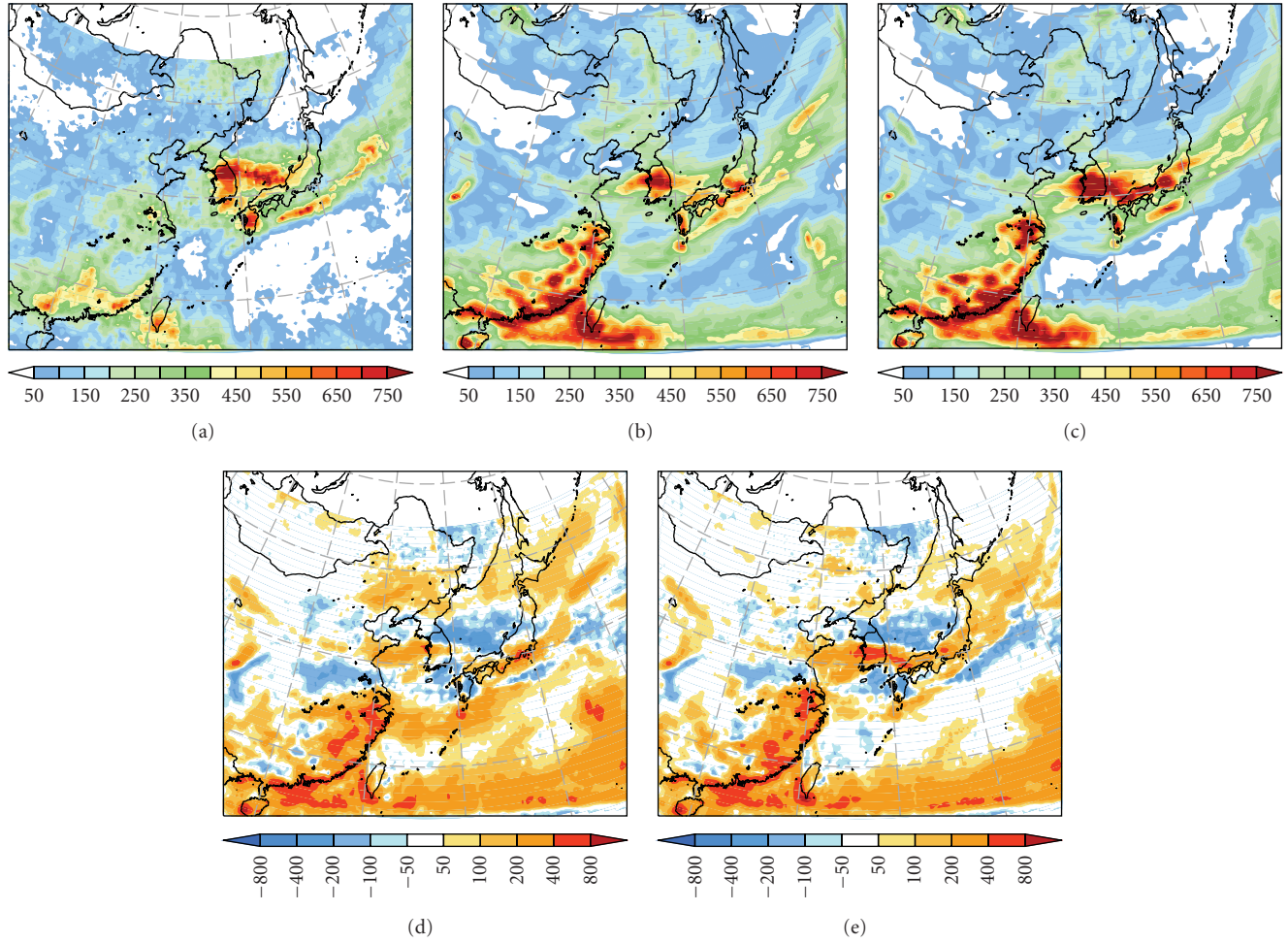


FIGURE 4: One-month accumulated rainfall (mm) from 0000 UTC 1 July to 0000 UTC 1 August 2006, obtained from the (a) TMPA observation, (b) WSM6, and (c) WDM6 experiments. Differences in 7 one-month accumulated rainfall (mm) between the observation and the (d) WSM6 (WSM6-TMPA) 8 and (e) WDM6 experiment (WDM6-TMPA).

TABLE 1: The pattern correlation coefficients (PC), bias score, and root mean square error (RMSE) of the 24 hours accumulated precipitation over South Korea with respect to surface observation, ending at 00 UTC 15 July 2001, for 5-km(45 km) resolution.

	Over the lands			Over the oceans		
	PC	Bias score	RMSE	PC	Bias score	RMSE
WSM6	0.71	20.41	128.97	0.53	70.36	170.01
WDM6	0.74	20.61	135.69	0.60	56.59	163.30

southeastern China Sea and the other in the mid-latitudes, where local maxima appears over Korea and Japan. These major summer rainfall features are simulated, irrespective of the microphysics scheme (Figure 4). One obvious deficiency in the WSM6 run is excessive rainfall over the northwestern Pacific Ocean, south of Japan. A large portion of the ocean is covered by the one-month accumulated rainfall of over 100 mm, which is largely alleviated in the WDM run. Table 1 shows the statistical skill score for precipitation over the lands and oceans. Even though the WDM6 shows slightly larger score in bias and root mean square error over lands, which is mainly due to heavy precipitation over Korea, significant improvement is shown over the oceans.

A close inspection reveals that a surplus rainfall in Manchuria and a deficit in the upper Yangtse river basin appear in the WSM run, which are improved in the WDM run. It is hard to interpret the physical reasoning for the different simulations within a 3D regional climate platform, thus, we compare the PDF of the simulated precipitation with those of the WSM6 and WDM6 schemes (Figure 5). It is clear that compared to the single-moment approach, the double-moment scheme suppresses the rainfall activity in the light precipitation categories, whereas it enhances the activities in the moderate and heavy categories. The above comparison of the two schemes qualitatively complies with the characteristics of the WDM microphysics over the WSM

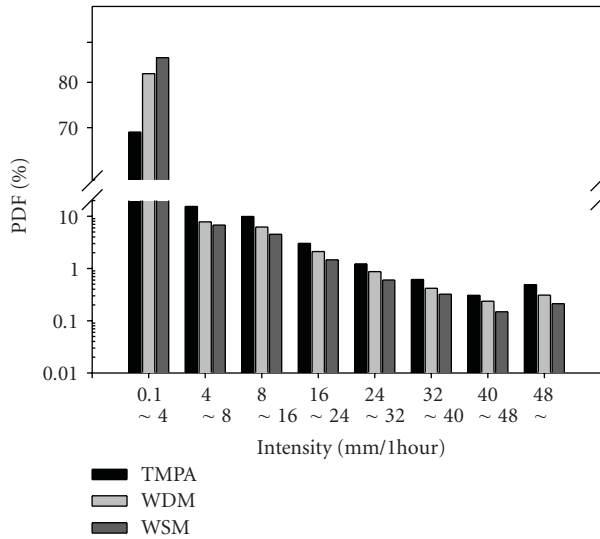


FIGURE 5: Probability Distribution Function (PDF) of three-hour accumulated rainfall intensity from the TMPA observations, and the corresponding results from the WDM6 and WSM6 experiments over the whole domain during the one month from 0000 UTC 1 July to 0000 UTC 1 August 2006.

algorithm in the 2D squall line case study of Lim and Hong [21], in that the WDM6 was responsible for the light (heavy) precipitation suppression (enhancement).

4. Concluding Remarks

The WRF model sensitivity to microphysical parameterization was analyzed from the WSM6 to the WDM6 scheme for the selected 3D test platforms. The case study for a squall line over the US Great Plains showed that the traveling speed of the simulated squall line is faster with the higher radar reflectivity when the double-moment scheme is used. It also appears that the double-moment approach of the WDM6 scheme tends to resolve known systematic deficiencies in the corresponding single-moment approach of the WSM6 scheme. The WDM6 run suppressed spurious light precipitation over the oceans. The simulated monsoonal summer rainfall climate over East Asia was improved by suppressing the light precipitation and enhancing the heavy precipitation.

A statistical evaluation of the precipitation forecast skill over South Korea in summer 2008 was made (Figure 6). The Korea Local Analysis and Prediction System (KLAPS) was developed for the operational very short range forecast with 5 km horizontal resolution [9]. A diabatic initialization technique was applied to the KLAPS with the use of radar reflectivity and satellite data. The scores confirmed that the forecasted precipitation using the WDM6 scheme was better than that with the WSM6 scheme for both the light and heavy precipitation categories in terms of the equitable threat score (ETS; [43]). In contrast to the previous evaluation cases, the amount of light precipitation is also increased during the first 6 hours forecast period. This may be a negative impact of

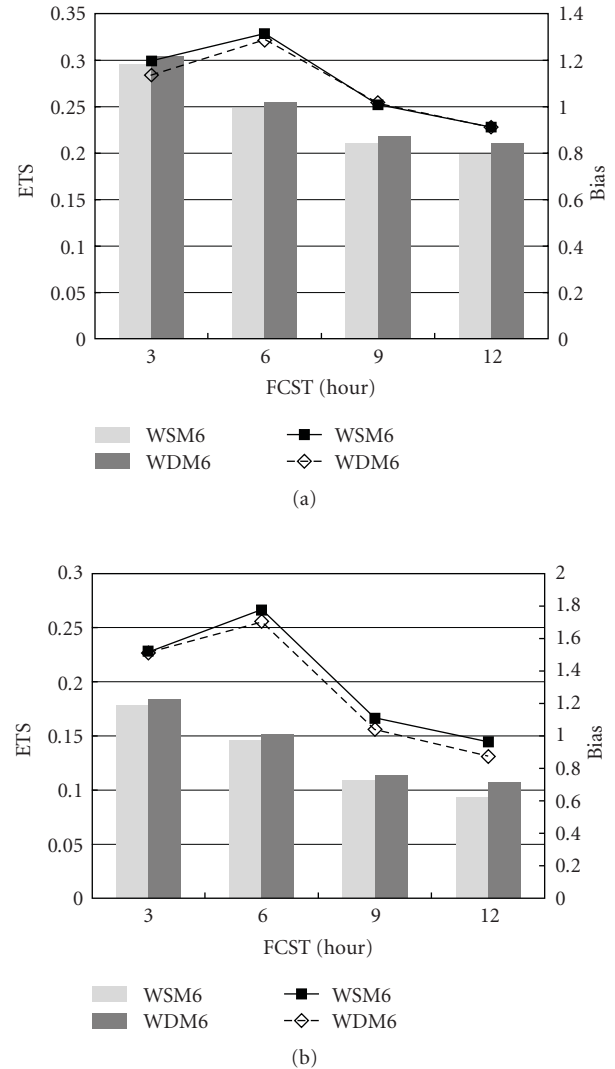


FIGURE 6: The time series of the equitable threat score (ETS; bars) and bias score (Bias; lines) for 3 hours accumulated precipitation over South Korea during the 12 hours forecast period, for (a) light precipitation (1 mm/3 hours) and (b) heavy precipitation (10 mm/3 hours) categories. The total number of samples is 976, which consists of 8 times a day for June-July-August 2008. The number of observation used is about 600, which is about 13 km apart over South Korea. The horizontal grid spacing is 5 km covering the Korean peninsula, which is nested by the 15 km grid.

a diabatic initialization that carries the hydrometeors at the initial time.

Further study is needed to clarify the physical reasons for the different features in precipitation, but it is assumed that a more realistic variability in cloud and rain number concentrations in the WDM6 scheme provides a realistic convective environment and feedback to cloud microphysics associated with the rainfall embedded within various weather phenomena, including a summer monsoon over East Asia and a squall line in the US. A robust evaluation of microphysical properties such as hydrometeors and associated cloud dynamics should be followed as a future study.

Acknowledgments

This research was supported by the Basic Science Research Program through the National Research Foundation of Korea (NRF) funded by the Ministry of Education, Science and Technology (2010-0000840), by the Korean Foundation for International Cooperation Science & Technology (KICOS) through a grant provided by the Korean Ministry of Science & Technology (MOST) in 2009, by the project, "Development of the numerical prediction technique for the improved military weather support," through a grant provided by the Republic of Korea Air Force (ROKAF) in 2010, and by the National Institute of Meteorological Research of the Korea Meteorological Administration under a major project "NIMR-2009-C-1." The comments from the anonymous reviewers were helpful. WSI IHOP Sector Mosaic Reflectivity Imagery (2-km) [NCAR/EOL] provided by NCAR/EOL under sponsorship of the National Science Foundation.

References

- [1] W. C. Skamarock, J. B. Klemp, J. Dudhia, et al., "A description of the advanced research WRF version 3," Technical Note TN-475+STR, NCAR, 2008.
- [2] L. R. Leung, Y.-H. Kuo, and J. Tribbia, "Research needs and directions of regional climate modeling using WRF and CCSM," *Bulletin of the American Meteorological Society*, vol. 87, no. 12, pp. 1747–1751, 2006.
- [3] J. S. Kain, S. J. Weiss, J. J. Levit, M. E. Baldwin, and D. R. Bright, "Examination of convection-allowing configurations of the WRF model for the prediction of severe convective weather: the SPC/NSSL Spring Program 2004," *Weather and Forecasting*, vol. 21, no. 2, pp. 167–181, 2006.
- [4] M. L. Weisman, C. Davis, W. Wang, K. W. Manning, and J. B. Klemp, "Experiences with 0–36-h explicit convective forecasts with the WRF-ARW model," *Weather and Forecasting*, vol. 23, no. 3, pp. 407–437, 2008.
- [5] S.-Y. Hong and J.-O. J. Lim, "The WRF single-moment 6-class microphysics scheme (WSM6)," *Journal of the Korean Meteorological Society*, vol. 42, no. 2, pp. 129–151, 2006.
- [6] S.-Y. Hong, J. Dudhia, and S.-H. Chen, "A revised approach to ice microphysical processes for the bulk parameterization of clouds and precipitation," *Monthly Weather Review*, vol. 132, no. 1, pp. 103–120, 2004.
- [7] C. M. Shafer, A. E. Mercer, C. A. Doswell III, M. B. Richman, and L. M. Leslie, "Evaluation of WRF forecasts of tornadic and nontornadic outbreaks when initialized with synoptic-scale input," *Monthly Weather Review*, vol. 137, no. 4, pp. 1250–1271, 2009.
- [8] C. S. Schwartz, J. S. Kain, S. J. Weiss, et al., "Next-day convection-allowing WRF model guidance: a second look at 2-km versus 4-km grid spacing," *Monthly Weather Review*, vol. 137, no. 10, pp. 3351–3372, 2009.
- [9] J.-C. Ha, Y.-H. Lee, J.-S. Lee, H.-C. Lee, and H.-S. Lee, "Development of short range analysis and prediction system," in *Proceedings of the 9th Weather Research and Forecasting Model Workshop*, pp. 1–4, NCAR Mesoscale and Microscale Meteorology Division, Boulder, Colo, USA, 2008, <http://www.mmm.ucar.edu/wrf/users/workshops/>.
- [10] U.-Y. Byun, H.-W. Kim, Y.-K. Son, and Y.-K. Yum, "Evaluation of the KAF-WRF model during a summer season," in *Autumn Meeting, Korean Meteorological Society*, pp. 324–325, Kyungpook National University, Daegu, South Korea, 2009, http://www.komes.or.kr/journal_search/ISS.GotoSearch.php.
- [11] K. A. James, D. J. Stensrud, and N. Yussouf, "Value of real-time vegetation fraction to forecasts of severe convection in high-resolution models," *Weather and Forecasting*, vol. 24, no. 1, pp. 187–210, 2009.
- [12] X. Li and Z. Pu, "Sensitivity of numerical simulation of early rapid intensification of Hurricane Emily (2005) to cloud microphysical and planetary boundary layer parameterizations," *Monthly Weather Review*, vol. 136, no. 12, pp. 4819–4838, 2008.
- [13] H. Shin and S.-Y. Hong, "Quantitative precipitation forecast experiments of heavy rainfall over Jeju Island on 14–16 September 2007 using the WRF model," *Asia-Pacific Journal of Atmospheric Sciences*, vol. 45, no. 1, pp. 71–89, 2009.
- [14] J. G. Powers, "Numerical prediction of an Antarctic severe wind event with the Weather Research and Forecasting (WRF) model," *Monthly Weather Review*, vol. 135, no. 9, pp. 3134–3157, 2007.
- [15] X.-Y. Huang, Q. Xiao, D. M. Barker, et al., "Four-dimensional variational data assimilation for WRF: formulation and preliminary results," *Monthly Weather Review*, vol. 137, no. 1, pp. 299–314, 2009.
- [16] J. A. Otkin and T. J. Greenwald, "Comparison of WRF model-simulated and MODIS-derived cloud data," *Monthly Weather Review*, vol. 136, no. 6, pp. 1957–1970, 2008.
- [17] J. J. Shi, W.-K. Tao, S. Lang, S. S. Chen, S.-Y. Hong, and C. Peters-Lidard, "An improved bulk microphysical scheme for studying precipitation processes: comparisons with other schemes," in *AGU Joint Assembly*, Acapulco, Mexico, May 2007, American AU11 Geophysical Union, ID A41D-02, <http://www.agu.org/>.
- [18] Y. Lin and B. A. Colle, "The 4–5 December 2001 IMPROVE-2 event: observed microphysics and comparisons with the weather research and forecasting model," *Monthly Weather Review*, vol. 137, no. 4, pp. 1372–1392, 2009.
- [19] I.-H. Jo, K.-D. An, E.-H. Lim, and D.-U. Chang, "Improvement of the precipitation forecasting of a light-precipitation category in the WRF microphysics scheme during a winter season," in *Autumn Meeting, Korean Meteorological Society*, pp. 248–249, Kongju National University, Daejeon, South Korea, 2008, http://www.komes.or.kr/journal_search/ISS.GotoSearch.php.
- [20] J. Dudhia, S.-Y. Hong, and K.-S. Lim, "A new method for representing mixed-phase particle fall speeds in bulk microphysics parameterizations," *Journal of the Meteorological Society of Japan*, vol. 86A, pp. 33–44, 2008.
- [21] K.-S. S. Lim and S.-Y. Hong, "Development of an effective double-moment cloud microphysics scheme with prognostic Cloud Condensation Nuclei (CCN) for weather and climate models," *Monthly Weather Review*, vol. 138, pp. 1587–1612, 2010.
- [22] H. Morrison, G. Thompson, and V. Tatarskii, "Impact of cloud microphysics on the development of trailing stratiform precipitation in a simulated squall line: comparison of one- and two-moment schemes," *Monthly Weather Review*, vol. 137, no. 3, pp. 991–1007, 2009.
- [23] S. Twomey, "The nuclei of natural cloud formation part II: the supersaturation in natural clouds and the variation of cloud droplet concentration," *Pure and Applied Geophysics*, vol. 43, no. 1, pp. 243–249, 1959.
- [24] M. Khairoutdinov and Y. Kogan, "A new cloud physics parameterization in a large-eddy simulation model of marine

- stratocumulus," *Monthly Weather Review*, vol. 128, no. 1, pp. 229–243, 2000.
- [25] J.-M. Cohard and J.-P. Pinty, "A comprehensive two-moment warm microphysical bulk scheme. I: description and tests," *Quarterly Journal of the Royal Meteorological Society*, vol. 126, no. 566, pp. 1815–1842, 2000.
- [26] J. S. Kain and J. Kain, "The Kain-Fritsch convective parameterization: an update," *Journal of Applied Meteorology*, vol. 43, no. 1, pp. 170–181, 2004.
- [27] F. Chen and J. Dudhia, "Coupling and advanced land surface-hydrology model with the Penn State-NCAR MM5 modeling system. Part I: model implementation and sensitivity," *Monthly Weather Review*, vol. 129, no. 4, pp. 569–585, 2001.
- [28] J. Dudhia, "Numerical study of convection observed during the winter monsoon experiment using a mesoscale two-dimensional model," *Journal of the Atmospheric Sciences*, vol. 46, no. 20, pp. 3077–3107, 1989.
- [29] E. J. Mlawer, S. J. Taubman, P. D. Brown, M. J. Iacono, and S. A. Clough, "Radiative transfer for inhomogeneous atmospheres: RRTM, a validated correlated-k model for the longwave," *Journal of Geophysical Research D*, vol. 102, no. 14, pp. 16663–16682, 1997.
- [30] S.-Y. Hong, Y. Noh, and J. Dudhia, "A new vertical diffusion package with an explicit treatment of entrainment processes," *Monthly Weather Review*, vol. 134, no. 9, pp. 2318–2341, 2006.
- [31] Z. Janjic, "Nonsingular implementation of the Mellor-Yamada level 2.5 scheme in the NCEP global model," NCEP Office Note, no. 437, 2002.
- [32] G. L. Mellor and T. Yamada, "Development of a turbulence closure model for geophysical fluid problems," *Reviews of Geophysics & Space Physics*, vol. 20, no. 4, pp. 851–875, 1982.
- [33] M.-S. Koo and S.-Y. Hong, "Diurnal variations of simulated precipitation over East Asia in two regional climate models," *Journal of Geophysical Research D*, vol. 115, no. 5, Article ID D05105, 17 pages, 2010.
- [34] G. J. Huffman, R. F. Adler, D. T. Bolvin, et al., "The TRMM multisatellite precipitation analysis (TMPA): quasi-global, multiyear, combined-sensor precipitation estimates at fine scales," *Journal of Hydrometeorology*, vol. 8, no. 1, pp. 38–55, 2007.
- [35] T. D. Crum and R. L. Alberty, "The WSR-88D and the WSR-88D operational support facility," *Bulletin of the American Meteorological Society*, vol. 74, no. 9, pp. 1669–1687, 1993.
- [36] W. Heiss, D. McGrew, and D. Sirmans, "NEXRAD: next generation weather radar (WSR-88D)," *Microwave Journal*, vol. 33, pp. 79–98, 1990.
- [37] G. Thompson, P. R. Field, W. D. Hall, and R. M. Rasmussen, "A new bulk microphysical parameterization for WRF and MM6," in *Proceedings of the 7th Weather Research and Forecasting Model Workshop*, pp. 1–11, NCAR Mesoscale and Microscale Meteorology Division, Boulder, Colo, USA, 2006, <http://www.mmm.ucar.edu/wrf/users/workshops/>.
- [38] M. L. Weisman, W. Wang, and K. Manning, "The use of the RUC DFI initialization for the 2009 WRF-ARW 3 km explicit convective forecasts," in *Proceedings of the 10th Weather Research and Forecasting Model Workshop*, pp. 1–18, NCAR Mesoscale and Microscale Meteorology Division, Boulder, Colo, USA, 2009, <http://www.mmm.ucar.edu/wrf/users/workshops/>.
- [39] G. Thompson, P. R. Field, R. M. Rasmussen, and W. D. Hall, "Explicit forecasts of winter precipitation using an improved bulk microphysics scheme. Part II: implementation of a new snow parameterization," *Monthly Weather Review*, vol. 136, no. 12, pp. 5095–5115, 2008.
- [40] J. W. Wilson and R. D. Roberts, "Summary of convective storm initiation and evolution during IHOP: observational and modeling perspective," *Monthly Weather Review*, vol. 134, no. 1, pp. 23–47, 2006.
- [41] G. A. Grell, J. Dudhia, and D. R. Stauffer, "A description of the Fifth-Generation Penn State/NCAR mesoscale model (MM5)," Technical Note TN-398+STR, NCAR, 1994.
- [42] S. J. Ghan, L. R. Leung, and J. McCaa, "A comparison of three different modeling strategies for evaluating cloud and radiation parameterizations," *Monthly Weather Review*, vol. 127, no. 9, pp. 1967–1984, 1999.
- [43] F. Su, Y. Hong, and D. P. Lettenmaier, "Evaluation of TRMM multisatellite precipitation analysis (TMPA) and its utility in hydrologic prediction in the La Plata Basin," *Journal of Hydrometeorology*, vol. 9, no. 4, pp. 622–640, 2008.

Research Article

Sensitivity Study of Four Land Surface Schemes in the WRF Model

Jiming Jin,¹ Norman L. Miller,² and Nicole Schlegel³

¹ Departments of Watershed Sciences & Plants, Soils, and Climate, UT 84322-1400 State University, Logan, Utah, USA

² Lawrence Berkeley National Laboratory, Earth Sciences Division, Department of Geography,
University of California at Berkeley, Berkeley, CA 94720, USA

³ Department of Earth and Planetary Science, University of California at Berkeley, Beverley, CA 94720, USA

Correspondence should be addressed to Jiming Jin, jimingjin99@gmail.com

Received 1 January 2010; Revised 14 April 2010; Accepted 1 May 2010

Academic Editor: Song Y. Hong

Copyright © 2010 Jiming Jin et al. This is an open access article distributed under the Creative Commons Attribution License, which permits unrestricted use, distribution, and reproduction in any medium, provided the original work is properly cited.

The Weather Research and Forecasting (WRF) model version 3.0 developed by the National Center for Atmospheric Research (NCAR) includes three land surface schemes: the simple soil thermal diffusion (STD) scheme, the Noah scheme, and the Rapid Update Cycle (RUC) scheme. We have recently coupled the sophisticated NCAR Community Land Model version 3 (CLM3) into WRF to better characterize land surface processes. Among these four land surface schemes, the STD scheme is the simplest in both structure and process physics. The Noah and RUC schemes are at the intermediate level of complexity. CLM3 includes the most sophisticated snow, soil, and vegetation physics among these land surface schemes. WRF simulations with all four land surface schemes over the western United States (WUS) were carried out for the 1 October 1995 through 30 September 1996. The results show that land surface processes strongly affect temperature simulations over the (WUS). As compared to observations, WRF-CLM3 with the highest complexity level significantly improves temperature simulations, except for the wintertime maximum temperature. Precipitation is dramatically overestimated by WRF with all four land surface schemes over the (WUS) analyzed in this study and does not show a close relationship with land surface processes.

1. Introduction

Fossil fuel emissions have caused a 0.6°C increase in global temperature during the last 100 years (Hansen et al. [1]), with an anticipated additional 2–5°C temperature increase by the end of this century (The Intergovernmental Panel on Climate Change Fourth Assessment Report (IPCC AR4) 2007). Climate change impacts (e.g., extreme heat, severe storms, and air pollution inversion episodes) are especially significant at regional scales, where society and ecosystems are most sensitive (IPCC AR4 2007). Thus, accurate regional climate model (RCM) simulations with reduced uncertainties are needed to better assess the limits of climate change impacts. RCM uncertainties include the spatiotemporal distribution of precipitation, its type, amount, and intensity, snow mass accumulation and melt rates, and daily minimum and maximum temperature. Quantifying these uncertainties and improving operational monthly to interannual regional climate predictions are especially important for sustaining the health of local human and ecosystems environments.

To improve the accuracy of RCM forecasts, we need to understand physical mechanisms and processes that control regional climate change. An important process that regulates regional climate is the global increase in the concentration of atmospheric greenhouse gases (GHGs). It is well recognized that increasing GHG concentrations nonlinearly increases the atmospheric water-holding capacity, resulting in large variations in precipitation events. Theoretically, the Clausius-Clapeyron relationship indicates that a 3°C temperature increase over the 21st century will result in a 20% increase in the atmospheric water-holding capacity [2], leading to an increased likelihood of more severe flood and hydrologic drought conditions (frequency, intensity, and duration). Such an increase in temperature will also change the pressure gradients over the mid-latitudes, shifting storm tracks poleward [3] and strengthening the likelihood of droughts in parts of the US. The El Niño-Southern Oscillation (ENSO) also changes global climate circulation and alters atmospheric moisture transport. The western United States (WUS) is a particularly vulnerable dipole, where ENSO

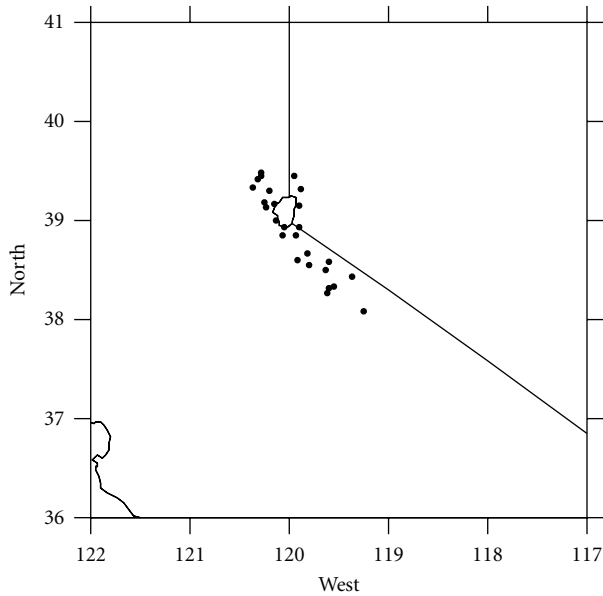


FIGURE 1: 26 Snotel Stations located in the California and Nevada areas.

episodes produce anomalously wet (dry) winter precipitation and snow mass amount and spatial distribution in the southern (northern) WUS [4].

In addition to the role of global-scale climate change, the regional climate system is often disturbed by land-surface and land use changes due to human activities (e.g., agricultural expansion, urbanization) and natural processes (e.g., drought-related vegetation mortality in the U.S. south-west and global-warming-induced snow cover and glacier retreat). Breshears et al. [5] indicate that a recent drought in the southern WUS resulted in significant vegetation mortality, with reduction in vegetation abundance that further modified the surface flux exchanges between the land surface and atmosphere and ultimately reduced cloudiness and precipitation [6] and raised the temperature [7].

Regional climate forecasts have advanced at the European Centre for Medium-Range Weather Forecasts [8], the Australian Commonwealth Scientific and Research Organization [9], and the National Centers for Environmental Predictions (NCEP) [10]. These efforts are based on numerical computer models at global or near-global scales. However, the horizontal spatial resolution for current climate forecasts ranges over hundreds of kilometers and is too coarse to provide important details of sub-100 km regional-scale climate phenomena and processes. It is well acknowledged that RCMs with spatial resolution at or coarser than 30 km are unable to produce accurate precipitation forecasts for the California mountainous areas [11], and that global climate models at resolutions of 30 km or higher require computing and human resources that are currently not feasible, especially if multiyear ensemble integrations are required. At present, only a few operational institutions are capable of this level of computation and data storage, while the majority of global climate models usually have oversimplified

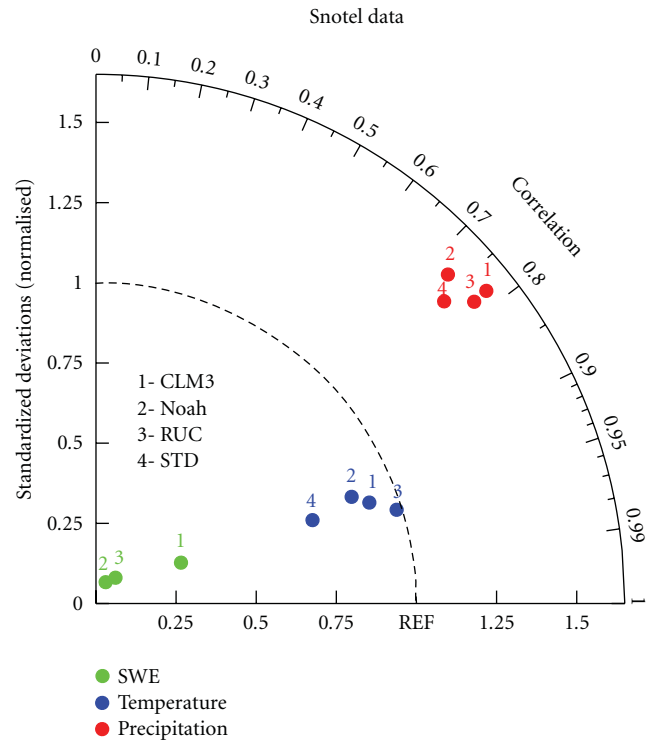


FIGURE 2: Comparison of the WRF-simulations with CLM3, Noah, RUC, and STD land surface schemes. Green dots are for SWE, red dots are for precipitation, and blue dots are for temperature. The standard deviations and correlation coefficients are derived from the daily simulations and observations for 1 October 1995 through 30 September 1996.

physics and parameterized structures that are unable to adequately describe regional-scale processes and phenomena with sufficient accuracy. Therefore, RCMs driven by global climate forecast products are more appropriate tools to overcome these limitations for exploring regional climate predictability.

In this study, the Weather Research, and Forecasting (WRF) model version 3.0 developed by the National Center for Atmospheric Research (NCAR) is used to perform regional climate simulations over the WUS. The WRF model is a limited-area, nonhydrostatic, terrain-following sigma-coordinate model designed to simulate or predict regional weather and climate. This model represents the recent advances of RCMs that combine the expertise and experience for mesoscale meteorology and land-surface and climate science developed over the last several decades. The version 3.0 of the WRF model includes three land surface schemes, which are the simple soil thermal diffusion (STD) scheme, the Noah scheme (Ek and Mahrt [12]), and the Rapid Update Cycle (RUC; [13, 14]) scheme. However, the snow physics in these land surface schemes embedded in WRF is oversimplified. The lack of a dynamic vegetation component within these schemes makes WRF unable to simulate future climate-forced vegetation shifts. Hence, we have recently coupled the advanced NCAR Community Land Model version 3 (CLM3) [15] into WRF to better characterize land

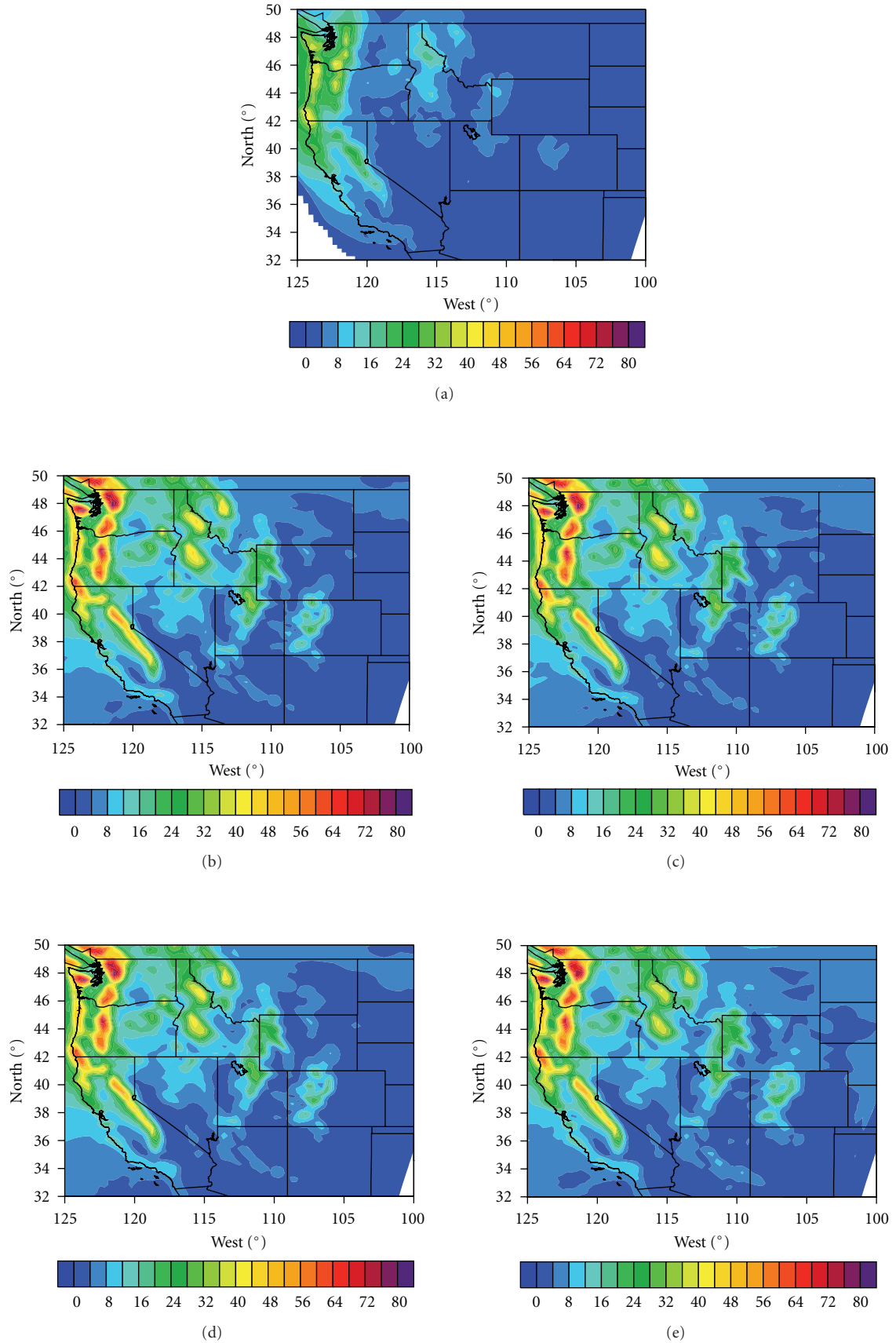


FIGURE 3: The geographic distribution of observed and WRF-simulated monthly winter precipitation (Unit: mm) averaged over November 1995 through March 1996. (a) Observations; (b) CLM3; (c) Noah; (d) RUC; (e) STD.

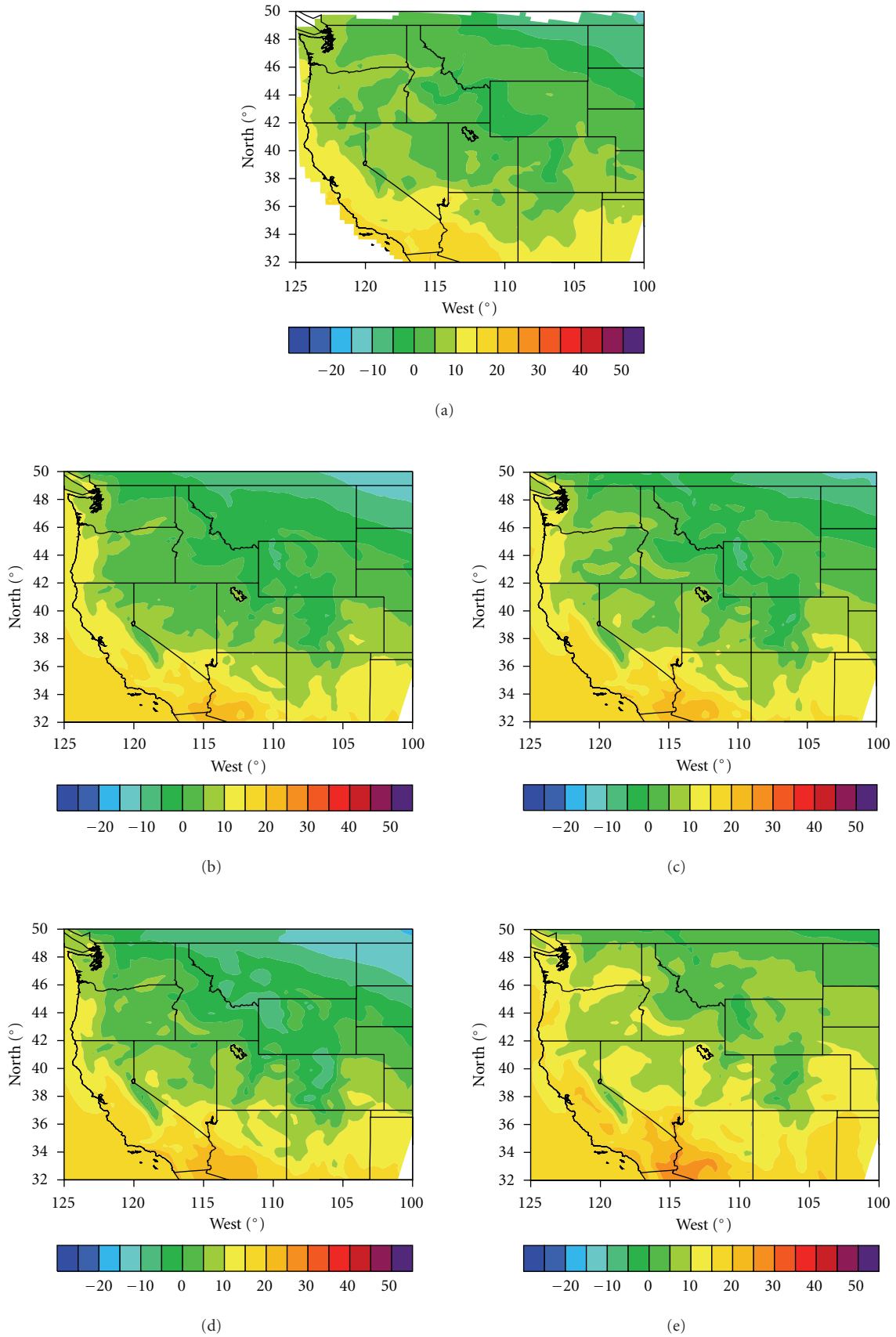


FIGURE 4: The geographic distribution of observed and WRF-simulated winter (December, January, and February) daily maximum temperature (Unit: $^{\circ}\text{C}$). (a) Observations; (b) CLM3; (c) Noah; (d) RUC; (e) STD.

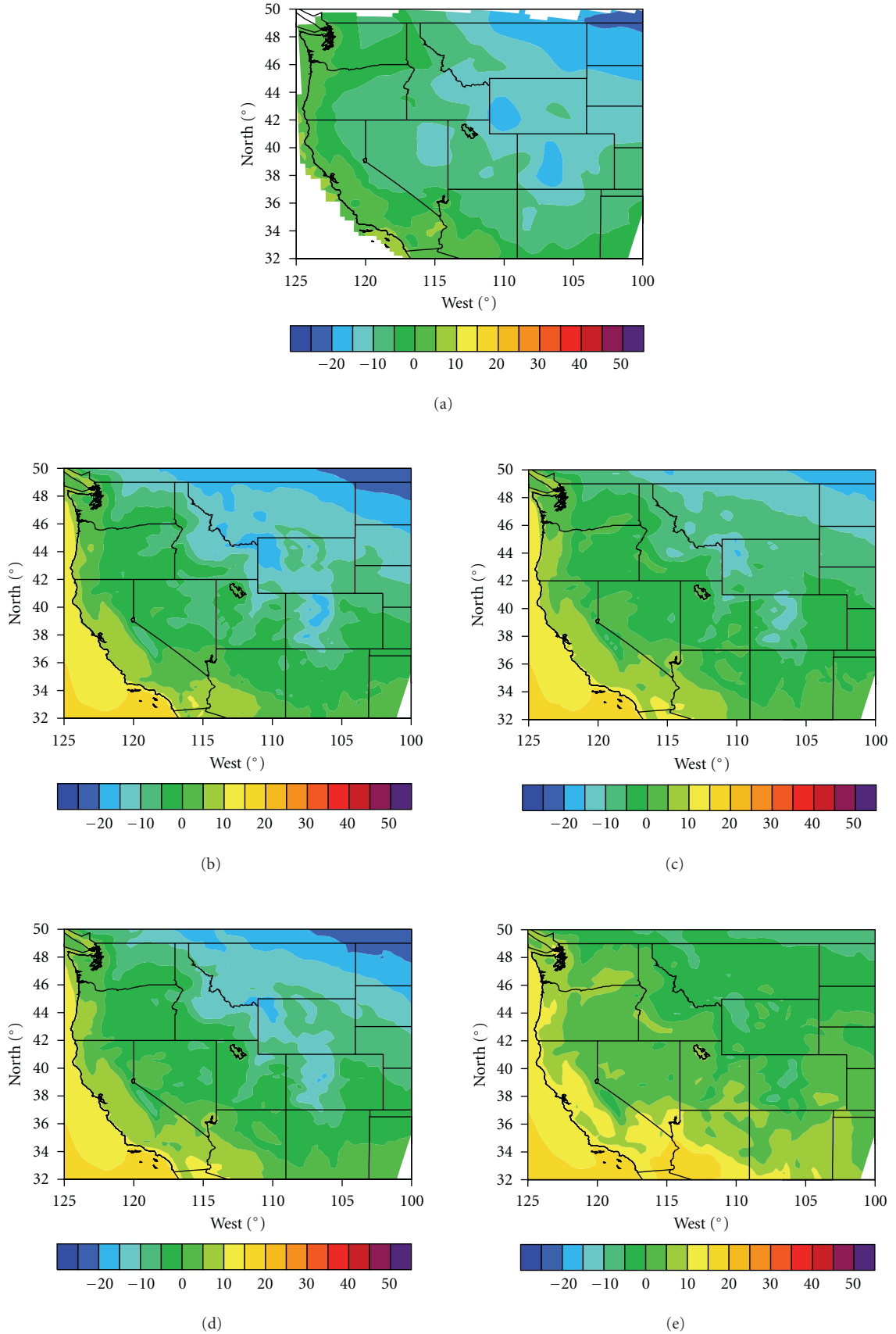


FIGURE 5: The geographic distribution of observed and WRF-simulated winter (December, January, and February) daily minimum temperature (Unit: $^{\circ}\text{C}$). (a) Observations; (b) CLM3; (c) Noah; (d) RUC; (e) STD.

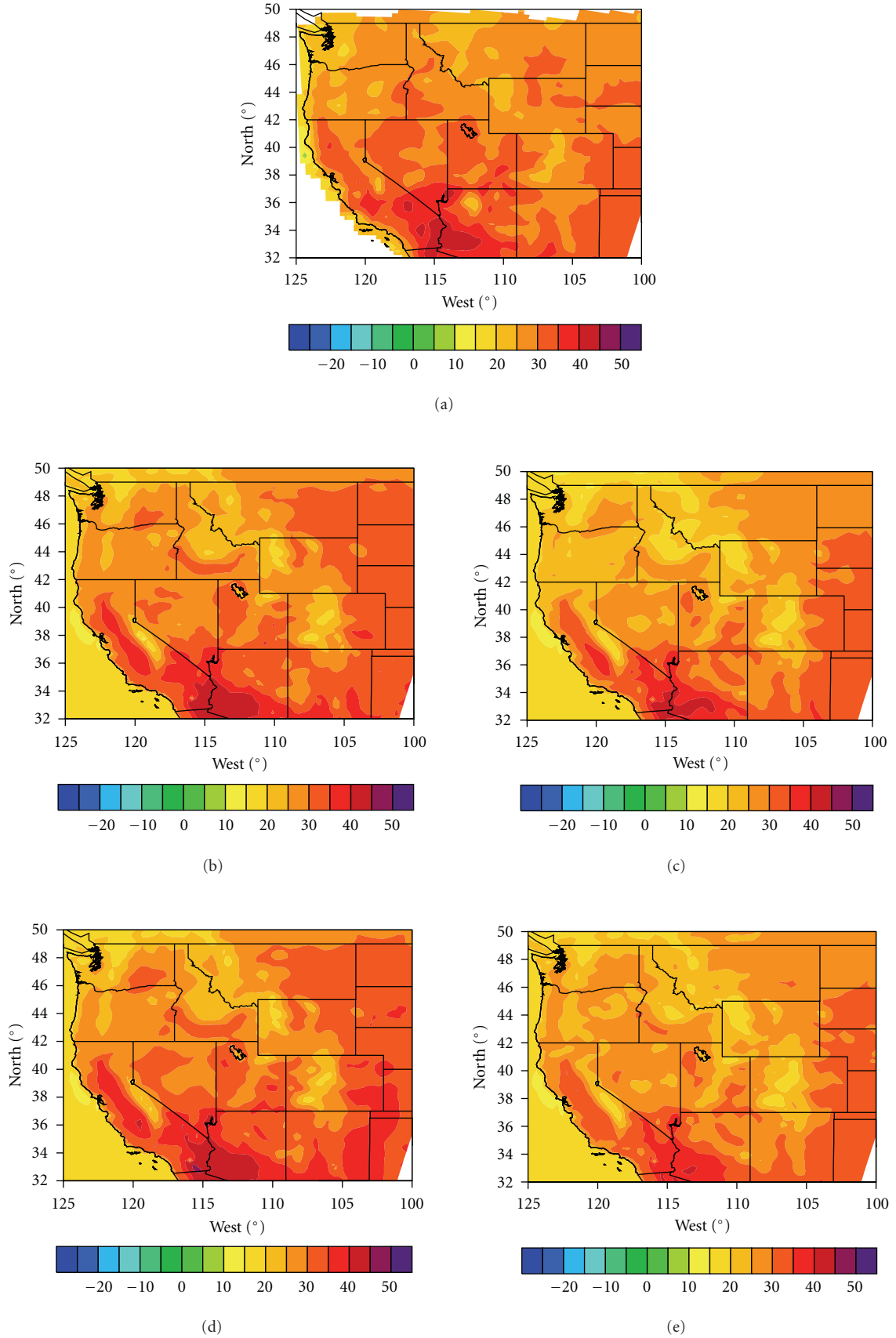


FIGURE 6: The geographic distribution of observed and WRF-simulated summer (June, July, and August) daily maximum temperature (Unit: °C). (a) Observations; (b) CLM3; (c) Noah; (d) RUC; (e) STD.

TABLE 1: Comparison of the STD, Noah, RUC, and CLM3 land surface schemes in WRF.

	Vegetation	Soil	Snow	Lake	River routing
STD	N/A	5 layer temperatures, but no moisture and frozen soil	N/A	N/A	N/A
Noah	One vegetation type in one grid cell without dynamic vegetation and carbon budget	4 layer temperatures and moistures and frozen soil	1 layer snow lumped with the top soil layer No liquid water fixed snow density	N/A	N/A
RUC	One vegetation type in one grid cell without dynamic vegetation and carbon budget	6 layer temperatures and moistures and frozen soil	2 layer snow No liquid water Fixed snow density	N/A	N/A
CLM3	Subgrids with up to 10 vegetation types in one grid cell with dynamic vegetation and carbon budget	10-layer temperatures and moistures and frozen soil	5 layer snow with liquid water Variable snow density	10 layer lake with lake ice and snow included	A Digital Elevation Model (DEM) to calculate water flow directions

surface processes and their feedbacks to the atmosphere. The application of the coupled WRF-CLM3 uniquely adds a special strength to this study, as CLM3 reflects the most recent development of land surface process modeling [15–17]. The dynamic vegetation scheme in CLM3 now enables WRF to predict future climate-related vegetation changes. A simple comparison of the features within these four land surface schemes in WRF is given in Table 1.

The objective of this study is to quantify the role of land surface processes in the regional climate system by performing a series of WRF runs using the four available land surface scheme options (STD, Noah, RUC, and CLM3) with their different complexity levels. Among these four schemes (Table 1), the STD scheme is the simplest, where only soil temperature is calculated. The representations of snow, vegetation, and soil moisture processes are missed. The Noah and RUC schemes are at the intermediate level of complexity, but RUC has a relatively more complex snow scheme when compared to Noah (Table 1). CLM3 includes the most sophisticated snow, soil, and vegetation physics among the four land surface schemes. Comparison of these land surface schemes coupled with WRF can lead to a better understanding of how land surface processes affect regional climate and also give insight on how the level of the land surface model complexity affects the accuracy of regional climate simulations.

2. Methodology and Data

As mentioned above, CLM3 was recently coupled with the WRF model. The initialization of CLM3 follows the same setup as that of Noah and RUC and is performed in the WRF initialization module. Atmospheric variables at the lowest atmospheric level (about 50 meter height) are inputted into the CLM3 module to force land surface processes. These atmospheric variables include incoming solar radiation, longwave radiation, temperature, specific humidity, wind speed, precipitation, and surface pressure. The reflected solar radiation, surface longwave emission, and latent and sensible

heat fluxes are outputted to the atmospheric modules in WRF.

Four WRF runs with the available land surface schemes (STD, Noah, RUC, and CLM3) were performed with a 30 km resolution for a domain that includes the WUS (31°N 125°W, 50°N 100°W). These WRF runs were for 1 September 1995 through 30 September 1996 representing a total integration period of 13 months. The first month of model outputs is discarded to alleviate the effects of the model initializations, and the remaining one-year simulations are analyzed. This period was chosen, because the Sea Surface Temperature (SST) over the tropical Pacific region is under *normal conditions* during 1995–1996 [18], and the climate pattern shows a similarity to its climatology over our study area, the WUS. By choosing a neutral ENSO year, we are able to effectively identify the regional impact of land surface processes that can often be mixed within anomalous weather and climate conditions [19].

In WRF, all the model atmospheric settings are exactly the same except for the land-surface schemes. The Kain-Fritsch convection scheme is chosen to parameterize cumulus clouds [20]. The Yonsei University (YSU) planetary boundary layer (PBL) scheme [21] is applied to solve boundary layer processes. The microphysics scheme selected is the WRF Single-Moment 3-class (WSM3) scheme [22]. The Rapid Radiative Transfer Model (RRTM) based on Mlawer et al. [23] is selected for describing longwave radiation transfer within the atmosphere and to the surface, and the shortwave scheme chosen is that developed by Dudhia [24].

The National Centers for Environmental Prediction-Department of Energy Atmospheric Model Intercomparison Project II Reanalysis (NCEP-2) data were used for the WRF initial conditions that include initial soil temperature and moisture in the Noah, RUC, and CLM land surface schemes. In STD, only soil temperatures were initialized, and no soil moistures were calculated. The NCEP-2 data were also used for the lateral boundary conditions and the SST in WRF that were updated every six hours. The WRF outputs

were saved hourly. Here, we evaluate the model performance with 26 observation sites from the Snow Telemetry (Snotel; <http://www.wcc.nrcs.usda.gov/snow/>) station data over the Sierra Nevada area that include daily snow water equivalent (SWE), 2 m height temperature, and precipitation (Figure 1). Gridded daily maximum and minimum temperature ($0.5^\circ \times 0.5^\circ$ resolution) and precipitation ($0.25^\circ \times 0.25^\circ$ resolution) data were used to examine the spatial distribution of simulated temperature and precipitation. Both temperature and precipitation datasets were developed by the National Oceanic and Atmospheric Administration Climate Prediction Center.

3. Results

Precipitation, temperature, and snow water equivalent (SWE) simulations from the four WRF runs at 30 km resolution with different land surface schemes are compared in a Taylor diagram (Figure 2). These simulations are the average over the 26 Snotel stations that are located in the Sierra Nevada region (Figure 1). All the simulated variables from different land surface schemes have high correlations with observations. The correlation coefficients for precipitation are between 0.7 and 0.8 for all models and for temperature are above 0.9. The correlation coefficient for the CLM3 SWE is above 0.9, and it is slightly lower than 0.9 for the Noah and RUC SWEs. These results show that the WRF code can well simulate the phases of the variations in these variables. However, the simulated standard deviations exhibit a large range. The temperature standard deviation has the best range of values among these variables, the standard deviation is overestimated for precipitation and underestimated for SWE, indicating the WRF model, regardless of the land surface scheme, produces large errors in simulating the magnitude of precipitation and SWE. SWE is best simulated in CLM3, where the most sophisticated snow physics is included, when compared to the Noah and RUC land surface schemes, however, SWE is not predicted in STD. In addition, without SWE and vegetation components in the STD model, WRF-STD produces the lowest temperature standard deviation, implying that the seasonal evolution of SWE and vegetation amplifies the temperature variations.

Figure 3 shows the spatial distribution of monthly precipitation averaged over November 1995 through March 1996, a period when a significant amount of precipitation generated. It is seen that the WRF model with the different land surface schemes can reasonably simulate the spatial pattern of the precipitation, but the domain-wide averaged precipitation amounts are more than doubled by WRF (Table 2), as compared to observations. The change of the land surface scheme in WRF does not significantly change the precipitation simulations, indicating that the overestimated precipitation most possibly is related to atmospheric processes and the reanalysis data used for initial and lateral boundary conditions. The summer precipitation is not shown here, because it is quite small in magnitude when compared to the winter precipitation for the WUS. Figures

TABLE 2: Domain-wide averaged observations and simulations for precipitation and surface air temperature as shown in Figure 2. Summer is June, July, and August, and winter for temperature is December, January, and February. Precipitation is for November 1995 through March 1996 only.

		OBS	CLM	NOAH	RUC	STD
Summer	Tmax ($^\circ\text{C}$)	29.1	28.1	25.6	28.7	26.1
	Tmin ($^\circ\text{C}$)	11.6	11.7	13.2	13.9	13.4
Winter	Tmax ($^\circ\text{C}$)	5.5	2.9	4.2	2.5	8.7
	Tmin ($^\circ\text{C}$)	-7.4	-6.4	-3.4	-5.3	2.0
	Precip (cm/month)	4.8	10.7	10.7	10.4	10.9

4, 5, 6, and 7 show winter (December, January, and February) and summer (June, July, and August) maximum and minimum temperature (hereafter Tmax and Tmin, resp.), observations and simulations. The simulated temperature spatial patterns are similar to the observations in these four maps. WRF-CLM3 produces the best results for winter Tmin and both summer Tmax and Tmin among the four land surface schemes (Table 2). However, this most sophisticated model of the four does not show any advantage in computing winter Tmax, where a 2.6°C cold bias is seen, and WRF-RUC gives a similar result. In the winter Tmax maps, it is seen that both CLM3 and RUC underestimate the temperature mostly over snow abundant mountainous areas (e.g., western Montana and nearby areas) where stronger precipitation occurs (Figure 3). Therefore, it is speculated that the overestimated precipitation simulated in these areas results in a larger snow cover area than observations, leading to more solar radiation reflected during the daytime, and in turn, lower surface air temperature. In WRF-CLM3 and WRF-RUC with a multilayer snow scheme, the erroneous precipitation has a more severe impact on snow simulations than in WRF-Noah, where snow is lumped with the top soil layer, with underestimated snow mass and snow cover area often seen [11]. As such, Tmax is only 1.3°C lower in WRF-Noah than the observations, and WRF-STD, which does not have a snow scheme and produces a 3.2°C higher Tmax. Similar cold biases are not seen in WRF-CLM3 and WRF-RUC during the nighttime when solar radiation is not present, which further verifies our speculation. Table 2 shows that all land surface models in WRF overestimate the winter surface air temperature during the nighttime, but CLM3 gives the closest result, indicating that detailed descriptions of land surface processes in CLM3 play a role in such an improvement.

Based on the above discussion, it is shown that the most sophisticated model, WRF-CLM3, improves surface air temperature simulations, except for winter Tmax, when compared to WRF with the other three land surface schemes. While the simplest model, WRF-STD, produces the worst results for Tmax. Although an improvement in snow simulation is seen in WRF-CLM3 over the Sierra Nevada region, the overall performance for snow simulation is still unable to be fully judged due to the erroneous precipitation simulations

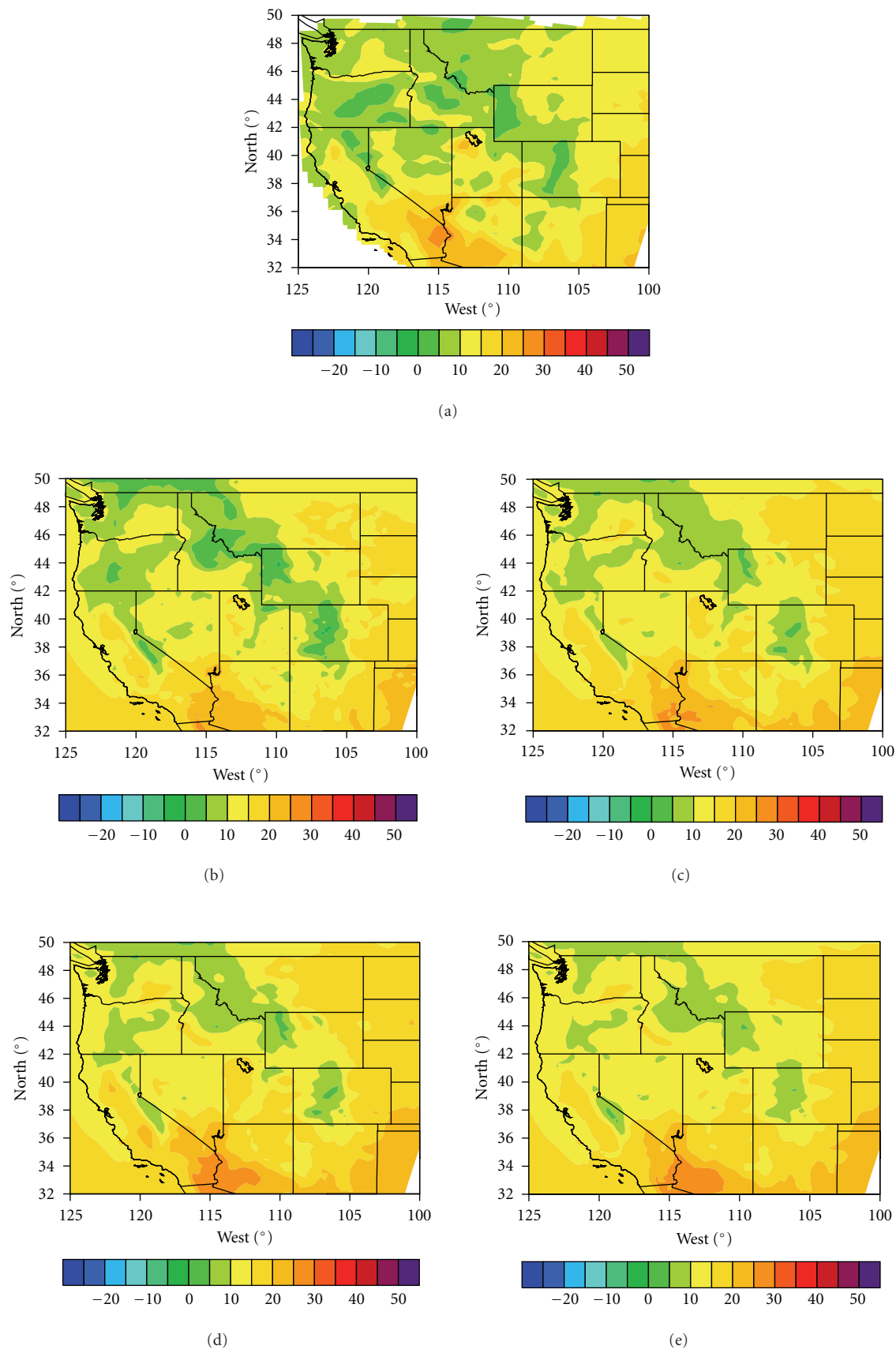


FIGURE 7: The geographic distribution of observed and WRF-simulated summer (June, July, and August) daily minimum temperature (Unit: °C). (a) Observations; (b) CLM3; (c) Noah; (d) RUC; (e) STD.

that are found to be largely independent of the land surface schemes.

4. Conclusions and Discussions

The objective of this study is to quantitatively understand the role of land surface processes in the regional climate system using the state-of-the-art WRF model coupled with four land surface schemes each with different levels of complexity (STD, Noah, RUC, and CLM3). The coupling of WRF-CLM3 represents our most recent effort to improve land-surface process simulations and predictions in the regional climate system. The results from WRF with these land-surface schemes show that land-surface processes strongly affect temperature simulations. The coupling of WRF-CLM3 with the highest complexity level improves the temperature simulations to a large extent (except for winter Tmax). Precipitation over the WUS is significantly overestimated by all four of the WRF land surface schemes analyzed here. However, this overestimation does not show a close relationship with land surface processes. As such, the resulting snow simulations cannot be quantitatively evaluated, although an improvement in snow simulation is found in WRF-CLM3 over the Sierra Nevada area.

To better estimate precipitation in WRF, more extensive modeling experiments are being performed. These experiments include the tests with several sets of combinations of radiation schemes, different cumulus parameterizations, PBL schemes, and microphysics schemes that have been embedded in the WRF model. Additionally, spatial resolution and domain size need to factor into the accuracy of these WUS precipitation simulations

Acknowledgments

Jiming Jin was supported by the Utah Agricultural Experiment Station, USDA Special Grants no. 2008-34610-19175 and no. 2009-34610-19925. The study was also supported by the NOAA CPPA Grant no. NA090AR4310195.

References

- [1] J. Hansen, M. Sato, R. Ruedy, K. Lo, D. W. Lea, and M. Medina-Elizade, "Global temperature change," *Proceedings of the National Academy of Sciences of the United States of America*, vol. 103, no. 39, pp. 14288–14293, 2006.
- [2] I. M. Held and B. J. Soden, "Robust responses of the hydrological cycle to global warming," *Journal of Climate*, vol. 19, no. 21, pp. 5686–5699, 2006.
- [3] C. M. Mitas and A. Clement, "Has the Hadley cell been strengthening in recent decades?" *Geophysical Research Letters*, vol. 32, no. 3, pp. 1–5, 2005.
- [4] J. Jin, N. L. Miller, S. Sorooshian, and X. Gao, "Relationship between atmospheric circulation and snowpack in the western USA," *Hydrological Processes*, vol. 20, no. 4, pp. 753–767, 2006.
- [5] D. D. Breshears, N. S. Cobb, P. M. Rich et al., "Regional vegetation die-off in response to global-change-type drought," *Proceedings of the National Academy of Sciences of the United States of America*, vol. 102, no. 42, pp. 15144–15148, 2005.
- [6] C. P. Weaver and R. Avissar, "Atmospheric disturbances caused by human modification of the landscape," *Bulletin of the American Meteorological Society*, vol. 82, no. 2, pp. 269–281, 2001.
- [7] G. B. Bonan, "Effects of land use on the climate of the United States," *Climatic Change*, vol. 37, no. 3, pp. 449–486, 1997.
- [8] D. L. T. Anderson, "Comparison of the ECMWF seasonal forecast systems 1 and 2, including the relative performance for the 1997/8 El Niño," Tech. Rep. Technical Memoranda 404, ECMWF, Shinfield Park, Reading, UK, 2003.
- [9] G. Wang, R. Kleeman, N. Smith, and F. Tseitkin, "The BMRC coupled general circulation model ENSO forecast system," *Monthly Weather Review*, vol. 130, no. 4, pp. 975–991, 2002.
- [10] S. Saha, S. Nadiga, C. Thiaw et al., "The NCEP climate forecast system," *Journal of Climate*, vol. 19, no. 15, pp. 3483–3517, 2006.
- [11] J. Jin and N. L. Miller, "Analysis of the impact of snow on daily weather variability in mountainous regions using MM5," *Journal of Hydrometeorology*, vol. 8, no. 2, pp. 245–258, 2007.
- [12] M. Ek and L. Mahrt, *OSU 1-D PBL Model User's Guide. Version 1.04*, Department of Atmospheric Sciences, Oregon State University, Corvallis, Ore, USA, 1991.
- [13] T. G. Smirnova, J. M. Brown, and S. G. Benjamin, "Performance of different soil model configurations in simulating ground surface temperature and surface fluxes," *Monthly Weather Review*, vol. 125, no. 8, pp. 1870–1884, 1997.
- [14] T. G. Smirnova, J. M. Brown, S. G. Benjamin, and D. Kim, "Parameterization of cold-season processes in the MAPS land-surface scheme," *Journal of Geophysical Research D*, vol. 105, no. 3, pp. 4077–4086, 2000.
- [15] K. W. Oleson, Y. Dai, G. Bonan, et al., "Technical description of the community land model (CLM)," Tech. Note NCAR/TN-461+STR, National Center for Atmospheric Research, Boulder, Colo, USA, 2004.
- [16] G. B. Bonan, K. W. Oleson, M. Vertenstein et al., "The land surface climatology of the community land model coupled to the NCAR community climate model," *Journal of Climate*, vol. 15, no. 22, pp. 3123–3149, 2002.
- [17] X. Zeng, M. Shaikh, Y. Dai, R. E. Dickinson, and R. Myneni, "Coupling of the common land model to the NCAR community climate model," *Journal of Climate*, vol. 15, no. 14, pp. 1832–1854, 2002.
- [18] K. E. Trenberth, "The definition of El Niño," *Bulletin of the American Meteorological Society*, vol. 78, no. 12, pp. 2771–2777, 1997.
- [19] J. J. Feddema, K. W. Oleson, G. B. Bonan et al., "Atmospheric science: the importance of land-cover change in simulating future climates," *Science*, vol. 310, no. 5754, pp. 1674–1678, 2005.
- [20] J. S. Kain and J. M. Fritsch, "Convective parameterization for mesoscale models: the Kain-Fritsch scheme," in *The Representation of Cumulus Convection in Numerical Models*, K. A. Emanuel and D. J. Raymond, Eds., p. 246, The American Meteor. Society, 1993.
- [21] S.-Y. Hong and H.-L. Pan, "Nonlocal boundary layer vertical diffusion in a medium-range forecast model," *Monthly Weather Review*, vol. 124, no. 10, pp. 2322–2339, 1996.
- [22] S.-Y. Hong, J. Dudhia, and S.-H. Chen, "A revised approach to ice microphysical processes for the bulk parameterization of clouds and precipitation," *Monthly Weather Review*, vol. 132, no. 1, pp. 103–120, 2004.

- [23] E. J. Mlawer, S. J. Taubman, P. D. Brown, M. J. Iacono, and S. A. Clough, "Radiative transfer for inhomogeneous atmospheres: RRTM, a validated correlated-k model for the longwave," *Journal of Geophysical Research D*, vol. 102, no. 14, pp. 16663–16682, 1997.
- [24] J. Dudhia, "Numerical study of convection observed during the Winter Monsoon Experiment using a mesoscale two-dimensional model," *Journal of the Atmospheric Sciences*, vol. 46, no. 20, pp. 3077–3107, 1989.

Research Article

Impact of Land Use Change on the Local Climate over the Tibetan Plateau

Jiming Jin,¹ Shihua Lu,² Suosuo Li,² and Norman L. Miller³

¹ Departments of Watershed Sciences & Plants, Soils, and Climate, Utah State University, Logan, UT, USA

² Cold and Arid regions Environmental and Engineering Research Institute, Chinese Academy of Sciences, Lanzhou, China

³ Earth Sciences Division, Lawrence Berkeley National Laboratory, and Department of Geography, University of California at Berkeley, Berkeley, CA, USA

Correspondence should be addressed to Jiming Jin, jimingjin99@gmail.com

Received 1 January 2010; Revised 30 April 2010; Accepted 27 May 2010

Academic Editor: Zhaoxia Pu

Copyright © 2010 Jiming Jin et al. This is an open access article distributed under the Creative Commons Attribution License, which permits unrestricted use, distribution, and reproduction in any medium, provided the original work is properly cited.

Observational data show that the remotely sensed leaf area index (LAI) has a significant downward trend over the east Tibetan Plateau (TP), while a warming trend is found in the same area. Further analysis indicates that this warming trend mainly results from the nighttime warming. The Single-Column Atmosphere Model (SCAM) version 3.1 developed by the National Center for Atmospheric Research is used to investigate the role of land use change in the TP local climate system and isolate the contribution of land use change to the warming. Two sets of SCAM simulations were performed at the Xinghai station that is located near the center of the TP Sanjiang (three rivers) Nature Reserve where the downward LAI trend is largest. These simulations were forced with the high and low LAIs. The modeling results indicate that, when the LAI changes from high to low, the daytime temperature has a slight decrease, while the nighttime temperature increases significantly, which is consistent with the observations. The modeling results further show that the lower surface roughness length plays a significant role in affecting the nighttime temperature increase.

1. Introduction

It has become apparent that climate change over high-elevation regions is occurring at a faster rate than over low-elevation regions [1]. This high-elevation rate of change often generates stronger disturbances within the climate system than low-elevation changes [2]. The Tibetan Plateau (TP) is an immense upland area (3500×1500 km), with an average elevation greater than 5,000 m. Over the TP, 46% of the forest cover and 50% of the grassland have been converted to farmland, urban areas, or desert during the last century (X. Liu, personal communication). The TP is the source of snowmelt runoff, supplying water resources to users in China and surrounding areas. The mechanisms influencing the observed rapid climate change and their impacts at this high-elevation region are not well understood. In order to reduce these types of uncertainties and provide society with more reliable projections of future outcomes, detection and analysis of these processes need to be determined.

Many researchers have shown that land use and land cover change has remarkably interacts with climate systems

[3, 4]. A statistical analysis of the southern half of the Central Valley was performed by Christy et al. [5] using high-quality temperature observations for the San Joaquin Valley in California, where land use has changed dramatically since the presettlement (circa 1860s), due to extensive agricultural expansion. Their study indicated that the daily maximum near-surface air temperature exhibited a cooling trend over the last century for this region. This finding is in opposition to the observed warming trends that prevail over most other regions (see [6, 7]; many others), suggesting that agricultural activity and associated irrigation processes most likely play a key role in producing this cooling trend. Modeling studies have shown that land use change affects regional climate by altering the components in the surface energy budget [8]. Based on the results from a general circulation model (GCM), Snyder et al. [9] indicate that removing all temperate forest and replacing it with bare soil produce cooling in the winter and spring over tropical and boreal areas due to an increase in the surface albedo, but a warming during the summer due to reduced evapotranspiration. If forced with a moderate amount of carbon dioxide, GCMs could produce

similar results for the entire 21st century [10]. These GCM predictions also indicate that the response of land use change could be overridden by a strong atmospheric circulation system such as the Asian Monsoon circulation.

However, due to the lack of detailed long-term and densely distributed spatial observations, researchers have not been able to determine how and to what extent these land use changes affect the early and accelerated warming observed on the TP [11]. A high-quality climate model is an efficient tool to advance our understanding of this problem, and observed climate change could be quantitatively interpreted through the model details. The modeling results would further yield new insight into future field experimental design. Therefore, in this study, we use the Single-Column Atmosphere Model (SCAM) version 3.1 coupled with the Community Land Model version 3 (<http://www.cesm.ucar.edu/models/atm-cam/docs/scam/>) to investigate the role of land use change in the TP local climate system and isolate the contribution of land use change to the warming of the TP from that of greenhouse gas emissions. The SCAM was developed by the National Center for Atmospheric Research (NCAR). In addition, the mechanisms associated with land use change signals are adequately quantified with the model output and our existing quality-controlled observations.

2. Model, Data, and Methodology

The SCAM used in this study is a one-dimensional time-dependent single-column atmospheric model. The SCAM is embedded in the NCAR Community Atmospheric Model version 3. Since the SCAM includes only one model grid cell, it can be used to effectively study land atmosphere interactions. This grid cell can include up to 10 land use types, giving a benefit to characterize land surface heterogeneity. In this study, the land use types are prescribed in the SCAM to represent land surface features in the TP. The SCAM is also configured with 26 vertical layers ranging from approximately 3 mb to the surface, and it includes all the physical schemes existing in its global counterpart, CAM3. The reanalyzed data by National Centers for Environmental Prediction (NCEP-R1) provide the initial and lateral boundary conditions for SCAM. The latter were updated every 6 hours. The initial conditions include soil moisture and temperature and atmospheric pressure, moisture, temperature, and winds. The 16 km resolution Advanced Very High Resolution Radiometer (AVHRR) leaf area indices (LAIs) were used to examine vegetation changes over the TP and also were inputted into SCAM to more realistically reflect vegetation variations. Station observations were used to analyze climate change over the TP and compare with modeling results.

3. Results

3.1. LAI, Temperature, and Precipitation Analysis. Land use and land cover on the TP have been changed significantly. Such change can be indentified with the AVHRR LAI

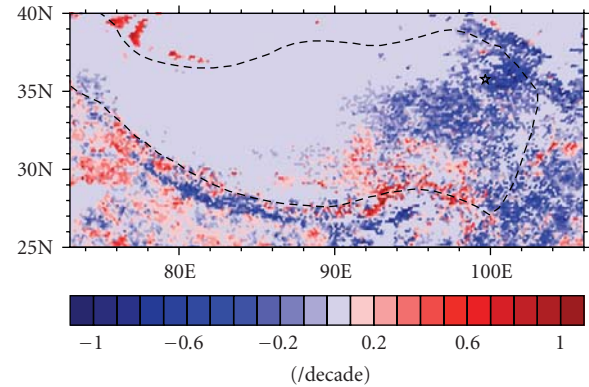


FIGURE 1: The LAI trend in the TP over the period of 1983–2000 (unit: /decade). The dashed line represents the scope of the TP. The black star is the location of the Xinghai station where the SCAM simulations were performed.

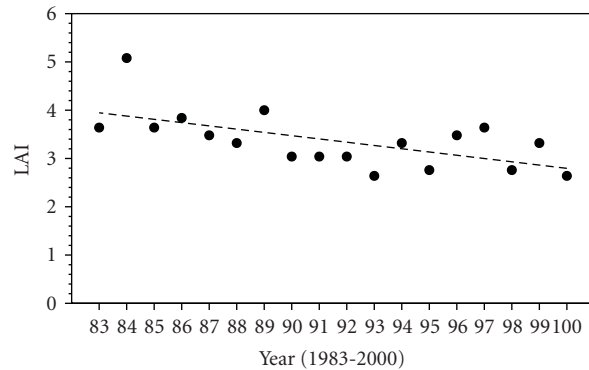


FIGURE 2: The trend of the annual maximum LAI at the Xinghai station for the period of 1983–2000. The dashed line represents the trend. The black dot is the maximum LAI for each year.

trends over the period of 1983–2000 for July, August, and September, a season that the LAIs usually reach their maximum values (Figure 1). It is clearly seen that the LAIs have negative trends (blue colors) in the northeast TP, and the maximum trend can reach around $-1.0/\text{decade}$. These trends are calculated through a linear regression method. The region with the negative trends contains the headwaters of the Yellow River (Huang He), the Yangtze River (Chang Jiang), and the Mekong River (Lancang Jiang) that provide a significant amount of water resources for China. This area is also called Sanjiang (three rivers) Headwaters Nature Reserve. In some locations of the southeast TP, LAIs also show positive trends (red colors). Figure 2 shows the time series of the annual maximum LAI at a station called Xinghai that is located near the center of the Sanjiang area. This figure shows that the annual maximum LAI has a downward trend with a value of $-0.67/\text{decade}$ over the period of 1983–2000. According to the United States Geological Survey data, Xinghai has a flat terrain and mostly is covered by grassland during the summer. All the following simulations were performed at this station to understand how vegetation affects local climate.

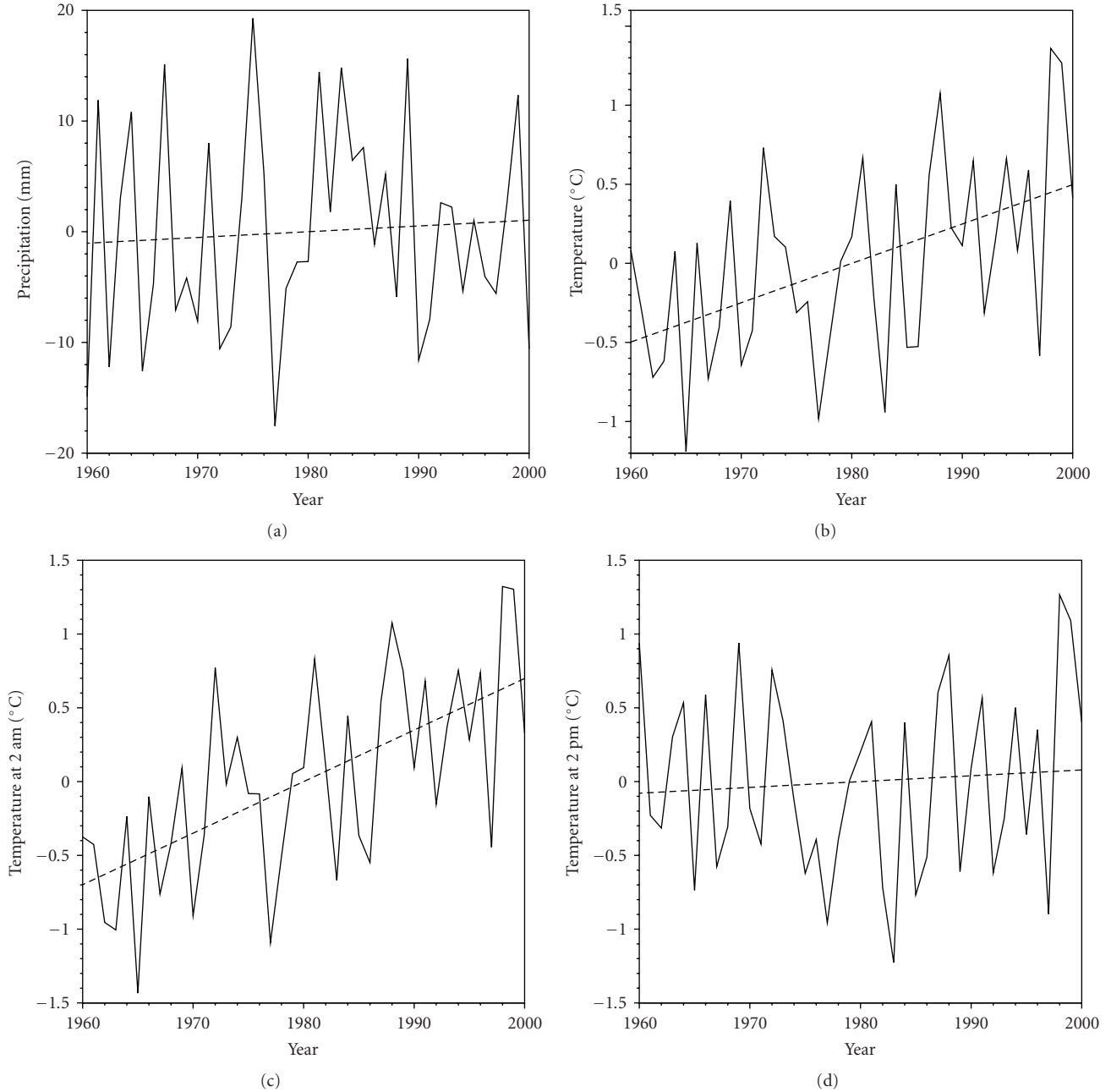


FIGURE 3: The time series of annual precipitation and temperature anomalies at the Xinghai station. (a) Precipitation (mm); (b) temperature (°C); (c) temperature at 2 AM (°C); temperature at 2 PM. The dashed line in each figure represents the trend.

Figure 3(a) shows the time series of the annual precipitation anomalies at the Xinghai station for the period of 1960–2000. It is shown that the trend is 0.5 mm/decade that is quite insignificant. However, the annual mean temperature trend is 0.25°C/decade (Figure 3(b)). The temperature increase is about 1°C at this station over the study period. When temperatures at 2 AM and 2 PM are examined, it can be seen that the nighttime temperature trend is 0.35°C/decade (Figure 3(c)) while the daytime temperature trend is only 0.04°C/decade (Figure 3(d)). Thus, the annual mean temperature increase results from the nighttime warming.

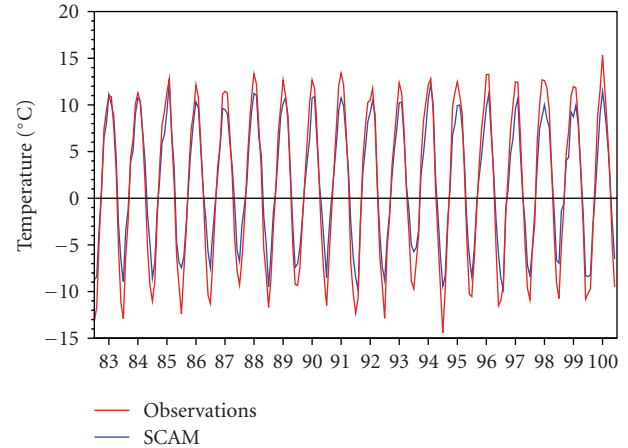
Identifying physical factors and processes that contribute to the nighttime warming is the major focus in the following sections, and the SCAM is used for such purpose.

3.2. SCAM Evaluation. Before physical processes that affect temperature change are studied, the SCAM needs to be fully evaluated with observations to ensure that it can reasonably describe climate processes in our study area. SCAM simulations at the Xinghai station were performed over the period of 1951–2000. The first 32-year (1951–1982) simulations were discarded for spinning up the model,

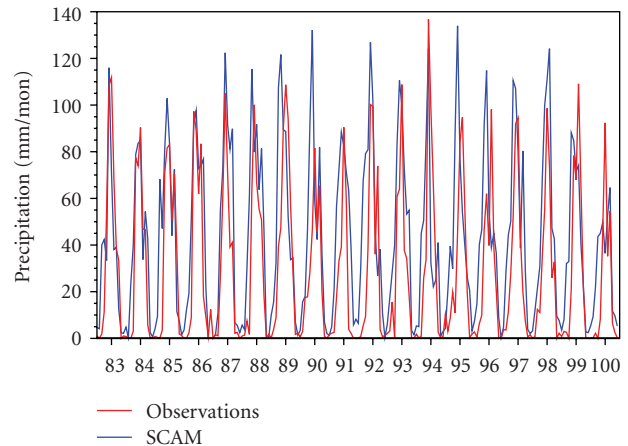
and only the simulations over the period of 1983–2000 were analyzed. Figure 4(a) shows that although the SCAM produces a weaker seasonal cycle of the temperature it still generates reasonable temperature simulations at the Xinghai station when compared to the observations. The correlation coefficient between the observation and the simulation is 0.98, the RMSE is 2.2°C , and the bias is 0.29°C . The model can also reproduce the observed precipitation, where the correlation coefficient, RMSE, and bias are 0.74, 28 mm/month, and 13 mm/month, respectively (Figure 4(b)). These results show that the SCAM can simulate well for the seasonal cycles of precipitation and temperature at the Xinghai station, indicating that this model can be used to further explore physical processes that affect temperature and precipitation changes in this area.

3.3. Sensitivity Studies for Understanding the Temperature Changes. To examine how vegetation affects the warming in this area, two additional sets of simulations were performed with high and low LAIs for 1983–2000, a period where the remotely sensed LAIs are available. Figure 5 shows seasonal variations of high and low LAIs. The high LAIs are the average over 1983–1985, while the low LAIs are the average over 1998–2000. The largest difference between the high and low LAIs is more than one. The first set of simulations was forced with the high LAIs, where the LAI only varied seasonally but did not have interannual variations. The modeling settings for the second set of simulations were exactly the same as those for the first set of simulations but with the low LAIs. Figure 6(a) shows the 2 m height temperature difference between the high LAI and the low LAI cases averaged over the 18-year period (1983–2000). It is seen that the major changes in temperature (low LAI minus high LAI) occur in the warm season where the LAI difference between the two cases is the largest. During the cold season (from October through next May), there is almost no change for the temperature. Precipitation has very minor changes with a maximum difference of less than 1 mm/month (figure not shown). Figure 6(a) indicates that the lower LAI in this region generates a slight cooling during the summer at noontime with a maximum temperature change of -0.2°C in July (solid line). All the components in the energy balance equation are examined. The results show that the sensible heat flux has most significant changes that affect 2 m height temperature (Figure 6(b)). It is seen that sensible heat flux decreases by 10 W/m^2 at noontime during the summer (solid line). Further analysis indicates that such a decrease results from the lower roughness in the low LAI case. In SCAM, the roughness length for vegetation in this area is 0.06 m, and for bare soil, it is 0.024 m. The low LAI reduces the areal weight of vegetation in the model grid cell, but increases the weight of bare soil when compared to the settings in the high LAI case. Thus, on average, the low LAIs generate a flatter surface than the high LAIs, which decreases the upward sensible heat flux during daytime and slightly lower the near-surface temperature.

Figure 6(a) shows the nighttime temperature difference between the low and high LAI cases (low-high), indicating that the near-surface temperature increases by more than 1°C



(a)



(b)

FIGURE 4: Comparison of SCAM simulations (blue line) and observations (red line) at the Xinghai station: (a) Precipitation; (b) temperature.

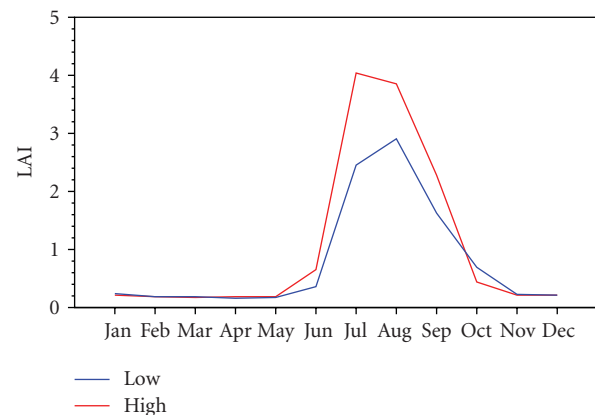


FIGURE 5: The seasonal variations of the low (blue) and high (red) LAIs. The high LAI is the average over 1983–1985, while the low LAI is the average over 1998–2000.

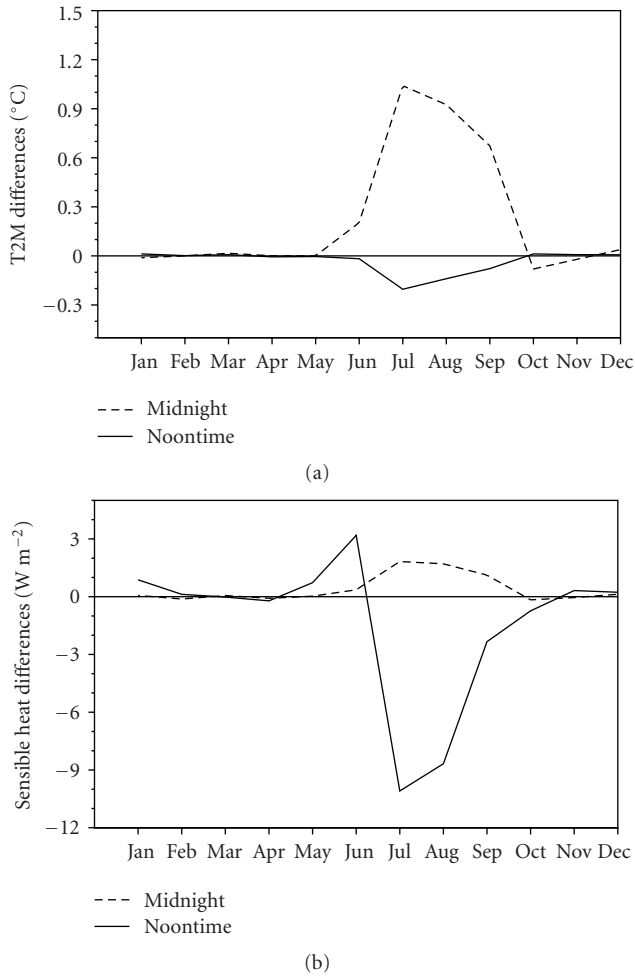


FIGURE 6: The (a) temperature (unit: $^{\circ}\text{C}$) and (b) sensible heat flux (unit: W m^{-2}) differences between the low and high LAI cases (low-high). The solid line is for noontime, and the dashed line is for midnight.

in July due to changing the LAI from high to low (dashed line). During the evening, the sensible heat flux is downward (negative). The reduced roughness length in the low LAI case suppresses the energy exchanges between the surface and near-surface air. Figure 6(b) shows that the increase in sensible heat flux at midnight is up to 2 W m^{-2} (dashed line) that leads to more energy remaining in the near-surface air (less downward sensible heat) and increases the temperature there. Detailed calculation of sensible heat flux and how it is related to the roughness length are described by Oleson et al. in [12].

The above modeling results strongly suggest that the warming results from nighttime temperature changes that are consistent with the observations. The decreased vegetation LAI in this area significantly contributes to the nighttime temperature increase. The LAI decrease may not be a controlling factor that produces the observed warming trend, but most likely it reinforces the existing warming trend that is believed to be triggered by the carbon increase in the atmosphere [4].

4. Conclusions and Discussions

In northeast Tibetan Plateau, the remotely sensed LAIs show a significant downward trend, while a warming trend is observed for temperature. Our modeling results indicate that such a vegetation change is an important factor that contributes to the warming in this region. Further analysis indicates that this contribution largely comes from the evening temperature increase. The evening temperature increase results from the more stable near-surface boundary layer that restricts the downward sensible heat flux and keeps more energy in the near-surface air. The deterioration of vegetation leads to a flatter area, reduces the surface roughness, and results in more stable near-surface boundary layer.

This study is not intended to indicate that vegetation deterioration is a determining factor that leads to a warming in this area that is most likely related to global climate change triggered by the atmospheric carbon increase. Instead, the analysis shown in this study describes a fact that the reduced biomass in this area could strengthen the warming trend in this region. This study is based on the modeling results that need to be further verified with more observed evidence. The large- and mesoscale atmospheric information in the SCAM was introduced through the lateral boundary data. Thus, the atmosphere in the model column does not produce any feedback to that outside the column. This drawback could be overcome by applying a regional or global climate model to this region, which could be a future research topic. However, these modeling results give strong insight into future modeling and observational studies for climate change in this high-elevation area.

Acknowledgments

Support for this work was provided by the Utah Agricultural Experiment Station. J. Jin was also supported by K. C. Wong Fellowships, Chinese Academy of Sciences.

References

- [1] H. F. Diaz and R. S. Bradley, "Temperature variations during the last century at high elevation sites," *Climatic Change*, vol. 36, no. 3-4, pp. 253-279, 1997.
- [2] J. Jin and N. L. Miller, "Toward understanding the role of ground water in hydroclimate over the Merced watershed using a single column climate model," in *The American Geophysical Union Fall Meeting*, San Francisco, Calif, USA, December 2006.
- [3] Q. Li and Y. Xue, "Simulated impacts of land cover change on summer climate in the Tibetan Plateau," *Environmental Research Letters*, vol. 5, no. 1, Article ID 015102, 2010.
- [4] X. Cui, H.-F. Graf, B. Langmann, W. Chen, and R. Huang, "Climate impacts of anthropogenic land use changes on the Tibetan Plateau," *Global and Planetary Change*, vol. 54, no. 1-2, pp. 33-56, 2006.
- [5] J. R. Christy, W. B. Norris, K. Redmond, and K. P. Gallo, "Methodology and results of calculating central California surface temperature trends: evidence of human-induced climate change?" *Journal of Climate*, vol. 19, no. 4, pp. 548-563, 2006.

- [6] J. Hansen, M. Sato, R. Ruedy, K. Lo, D. W. Lea, and M. Medina-Elizade, "Global temperature change," *Proceedings of the National Academy of Sciences of the United States of America*, vol. 103, no. 39, pp. 14288–14293, 2006.
- [7] J. T. Houghton, Y. Ding, D. J. Griggs, et al., *Climate Change 2001: The Scientific Basis: Contribution of Working Group I to the Third Assessment Report of the Intergovernmental Panel on Climate Change*, Cambridge University Press, 2001.
- [8] L. M. Kueppers, M. A. Snyder, L. C. Sloan et al., "Seasonal temperature responses to land use change in the western United States," *Global and Planetary Change*, vol. 60, no. 3-4, pp. 250–264, 2008.
- [9] P. K. Snyder, C. Delire, and J. A. Foley, "Evaluating the influence of different vegetation biomes on the global climate," *Climate Dynamics*, vol. 23, no. 3-4, pp. 279–302, 2004.
- [10] J. J. Feddema, K. W. Oleson, G. B. Bonan et al., "Atmospheric science: the importance of land cover change in simulating future climates," *Science*, vol. 310, no. 5754, pp. 1674–1678, 2005.
- [11] O. W. Frauenfeld, T. Zhang, and M. C. Serreze, "Climate change and variability using European Centre for Medium-Range Weather Forecasts reanalysis (ERA-40) temperatures on the Tibetan Plateau," *Journal of Geophysical Research D*, vol. 110, no. 2, pp. 1–9, 2005.
- [12] K. W. Oleson, Y. Dai, G. Bonan, et al., "Technical description of the community land model (CLM)," Technical Note NCAR/TN-461+STR, NCAR, 2004.

Review Article

Beating the Uncertainties: Ensemble Forecasting and Ensemble-Based Data Assimilation in Modern Numerical Weather Prediction

Hailing Zhang and Zhaoxia Pu

Department of Atmospheric Sciences, University of Utah, 135 S 1460 E, Rm. 819, Salt Lake City, UT 84112, USA

Correspondence should be addressed to Hailing Zhang, hailing.zhang@utah.edu

Received 1 January 2010; Revised 31 March 2010; Accepted 3 June 2010

Academic Editor: Hann-Ming Henry Juang

Copyright © 2010 H. Zhang and Z. Pu. This is an open access article distributed under the Creative Commons Attribution License, which permits unrestricted use, distribution, and reproduction in any medium, provided the original work is properly cited.

Accurate numerical weather forecasting is of great importance. Due to inadequate observations, our limited understanding of the physical processes of the atmosphere, and the chaotic nature of atmospheric flow, uncertainties always exist in modern numerical weather prediction (NWP). Recent developments in ensemble forecasting and ensemble-based data assimilation have proved that there are promising ways to beat the forecast uncertainties in NWP. This paper gives a brief overview of fundamental problems and recent progress associated with ensemble forecasting and ensemble-based data assimilation. The usefulness of these methods in improving high-impact weather forecasting is also discussed.

1. Introduction

Numerical weather prediction (NWP) is an initial value problem: it forecasts the atmospheric state by integrating a numerical model with given initial conditions. Commonly, two fundamental factors account for an accurate numerical weather forecast: (1) the present state of the atmosphere must be characterized as accurately as possible; (2) the intrinsic laws, according to which the subsequent states develop out of the preceding ones, must be known [1]. These so-called laws are composed of a set of partial differential equations, including the laws of momentum, mass, and energy conservations.

Since the first successful NWP in early 1950s by Charney et al. [2], much progress has been made in enhancing the skill of NWP. These include efforts in improving initial conditions through advances in observing systems and the development of atmospheric data assimilation techniques. Many studies also devoted to improve numerical modeling with advanced numerical methods, better representation of dynamics processes of the atmosphere, and improved physical parameterization schemes [3–5]. Today, NWP has become a major forecasting tool in many operational centers around the world.

However, due to inadequate observations, our limited understanding of the physical processes of the atmosphere, and the chaotic nature of the atmospheric flow, uncertainties always exist in both initial conditions and numerical models. Thus, reducing forecast errors caused by these uncertainties remains a large area of research and operational implementation.

Recent developments have proved that ensemble forecasting and ensemble-based data assimilation are promising ways to beat the forecast uncertainties in NWP. The objective of this paper is to give a brief overview of the fundamental problems and recent progress associated with ensemble forecasting and ensemble-based data assimilation. The usefulness of these methods in improving high-impact weather forecasting is also discussed.

The paper is organized as follow. Section 2 addresses the fundamental concepts of atmospheric predictability; Section 3 introduces stochastic theory and ensemble weather forecasting; Section 4 describes the Bayes theorem and ensemble Kalman filtering data assimilation; Section 5 addresses the implementation and practical issues associated with the ensemble Kalman filter; Section 6 briefly summarizes current applications of ensemble forecasting and ensemble-based data assimilation methods on high-impact

weather prediction; and a summary and concluding remarks are presented in Section 7.

2. Forecast Uncertainties and Predictability

2.1. Predictability. Predictability refers to the extent to which the future state of the atmosphere or a specific weather system may be predicted based on current ability of NWP. Corresponding to the aforementioned two fundamental factors that influence the numerical forecast, there are two kinds of predictabilities as addressed by Lorenz in [6]: (1) attainable predictability, which is limited by the inaccuracy of measurement and (2) practical predictability that is limited by our inability to express the precise equations of the atmosphere motion and physical processes in the numerical model. The errors in measurement include instrumental errors and errors due to interpolation over regions where there are no measurements at all. These errors can be decreased by enlarging our network of observation stations and improving the techniques of interpolation or data assimilation. Errors in model equations rely much on the computational methods used to solve the equations and our current ability to understand the physical processes, as well as the model resolution to resolve these physical processes in the numerical models.

2.2. The Unpredictable Nature of the Atmosphere. While attainable and practical predictabilities are associated with uncertainties in the initial conditions and imperfect models, what would the predictability be if the model (dynamical and physical processes) is perfect and the initial conditions are accurate? Lorenz [6, 7] asserted that the atmosphere, as a kind of unstable dynamical system, has a finite limit of predictability depending upon a particular flow. As is well known, Lorenz [6] found that a slight departure in initial conditions would evolve into totally different atmospheric states in the numerical forecasts regardless of how small the errors in the initial conditions were.

The chaotic nature of the atmosphere determines that the predictability of the model depends upon not only the realism of the model and the accuracy of initial conditions but also the system itself. Atmospheric motion, as a nonlinear dynamic system, is supposed to have finite limit predictability. The stochastic characteristics account for the extent to which the atmosphere could be predicted. The number of days we can forecast accurately in advance is dependent upon the evolution of the atmosphere.

Figure 1 shows the motion trajectories of stable and unstable dynamic systems. In Figure 1(a), the trajectories drift away from each other although the initial conditions are very close; for Figure 1(b), the trajectories in a stable system stay close to each other with time. This suggests that the intrinsic predictability becomes completely impossible for the unstable flow just as seen from Figure 1(a). Even two very close initial conditions may result in markedly different outcomes. Since we do not know the true atmospheric state, we therefore have no idea about how to ascertain the true

value from those totally different forecast states. This brings us a great challenge in numerical weather forecasting.

Figure 2 illustrates a real scenario in the Lorenz 63 model [6]. Given a cloud of close initial states, the trajectories depart from each other after the model was integrated forward only 10 seconds. This suggests, in a nonlinear system, that it is almost impossible to predict even in which lobe the states would be.

The uncertain properties of the atmospheric system call for more suitable methods to represent the initial conditions and forecast the atmospheric states, instead of the traditional way that describes the initial values with the single analysis best state and integrate the single best guess forward. This will be illustrated in Sections 3 and 4.

3. The Stochastic Prediction and Ensemble Forecasting

In view of the uncertain properties of the atmospheric system, a theory of stochastic dynamic prediction is proposed by Epstein [9]. In a stochastic context, the initial and forecast states of the atmosphere are represented as probability distributions. That is, the probability density function (PDF) of the present model state should be estimated first according to all the prior information and available observations; then, a method for forecasting the evolution of this PDF forward in time is needed. Based on the stochastic dynamic prediction, it is possible to make the probabilistic forecasts in addition to a deterministic forecast using a single model with single initial conditions. Although early experiments by Epstein are very different from the ensemble forecasting done today, the theory of stochastic dynamic predictions offers a stepping stone with which to develop ensemble forecasting.

The advance in parallel processing computers in the early 1990s and improved operational forecasting systems—improvements in both model physics and data assimilation—has led to operational stochastic dynamic prediction at the European Centre for Medium-Range Weather Forecasts (ECMWF), U. S. National Centers for Environmental Prediction (NCEP), and the Meteorological Service of Canada (MSC) in the early 1990s. These operational stochastic prediction systems are referred to as ensemble forecasting systems. Instead of using only one model with a single set of initial conditions, a group of forecasts with slightly different initial conditions are made in an ensemble forecast. The approach to ensemble prediction used at operational centers exhibits subtle differences when compared with the standard Monte Carlo method that was used in the stochastic dynamic prediction. In Monte Carlo, it is assumed that the initial probability density function (PDF) is known and that it is sampled randomly. In most of the methods used in current ensemble forecasting, the PDF is generally not sampled in a random way. There are different ways to generate the initial perturbations in the different operational ensemble systems, including the following.

- (i) *Breeding of Growing Modes (BGM)*: Developed by Toth and Kalnay [10, 11], the BGM scheme is a simple and inexpensive method to generate the

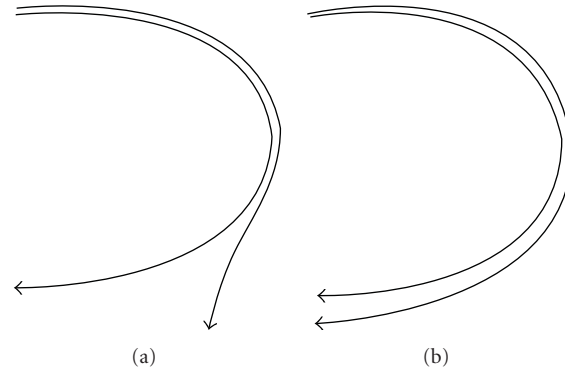


FIGURE 1: The evolutions of slightly different initial states (a) unstable trajectories; (b) stable trajectories [courtesy of Lorenz (1963)].

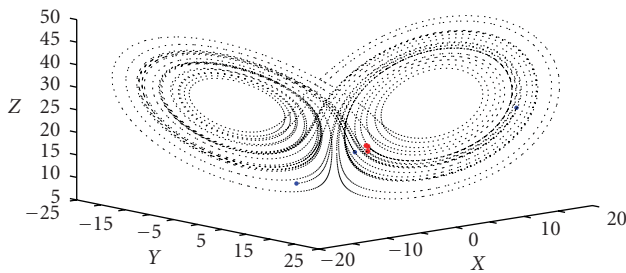


FIGURE 2: The evolutions of slightly different initial states in the Lorenz-63 model. Red stars represent initial states; blue circles represent states after 10 seconds. (The figure follows that of Palmer in [8].)

initial perturbation. It eliminates the difference in the growth rate of errors (growing modes) due to convection or baroclinic instability. The BGM consists of the following steps: (a) Add a small arbitrary perturbation to the atmospheric analysis; (b) integrate the model for 6 hours from both the unperturbed (control) and the perturbed initial condition; (c) subtract the 6-hour control forecast from the perturbed forecast; (d) scale down the difference field so that it has the same size (in RMS) as the initial perturbation; and (e) repeat the above process in time. Thus, the perturbation evolves along with the time-dependant analysis fields, ensuring that after a few days of cycling the perturbation field consist of a superposition of fast-growing modes corresponding to the contemporaneous atmosphere, akin to local Lyapunov vectors.

- (ii) A *Singular vector (SV) method*: ECWMF developed and implemented the Singular Vector scheme [12, 13], which is based on the observation that perturbations pointing along different axes of the phase space of the system are characterized by different amplification rates. Given an initial uncertainty, perturbations along the directions of maximum growth amplify more than those along other directions. For defining the SVs in the ensemble prediction system, growth is measured by a matrix based on the total energy norm.

The SVs are computed by solving an eigenvalue problem, which is defined by an operator that is a combination of the tangent forward and adjoint model, integrated during a time period named the optimization time interval. The advantage of using singular vectors is that, if the forecast error evolves linearly and the proper initial norm is used, the resulting ensemble captures the largest amount of forecast-error variance at optimization time [14].

- (iii) A *Perturbed-observation approach*: The MSC perturbed-observation approach attempts to obtain a representative ensemble of perturbations by comprehensively simulating the behavior of errors in the forecasting system. The system is based on an ensemble of data assimilation systems using perturbed observations. Because the analysis and forecast process is repeated several times with different random input, the perturbed-observation method is a classic example of the Monte Carlo approach. Arguments for the use of nonselective, purely random ensemble perturbations are presented by Houtekamer et al. [15] and Anderson [16].
- (iv) *Ensemble transform Kalman filter (ETKF)*: It was first introduced as an adaptive sampling method [17]. The formulation of ETKF is based on the application of a Kalman filter, with the forecast and analysis covariance matrices being represented by ensembles of forecast and analysis perturbations. Thus, it produces analysis perturbations (initial perturbation for ensemble) in ensemble representation based on the ensemble forecast from previous cycle and observations. One argued that the ETKF is able to make perturbations more independent and flow dependent [18].

All of the methods discussed above only include perturbations in the initial conditions, assuming that the error growth due to model deficiencies is small compared to that due to unstable growth of initial errors. However, in reality, uncertainties in model physical parameterizations cannot be ignored in many cases. Therefore, in addition to the aforementioned initial perturbation methods, ensemble forecast systems have also been designed to account for

model errors and model uncertainty. Current methods and progress include the multimodel ensemble (see, e.g., [19, 20]), stochastic physical parameterizations (see, e.g., [21–23]), nonlocal stochastic-dynamic parameterization schemes [24], kinetic energy backscatter [25], performing ensemble simulations with different time steps to study the impact of model truncation error [26], and using different parameterizations within the ensemble prediction system [27]. Krishnamurti et al. [19] commented that the performance of multimodel ensemble forecasts shows superior forecast skill compared to all individual models used. Reynolds et al. [23] illustrated that a stochastic convection scheme improves the ensemble performance in the tropics.

Since ensemble forecasting takes account of the uncertainties in NWP, it has major advantages over a single deterministic forecast [28], like, for example, the following.

- (i) It improves the forecasting skill by reducing the non-linear error growth and averaging out unpredictable components.
- (ii) It predicts the skill, by relating it to the agreement among ensemble forecast members. If the ensemble forecasts are quite different from each other, it is clear that at least some of them are wrong, whereas if there is good agreement among the forecasts, there is more reason to be confident about the forecast.
- (iii) It provides an objective basis for forecasts in a probabilistic form. In a chaotic system such as the atmosphere, probabilistic information is recognized as the optimum format for weather forecasts both from a scientific and a user perspective.

In addition, ensemble forecasts also show the potential value in a new area of research, such as targeted weather observations (see, e.g., [29]) and data assimilation (see next section)..

4. Bayes Theorem and Ensemble-based Data Assimilation

As mentioned in the previous section, uncertainties of the initial conditions are the major source of error in NWP. Thus, improved data assimilation techniques will be useful to beat the uncertainties in the initial conditions. We continue this subject with the stochastic dynamic prediction.

4.1. Bayes Theorem of Data Assimilation. In a stochastic context, the initial and forecast states of the atmosphere are represented as probability distributions. Therefore, the probability density function of the present model state should be estimated first according to all the prior information and available observations and then a method for forecasting the evolution of this PDF forward in time is needed. Usually, getting the current PDF is referred to Bayes data assimilation theory [30, 31].

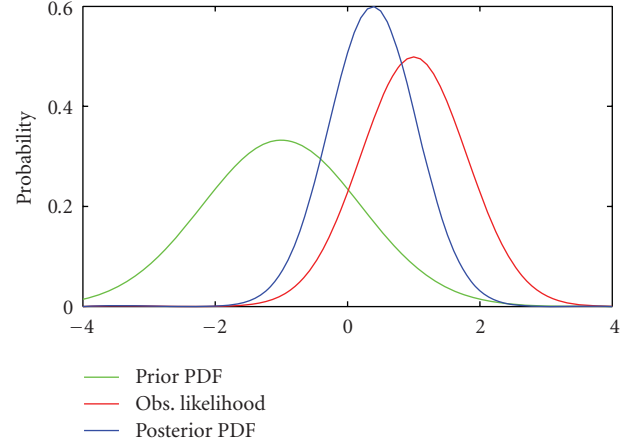


FIGURE 3: The observations (red curve), prior (green curve), and posterior (blue curve) probability density function given Gaussian error [32].

In the application of data assimilation, Bayes' theorem can be expressed as

$$P(X_t | Y_t) = \frac{P(Y_t | X_t)P(X_t | Y_{t-1})}{\text{denominator}}, \quad (1)$$

where $P(X_t | Y_t)$ denotes the probability density of the model state at time t ; X and Y are the state variables; $P(Y_t | X_t)$ denotes the probability density of the observations at time t ; and $P(X_t | Y_{t-1})$ is viewed as a kind of prior and represents the probability density of the prior ensemble forecast at time t . The denominator is a kind of normalization for guaranteeing that the total probability of all possible states is 1.

As shown above, (1) describes the way in which new observations are incorporated to modify the prior conditional probability density available from predictions based on earlier observations.

Taking an example, for Gaussian probability density, the prior is

$$P(X_t | Y_{t-1}) = \text{Normal}(\mu_p, \sigma_p), \quad (2)$$

where μ and σ are the mean and standard deviations, respectively. The subscript “ p ” denotes the “prior” state.

The observation PDF is given as

$$P(Y_t | X_t) = \text{Normal}(\mu_o, \sigma_o), \quad (3)$$

where the Gaussian probability density function given the mean μ and standard derivation error σ is

$$P(\mu, \sigma^2) = \frac{1}{\sqrt{2\pi\sigma^2}} e^{-(x-\mu)^2/2\sigma^2}. \quad (4)$$

Divide the product (named P' temporarily) of $P(Y_t | X_t)$ times $P(X_t | Y_{t-1})$ by a normalization denominator gives the posterior PDF as shown in Figure 3.

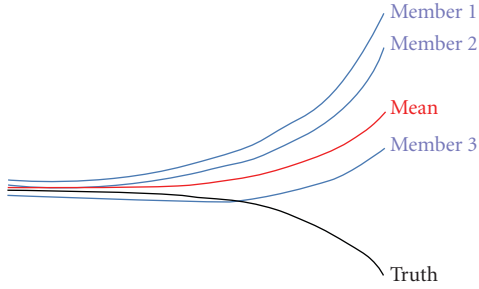


FIGURE 4: Monte Carlo forecast with finite sample.

After the above processes, we get the posterior estimate:

$$P(X_t | Y_t) = \text{Normal}(\mu_u, \sigma_u^2). \quad (5)$$

Here

$$\begin{aligned} \sigma_u^2 &= (\sigma_p^{-2} + \sigma_o^{-2})^{-1}, \\ \mu_u &= \sigma_u^2 [\sigma_p^{-2} \mu_p + \sigma_o^{-2} \mu_0]. \end{aligned} \quad (6)$$

4.2. Monte Carlo Method. Although we can solve for the posterior PDF in the previous section, it is not easy to express the PDF of the observations and the prior information explicitly in real operational numerical implementation. Therefore, it is difficult to obtain the posterior PDF of initial conditions directly from Bayes theorem.

Fortunately, the implementation of the Monte Carlo method provided us an effective approach to simulate the desired PDF with a random sample and to some extent solve the uncertainties of the initial conditions. However, the Monte Carlo method was conditionally effective only under an assumption that the number of sample members is sufficiently large in order to represent the PDF suitably. Consequently, the difficulty comes with the “large sample.” For instance, for a common real model with 10^7 degree of freedom, a $10^7 \times 10^7$ dimension calculation for estimating the PDF will be involved. That is demanding considering even the most recent computational advances.

Figure 4 shows schematically the forecast results under conditions when there are too few sample members doing the estimating. The mean forecast drifts away from the truth with time.

4.3. Ensemble Kalman Filter. Considering the limitations of traditional Bayes and Monte Carlo methods, a more practical technique is needed. With the most recent developments, ensemble Kalman filter data assimilation techniques, originated from the basic idea of the Monte Carlo theory and the well-known Kalman filter method, are successfully applied in many research and operational practices.

4.3.1. Basic Equations of Kalman Filter. As a sequential data assimilation method, the implementation of the Kalman filter [5, 33–35] includes two steps, which are named a forecast step and an analysis step. The model is integrated forward with time and used to update the model state by assimilating new observations when observations are available.

Kalman filter assumes that the prior conditional probability distribution is Gaussian and expresses it with its mean and covariance.

The analysis equation is

$$X^a = X^f + P^f H^T (H P^f H^T + R)^{-1} (d - H X^f), \quad (7)$$

where X^a is the analysis variables, X^f is the background fields (prior estimate), and d denotes observations. H , called the observational operator, connects the true state with observations within particular measurement errors:

$$d = H X^t + \varepsilon. \quad (8)$$

K is the so-called gain matrix:

$$K = P^f H^T (H P^f H^T + R)^{-1}. \quad (9)$$

In an extended Kalman filter, one must integrate the linear tangent model L_{i-1} in each forecast step to evolve the flow dependent forecast error covariance $P^f(t_i)$:

$$P^f(t_i) = L_{i-1} P^a L_{i-1}^T, \quad (10)$$

where the analysis error covariance is given as

$$P^a = P^f - P^f H^T (H P^f H^T + R)^{-1} H P^f. \quad (11)$$

Equations (9) and (10) perform as forecast step and (11) and (7) as the analysis step.

4.3.2. Ensemble Kalman Filter Theory. There are two main drawbacks of the extended Kalman filter method [36, 37]. One is that the simplified closure scheme used for estimating the error covariance results in an unbounded error growth while neglecting the third- and higher-order terms in the apparent closure scheme. Another is that Kalman filter poses an expensive cost due to the computational requirement of the error covariance matrix for the model forecast. From the previous Section 4.3.1, it is known that extended Kalman filter requires integrating the tangent linear model forward to get the error covariance estimation and hence expensive computational cost.

In theory, the error covariance of forecast estimation (background) is defined as:

$$P^f = \overline{(X^f - X^t)(X^f - X^t)^T}. \quad (12)$$

However, we never know the true atmosphere state (X^t). This makes the estimation of the background error covariance very difficult.

From Section 3, we have already learned that the ensemble mean could be the best estimation of the true state. Using this, the ensemble Kalman filter employs a group of ensemble members to represent the covariance statistics of the analyzed state. The ensemble is integrated in the nonlinear model to get a sample of the prior distribution at the next time when the observation is available as follows:

$$P^f = \overline{(X_i^f - \bar{X}^f)(X_i^f - \bar{X}^f)^T}. \quad (13)$$

Equation (13) indicates that a flow-dependent error covariance of forecast estimation can be obtained by using ensemble forecasting in practical implementation.

5. Implementation and Practical Issues on Ensemble Kalman Filter

5.1. Implementation of Ensemble Kalman Filters. Since the first attempt by Evensen [37], ensemble Kalman filter methods have been developed rapidly and used widely in data assimilation applications. There are two classes of basic approaches, referred to as the method with perturbed observations and the square root filter (without perturbed observations), to implement the ensemble Kalman filter as aforementioned. The perturbed observation algorithm updates each ensemble member with a different set of observations perturbed with random noise. Because randomness is introduced in every assimilation cycle, the update is considered stochastic. The square root filter methods do not add stochastic noise to the observations and are called deterministic algorithms. Evensen [37], Evensen and Van Leeuwen [38], as well as Houtekamer and Mitchell [39] originally implemented the ensemble Kalman filter with perturbed observations. Anderson [40], Bishop et al. [17], Baek et al. [41], Corazza et al. [42], Hunt et al. [43], Miyoshi and Yamane [44], Harlim and Hunt [45], as well as Yang et al. [46] contributed various square root filter algorithms including an ensemble adjustment Kalman filter [40], an ensemble transform Kalman filter [17], a local ensemble Kalman filter (for LEKF, see [41, 42]) and a local ensemble transform Kalman filter (for LETKF, see [43–46]). Whitaker and Hamill [47] indicated that the perturbed observations approach might introduce another kind of sampling errors; thus the square root algorithms methods are more accurate for a given ensemble size.

5.2. Comparison of the Ensemble Kalman Filter with 4DVar. Since the ensemble Kalman filter is becoming part of the operational choice, progress has been made to compare it with advanced data assimilation methods that are currently available. Specifically, a four-dimensional variational data assimilation (4DVar) method has been widely adopted in operational centers around the world. Owing to its capability in assimilating asynchronous observations and high-resolution observations such as satellite radiance and radar reflectivity, 4DVar method is indeed helpful for improving current numerical forecasting [48–50]. However, the requirement of the tangent linear and adjoint models

made the 4DVar method complicated in its implementation. Compared to 4DVar, the major merit of the ensemble Kalman filter is its simplicity of implementation. It does not need to develop and maintain tangent linear and adjoint model. It is model independent. One can easily switch to other models using ensemble methods [51, 52]. In addition, the ensemble Kalman filter represents and forwards forecast covariance using the ensemble sample without much effort. The main disadvantage of the ensemble Kalman filter comes with the sampling problem. The low ensemble size brings up sampling errors in the estimation of the background error covariance. The inflation tuning is employed to adjust this sample error in the practice.

Fertig et al. [53] studied the performance of 4DVar and 4D-LETKF in assimilating the asynchronous observations using the Lorenz 96 model [54]. Both schemes have comparable error when 4D-LETKF is cycled frequently and when 4DVar is performed over a sufficiently long analysis time window. Yang et al. [55] explored the relative advantages and disadvantages of the 4DVar and LEKF using a quasigeostrophic model and asserted that LEKF did better on both computational cost and accuracy when assimilating the same rawinsonde observations. Buehner et al. [56] evaluated the operational performance of both methods in Environment Canada using the same model and observations and obtained equivalent forecast scores. Kalnay et al. [51] offered a comprehensive comparison between 4DVar and ensemble Kalman filter. Based on results obtained using operational models and both simulated and real observations, they concluded that currently the ensemble Kalman filter is becoming competitive with 4DVar, and that the experience acquired with each of these methods can be used to improve the other.

In brief, due to its simple implementation and equivalent ability compared to 4DVar, the ensemble Kalman filter is becoming an attractive operational choice in more centers. However, the current ability of the ensemble Kalman filter is not equal to that of 4DVar in terms of assimilating satellite and radar observations. In order to utilize advantages from both methods, a hybrid approach, originally proposed by Hamill and Snyder [57], has received significant attention. Lorenc [52] asserted that hybrid approaches of variational methods and ensemble methods would be better than either single approach. Buehner et al. [56] showed that a hybrid approach based on 4DVar but using forecast covariance error estimation from the ensemble Kalman filter gave an improvement in 5-day forecasts in the southern hemisphere.

From the results of current studies, the hybrid method of the ensemble Kalman filter and 4DVar has a promising future since it combines the advantages of both methods and eliminates the existing disadvantages.

5.3. Nonlinear Issues in Ensemble Kalman Filter. Previous studies have proven that ensemble Kalman filter is capable of dealing with data assimilation in nonlinear system (e.g. [58]). However, nonlinearity is still an important issue in the implementation of ensemble Kalman filter. The equations introduced in Section 4.3.2 are valid only when the error

PDF are Gaussian. Unfortunately, in reality, even if the error PDF were Gaussian at the initial time, it would be non-Gaussian when the model is integrated forward due to the strongly non-linear model. In the case, the PDFs of errors cannot be represented by a Gaussian function. In addition, it is operationally impossible to assume a non-Gaussian error PDFs, although it looks feasible based on the current ensemble.

There have been many studies devoted to dealing with the nonlinear and non-Gaussian problem, mainly focusing on the development and implementation of the ensemble Kalman filter. For instance, Van Leeuwen [59] presented a true variance minimizing filter method. Its performance was tested by the Korteweg-DeVries equation and a quasi-geostrophic model. He addressed that the method works satisfactorily with a strongly nonlinear system. Hoteit et al. [60] evaluated a new particle-type filter based on a Gaussian mixture representation of the state PDFs using the Lorenz 96 model and discussed its application in real meteorological and oceanographic models. Yang and Kalnay [61] applied the outer-loop in LETKF to handle the nonlinear problem with the Lorenz 63 model. Results indicated that the LETKF with outer-loop could use a longer assimilation window and improve the analysis accuracy during highly nonlinear time periods.

6. Applications of Ensemble Forecasting and Ensemble Kalman Filters to High-Impact Weather Prediction

Owing to their advantages in beating the uncertainties and dealing with the nonlinearity, ensemble forecasting and ensemble-based data assimilation have received a lot of attention in the research and operational communities during the last decade. Specifically, they have been applied to high-impact weather forecasting. Many studies have documented results from these applications. The ensemble forecasting was used in short-range ensemble forecasting (SREF) [62–67], tropical cyclone forecasts [68, 69], as well as the flooding warning [70], and so forth. The ensemble-based Kalman filtering techniques were also applied for the studying and numerical simulation of hurricanes (see, e.g., [71]) and storm scale forecasts at high resolution (see, e.g., [72, 73]).

Du et al. [62] applied ensemble forecasting in quantitative precipitation forecasting (QPF). They found a remarkable reduction of root-mean-square error for QPF due to the ensemble application and asserted that the improvements from SREF techniques exceed the effect due to resolution doubling. After a short-range ensemble forecasting system was implemented in real-time operational at NCEP in 2001 [65], Du et al. [66] added another 6 members, which were generated from a weather research and forecasting (WRF) model, into the ensemble forecasting and obtained forecast improvements with increased ensemble spreads. Yuan et al. [67] studied the QPFs and probabilistic QPFs (PQPFs) over the southwest United States, the area that is marked by highly heterogeneous topography and diverse vegetation.

The hurricane track forecasting by Zhang and Krishnamurti [68] showed that the ensemble forecasts are superior to the results from single-model control experiments and the track position errors are largely reduced by the ensemble prediction. Mackey and Krishnamurti [70] combined ensemble forecasts with a high-resolution regional spectral model to postpredict the track, intensity, and flooding precipitation arising from Typhoon Winnie in August, 1997. They evaluated the effectiveness of the ensemble forecasting and found that the ensemble mean track would be superior only if the forecast uncertainty is properly sampled.

Zhang et al. [71] studied Hurricane Humberto (2007) using the ensemble Kalman filter method for assimilating Doppler radar radial velocity. Results indicated that the ensemble Kalman filtering analysis improved the representation of the track and intensity of Humberto. Tong and Xue [72] and Xue et al. [73] used the ensemble Kalman filter method and radar reflectivity to correct errors in fundamental microphysical parameters that are of great importance to microphysics schemes. The results show that the ensemble Kalman filter successfully corrected model errors in microphysical parameters.

7. Concluding Remarks

NWP is an initial value problem: it forecasts the atmospheric state by integrating a numerical model with given initial conditions. Due to inadequate observations, our limited understanding in physical processes of atmosphere, and the chaotic nature of the atmospheric flow, uncertainties always exist in modern NWP. Enhancing the predictability becomes a key issue in improving the skill of NWP.

In this paper, the ensemble forecasting and ensemble-based Kalman filter methods, both derived from concepts of the stochastic prediction, are overviewed. It can be concluded as follows.

- (i) Atmospheric motion, as an unstable system, has a finite predictability. NWP is strongly sensitive to the initial conditions. Uncertainties in the model physical parameterization also introduce errors into NWP. Due to strong nonlinearity and chaotic nature of the atmospheric flow, unpredictable components exist in reality.
- (ii) Ensemble forecasting takes uncertainties into account in initial conditions and/or model physical parameterizations to help produce improved forecasts over a single deterministic forecast in NWP and also provide probabilistic forecasts.
- (iii) The Ensemble Kalman filter refines the Monte Carlo method and traditional Kalman filter. It uses ensemble forecasts to express the flow-dependent error covariance of the forecast estimation. Ensemble Kalman filters present an effective way for data assimilation to improve model initial conditions, while at the same time also take uncertainties into account.

Owing to their advantages in beating the uncertainties and dealing with the nonlinearity in NWP, ensemble forecasting and ensemble-based data assimilation received a lot of attention in the research and operational communities during the last decade. Specifically, they have been applied to improve high-impact weather forecasting.

However, there are issues outstanding. As the ensemble forecasting requires large computational resources, many operational ensemble systems were implemented in coarser resolutions, compared with the high-resolution deterministic weather prediction models. Meanwhile, the small size of the ensemble could cause the underrepresentation problem when generating the background covariance for ensemble-based data assimilation. In addition, with perturbed initial conditions and various physical parameterizations, ensemble forecasts take into account both initial and model errors; however, there has not yet been a consensus regarding which one of these two methods is more efficient for accurate NWP in general. Moreover, the ensemble Kalman filter has many advantages over the current variational data assimilation systems. However, so far, the use of the ensemble Kalman filter in operational forecasts has been in a test phase. More studies are needed to make it a more powerful tool for assimilating real observations. In the meantime, a hybrid variational and ensemble Kalman filter method could be a promising technique in the near future.

Acknowledgments

The authors are grateful to three anonymous reviewers for their review comments that were helpful in improving this manuscript. This study is supported by U. S. National Science Foundation through Award no. ATM-0833985.

References

- [1] V. Bjerknes, *Dynamic Meteorology and Hydrography. Part II. Kinematics*, Carnegie Institute, Gibson Bros, New York, USA, 1911.
- [2] J. G. Charney, R. Fjörtoft, and J. V. Neumann, "Numerical integration of the barotropic vorticity equation," *Tellus*, vol. 2, pp. 237–254, 1950.
- [3] P. Thompson, *Numerical Weather Analysis and Prediction*, The Macmillan Company, New York, NY, USA, 1961.
- [4] G. J. Haltine, *Numerical Weather Prediction*, John Wiley & Sons, New York, NY, USA, 1971.
- [5] E. Kalnay, *Atmospheric Modeling, Data Assimilation and Predictability*, Cambridge University Press, Cambridge, UK, 2003.
- [6] E. N. Lorenz, "The predictability of hydrodynamics flow," *Transactions of the New York Academy of Sciences Series II*, vol. 25, no. 4, pp. 409–432, 1963.
- [7] E. N. Lorenz, "A study of the predictability of a 28-variable atmospheric model," *Tellus*, vol. 12, pp. 321–333, 1965.
- [8] T. N. Palmer, "Predictability of weather and climate: from theory to practice," in *Predictability of Weather and Climate*, chapter 1, pp. 1–29, Cambridge University Press, Cambridge, UK, 2006.
- [9] E. S. Epstein, "Stochastic dynamic prediction," *Tellus*, vol. 6, pp. 739–759, 1969.
- [10] Z. Toth and E. Kalnay, "Ensemble forecasting at NCEP: the generation of perturbations," *Bulletin of the American Meteorological Society*, vol. 74, pp. 2371–2330, 1993.
- [11] Z. Toth and E. Kalnay, "Ensemble forecasting at NCEP and the breeding method," *Monthly Weather Review*, vol. 125, no. 12, pp. 3297–3319, 1997.
- [12] R. Buizza and T. N. Palmer, "The singular-vector structure of the atmospheric global circulation," *Journal of the Atmospheric Sciences*, vol. 52, no. 9, pp. 1434–1456, 1995.
- [13] F. Molteni, R. Buizza, T. N. Palmer, and T. Petroliagis, "The ECMWF Ensemble prediction system: methodology and validation," *Quarterly Journal of the Royal Meteorological Society*, vol. 122, no. 529, pp. 73–119, 1996.
- [14] M. Ehrendorfer and J. J. Tribbia, "Optimal prediction of forecast error covariances through singular vectors," *Journal of the Atmospheric Sciences*, vol. 54, no. 2, pp. 286–313, 1997.
- [15] P. L. Houtekamer, L. Lefavre, J. Derome, H. Ritchie, and H. L. Mitchell, "A system simulation approach to Ensemble prediction," *Monthly Weather Review*, vol. 124, no. 6, pp. 1225–1242, 1996.
- [16] J. L. Anderson, "The impact of dynamical constraints on the selection of initial conditions for Ensemble predictions: low-order perfect model results," *Monthly Weather Review*, vol. 125, no. 11, pp. 2969–2983, 1997.
- [17] C. H. Bishop, B. J. Etherton, and S. J. Majumdar, "Adaptive sampling with the Ensemble transform Kalman filter. Part I: theoretical aspects," *Monthly Weather Review*, vol. 129, no. 3, pp. 420–436, 2001.
- [18] M. Wei, Z. Toth, R. Wobus, and Y. Zhu, "Initial perturbations based on the Ensemble transform (ET) technique in the NCEP global operational forecast system," *Tellus*, vol. 60, no. 1, pp. 62–79, 2008.
- [19] T. N. Krishnamurti, C. M. Kishtawal, Z. Zhang et al., "Multimodel Ensemble forecasts for weather and seasonal climate," *Journal of Climate*, vol. 13, no. 23, pp. 4196–4216, 2000.
- [20] V. V. Kharin and F. W. Zwiers, "Climate predictions with multimodel Ensembles," *Journal of Climate*, vol. 15, no. 7, pp. 793–799, 2002.
- [21] R. Buizza, M. Miller, and T. N. Palmer, "Stochastic representation of model uncertainties in the ECMWF Ensemble prediction system," *Quarterly Journal of the Royal Meteorological Society*, vol. 125, no. 560, pp. 2887–2908, 1999.
- [22] G. Shutts and T. N. Palmer, "The use of high-resolution numerical simulations of tropical circulation to calibrate stochastic physics schemes," in *Proceedings of the Simulation and Prediction of Intra-seasonal Variability with Emphasis on the MJO (ECMWF/CLIVAR '04)*, pp. 83–102, European Centre for Medium-Range Weather Forecasts, Reading, UK, 2004.
- [23] C. A. Reynolds, J. Teixeira, and J. G. McLay, "Impact of stochastic convection on the Ensemble transform," *Monthly Weather Review*, vol. 136, no. 11, pp. 4517–4526, 2008.
- [24] T. N. Palmer, "A nonlinear dynamical perspective model error: a proposal for non-local stochastic-dynamic parametrization in weather and climate prediction models," *Quarterly Journal of the Royal Meteorological Society*, vol. 127, no. 572, pp. 279–304, 2001.
- [25] G. Shutts, "A kinetic energy backscatter algorithm for use in Ensemble prediction systems," *Quarterly Journal of the Royal Meteorological Society*, vol. 131, no. 612, pp. 3079–3102, 2005.
- [26] J. Teixeira, C. A. Reynolds, and K. Judd, "Time step sensitivity of nonlinear atmospheric models: numerical convergence, truncation error growth, and Ensemble design," *Journal of the Atmospheric Sciences*, vol. 64, no. 1, pp. 175–189, 2007.

- [27] P. L. Houtekamer, L. Lefavre, J. Derome, H. Ritchie, and H. L. Mitchell, "A system simulation approach to Ensemble prediction," *Monthly Weather Review*, vol. 124, no. 6, pp. 1225–1242, 1996.
- [28] M. S. Tracton and E. Kalnay, "Operational Ensemble prediction at the National Meteorological Center: practical aspects," *Weather & Forecasting*, vol. 8, no. 3, pp. 379–398, 1993.
- [29] Z.-X. Pu and E. Kalnay, "Targeting observations with the quasi-inverse linear and adjoint NCEP global models: performance during FASTEX," *Quarterly Journal of the Royal Meteorological Society*, vol. 125, no. 561, pp. 3329–3337, 1999.
- [30] A. C. Lorenc, "Analysis methods for numerical weather prediction," *Quarterly Journal of the Royal Meteorological Society*, vol. 112, pp. 1177–1194, 1986.
- [31] T. M. Hamill, "Ensemble-based atmospheric data assimilation," in *Predictability of Weather and Climate*, pp. 124–156, Cambridge University Press, Cambridge, UK, 2006.
- [32] J. L. Anderson, "Data assimilation research testbed tutorial note," 2006, http://www.image.ucar.edu/DAReS/DART/DART_Documentation.php#tutorial_simple.
- [33] R. E. Kalman, "A new approach to linear filtering and prediction problems," *Transactions of the ASME: Journal of Basic Engineering, Series D*, vol. 82, pp. 35–45, 1960.
- [34] R. E. Kalman and R. Bucy, "New results in linear filtering and prediction theory," *Transactions of the ASME: Journal of Basic Engineering, Series D*, vol. 83, pp. 95–108, 1961.
- [35] G. Evensen, "The Ensemble Kalman filter: theoretical formulation and practical implementation," *Ocean Dynamics*, vol. 53, pp. 343–367, 2003.
- [36] G. Evensen, "Using the extended Kalman filter with a multi-layer quasi-geostrophic ocean model," *Journal of Geophysical Research*, vol. 97, no. 11, pp. 17905–17924, 1992.
- [37] G. Evensen, "Sequential data assimilation with a non-linear quasi-geostrophic model using Monte Carlo methods to forecast error statistics," *Journal of Geophysical Research*, vol. 99, no. 5, pp. 143–162, 1994.
- [38] G. Evensen and P. J. van Leeuwen, "Assimilation of geosat altimeter data for the agulhas current using the Ensemble kalman filter with a quasigeostrophic model," *Monthly Weather Review*, vol. 124, no. 1, pp. 85–96, 1996.
- [39] P. L. Houtekamer and H. L. Mitchell, "Data assimilation using an Ensemble Kalman filter technique," *Monthly Weather Review*, vol. 126, no. 3, pp. 796–811, 1998.
- [40] J. L. Anderson, "An Ensemble adjustment Kalman filter for data assimilation," *Monthly Weather Review*, vol. 129, no. 12, pp. 2884–2903, 2001.
- [41] S.-J. Baek, B. R. Hunt, E. Kalnay, E. Oott, and I. Szunyogh, "Local Ensemble Kalman filtering in the presence of model bias," *Tellus*, vol. 58, no. 3, pp. 293–306, 2006.
- [42] M. Corazza, E. Kalnay, and S. C. Yang, "An implementation of the Local Ensemble Kalman Filter in a quasigeostrophic model and comparison with 3D-Var," *Nonlinear Processes in Geophysics*, vol. 14, no. 1, pp. 89–101, 2007.
- [43] B. R. Hunt, E. J. Kostelich, and I. Szunyogh, "Efficient data assimilation for spatiotemporal chaos: a Local Ensemble transform Kalman filter," *Physica D*, vol. 230, no. 1–2, pp. 112–126, 2007.
- [44] T. Miyoshi and S. Yamane, "Local Ensemble transform Kalman filtering with an AGCM at a T159/L48 resolution," *Monthly Weather Review*, vol. 135, no. 11, pp. 3841–3861, 2007.
- [45] J. Harlim and B. R. Hunt, "Four-dimensional local Ensemble transform Kalman filter: numerical experiments with a global circulation model," *Tellus*, vol. 59, no. 5, pp. 731–748, 2007.
- [46] S.-C. Yang, E. Kalnay, B. Hunt, and N. E. Bowler, "Weight interpolation for efficient data assimilation with the Local Ensemble Transform Kalman filter," *Quarterly Journal of the Royal Meteorological Society*, vol. 135, no. 638, pp. 251–262, 2009.
- [47] J. S. Whitaker and T. M. Hamill, "Ensemble data assimilation without perturbed observations," *Monthly Weather Review*, vol. 130, no. 7, pp. 1913–1924, 2002.
- [48] C. Köpken, G. Kelly, and J.-N. Thépaut, "Assimilation of Meteosat radiance data within the 4D-Var system at ECMWF: assimilation experiments and forecasts impact," *Quarterly Journal of the Royal Meteorological Society*, vol. 130, no. 601, pp. 2277–2292, 2004.
- [49] J.-F. Mahfouf, P. Bauer, and V. Maréchal, "The assimilation of SSM/I and TMI rainfall rates in the ECMWF 4D-Var system," *Quarterly Journal of the Royal Meteorological Society*, vol. 131, no. 606, pp. 437–458, 2005.
- [50] P. Bauer, P. Lopez, A. Benedetti, D. Salmond, and E. Moreau, "Implementation of 1D+4D-Var assimilation of precipitation-affected microwave radiances at ECMWF. I: 1D-Var," *Quarterly Journal of the Royal Meteorological Society*, vol. 132, no. 620, pp. 2277–2306, 2006.
- [51] E. Kalnay, H. Li, T. Miyoshi, S.-C. Yang, and J. Ballabrera-Poy, "4-D-Var or Ensemble Kalman filter?" *Tellus*, vol. 59, no. 5, pp. 758–773, 2007.
- [52] A. C. Lorenc, "The potential of the Ensemble Kalman filter for NWP—a comparison with 4D-Var," *Quarterly Journal of the Royal Meteorological Society*, vol. 129, no. 595, pp. 3183–3203, 2003.
- [53] E. J. Fertig, J. Harlim, and B. R. Hunt, "A comparative study of 4D-Var and a 4D Ensemble Kalman filter: perfect model simulations with Lorenz-96," *Tellus*, vol. 59, no. 1, pp. 96–100, 2007.
- [54] E. N. Lorenz, "Predictability—a problem partly solved," in *Proceedings of the Seminar on Predictability*, ECMWF, September 1996.
- [55] S.-C. Yang, M. Corazza, A. Carrassi, E. Kalnay, and T. Miyoshi, "Comparison of Ensemble-based and variational-based data assimilation schemes in a quasi-geostrophic model," in *Proceedings of the 10th Symposium on Integrated Observing and Assimilation Systems for the Atmosphere, Oceans, and Land Surface*, 2007, <http://ams.confex.com/ams/pdfpapers/101581.pdf>.
- [56] M. Buehner, C. Charente, B. He, et al., "Intercomparison of 4-DVar and EnKF systems for operational deterministic NWP," 2008, http://4dvarekf.cima.fcen.uba.ar/Download/Session_7/Intercomparison_4D-Var_EnKF_Buehner.pdf.
- [57] T. M. Hamill and C. Snyder, "A hybrid Ensemble Kalman filter-3D variational analysis scheme," *Monthly Weather Review*, vol. 128, no. 8, pp. 2905–2919, 2000.
- [58] Z. Pu and J. Hacker, "Ensemble-based Kalman filters in strongly nonlinear dynamics," *Advances in Atmospheric Sciences*, vol. 26, pp. 373–380, 2009.
- [59] P. J. Van Leeuwen, "A variance-minimizing filter for large-scale applications," *Monthly Weather Review*, vol. 131, no. 9, pp. 2071–2084, 2003.
- [60] I. Hoteit, D.-T. Pham, G. Korres, and G. Triantafyllou, "Particle Kalman filtering for data assimilation in meteorology and oceanography," in *Proceedings of the 3rd International Conference on Reanalysis (WCRP '08)*, p. 6, Tokyo, Japan, 2008.
- [61] S.-C. Yang and E. Kalnay, "Handling nonlinearity and non-Gaussianity in Ensemble Kalman filter: Experiments with the three-variable Lorenz model," 2010, <http://www.atmos.umd.edu/~ekalnay/YangKalnay2010Rev.pdf>.

- [62] J. Du, S. L. Mullen, and F. Sanders, "Short-range Ensemble forecasting of quantitative precipitation," *Monthly Weather Review*, vol. 125, no. 10, pp. 2427–2459, 1997.
- [63] S. L. Mullen, J. Du, and F. Sanders, "The dependence of Ensemble dispersion on analysis-forecast systems: implications to short-range Ensemble forecasting of precipitation," *Monthly Weather Review*, vol. 127, no. 7, pp. 1674–1686, 1999.
- [64] H. Yuan, S. L. Mullen, X. Gao, S. Sorooshian, J. Du, and H.-M. H. Juang, "Verification of probabilistic quantitative precipitation forecasts over the southwest United States during winter 2002/03 by the RSM Ensemble system," *Monthly Weather Review*, vol. 133, no. 1, pp. 279–294, 2005.
- [65] J. Du and M.S. Tracton, "Implementation of a real time short-range Ensemble forecasting system at NCEP: an update," in *Proceedings of the 9th conference on Mesoscale processes*, pp. 355–356, American Meteorological Society, Fort Lauderdale, Fla, USA, 2001.
- [66] J. Du, J. McQueen, G. DiMego, et al., "New dimension of NCEP short-range Ensemble forecasting (SREF) system: inclusion of WRF members," WMO Expert Team Meeting on Ensemble Prediction System, Exeter, UK, February 2006, 5 pages, <http://www.emc.ncep.noaa.gov/mmb/SREF/reference.html>, Preprint.
- [67] H. Yuan, S. L. Mullen, X. Gao, S. Sorooshian, J. Du, and H.-M. H. Juang, "Verification of probabilistic quantitative precipitation forecasts over the southwest United States during winter 2002/03 by the RSM Ensemble system," *Monthly Weather Review*, vol. 133, no. 1, pp. 279–294, 2005.
- [68] Z. Zhang and T. N. Krishnamurti, "Ensemble forecasting of hurricane tracks," *Bulletin of the American Meteorological Society*, vol. 78, no. 12, pp. 2785–2795, 1997.
- [69] S. D. Abersson, M. A. Bender, and R. E. Tuleya, "Ensemble forecasting of tropical cyclone tracks," in *Proceedings of the 12th Conference on Numerical Weather Prediction*, pp. 290–292, American Meteorological Society, Phoenix, Ariz, USA, 1998.
- [70] B. P. Mackey and T. N. Krishnamurti, "Ensemble forecast of a typhoon flood event," *Weather & Forecasting*, vol. 16, no. 4, pp. 399–415, 2001.
- [71] F. Zhang, Y. Weng, J. A. Sippel, Z. Meng, and C. H. Bishop, "Cloud-resolving hurricane initialization and prediction through assimilation of doppler radar observations with an Ensemble Kalman filter," *Monthly Weather Review*, vol. 137, no. 7, pp. 2105–2125, 2009.
- [72] M. Tong and M. Xue, "Simultaneous estimation of micro-physical parameters and atmospheric state with simulated radar data and Ensemble square root Kalman filter. Part II: parameter estimation experiments," *Monthly Weather Review*, vol. 136, no. 5, pp. 1649–1668, 2008.
- [73] M. Xue, M. Tong, and G. Zhang, "Simultaneous state estimation and attenuation correction for thunderstorms with radar data using an Ensemble Kalman filter: tests with simulated data," *Quarterly Journal of the Royal Meteorological Society*, vol. 135, no. 643, pp. 1409–1423, 2009.